



# THÈSE

En vue de l'obtention du

## DOCTORAT DE L'UNIVERSITÉ DE TOULOUSE

Délivré par :

École Nationale Supérieure des Mines d'Albi-Carmaux conjointement avec l'INP Toulouse

---

**Présentée et soutenue par :**

**Marion Ducouso**

le jeudi 5 novembre 2015

**Titre :**

Gasification biochar reactivity toward methane cracking

---

**École doctorale et discipline ou spécialité :**

ED MEGEP : Génie des procédés et de l'Environnement

**Unité de recherche :**

Centre RAPSODEE, CNRS - UMR 5302, Ecole des Mines d'Albi-Carmaux

**Directeur/trice(s) de Thèse :**

Pr. Ange Nzihou  
Pr. Marco J. Castaldi

**Jury :**

M. Yann Rogaume Professeur, ENSTIB, INPL et Université de Lorraine, Rapporteur, Président  
M. Alain Thorel, Directeur de recherche, Mines ParisTech, Rapporteur  
Mme. Claire Courson, Maître de Conférences, ICPEES, Université de Lorraine, Examinatrice  
M. Ange Nzihou, Professeur, Ecole des Mines d'Albi-Carmaux, Directeur  
M. Marco J. Castaldi, Professeur, The City College of New York, Directeur  
Mme Elsa Weiss-Hortala, Maître assistant, Ecole des Mines d'Albi-Carmaux, Examinatrice



# Remerciements

Ces trois années de thèse ont été un réel parcours initiatique pendant lequel j'ai été encadrée, soutenue, aidée, écoutée, entourée par de nombreuses personnes pour qui j'ai beaucoup d'estime. Les mots justes ne sont pas faciles à trouver pour vous remercier comme il se doit !

Mes premiers remerciements vont pour mes encadrants, qui même s'ils m'ont mené la vie dure, ont su me donner des ailes ! Je souhaite ainsi remercier du fond du cœur mes deux directeurs de thèse Pr. Ange Nizhou et Pr Marco J. Castaldi pour m'avoir guidée vers le but à atteindre et, mon encadrante, Dr. Elsa Weiss-Hortala pour m'avoir accompagnée tout au long du chemin avec autant d'enthousiasme, d'écoute et de patience face à mes doutes. Je me suis réellement épanouie auprès de vous. Je garderai en mémoire des personnes passionnées par leur métier, qui savent transmettre leurs connaissances tout en laissant l'apprenant évoluer par lui-même. J'espère un jour pouvoir faire de même. A vous trois, un grand merci !

Au cours de ces trois années, j'ai sollicité toute une équipe de recherche : techniciens, ingénieurs, chercheurs, secrétaires qui m'ont apporté leur aide sans retenue. J'ai ainsi pu mener à bien le projet sereinement. Ainsi merci à : Mickaël Ribeiro, Pierre Bertorelle, Denis Marty, Jean-Marie Sabathier, Céline Boachon, Sylvie Delconfetto, Séverine Patry, Christine Rolland, Laurène Haurie, Nathalie Lyczko, Valérie Vérès, Christel Auriol et Anne-Marie-Fontès pour votre aide et votre bonne humeur !

Pendant cette formation, j'ai eu l'opportunité de participer aux activités d'enseignement à l'Ecole des Mines d'Albi. Ceci a été très formateur et j'ai beaucoup appris auprès des enseignants-chercheurs. Je souhaite spécialement remercier Dr. Jean-Jacques Letourneau, Dr. Patricia Arlabosse et Dr. Elsa-Weiss-Hortala.

« Mes compagnons de galère » étaient nombreux et je garde moult souvenirs de partage, d'entraide, également de stress mais aussi de joie avec bon nombre d'entre eux ! Du côté d'Albi, ma première pensée va à Marta, mon amie de toujours et pour toujours je l'espère ! Je suis très heureuse que nos routes se soient croisées. Je remercie également « les anciens » : Chams, Charlou, Baptiste, Hélène, Santiago, Moussa, Raphaele, Maxime, Masram, Haroun qui m'ont montré la voie et les trucs pour tenir bon ! Comme par exemple, « Ciel mon doctorat ». Pour les multiples bons moments quotidiens (le café du matin, Eurest à midi, les gâteaux d'anniversaire...) et l'aide inestimable au laboratoire (changer les bouteilles de gaz !!, étalonner la micro-GC !!....) je voudrais dire mille mercis à tous les copains : Bruna, Marwa, Elias, Maxime, Alex, Augustina, Rababe, Lucia,

Margot, Hugo, Haitem, Andrea, Paolo, Ludovic, Chaïma, Fanny, Léonard, Lina, Dung, Jun, Guillaume, Victor. Du côté de New York, j'ai été reçue très chaleureusement et j'ai passé d'excellents séjours grâce à Jeff, Naomi, Simona, Madhu, Franscesco, Swanand, Steven, Stéphanie, Timothy, Demetra, Robyn, Michaela, Kevin, Linnea. La vie est bien plus agréable quand on est bien entourée!

Pour finir, je voudrais dire encore une fois M E R C I à mes parents, ma sœur, ma tante, mon copain et sa famille, mes amis pour leur soutien avant, pendant et après la thèse ;).

à tous, - M E R C I -

# Content

<b>Résumé long français .....</b>	<b>V</b>
<b>Introduction .....</b>	<b>1</b>
<b>I. Chapter 1: Literature review .....</b>	<b>7</b>
Introduction: motivation to perform pyro-gasification .....	7
1. Biomass pyro-gasification basics .....	8
1.1. Biomass resources .....	8
1.2. Main steps and reactions in pyro-gasification process .....	12
1.3. Products: syngas, gas-phase co-products, tars, biochars and soots .....	15
1.4. Technologies consideration.....	17
1.5. Partial conclusion .....	19
2. Focus on the biochars.....	20
2.1. Surface physico-chemical properties .....	20
2.2. Origin of the reactivity of biochars in pyro-gasification process.....	31
2.3. Applications .....	37
2.1. Functionalisation .....	38
2.2. Partial conclusion .....	41
3. Catalytic methane cracking .....	42
3.1. Thermodynamics aspects .....	42
3.2. Metal supported catalysts.....	45
3.3. Carbonaceous materials .....	45
3.4. Partial conclusion .....	54
4. Conclusion .....	55
Bibliography.....	57
<b>II. Chapter 2: Materials and methods .....</b>	<b>65</b>
1. Experimental capabilities .....	65
1.1. Pyro-gasification of poplar wood under an H <sub>2</sub> O/N <sub>2</sub> mixture in a fluidized bed .....	66
1.2. Functionalization of the biochars surface .....	70

1.3.	Catalytic methane cracking on a fixed bed of biochars.....	73
2.	Biochars surface characterizations.....	79
2.1.	Proximate and ultimate analysis .....	80
2.2.	Minerals content .....	80
2.3.	Textural properties.....	83
2.4.	Oxygenated content.....	87
2.5.	Carbon structures.....	91
3.	Summary .....	97
	Bibliography.....	99
<b>III.</b>	<b>Chapter 3: Characterization of the raw and functionalized biochars .....</b>	<b>101</b>
1.	Raw biochar surface properties .....	101
1.1.	Oxygenated functions of the raw biochar.....	102
1.2.	Mineral content of the raw biochar .....	104
1.3.	Carbon matrix of the raw biochar .....	107
1.4.	Specific surface area and porosity of the raw biochar.....	109
1.5.	Partial conclusion on the physico-chemical properties of the raw biochar.....	110
2.	Oxygenated biochars surface properties .....	111
2.1.	Oxygenated functions on the oxygenated biochars.....	113
2.2.	Mineral content of the oxygenated biochars.....	120
2.3.	Carbon matrix of the oxygenated biochars.....	121
2.4.	Specific surface area and porosity of the oxygenated biochars.....	128
2.5.	Partial conclusion on the physico-chemical properties of the oxygenated biochars .....	130
3.	Impregnated biochars surface properties.....	132
3.1.	Oxygenated functions of the impregnated biochars.....	135
3.2.	Mineral content of the impregnated biochars.....	136
3.3.	Carbon matrix of the impregnated biochars.....	143
3.4.	Specific surface area and porosity of the impregnated biochars.....	145
3.5.	Partial conclusion on the physico-chemical properties of the impregnated biochars .....	146
4.	Conclusion on the characterization of the raw and functionalized biochars.....	148
	Bibliography.....	150

<b>IV. Chapter 4: Biochars reactivity towards methane cracking and the relation with their physico-chemical properties.....</b>	<b>153</b>
1. Comparison of the activities of the raw and functionalized biochars for methane cracking .....	154
1.1. Activity of the mineral impregnated biochars.....	155
1.2. Activity of the oxygenated biochars.....	157
1.3. Partial conclusion on the activities of the raw and functionalized biochars.....	159
2. Interaction between the biochars reactivity and their physico-chemical properties.....	160
2.1. Initial conversion .....	161
2.2. Deactivation by carbon deposit.....	179
3. Conclusion .....	184
Bibliography.....	188
<b>V. Chapter 5: Kinetics, mass transfer and modeling at the pore scale .....</b>	<b>191</b>
1. Apparent initial kinetics parameters and fitting of the deactivation equation .....	193
1.1. Mass balance in the plug-flow reactor and kinetics parameters determination.....	193
1.2. Initial kinetics parameters determination: experimental results.....	195
1.3. Deactivation of the biochars surface.....	197
2. Model of H <sub>2</sub> production at the pore scale.....	199
2.1. Introduction to heterogeneous reaction.....	199
2.2. Description of the hydrogen concentration evolution into a micropore.....	203
2.3. Results .....	214
3. Conclusion .....	222
Bibliography.....	224
<b>Conclusions and Prospects .....</b>	<b>225</b>
4. Conclusions.....	225
5. Prospects .....	231
Bibliography.....	236
<b>Appendices .....</b>	<b>A</b>
<b>Nomenclature .....</b>	<b>E</b>
List of Figures.....	x
List of tables .....	xvi



# **Résumé long en français**



Les problématiques de production énergétique et d'impact de notre mode de vie actuel sur le réchauffement climatique planétaire sont au cœur des débats politiques, sociétaux et scientifiques actuels. Un enjeu majeur de notre siècle est de résilier notre dépendance aux ressources fossiles et de développer des filières de production d'énergie respectueuses de l'environnement, des hommes et viables sur le long terme. Plusieurs voies se basant sur l'exploitation de ressources naturelles et renouvelables, telles les énergies solaires et éoliennes, sont actuellement explorées et offrent un avenir prometteur. Cependant, ces ressources ont pour majeur point faible une livraison d'énergie intermittente et dans une certaine mesure aléatoire. L'exploitation de la ressource biomasse a l'avantage de présenter une réserve « continue » d'énergie dont la quantité peut être planifiée et contrôlée. Elle permet ainsi une gestion sûre et efficace de l'énergie produite. La valorisation énergétique de la biomasse peut être opérée par deux types de procédés : biochimique et thermochimique. La conversion biochimique type estérification, digestion ou fermentation permet de produire notamment des biocarburants (bioéthanol, biodiesel) à partir de biomasse fourragère, betterave, tournesol ou canne à sucre. Elle représente une voie d'avenir pour notamment l'industrie des transports. Son inconvénient majeur est la compétition de ressource avec le secteur agricole. La valorisation de la biomasse peut également se faire par voie thermochimique. La torréfaction, la pyrolyse et la gazéification représentent les trois procédés principaux. Ils diffèrent de part la température de réaction et le réactif utilisé pour extraire l'énergie. La réaction de gazéification s'opère à haute température (700 à 1200°C) dans une atmosphère oxydante (H<sub>2</sub>O, CO<sub>2</sub>, O<sub>2</sub> ou air). Le carbone fixe constituant la biomasse réagit avec le gaz réactif par des réactions thermochimiques complexes pour former un gaz combustible riche en CO et H<sub>2</sub> appelé « gaz de synthèse » ou syngas en anglais. Selon le gaz réactif, nous observons préférentiellement l'un des deux réactions endothermiques présentées ci-dessous :



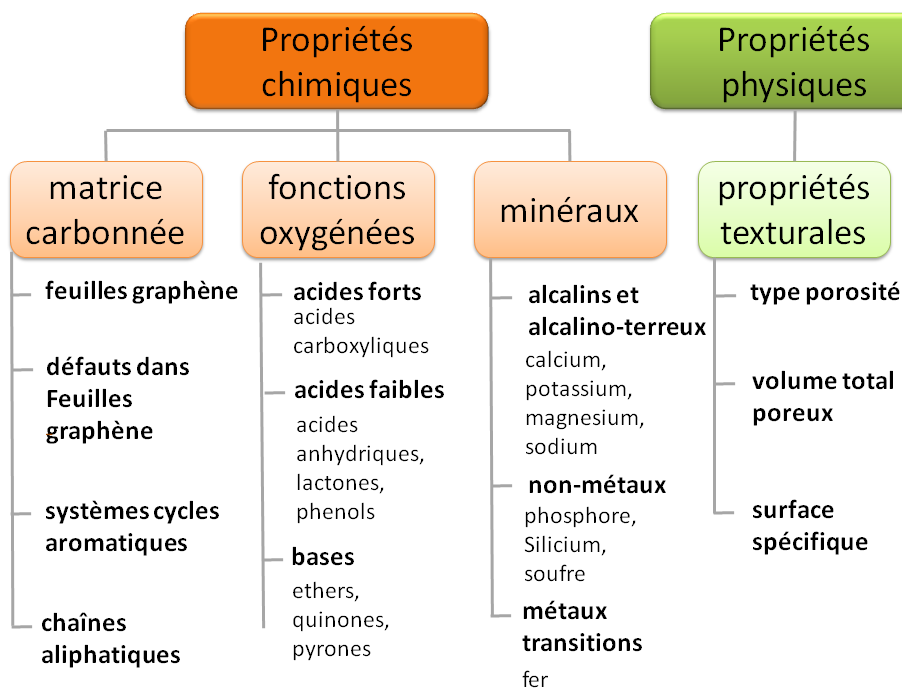
Ainsi le principal objectif du procédé de gazéification est de produire du gaz de synthèse qui pourra être par la suite valorisé pour de multiples applications telles que la production d'électricité, d'intermédiaires chimiques et de biocarburants. Ce procédé est très prometteur, cependant son développement à l'échelle industrielle est ralenti par des contraintes techniques, technologiques et

scientifiques. En effet, au cours de la chauffe, la biomasse se décompose en divers éléments organiques qui forment une fraction liquide à température ambiante et sont généralement regroupés sous le terme goudrons. Sont également produits des hydrocarbures légers notamment du méthane qui représente le deuxième co-produit gazeux après le dioxyde de carbone. Des polluants type sulfure d'hydrogène, ammoniac et des hydrocarbures aromatiques polycycliques (HAP) peuvent être présents dans la phase gazeuse, leurs concentrations varient selon le type d'entrant et des conditions de traitement. Enfin, le charbon ou char en anglais constitue la fraction solide au terme de la réaction. Ainsi la gazéification de la biomasse est un processus complexe donnant lieu à de nombreux co-produits. Pour accroître l'attractivité du procédé, il est nécessaire de traiter et valoriser ces différents co-produits.

L'objectif principal de cette étude consiste en la valorisation du résidu solide, le charbon, en tant que catalyseur de réaction de craquage d'hydrocarbures. L'idée qui sous-tend le projet est de réintroduire le charbon dans le procédé de gazéification, en aval du réacteur principal pour améliorer le rendement et purifier en gaz de synthèse. Un projet de doctorat, mené par Naomi Klinghoffer, qui représentait la première collaboration entre le centre RAPSODEE et le « Combustion and Catalysis laboratory », a démontré le pouvoir catalytique des charbons de gazéification de biomasse pour des réactions de craquage d'hydrocarbures. Cependant, la complexité des propriétés physico-chimiques des charbons a représenté un verrou pour la compréhension du mécanisme catalytique. Cette étape de compréhension est cruciale pour envisager une introduction des charbons en tant que catalyseurs à l'échelle industrielle. Ainsi, ce second projet de doctorat fait suite à l'étude menée par Naomi Klinghoffer et est axé sur la compréhension des phénomènes mis en jeu lors du craquage catalytique d'hydrocarbures sur lit de charbons de gazéification. Nous avons sélectionné le méthane comme gaz réactif pour différentes raisons : il est le second co-produit gazeux après le méthane, il est une molécule modèle pour le craquage de la liaison C-H, il est également l'hydrocarbure le plus stable. De plus, la réaction de craquage du méthane conduit à une amélioration du rendement de production d'hydrogène. Ainsi, cette étude s'attache à comprendre le mécanisme de craquage catalytique du méthane sur un lit de charbons issus de la gazéification de biomasse.

Les travaux précédents de l'équipe et la bibliographie ont identifié que l'activité catalytique des charbons était contrôlée par ses propriétés physico-chimiques. Cependant, le charbon est un matériau très complexe de part sa composition chimique et ses propriétés physiques. Propriétés, qui sont, de plus, dépendantes de la ressource et du mode de traitement thermique. Le charbon est un matériau hautement carboné, contenant une fraction faible de minéraux, notamment des alcalins et alcalino-terreux et des hétéroatomes types oxygène, azote, hydrogène. Ceux sont également des structures généralement poreuses et développant une surface spécifique importante. Pour la

réaction catalytique de craquage d'hydrocarbures, quatre propriétés physico-chimiques des charbons ont été identifiées comme importantes : la structure de la matrice carbonée, la composition en fonctions oxygénées, la composition minérale et la porosité/ surface spécifique. Dans ces quatre familles de propriétés, nous pouvons également dénombrer différentes sous-familles. La Figure\_R 1 schématise ces différentes propriétés.

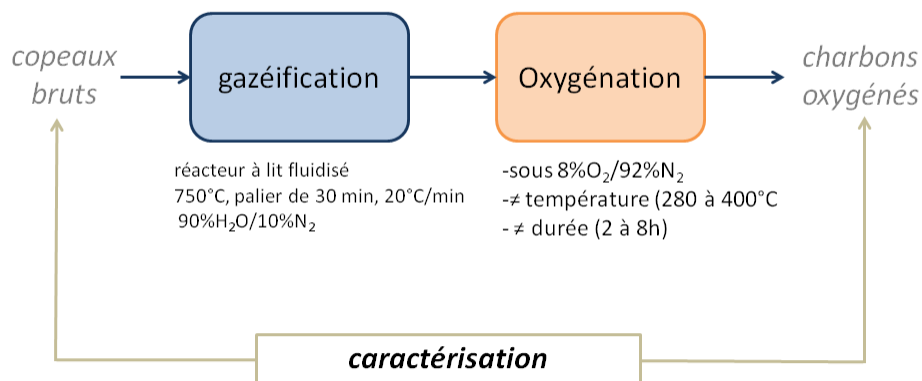


**Figure\_R 1 : Schéma présentant les 4 propriétés physico-chimiques importantes pour les charbons ainsi que les sous-familles**

Pour comprendre la réactivité des charbons, nous avons fait le choix de comparer l'activité catalytique de charbons dont les propriétés physico-chimiques étaient différentes. Dans un premier temps, nous avons produit un charbon dit « brut » à partir de la gazéification de copeaux de bois de peuplier dans un réacteur à lit fluidisé à 750°C, 90% $H_2O$ /10% $N_2$  pour un palier de 30 min et avec une vitesse de chauffe de 20°C/min. Puis nous avons réalisé des traitements dits de « fonctionnalisation » afin de modifier les propriétés de surface ciblées. Le premier traitement avait pour objectif d'augmenter la teneur en fonctions oxygénées à la surface des charbons, nous avons donc opéré une campagne d'oxygénation des charbons sous une atmosphère contrôlée (8% $O_2$ / 92% $N_2$ ) pour différentes températures et durées. Le second traitement visait à augmenter la concentration en minéraux et notamment en calcium et potassium dans les chars. Pour se faire, nous avons imprégné

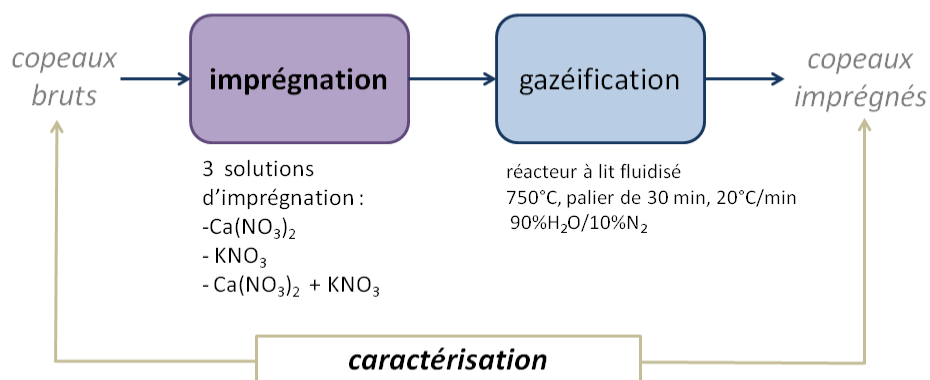
les copeaux de bois avant la gazéification dans des solutions de nitrate de calcium et de nitrate de potassium. Nous avons ainsi produits des charbons bruts et fonctionnalisés dont nous avons caractérisés les propriétés de surface et que nous avons testés pour la réaction de craquage catalytique du méthane. La Figure\_R 2 résume le processus de production et de fonctionnalisation des différents charbons. La Table\_R 1 résume les différents charbons produits.

## Oxygénation des charbons



Objectif : augmenter la concentration des fonctions oxygénées

## Imprégnation des copeaux de peuplier



Objectif : augmenter la teneur en calcium et potassium dans les chars imprégnés

Figure\_R 2 : Schémas présentant le processus de production et de fonctionnalisation des charbons

**Table\_R 1 : Résumé des charbons brut et fonctionnalisés produits dans cette étude**

#	Abréviation	Description
1	char_brut	Charbon brut de gazéification de bois de peuplier (réacteur à lit fluidisé à 750°C, 90%H <sub>2</sub> O/10%N <sub>2</sub> , 30 min, 20°C/min)
2	ox2h_280C	Charbon oxygéné pendant 2 h à 280°C (oxygénation)
3	ox4h_280C	Charbon oxygéné pendant 4 h à 280°C (oxygénation)
4	ox8h_280C	Charbon oxygéné pendant 8 h à 280°C (oxygénation)
5	ox16h_280C	Charbon oxygéné pendant 16 h à 280°C (oxygénation)
6	ox2h_340C	Charbon oxygéné pendant 2 h à 340°C (oxygénation)
7	ox2h_400C	Charbon oxygéné pendant 2 h à 400°C (oxygénation)
9	Ca-char	Char imprégné pendant 6h dans une solution de nitrate de calcium (0,5 % <sub>massique</sub> )
10	K-char	Char imprégné pendant 6h dans une solution de nitrate de potassium (0,5 % <sub>massique</sub> )
11	Ca+K-char	Char imprégné pendant 6h dans une solution de nitrate de calcium et potassium (0,25 % <sub>massique</sub> )

Une fois les différents charbons produits, nous avons mené une campagne de caractérisation de leurs propriétés physico-chimiques. Comme présenté précédemment, nous nous sommes attachés à caractériser la matrice carbonée, la nature et teneur en sites oxygénés et minéraux et nous avons également évalué la porosité et surface spécifique de ces différents charbons. Les différentes techniques qui ont été utilisées pour l'étude sont présentées dans la Table\_R 2. Le charbon brut est un résidu microporeux développant une surface spécifique de l'ordre de 660 m<sup>2</sup>/g. Sa matrice carbonée est très complexe contenant à la fois des structures graphitiques ordonnées, désordonnées, des systèmes cycliques aromatiques et des carbones insaturés. Il contient également une forte concentration en groupes oxygénés de différente nature (acides forts, faibles et bases) et une concentration de minéraux de 3%<sub>massique</sub> (majoritairement du calcium et du potassium). Concernant les charbons oxygénés, nous avons observé que l'oxygénation pour les trois températures testées et les différents temps de séjour ont conduit à augmenter la concentration globale en groupes oxygénés à la surface. Les concentrations maximales ont été obtenues pour les températures d'oxygénation les plus hautes (concentration globale multipliée par 2). Nous avons également pu observer que ce mode d'oxygénation favorisait la formation de sites oxygénés acides (faibles) à la surface des charbons. L'oxygénation a également eut un impact sur la porosité et la matrice carbonée des différents charbons. En effet, une partie de la matrice carbonée a réagit avec l'oxygène par combustion. Aux plus hautes températures de traitement (340 et 400°C), cela a conduit à augmenter la porosité et la surface spécifique des charbons (atteignant jusqu'à 859 m<sup>2</sup>/g au lieu de

662 m<sup>2</sup>/g) et a également augmenté la concentration de défauts dans la matrice. La Table\_R 3 résume les différents résultats. Pour les trois chars imprégnés, nous avons observé une augmentation de la concentration en calcium et potassium (selon l'imprégnation) de 2 à 10 fois celles du charbon brut (voir Table\_R 3). L'imprégnation, de part l'inclusion de particules de minéraux dans la matrice, a augmenté le nombre de défauts dans la structure et a réduit significativement la surface spécifique. Toutes les informations relatives aux caractérisations des charbons sont résumées dans la Table\_R 3.

**Table\_R 2 : Moyens de caractérisation utilisés pour l'étude des propriétés physico-chimiques des charbons**

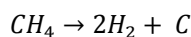
<b>Propriétés physico-chimiques</b>	<b>Type d'analyse</b>	<b>Informations récoltées</b>
<b>Matrice carbonée</b>	-Spectroscopie RAMAN -Microscopie à transmission électronique à balayage	-Distribution des structures carbonées -Nanostructure
<b>Fonctions oxygénées</b>	-Spectroscopie infra-rouge à transmission de Fourier -Programme de température de désorption	-Nature des fonctions oxygénées -Quantification
<b>Minéraux</b>	-Fluorescence-X -Diffraction de rayon-X -Microscopie électronique à balayage	-Analyse élémentaire -Structures cristallines -Distribution et morphologie de particules
<b>Propriétés texturales</b>	-Adsorption gaz	-Type de porosité -Surface spécifique -Surface spécifique

Table\_R 3 : Résumé des propriétés physico-chimiques des charbons brut et fonctionnalisés

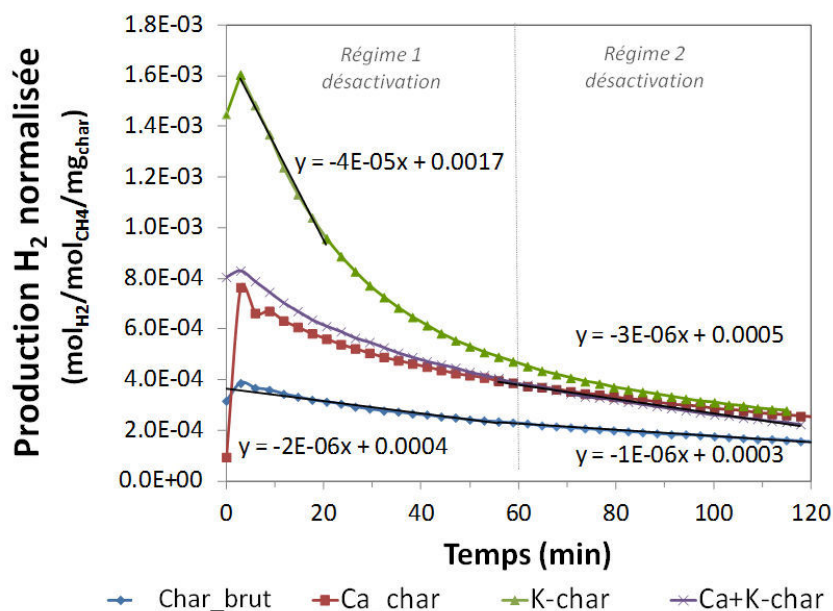
	Matrice carbonée			Groupes oxygénés		Minéraux		Propriétés texturales	
	Graphite %	Défauts %	Amorphe %	Concentration	Nature	Concentration	Structure	S <sub>spécifique</sub> m <sup>2</sup> /g <sub>char</sub>	V <sub>micropores</sub> cm <sup>3</sup> /g <sub>char</sub>
Char_brut	26	25	27	-	-	[Ca]≈ [K]	CaCO <sub>3</sub> K <sub>2</sub> CO <sub>3</sub>	662	0,22
Ox_2h_280°C	25	26	29	1,2*[O] <sub>cb</sub>	acides faibles	≈ cb*	≈ cb	622	0,22
Ox_4h_280°C	26	26	27	1,5*[O] <sub>cb</sub>	acides faibles	≈ cb	≈ cb	578	0,21
Ox_8h_280°C	23	28	28	1,5*[O] <sub>cb</sub>	acides faibles	≈ cb	≈ cb	564	0,21
Ox_2h_340°C	30	33	20	1,5*[O] <sub>cb</sub>	acides faibles	≈ cb	≈ cb	808	0,30
Ox_2h_400°C	28	39	16	1,2*[O] <sub>cb</sub>	acides faibles	≈ cb	≈ cb	859	0,32
Ca-char	23	33	22	-	-	4*[Ca] <sub>cb</sub>	CaCO <sub>3</sub>	619	0,24
K-char	24	30	24	-	-	10*[K] <sub>cb</sub>	KHCO <sub>3</sub>	446	0,15
Ca+K-char	22	31	23	-	-	2*[Ca] <sub>cb</sub> 5*[K] <sub>cb</sub>	CaCO <sub>3</sub> K <sub>2</sub> CaCO <sub>3</sub>	346	0,12

\*cb : charbon brut

L'étape suivante a consisté à tester le pouvoir catalytique des différents charbons lors du craquage du méthane à 700°C. La réaction principale de craquage du méthane produit de l'hydrogène et un dépôt de carbone à la surface du catalyseur (voir Eq\_R. 3). La Figure\_R 3 compare la production d'hydrogène lors du craquage du méthane sur les charbons bruts et imprégnés. Nous observons une nette augmentation de la production d'hydrogène pour les trois charbons préalablement imprégnés. Le charbon dont la concentration en potassium a été augmentée présente la production initiale d'hydrogène la plus élevée (4 fois plus élevée que celle du charbon brut). La production pour les deux autres charbons imprégnés est équivalente et est 2 fois plus élevée que celle du charbon brut. Ces résultats soulignent l'activité catalytique des minéraux type calcium et potassium pour cette réaction. Sur la Figure\_R 3, on peut également observer une diminution de la production d'hydrogène au cours du temps pour les différents charbons, ceci est dû au dépôt de carbone sur la surface du catalyseur qui désactive les sites actifs (voir Eq\_R. 3). Pour une meilleure compréhension du mécanisme et de son effet sur l'activité catalytique, nous avons développé un modèle à l'échelle du pore qui est présenté à la fin du résumé.

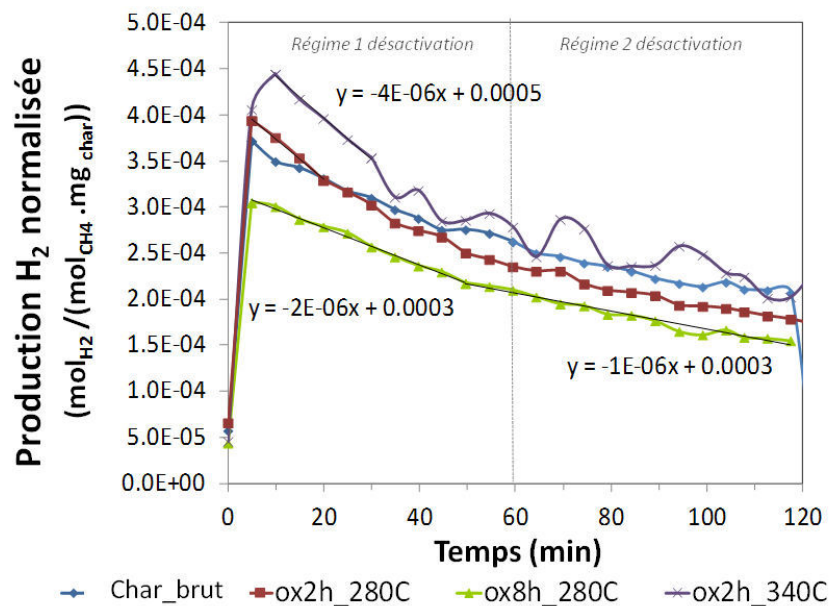


Eq\_R. 3



Figure\_R 3 : Comparaison des activités catalytiques des charbons brut et imprégnés dans des solutions de nitrates de calcium et potassium

Nous avons également comparé l'activité du charbon brut et des charbons oxygénés lors de la réaction du craquage du méthane. La production d'hydrogène pour les différents charbons est présentée en Figure\_R 4. Dans ce cas-ci, nous n'observons pas un gain significatif concernant la production initiale d'hydrogène. Nous identifions, cependant, une diminution de la production d'hydrogène, au cours du temps pour les différents charbons, qui est due à la désactivation du catalyseur. De part l'étape de caractérisation des charbons et l'étude bibliographique, nous pouvons conclure que le rendement du craquage d'hydrogène n'a pas été amélioré pour les charbons oxygénés car l'étape d'oxygénation a conduit à augmenter la concentration de sites oxygénés instables à 700°C (acides faibles). Cependant, les sites oxygénés basiques type quinone, stables à cette température, sont restés en concentration égale. Ainsi, nous pouvons conclure que seulement certains sites oxygénés, stables à haute température (sites basiques), peuvent être des sites actifs pour la réaction de craquage du méthane.



**Figure\_R 4 : Comparaison des activités catalytiques des charbons brut et oxygénés**

Ainsi, la comparaison des activités catalytiques des charbons brut et fonctionnalisés, couplée à une étape de caractérisation des propriétés physico-chimiques de surface des différents charbons a permis de classer les différentes propriétés par ordre d'importance pour le rendement catalytique. La concentration en minéraux type calcium et potassium est le critère majeur pour déterminer l'activité catalytique. La porosité et la surface spécifique se positionne en second. La concentration en sites oxygénés et la nature de la matrice carbonée sont également des critères importants.

Cependant, concernant les sites oxygénés, seuls les sites basiques, stables à haute température, peuvent être sites actifs. Pour la matrice carbonée, les défauts de structure type lacune, hétéroatomes dans les feuilles de graphène sont les principales structures réactives. En conclusion, le charbon idéal pour catalyser la réaction de craquage du méthane, doit être poreux et contenir des particules dispersées de minéraux type calcium et potassium. Il devrait également avoir une structure carbonée désordonnée contenant des sites oxygénés basiques.

Dans un dernier temps, nous avons travaillé sur la cinétique globale de la réaction et le développement d'un modèle à l'échelle du pore du charbon, couplant réaction de surface et diffusion dans le pore, pour mieux appréhender le mécanisme. En effet, pour comprendre les phénomènes de surface à l'échelle microscopique, l'expérimentation est limitée, nous avons donc travaillé sur un modèle numérique. Nous avons développé un modèle 2-D, à l'aide du logiciel Matlab®, qui représente l'évolution de la concentration d'hydrogène dans un pore cylindrique, produit par la réaction de craquage catalytique du méthane sur des sites actifs de la surface. Nous avons simplifié le modèle en ne prenant en compte que 2 types de sites actifs, ayant une concentration initiale et une réactivité différente. Nous avons regardé l'influence de 2 paramètres : la concentration initiale des sites actifs et la constante de vitesse cinétique associée. Nous avons ainsi observé que plus la constante de vitesse associée à un type de site actif était élevée, plus la désactivation du catalyseur était rapide, ce qui confirme l'expérimentation (voir Figure\_R 3). Concernant, la concentration initiale des 2 types de sites actifs, plus la concentration des sites actifs les plus réactifs est élevée, plus la production initiale d'hydrogène est élevée. Ainsi, nous avons développé un modèle qui peut être complexifié pour améliorer notre compréhension des phénomènes de catalyse hétérogène.

En conclusion, cette étude de doctorat, menée en collaboration au centre RAPSODEE et au Combustion & Catalysis Laboratory, s'est attachée à comprendre la réactivité des charbons de gazéification lors de la réaction du craquage du méthane. Pour mener à bien le projet, des charbons ont été produits, fonctionnalisés, caractérisés et testés pour la réaction du craquage du méthane. Nous avons ainsi pu hiérarchiser les différentes propriétés de surface pour un rendement optimum. Nous avons également développé un modèle, comme outil de compréhension du mécanisme catalytique à la surface du charbon.

# **Introduction**



A challenge of this century is to successfully manage the transition from a petroleum-based economy to the one based on sustainable energies. It has been recognized that the global warming is directly correlated to the extensive use of fossil fuels this past century which drastically increased the atmospheric concentration of greenhouse gases (since 2000, anthropogenic CO<sub>2</sub> emissions have risen by more than 3% annually) [1]. The continuous growth in the primary energy demand, the fossil fuels feedstocks rarefaction, and the alarming impact of our current mode of energy production on the climate change pushed the international community to consider alternative solutions to conciliate preservation of the environment and energy consumption of the actual modern life. Different strategies and political guidelines have been considered to introduce alternative energies in energy production and to consider a better energy efficacy to reduce the global consumption of the fossil fuels energies in the long-term. At the European scale, the strategic politic goal is described such as the “3 x 20” rule which aims to reach by 2020:

- 20% reduction of greenhouse gases emission compared to 1990,
- 20% energy savings regarding the storyboard described by the European commission,
- 20% of the energy final consumption from renewable sources [2].

In France, the “Plan d’action National” targets that 23% of global energy production will be produced from renewable resources by 2020 (in 2013 it represented 14.2%). The distribution of the renewable energies effort is planned such as following:

- 10% of the energy required for transportation,
- 27% of the electrical energy,
- 33% of the heating and cooling productions.

In 2013, the part of the renewable energy in the transportation field, renewable electricity and thermal energy represented 7.1, 17.1 and 18.3% of the total production respectively which corresponds to about 65% of the final objective by 2020 [3]. Among the different renewable energies (hydraulic, biomass, geothermal energy, wind and solar powers), biomass is one of the most often considered source of renewable energy [4], [5]. Technologies which have been developed to extract energy from biomass can support heating, electricity and transportations needs. Biodiesel, ethanol, biomass agglomerates are becoming important biofuels resources worldwide. In Europe, several community-based district heating projects are currently developed based on biomass feedstocks. Another European dynamics is the development of biomethane production from the fermentation of organics. This biomethane could be injected in the natural gas system and further utilized for heating, electricity or biofuels production. Worldwide in 2011, United States have been the first producer of electricity from biomass followed by Europe, Brazil, China, India and Japan. The

expansion of energies based on biomass feedstocks support the developing countries to access to energy. In fact, countries in Africa and Brazil which grow sugar cane manage to generate electricity and heating from bagasse feedstocks [6]. Hence, biomass offers a large variety of feedstocks which can be utilized for various applications and are adaptable to different scales of production.

Biofuels are often classified into three categories: 1<sup>st</sup> (rapeseed, sunflower, beet, wheat and corn starch), 2<sup>nd</sup> (ligno-cellulosic) and 3<sup>rd</sup> (algae) generations. The 1<sup>st</sup> generation of biofuels is based on biochemical processes such as fermentation, digestion and esterification to produce ethanol and biodiesel. However, this energy chain directly competes with the food and pharmaceutical fields. In the 2<sup>nd</sup> generation of biofuels, thermochemical processes have been developed to convert ligno-cellulosic biomass (which cannot be transformed via biochemical processes) into energy. A large variety of biomass such as wood, straw, agricultural, forestry or even municipal wastes can be potential feedstocks. Three thermochemical processes: combustion, pyrolysis and gasification are usually presented in the literature. They are all based on the thermal degradation of the biomass but differ from the final application and the operating conditions. Combustion mainly consists in producing heat from the burning of biomass while pyrolysis is dedicated to the production of liquid biofuels from the heating at moderate temperature (400-700°C) under inert atmosphere and gasification generates, at high temperature (700 to 1200°C) under an oxidizing atmosphere (air, H<sub>2</sub>O, CO<sub>2</sub>), a high energetic product called the syngas (gaseous mixture of hydrogen and carbon monoxide). Syngas could be utilized in various applications such as the production of biofuels, chemicals or electricity. Thus, outlet for syngas applications are multiple and represent a serious alternative to fossil fuels energy. However, gasification process suffers from scientific, technologic and technical bottlenecks which slow down its industrial development. Among the different issues, the syngas yield enhancement, its cleaning and upgrading (removal of tars: heavy organics co-products) drive the attention of many researchers from several years [5], [7], [8]. In addition, the management of the undesirable co-products of gasification, and notably the treatment of the solid carbonaceous residue so called biochar, is time-consuming and costly to treat. Recent researches highlighted the catalytic performances of biochars for hydrocarbon cracking (present in tars) [9], [10]. A promising project is the valorization of the biochar such as catalyst for syngas cleaning and upgrading. This represents an opportunity to directly valorize the biochar (without any transportation issue) and to replace costly commercial based catalysts (which are used for syngas upgrading so far). Our research team took part in this global investigation since several years [11], [12]. Previous work investigated the biochars catalytic activity for different hydrocarbons cracking such as toluene, propane and methane. In addition, researches focused on the understanding of its reactivity were carried out. However, the biochar structure is highly complex, since it comes from a

natural resource. Thus, different aspects of the biochars reactivity are not well understood yet. This study is in the continuity of the previous works performed in the team with the emphasis on the investigations of the catalytic reactivity of the biochar surface. The methane cracking has been selected as the model reaction to test the biochar activity. In fact, the methane is the second major co-product (after carbon dioxide) in the pyro-gasification process and it is also a model molecule for the C-H breaking which is present in hydrocarbons. To reach the objective foreseen, the catalytic activity of the biochar has been studied in relation with its surface physico-chemical properties. In addition, the surface deactivation mechanism over the methane cracking reaction (due to carbon deposit at the surface) is studied in relation with the biochars surface properties as well. To carry out this project, a standard biochar has been produced from the pyro-gasification at 700°C of poplar wood under steam. The conditions of the pyro-gasification have never been changed. However, to investigate the interactions between the physico-chemical properties of the biochars and its reactivity, several intermediate steps have been followed:

- A set of functionalization treatments (oxygenation and minerals impregnation) of the biochar surface has been performed. The main objective was to enhance the concentration of chemical species (oxygen groups, Alkali and Alkaline Earth Minerals: AAEMs) which have been highlighted to be active sites in catalytic reaction,

- A rigorous step of surface properties characterization to provide a screenshot of the global properties of the different biochars was carried out (oxygen groups, minerals content, carbon matrix and textural properties),

- A protocol of methane cracking tests on biochars has been developed,

- A kinetics study and a numerical modeling were investigated to go further in the understanding of the methane cracking reaction and deactivation.

Thus, this thesis work is composed of 5 chapters:

- **Chapter I** is dedicated to the literature review which first presents some basics of biomass gasification and main technologies followed by the description of the different technological, technical and scientific bottlenecks quoted previously. Then, an extensive presentation of the biochar surface properties, reactivity and potential applications is provided. In a third and last

section, the literature review regarding the catalytic methane cracking on carbonaceous materials is presented and more specifically the interaction between the physico-chemical surface properties and the reactivity.

- **Chapter II** presents the materials and methods which have been employed to carry out the different biochar production, functionalization, methane catalytic tests and surface characterization. Well-known techniques such as Brunauer-Emmett-Teller (BET) analysis, Transmission Electron Microscopy (TEM), Scanning Electron Microscopy (ESEM), X-ray Diffraction (XRD), X-ray fluorescence (XRF) and Fourier Transform Infrared spectroscopy (FTIR) have been used to investigate the physico-chemical surface properties of the biochars. In addition, some techniques more specific to the study of carbonaceous materials such as Raman spectroscopy and Temperature Programmed Desorption (TPD) have been carried out to study more specifically the carbon structures distribution and the oxygenated content.
- **Chapter III** is focused on the extensive characterization of the raw and functionalized biochars surface properties. In one hand, a part of the characterizations led to evaluate the efficiency and selectivity of the functionalization treatments (characterization of the oxygen groups and AAEMs minerals content). On the other hand, a second set of characterizations has been carried out to evaluate the indirect impact of the functionalization treatments on other physico-chemical properties (carbon structures and textural properties) of the surface which are depicted to be involved in the catalytic activity of the biochar during methane cracking.
- **Chapter IV** is dedicated to the catalytic methane cracking tests. First, it has been highlighted that the raw biochar is a catalyst for the methane cracking reaction at 700°C. Then, the global activities of the raw, oxygenated and minerals impregnated biochars are presented and compared (also performed at 700°C). The deactivation of the surface due to carbon deposit is also approached. In the second section, the reactivity of the different biochars is discussed in relation to their physico-chemical properties. This second part is composed of two sections: the first one is focused on the initial reactivity which corresponds to the activity of the fresh catalyst surface. Then, the deactivation is discussed in function of the coke deposit impact on the different physico-chemical properties.
- **Chapter V** presents the kinetics study at the reactor scale and the modeling work. The kinetics investigation has been performed at the reactor scale to determine initial apparent kinetics

parameters and more specifically the activation energy (from experimental data) which gives insights into the performances of the catalyst. In the same section, a fit of the experimental data with a well-known empirical expression of coke concentration deposit has been performed to confirm the phenomenon of surface deactivation. In a last section, a modeling at the pore scale to get better insights into the surface deactivation mechanism and hydrogen concentration into the micropore is discussed.

Finally, we will present the main conclusions on the present work and we will propose prospects for future research works to complete the current investigations.

## Bibliography

- [1] M. R. Raupach, G. Marland, P. Ciais, C. Le Quéré, J. G. Canadell, G. Klepper, and C. B. Field, "Global and regional drivers of accelerating CO<sub>2</sub> emissions.," *Proc. Natl. Acad. Sci. U. S. A.*, vol. 104, no. 24, pp. 10288–10293, 2007.
- [2] ADEME, "MARCHES ET EMPLOIS LIES A L ' EFFICACITE ENERGETIQUE ET AUX ENERGIES RENOUVELABLES : SITUATION 2012-2013 ET PERSPECTIVES A COURT TERME Novembre 2014," 2014. [Online]. Available: <http://www.ademe.fr/marches-emplois-lies-a-lefficacite-energetique-energies-renouvelables-situation-2012-2013-perspectives-a-court-terme>. [Accessed: 15-Sep-2015].
- [3] ADEME, "Les chiffres clés 2014 CLIMAT, AIR, ENERGIE," 2014. [Online]. Available: <http://www.ademe.fr/chiffres-cles-climat-air-energie-2014>. [Accessed: 01-Aug-2015].
- [4] C. R. Tsai, F. Chen, a. C. Ruo, M. H. Chang, H. S. Chu, C. Y. Soong, W. M. Yan, and C. H. Cheng, "An analytical solution for transport of oxygen in cathode gas diffusion layer of PEMFC," *Int. J. Hydrogen Energy*, vol. 31, no. 15, pp. 2179–2192, 2006.
- [5] M. Asadullah, "Technical Challenges of Utilizing Biomass Gasification Gas for Power Generation : An Overview," *J. Energy Technol. Policy*, vol. 3, no. 11, pp. 137–143, 2013.
- [6] R. Dixon, M. Eckhart, D. Hales, and G. Thompson, "Rapport mondial 2012 sur les énergies renouvelables 2012," 2012.
- [7] L. Devi, K. J. Ptasiński, and F. J. J. G. Janssen, "A review of the primary measures for tar elimination in biomass gasification processes," *Biomass and Bioenergy*, vol. 24, no. 2, pp. 125–

- 140, 2002.
- [8] P. C. A. Bergman, S. V. B. Van Paasen, and H. Boerrigter, "The novel ' OLGA ' technology for complete tar removal from biomass producer gas," no. October, 2002.
- [9] Y. Shen, "Chars as carbonaceous adsorbents/catalysts for tar elimination during biomass pyrolysis or gasification," *Renew. Sustain. Energy Rev.*, vol. 43, pp. 281–295, 2015.
- [10] K. Qian and A. Kumar, "Reforming of lignin-derived tars over char-based catalyst using Py-GC/MS," *Fuel*, vol. 162, pp. 47–54, 2015.
- [11] N. Klinghoffer, J. M. Castaldi, and A. Nzihou, "NAWTEC19-5421 BENEFICIAL USE OF ASH AND CHAR FROM BIOMASS GASIFICATION - DRAFT," in *NAWTEC19-5421*, 2011, p. 5.
- [12] N. Klinghoffer, M. Castaldi, and A. Nzihou, "Catalyst properties and Catalytic Performance of Char from Biomass Gasification," *Ind. Eng. Chem. Res.*, vol. 51, no. 40, pp. 13113–13122, 2012.

# **I. Chapter 1: Literature review**

# Content

Introduction: motivations to perform pyro-gasification .....	7
1. Biomass pyro-gasification basics .....	8
1.1. Biomass resources .....	8
1.2. Main steps and reactions in pyro-gasification process .....	12
1.3. Products: syngas, gas-phase co-products, tars, biochars and soots .....	15
1.4. Technological considerations .....	17
1.5. Partial conclusion .....	19
2. Focus on the biochars.....	20
2.1. Surface physico-chemical properties .....	20
2.2. Origin of the reactivity of biochars in pyro-gasification process.....	31
2.3. Applications .....	37
2.1. Functionalization .....	38
2.2. Partial conclusion .....	41
3. Catalytic methane cracking .....	42
3.1. Thermodynamic aspects.....	42
3.2. Metal supported catalysts.....	45
3.3. Carbonaceous materials .....	45
3.4. Partial conclusion .....	54
4. Conclusion .....	55
Bibliography.....	57

The objective of this chapter is to provide insights into the production and characterization of biochars, and the possible ways of its valorization. This will set the stage in identifying the choices made in pursuing the line of investigation. A brief introduction explains the motivations to perform biomass pyro-gasification followed by three subsections:

- The first subsection provides basic knowledge about biomass pyro-gasification
- A second subsection consists in the state-of-the-art regarding the relationship between the physico-chemical properties of the biochars surface and its reactivity in pyro-gasification process
- In the third subsection, catalytic methane cracking and more specifically on carbonaceous material is reviewed to evaluate the potential of the utilization of biochars.

## **Introduction: motivations to perform pyro-gasification**

Pyro-gasification is often compared to combustion to evaluate the benefits in terms of energy recovery. Both processes consist in extracting the energy from a fuel by heating it under an oxidizing atmosphere. The parameter which categorizes the process as a pyro-gasification or a combustion is the air to fuel ratio. Pyro-gasification is performed under sub stoichiometric conditions whereas combustion is operated with a stoichiometric or an excess of air. This difference has a great impact on the products formed from each reaction and thus the potential energy recovered. In fact, under excess of air fuel will be fully oxidized and thus the combustion mainly produces heat, carbon dioxide and steam. However pyro-gasification which consists in a partial oxidation of the fuel will mainly generate carbon monoxide and hydrogen. As far as energy recovery is concerned, the overall energy conversion is in favor of the pyro-gasification process. In fact, combustion is usually performed to produce heat which is used to generate steam and feed steam turbine for electricity production. Once the combustion is over, no added value products left. On the contrary, pyro-gasification converts energy from the fuel into chemical species so-called synthesis gas (mixture of CO+H<sub>2</sub>). This synthesis gas is further utilized in many various fields. It represents an intermediary building block for the production of various fuels such as synthetic natural gas, ammonia, methanol and synthetic petroleum fuel. It could be also used as a direct fuel source. In a purified state, the hydrogen can be used to directly power hydrogen fuel cells for electricity generation and fuel cell electric motor propulsion.

## 1. Biomass pyro-gasification basics

Pyro-gasification process takes part with combustion and torrefaction into the thermo-chemical processes of biomass conversion in opposition to the biochemical processes such as aerobic, anaerobic or fermentation processes. This section initially provides a characterization of the chemical, physical and thermodynamic properties of lignocellulosic biomass. Subsequently, a description of the mechanisms involved in pyro-gasification process is provided. The third part consists in a presentation and a brief characterization of the products from pyro-gasification. Finally, the different gasifier designs are discussed and a state-of-the-art regarding the scientific, technologic and technical bottlenecks is presented.

### 1.1. Biomass resources

#### 1.1.1. *Ligno-cellulosic biomass*

The term “Biomass” covers a wide spectrum of entities since it is a generic designation for organic materials from living species like plants and animals. A unique definition for the term “Biomass” does not exist even if all definitions are similar. In this study, we adopt the definition given by the United Nations Framework Convention on Climate Change (UNFCCC, 2005):

*“Biomass is non-fossilized and biodegradable organic material originating from plants, animals and micro-organisms. This shall also include products, by-products, residues and waste from agriculture, forestry and related industries as well as the non-fossilized and bio-degradable organic fractions of industrial and municipal wastes.”*

According to their applications, three classes of biomass have been depicted [1]:

- the first-generation of biomass is in direct competition with food and pharmaceutical industries. This group is generally composed of sugarcane, sugarbeet, rapeseed, soybean or starch-derived and other species of medical interest.
- the second-generation of biomass gathers the non-food crops, ligno-cellulosic materials and waste residues.
- the third-generation is composed of aquatic microorganisms like algae.

Pyro-gasification processes are usually carried out on second-generation biomass which is mainly composed of ligno-cellulosic materials. Husk, straw and wood are defined such as ligno-cellulosic materials. Wood could be further categorized into hardwood and softwood. A hardwood differs from

a softwood due to the fact their seeds contains flower and fruit. Maple, oak or poplar wood are considered to be hardwood whereas evergreens conifers such as pine or spruce are considered as softwood. A growing interest is put on cultivation dedicated to plants to produce energy such as miscanthus, willow, switchgrass and poplar wood. In fact, they present various advantages compared to other ligno-cellulosic materials: they have a short growing period and a high yield. They are densely planted (about 10, 000 trees/ha) and harvested every 2 or 4 years for very-short-rotation coppices which leads to a production of 8 to 20 T MS/ha/year [2]. In this study, poplar wood pellets have been utilized such as pyro-gasification inlet. Thus, the focus is put on wood characteristics thereafter.

Ligno-cellulosic material cannot be easily degraded by digestion or fermentation processes. High temperature or pressure are needed to decompose their major components: cellulose, hemicellulose and lignin. The composition of a ligno-cellulosic material is variable depending on its nature and origins. For hardwood the composition in lignin, cellulose and hemicellulose could vary between 18-25%, 40-44% and 15-35% respectively [3]. Regarding the definition of the constituent of the cellular makeup of wood, cellulose is represented by the formula of monomer unit ( $C_6H_{10}O_5$ ). It is a long polymer chain with a high degree of polymerization primarily composed of d-glucose which is the basic unit of the crystalline structure. In addition, hemicellulose is present which is an amorphous structure with a low degree of polymerization. According to the type of wood there is a variation in the hemicellulose composition. Its generic formula is ( $C_5H_8O_4$ ) and it is mainly composed of simple sugars such as D-xylose, D-glucose or D-galactose. Lignin is a complex three dimensional polymer of phenylpropane. The dominant monomeric unit in the polymer is the benzene ring. Lignin is highly recalcitrant.

### 1.1.2. ***Physical, chemical and thermal properties of wood***

#### 1.1.2.1. **Physical properties**

Density of the wood is an important parameter in pyro-gasification process. In fact the density affects the contact between the reactive gas and the solid and thus the efficiency of the process. Three types of density have been defined: true, apparent and bulk densities. They differ from the fact that the volume considered takes into account (or not) the emptiness into the particles (pores) and between the particles in a bed of material. The true density ( $\rho_{true}$ ) is the ratio between the mass of wood particle and its actual volume (without taking into account any empty space) whereas the

apparent density ( $\rho_{apparent}$ ) takes into account the internal pore volumes (intra-particle porosity:  $\varepsilon_p$ ). The bulk density ( $\rho_{bulk}$ ) depends on how wood particles are packed. Bulk volume includes interstitial spaces between the particles (inter-particle porosity:  $\varepsilon_b$ ).

### 1.1.2.2. Chemical properties

Proximate and ultimate analyses provide the composition of the wood. The proximate analysis determines the moisture, ash, fixed carbon and volatile matter content while the ultimate analysis provides the composition in carbon, oxygen, hydrogen, sulfur and nitrogen of the solid sample. According to the biomass feedstocks, the ultimate and proximate analyses could significantly vary. Figure I-1 presents the well known Van Krevelen diagram which shows the H:C over the O:C atomic ratio for different carbonaceous materials. One can observe that biomass is the fuel the richest in both hydrogen and oxygen with a O:C ratio comprised between 0.4-0.8 and a H:C ratio between 1.2 and 1.8. Thus, biomass is the most heterogeneous fuel regarding its chemical composition which should be taken into consideration for further applications.

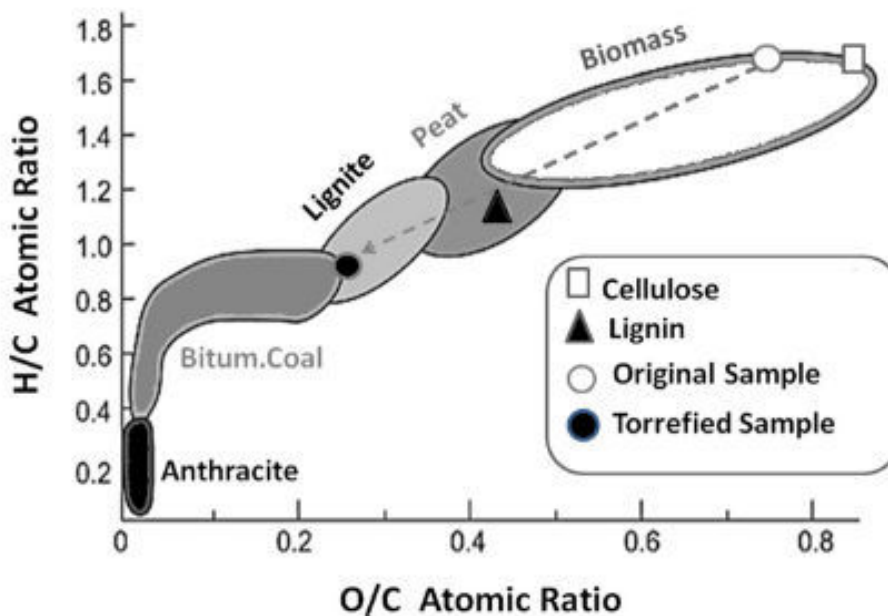


Figure I-1: Van Krevelen diagram which compares the chemical composition of different fuels [4]

Regarding wood chemical composition, it is mostly composed of carbon (50.9 wt%), oxygen (42.6 wt%), and hydrogen (6.1 wt%). Nitrogen and ash represent a minor fraction of the wood composition (see Table I-1).

**Table I-1: Ultimate analysis of hardwood and softwood [5]**

	<b>Mass fraction (dry basis) %</b>
<b>C</b>	50.9 (+/- 2.0)
<b>H</b>	6.1 (+/- 0.4)
<b>O</b>	42.6 (+/- 2.6)
<b>N</b>	0.37 (+/- 0.43)
<b>ash</b>	2.5 (+/- 4.4)

Thus the ultimate and proximate analyses give insights into the composition of the wood which is required to perform pyro-gasification in optimized conditions. For example the evaluation of the input carbon content is utilized to calculate the suitable oxygen concentration to perform the pyro-gasification. The determination of the moisture is also important to evaluate the energy which will be required to evaporate water contained in the biomass prior to pyro-gasification. The value of fixed carbon and the ashes give insights into the final composition of the solid.

### **1.1.2.3. Thermodynamic properties**

The pyro-gasification is a thermochemical process. Thus the thermodynamic properties of wood are relevant information. Four thermodynamic properties are presented: the thermal conductivity, the specific heat, the heat of formation and the heat of combustion.

#### *1.1.2.3.1. Thermal conductivity*

The thermal conductivity represents the ability of a material to transfer heat. It is dependent of the temperature, density and moisture of the material. Biomass and specifically wood is a bad heat conductor due to the porosity. Its thermal conductivity varies between 0.15 and 0.30  $\text{W}\cdot\text{m}^{-1}\cdot\text{K}^{-1}$  whereas steel for example is about 50  $\text{W}\cdot\text{m}^{-1}\cdot\text{K}^{-1}$  [6]. Evaluation of the thermal conductivity is useful to predict if the temperature will be homogeneous during the pyro-gasification reaction. Since the wood has been depicted to be a bad conductor one can anticipate that important gradient of temperatures could be measured into the bed of biomass during pyro-gasification.

#### 1.1.2.3.2. *Specific heat capacity*

The specific heat capacity ( $C_p$ ) is the amount of heat energy required to elevate the temperature of the material of one unit of temperature per unit of mass. The specific heat capacity is dependent of the temperature. Experimental determination of specific heat for various biomass have been performed in the literature. Dupont et al. [7] measured the specific heat capacity of 21 biomass representative of species potentially useable as feedstock in thermal processes by calorimetry. They stated that a linear equation linked the specific heat to the temperature between 353-513 K. In this temperature range the specific heat capacity of biomass is comprised between 1200 and 2000 J.K<sup>-1</sup>.kg<sup>-1</sup>.

#### 1.1.2.3.3. *Heat of formation*

The heat of formation or also so-called enthalpy of formation is the change in enthalpy when one mole of component is formed from its stable elements at the standard state.

#### 1.1.2.3.4. *Heat of combustion*

The heat of combustion is the energy released as heat when one mass unit of component undergoes complete combustion at temperature and pressure fixed (0°C and 1.013 bars). This characteristic is useful to compare the performances of different fuels during combustion. Two designations exist according to the condensation of water is taken into account (Higher Heating Value, HHV) or not (Lower Heating Value, LHV). Regarding the wood, its LHV is about 18 MJ/kg which is quite low compared to natural gas for example (47 MJ/kg) [8].

This section was dedicated to the description of the type of biomass utilized in the pyro-gasification process, and their properties. In the next paragraph, the theoretical bases related to the pyro-gasification process and the reactor technologies which have been developed are presented.

## 1.2. Main steps and reactions in pyro-gasification process

The objective of the pyro-gasification process is to convert the biomass into a high energetic gas so-called syngas which is a mixture of carbon monoxide and hydrogen and which is intended to feed gas turbines or conversion into chemicals or fuels. Pyro-gasification is a highly complex process which involved more than 100 reactions (reaction in chains, secondary or competitive reactions mainly

occurring in the gas phase) and in which biomass undergoes severe transformations to produce syngas. The progress of the pyro-gasification process is dependent from the type of biomass, its origins and conditioning. However some main steps can be described. Figure I-2 presents a scheme of the main reactions occurring during the pyro-gasification process.

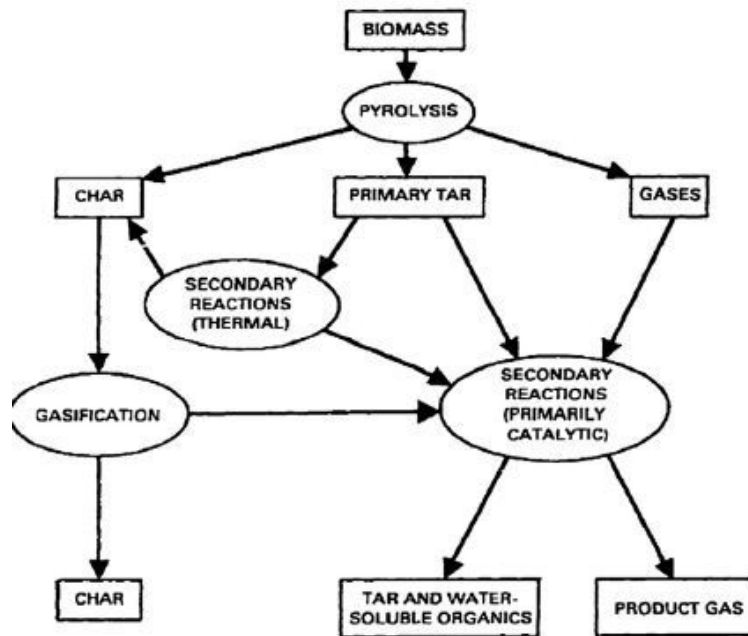


Figure I-2: Reaction scheme of biomass pyro-gasification [9]

Three main steps: drying, pyrolysis and pyro-gasification are presented below:

### 1.2.1. *Drying*

The drying step consists in the evaporation of the moisture (free water and bound water) inherently present in the biomass. This endothermic reaction occurs below 200°C range.

### 1.2.2. *Pyrolysis*

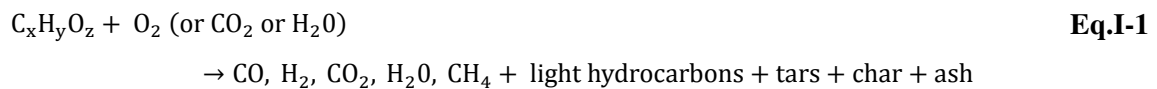
Pyrolysis consists in the chemical decomposition of the organic material at the temperature range of 300-700°C which corresponds to the thermal degradation of the main ligno-cellulosic components. In fact, it has been reported that the decomposition of hemicellulose, cellulose and lignin are consecutive at around 300°C, 300-400°C and 350-450°C respectively [10]. The products of the

pyrolysis step are the remaining carbonaceous solid so-called biochar and the volatile matters composed of condensable (tars) and non condensable fractions.

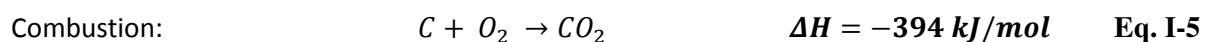
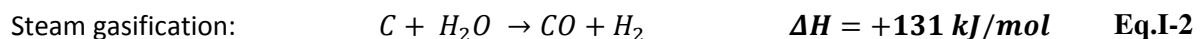
### 1.2.3. **Gasification**

Gasification consists in the partial oxidation of the char under the action of an oxidant agent which could be steam, air, carbon dioxide or oxygen. Biomass gasification generally occurred in the temperature range of 700 to 1300°C. The global reaction of biomass gasification is presented in Eq.I-1. However it is a sum of multiple reactions. Some of the main reactions occurring during the gasification are presented in Eq.I-2 to Eq.I-7 such as steam gasification, Boudouard reaction, methanation, combustion, Water gas-shift and reforming. Steam gasification and Boudouard reactions which are the actual reactions which produce the energetic syngas (CO + H<sub>2</sub>) are endothermic and thus an energy supply is required to maintain high temperature in the reactor.

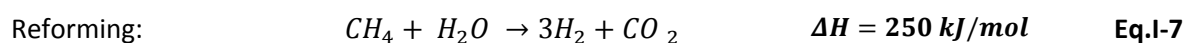
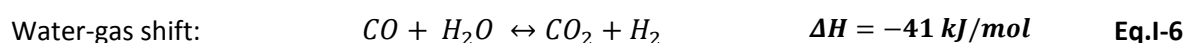
Global reaction:



Reactions between carbon from the char and the gaseous agent:



Reactions in the gas phase:



Syngas is produced via steam gasification (Eq.I-2) and Boudouard reaction (Eq.I-3). Even if combustion is the fastest reaction (50 times faster than the steam gasification) it is not the main reaction in the gasification process since the oxygen concentration is significantly lower than the one for the gasifying agent (below 5%) [6]. The Boudouard reaction is known to be 2 to 5 times slower than the steam gasification [11]. In addition Di Blasi et al. [10] stated that water gasification mechanism is more complex than CO<sub>2</sub> gasification since H<sub>2</sub>, CO and CO<sub>2</sub> are in equilibrium following the Water gas shift reaction (see Eq.I-6) in their review on the gasification and combustion rates of ligno-cellulosic biochars.

### 1.3. Products: syngas, gas-phase co-products, tars, biochars and soots

#### 1.3.1. *Syngas*

Syngas is composed of carbon monoxide and hydrogen. According to the subsequent use, the required ratio between the two constituents will differ. According to Nzihou et al. [12], the ratio of CO/H<sub>2</sub> in the syngas should ideally be near equimolar to provide hydrocarbons for transport fuels. Regarding application of the Fischer-Tropsch process, an excess of hydrogen over carbon monoxide is required. Bermudez et al. [13], highlighted that a low H<sub>2</sub>/CO ratio is suitable for the production of higher hydrocarbons and oxygenated derivatives. As methanol synthesis is concerned a ratio close to 2 is suitable.

#### 1.3.2. *Gas-phase co-products*

Methane, carbon dioxide and light hydrocarbons such as acetylene and ethylene are the major gas-phase co-products. High pressure tends to increase the production of methane [10]. Pollutants such as nitrogen and sulfur compounds coming from the biomass and which reacted with the gasifying agent are also present in the gas phase. Regarding the distribution of the different components in the gas-phase, it is varying according to the operating conditions (temperature and residence time). However hydrogen and carbon monoxide are the major components. Carbon dioxide is the third main component followed by methane. All other components are in minor concentration.

### 1.3.3. **Tars**

Tar are defined as a *complex mixture of condensable hydrocarbons* [14]. The devolatilization of the condensable matters from the biomass produce the so-called primary tars (derived products from the ligno-cellulosic components). Further reactions into the gas phase (which are enhanced with increasing the temperature and residence time of the pyrolysis) lead to the decomposition of these primary tars to produce secondary tars (olefins and phenolics) and tertiary tars (aromatic hydrocarbons). For temperature above 900°C, benzene rings resulting from tars cracking or light hydrocarbons polymerization growth with the addition of C<sub>2</sub>H<sub>2</sub> to form Polycyclic Aromatic Hydrocarbons (HAPs) which are highly toxic [15], [16].

### 1.3.4. **Biochars**

Biochars are the solid residues from the biomass pyro-gasification. They are composed of organic and inorganic components which were not devolatilized during the pyrolysis step. The section 2 of this chapter is entirely dedicated to a detailed presentation of the physico-chemical properties of the biochars and the different considerations regarding their reactivity, the potential applications and the ways of functionalization. However a quick description of the general biochars characteristics is provided in this paragraph.

Biochars are disordered carbonaceous solids which could have a short-rangeg ordered. They are mainly composed of carbon (about 85 wt%) but also contains oxygen (10 wt%), hydrogen (2 wt%), nitrogen (< 1 wt%), sulfur (< 1 wt%) and ashes (1 to 3 wt%). Most of the ashes which were present in the biomass remain in the biochars and their concentration is about few percents in the total mass of biochars. They are also porous materials due to the devolatilization of a part of the initial wood components. The characterization of their porosity (volume, pore size and structure) is of great interest. The pyro-gasification conditions (heating rate, temperature, gasifying agent) influence the yields and physico-chemical properties of the biochars. In fact, in a fast pyrolysis process (heating rate > 10°C/s), the yield of biochars tends to be lower than in a slow pyrolysis since the devolatilization of the condensable matters would be enhanced. Regarding the effect of the temperature, the higher the temperature process, the more condensed the structures. The physico-chemical properties of the biochars and the influence of the pyro-gasification conditions are presented and discussed more in details in the section 2.1.

### 1.3.5. **Soots**

Soot is a black solid material composed of carbon and hydrogen. It can be considered as an agglomeration of elementary primary particles from condensation of polyaromatic aromatic hydrocarbons (PAHs) which have been formed during the pyrolysis step. The nucleation of the primary soots happens once a critical size of PAHs is reached. Then phenomenon of surface growth and agglomeration are observed and increase the soot particle size. Thus, the soot formation is the results of a complex mechanism of chain reactions: first the primary tars are formed from the devolatilization of organic matters from the initial wood structure (400°C), which react in the gas-phase to form new components at higher temperature such as phenolics or ethers (at 600, 700°C) to finally produce PAH (at 900°C) which are the precursors of the soots particles. Hence, soots formation is observed at high gasification temperature (> 900°C).

## 1.4. **Technological considerations**

### 1.4.1. **Gasifier types**

Since over 100 years, researches related to gasifier design are conducted in order to optimize the biomass conversion. Several types of reactors have emerged with specific requirements and adaptability ranges in terms of feedstock tolerance, oxidant requirements and applications. The gasifiers are usually classified according to the type of gas-solid contacting mode. Three main categories can be quoted: fixed bed, fluidized bed and entrained flow gasifiers. In each category subsections exist such as downdraft and updraft reactors in the fixed bed category or circulating, bubbling reactors in the fluidized bed section. A type of gasifier is adapted to a range of applicability: the fixed bed is more adapted for small units (10 kWth to 10 MWth), the fluidized-bed has been designed for intermediate units (5-100 MWth) and entrained-flow reactor for large-capacity units (> 50 MWth). It exists several models of reactors in each category. However, here are presented some of the typical reactors design.

Regarding the fixed bed gasifiers, the Updraft reactor is one of the simplest and oldest technologies. The biomass and oxidizing agent are in countercurrent: the gas flow is introduced at the bottom of the reactor and exits from the top while the biomass is sent from the top and fall down into the reactor. Updraft reactors are suitable for high-ash (>25%) and high-moisture content (> 60%). However the drawback of this design is the quite high tar production (30-150 g/Nm<sup>3</sup>) [3]. The

Downdraft reactor is a co-current reactor. The gas flow is introduced in the middle of the vessel just above the high temperature gasification zone located at the bottom of the reactor. The gas flow has to go through the gasification zone to be evacuated at the bottom of the reactor. The biomass is introduced from the top of the vessel such as in the Updraft reactor. Since the tars, biochars and ashes pass through the high temperature zone in oxidizing atmosphere the conditions are favorable for tar cracking. Thus the tars production is lower than in the Updraft reactor ( $0.015\text{-}3.0\text{ g/Nm}^3$ ) [3].

The fluidized bed is depicted for their excellent mixing and temperature uniformity. The gasifier design has shown good performances for biomass pyro-gasification. The tars production is in between the Updraft and Downdraft gasifiers and evaluated to be of  $10\text{ g/Nm}^3$  [17]. The principle of this reactor is that the bed of biomass is in a semi-suspended condition due to the appropriate pressure drop created by the crossing of the gas through the biomass bed. Two principal technologies can be discussed: the bubbling and circulating beds. In the bubbling bed, the fluidized biomass remains in the reaction zone of the reactor. In the circulating bed the biomass is dispersed all over the vessel. The addition of a cyclone and a return leg is required in this type of technology to continuously trap the solids and return them into the reactor. Thus in a circulating bed the residence time is significantly longer than in the bubbling bed. The fluidization velocity is also higher ( $3.5\text{-}5.5\text{ m/s}$ ) compared to ( $0.5\text{-}1.0\text{ m/s}$ ) for the bubbling bed [3].

The entrained flow reactor is a co-current plug-flow reactor where gas and fuel are moving. In this type of reactor the pyro-gasification conditions are severe: gasification temperature is exceeding the  $1000^\circ\text{C}$ , fuel particles and oxidizing agent are pulverized and the contact time is really short. Into such conditions the syngas is almost tar free. This process has been depicted to be highly efficient for coal pyro-gasification. However dealing with biomass its utilization is not the most suitable since the very short contact time (a few seconds) requires that the fuel is introduced into very fine particles.

#### 1.4.2. **Pyro- gasification bottlenecks**

Syngas clean-up is one of the major issues which slow down the development of the pyro-gasification process at the industrial scale. Paragraph 1.3 has presented the co-products of pyro-gasification which are coming from the non-total conversion of the biomass into syngas. In addition to decrease the syngas yield they reduce the syngas quality and cause technological issues. In fact condensable tars which are in a gaseous form into the reactor liquefy when the temperature is cooled down and clog the pipes downstream the gasifier. Reviews reported different methods for syngas cleaning. For example Devi et al. [18] published a review on the primary measures for tar elimination in the early

2000s. Technologies for syngas cleaning can be gathered into two main groups depending on their location into the process. The first way to decrease the tar formation is to act directly in the pyro-gasification reactor. It could be by performing pyro-gasification at very high temperature ( $> 1200^{\circ}\text{C}$ ), using plasma torch or adding catalyst into the gasifier. Usually zeolite, Alkali and Alkaline Earth Metal (AAEMs) such as dolomite or olivine or transition metal and the biochars formed are used. However, when primary methods are successful, the amount of syngas produced is comparatively small [14]. Thus in the secondary method the gas cleaning is operated downstream the gasifier. The secondary method could be either a physical separation or treatment using membrane filter, scrubbing liquid or it could be a catalytic treatment in a second reactor. The advantage of the catalytic treatment compared to the physical one is that it increases the syngas yield in addition to clean it. This treatment is called a hot gas treatment. The same catalyst as in the primary method could be used. However the operating conditions could be different from the gasifier. Regarding type of catalyst in the hot gas cleaning, recent studies have shown the potential of the biochars to convert hydrocarbons from the tars [19]. For example, El Rub et al. [20] compared the efficiency of biochars with other common catalysts such as dolomite, nickel or olivine to convert naphthalene and phenol which are model molecules of tar. They reported that at  $700^{\circ}\text{C}$  the ranking of the different catalysts activity for phenol conversion was: nickel > dolomite > FCC > C.B. char > olivine > sand, while the ranking of the different catalysts activity for naphthalene conversion at  $900^{\circ}\text{C}$  is: nickel > C.B. char > biomass char > biomass ash > FCC > dolomite > olivine > silica sand.

### 1.5. Partial conclusion

Biomass pyro-gasification is performed to produce syngas to be further utilized for different applications (electricity, chemicals). It consists in the partial oxidation of ligno-cellulosic biomass which represents a highly complex mechanism involving many homogeneous (gas-phase) and heterogeneous reactions (solid-gas phase). During the pyro-gasification process, the biomass is not totally converted into syngas. Co-gaseous products such as  $\text{CO}_2$ ,  $\text{CH}_4$ , light hydrocarbons and pollutants are formed. Biochars (solid residue) and tars (heavy hydrocarbons) are also produced. Thus a cleaning step is essential to upgrade the quality of the syngas. The hot gas cleaning downstream the gasifier reactor seems to be the best solution since it leads to the highest syngas yield increased by cracking large hydrocarbons. Common catalysts such as AAEMs or transition metals have shown good results. However in terms of global upgrade of the pyro-gasification process, the use of the biochars (which is itself a co-product of pyro-gasification) seems to be a very

interesting solution. Even if biochars have been highlighted to be potential catalysts for hydrocarbons cracking reactions not clear correlation with their physico-chemical properties has been established yet. The next paragraph is dedicated to the literature review regarding the biochars physico-chemical properties.

## 2. Focus on the biochars

This section focuses on the carbonaceous residue so-called biochars. First the literature review is dedicated to the characterization of the physico-chemical properties of the surface. Subsequently the relationship between its physico-chemical properties and its reactivity towards pyro-gasification is presented and enlarged to other potential applications. Lastly, review on the possible ways of functionalization to enhance the oxygen groups and the mineral content is provided.

### 2.1. Surface physico-chemical properties

Four physico-chemical properties are of great interest in biochars surface: the carbon matrix structure, the mineral content, the O-containing group and the textural properties such as porosity and specific surface area.

#### 2.1.1. *Carbon matrix structure*

As described in the section 1.1, hemicellulose, cellulose and lignin which are complex polymers are the main constituents of wood. The range of temperature required to destroy them is typically about 300°C for hemicellulose, 300-400°C for cellulose and around 350-450°C for lignin [10]. The mechanism of their degradation is highly complex and final biochar structure is complicated to predict. Thus, analytical techniques are needed to investigate the biochars structure post-gasification. Biochars are described in the literature as highly amorphous carbons with a complex structure. In fact, most of the carbon rings arrangements do not have a true crystalline structure. X-ray diffraction (XRD) did not provide well defined peaks for char but a broad band characteristic from amorphous content. However saying biochars does not contain any ordered structures is not accurate. In the carbon matrix short-range ordered carbon structures interweave with amorphous ones. The ordered structures are mostly graphene-like sheets which are lattices composed of benzene units. The basal plane carbons of the graphene-sheets are considered to present low reactivity whereas edge carbons which contain the functional groups are thought to be more

reactive. Two main arrangements of the rings are possible: the zig-zag or armchair configurations which also impact the edge carbon reactivity (see Figure I-3). Regarding the disorder in the carbon skeleton it could be of different nature: point defects in the graphene-like sheets such as vacancies (carbon atom missing) and impurities (heteroatoms insertion) or it could also consist in amorphous aromatic rings with different ring sizes. The graphene-like sheets with scattered imperfections and not perfectly parallel anymore are called turbostratic structures. This state is between crystalline and amorphous structure [21]. Illustrations are given in Figure I-4 and Figure I-5. High Resolution Transmission Electron Microscopy (HRTEM) has been used in different studies to investigate the nanostructure of graphene-sheet in turbostratic carbonaceous materials [22]–[25]. For example, the evolution of the graphene-like sheets over thermal processes such as combustion or pyro-gasification can be monitored [26]. Several parameters related to the level of ordering such as fringe geometrical properties (length, tortuosity, local curvature) and stacks (ratio of surface covered by parallel fringes over the surface occupied by all fringes) of the graphene-like sheets can be determined from HRTEM analyses and imaging post-treatment [27], [28].

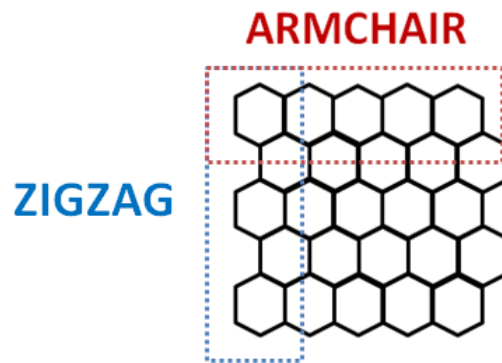


Figure I-3: Illustration of the armchair and zig-zag configurations of graphene

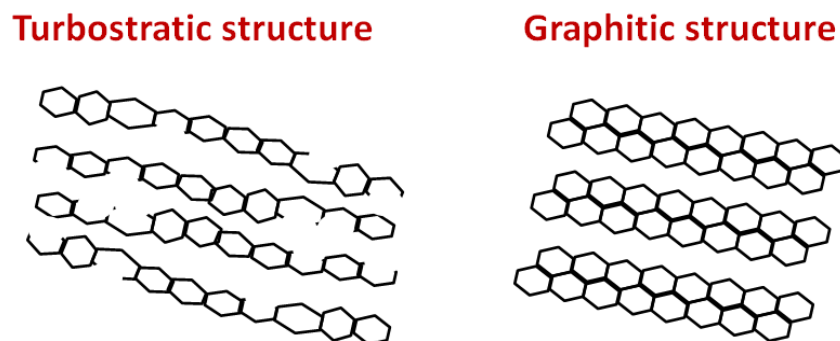
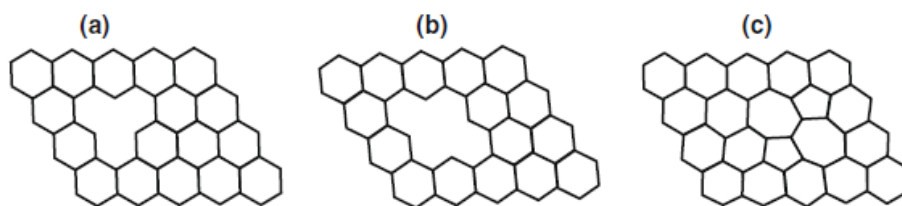


Figure I-4: Illustration of turbostratic and graphite structures



**Figure I-5: Three different point defects in graphene: (a) a mono-vacancy defect, (b) a di-vacancy defect, and (c) a Stone-Wales defect [29]**

To get global insights into the state of the carbon matrix, Raman spectroscopy is a powerful technique which has been widely used to investigate biochars from pyro-gasification [30]–[32]. As noticed by Vautard et al. [33], “Raman spectroscopy is less sensitive to the interlayer distance between graphitic layers than XRD but it is more sensitive to a change of the order existing in the graphitic structure”. This technique provides semi-quantitative information about the distribution of the ordered and disordered carbon structures. Typical Raman spectrum of a disordered structure contained two main bands the G band ( $1590\text{ cm}^{-1}$ ) and the D band ( $1350\text{ cm}^{-1}$ ) which represent respectively the Defective and the Graphitic structures respectively. The D band is representative to the imperfections (quoted previously) which can be encountered in the graphene-like sheets such as point defects, multiple vacancies and heteroatoms inserted. They also represent the large aromatic rings systems ( $> 6$  rings). The band, in the overlap between the G and D bands, is assigned to amorphous content such as small aromatic rings systems (3-5 rings). Then rich  $sp^2$ - $sp^3$  structures are also Raman sensitive and are assigned to the peak at  $1200\text{ cm}^{-1}$ . Figure I-6 is an illustration of a Raman spectrum of an amorphous carbon and the assignment of bands. The knowledge of the different carbon structure distribution in the carbon matrix is a crucial point when investigating the reactivity of a carbonaceous material. In fact it will be discussed further that amorphous structures have been highlighted to be the active phase in the carbon structure while ordered graphene-like sheets have been depicted to be almost inactive.

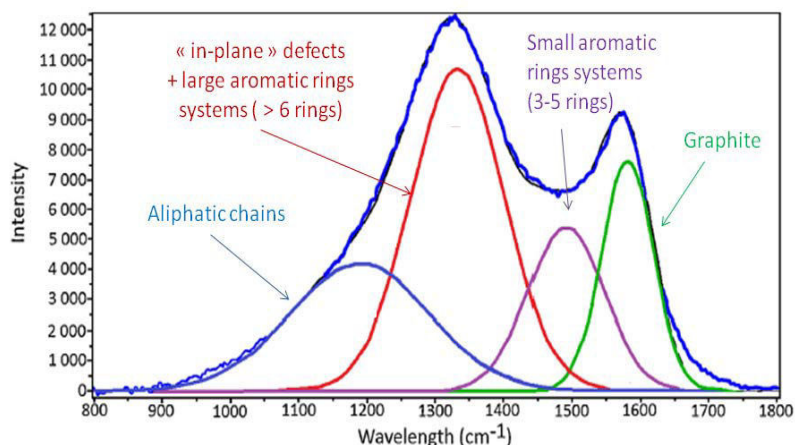


Figure I-6: Fitting of Raman spectrum and functions distributions adapted from [33]

### 2.1.2. Mineral content

Biomass contains inherently minerals which are present in the soil. The part of inorganics in the biochar is called ash. It is composed of alkali and alkaline earth metal (AAEM), transition and semi metals and halogens. Composition and concentration of the ash is highly dependent on the nature of the parent biomass, the feedstock they are coming from and the operating conditions of the thermal treatments. The AAEMs and more specifically calcium, potassium, magnesium and sodium are the major components in the ash. Aluminum, silicon, phosphorus, sulphur and chlorine are also present. In a minor percentage manganese, iron, cobalt, nickel, copper and zinc are detected. Mermoud et al. [6] investigated the ash composition of beech wood post steam gasification by Inductive Coupled Plasma analysis (ICP). Calcium, potassium and magnesium represented 45.5, 38.0 and 8.9% respectively of the ash content. Phosphorus, manganese, sodium and iron percentages were below 2%. Wu et al. [34] also performed ICP on rice straw biochars. Silicon and potassium concentrations were found to be the highest, calcium, magnesium, sodium and iron concentrations were ten times smaller.

Investigation of the speciation of the minerals in the biochars post-gasification is also of great interest since its impact their reactivity. X-ray diffraction is powerful technique to investigate the structure of minerals. Even if biochars are highly amorphous XRD provides information on the crystalline arrangements. A large variety of minerals forms are depicted in the literature which can be very complex such as alumino silicate components. The crystalline arrangement is highly dependent on the concentration and nature of the inorganic elements and the operating conditions of the thermal treatment. Even if various structures of mineral salts at the biochars surface have

been presented in the literature there is a general agreement that biochars from pyro-gasification contain predominantly carbonate and oxide forms of the different minerals. Link et al. [35] presented the chemical analysis of the ash expressed as oxides. A large amount of silicon dioxide was detected, alkali and alkaline earth oxides were also present such as aluminum oxide. In addition the formation of complex arrangements between minerals is also expected [36]. Link et al. [35] stated that the formation of AAEMs and alumino silicates during the thermal treatment should occur. The amount of silicon in the ash of biochars and its effect on the structural arrangement of AAEM has been also discussed in their study. They mentioned that the high silicon amount in their Douglas fir biochars was responsible for the formation of potassium silicate rather than potassium carbonate. The possibilities of finding metal carbides has been studied by Devi et al. [37]. They performed XRD on cellulosic biochars and compared experimental results to Ellingham diagrams which provide insights into the thermodynamic possibility of metal oxide to be reduced by carbon (biochars). Formation of reduced metal is possible however high temperature is required.

### 2.1.3. ***Oxygenated functions***

Biochars are mainly composed of large and small aromatic rings with oxygen atoms inserted into the carbon skeleton. The different arrangements of the oxygen atoms insertion into the carbon matrix gives rise to a various number of oxygenated functions at the surface of a carbonaceous material. Most common functions described in the literature are carboxylic acid, anhydride acid, phenol, lactone, ester and quinone or carbonyl groups. Some studies proposed additional functions such as peroxides, hydroxyl, chromene or pyrone-like structures. Phenol and hydroxyl are represented by an hydroxyl group which is linked to a carbon atom from an aromatic ring or an aliphatic chain. Carbonyl, quinone and pyrone-like structure are characterized by a double bond C=O with a carbon from a ring which is itself only linked to hydrogen or other carbon atoms. If the carbon involved in the double bond is linked to another oxygen function the oxygenated group is called carboxylic acid, anhydride acid or lactone. Ether and peroxide functions are C-O-C and C-O-O-C functions respectively. Figure I-7 summarizes the different functions. According to the linkage with the surrounding carbons and their position in the carbon matrix, the oxygenated functions have different properties. Most of the oxygenated groups have been likely identified as acid functions. Carboxylic acids are depicted to be the strongest acid, and phenol and lactone as weak acids. Double bond C=O functions such as carbonyl, quinone or pyrone functions have been identified as basic functions.

Various analytical techniques have been developed to study the oxygenated functions at the surface of a carbonaceous material. Salame et al. [38] have done the distinction between the “wet” and “dry” techniques. The most classical wet technique is the Boehm titration. It consists in multiple titrations. The X-ray Photon Electron (XPS), Fourier Transform InfraRed (FTIR) spectroscopies and the Temperature Programmed desorption (TPD) are the common “dry” techniques which have been employed in the literature. XPS and FTIR such as all spectroscopies techniques rely on the matter-light interactions to study the uppermost layer of the sample surface. TPD is based on the distribution of desorption activation energies theory [39]. It consists in heating the sample under an inert atmosphere to 1100°C and to record the CO<sub>2</sub> and CO desorption versus temperature. Five analytical techniques (XPS, FTIR, Boehm titration, TPD and XPS) have been presented to investigate the oxygenated functions. In fact, identification and quantification of oxygen functional groups at the carbon based material surface is not straightforward. FTIR gives insights into the nature of the oxygenated groups. However a deconvolution of the signal such as for XPS and TPD is required to obtain quantitative data. Regarding the Boehm titration, analytical errors due to multiple steps in the titrations have to be taken into account. Thus, various studies coupled at least two of these techniques to be able to identify and quantify the oxygenated functions. For example Figueiredo et al. [40] performed XPS, FTIR and TPD to characterize activated carbons surface. Zielke et al. [41] carried out XPS and TPD to investigate the surface of oxidized carbon fibers.

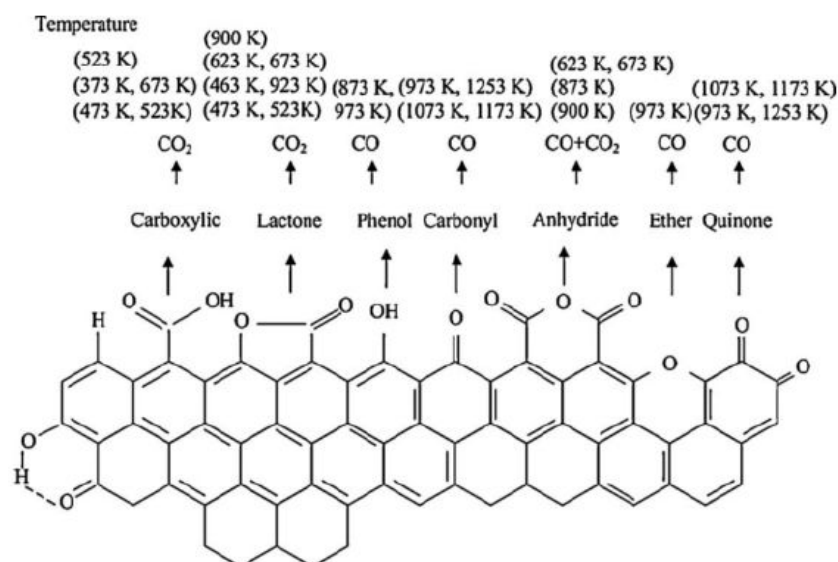


Figure I-7: Example of functional groups that can potentially exist on the biochar surface [40]

#### 2.1.4. **Specific surface area and porosity**

Characterization of the biochars textural properties is a key point. In fact they represent the interface between the active sites of the surface and the reacting agent in the gas phase. Textural properties gather the characterization of the porosity and the specific surface area of the material. The porosity  $\varepsilon_p$  is the evaluation of the part of emptiness in the sample which corresponds to a characterization of the cavities (see Eq.I-8).

$$\varepsilon_p = \frac{V_p}{V_{tot}} \quad \text{Eq.I-8}$$

with:

$\varepsilon_p$ : porosity

$V_p$ : pores volume ( $m^3$ )

$V_{tot}$ : total volume ( $m^3$ )

The evaluation of the pore volume is of great importance since it gives insights into the potential interface of exchange between the gaseous reactant and the active sites on the biochars surface. This volume is dependent from the pore geometry and structure. In fact, pores have a very complex geometry but can be represented with a cylindrical or slot shape. They could be opened if at least one of their entrances is accessible or closed. They could also be interconnected creating a network (see Figure I-9). However these information are difficult to collect [27]. Another important parameter regarding pores is their size which influences their reactivity. In fact, it influences the mass transfer during the reaction. Pores are commonly classified into 3 groups (IUPAC) (see Figure I-8):

- micropore:  $d_{pore} < 2 \text{ nm}$
- mesopore:  $2 < d_{pore} < 50 \text{ nm}$
- macropore:  $d_{pore} > 50 \text{ nm}$

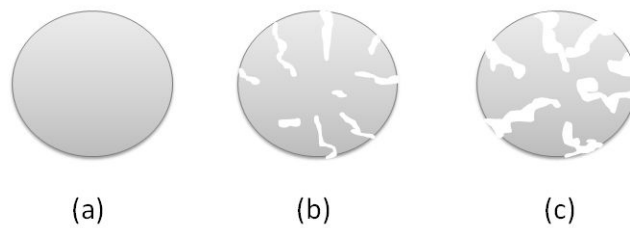


**Figure I-8: Schematic presentation of different matrix types (a) non-porous particle (b) microporous particle (c) macroporous particle**

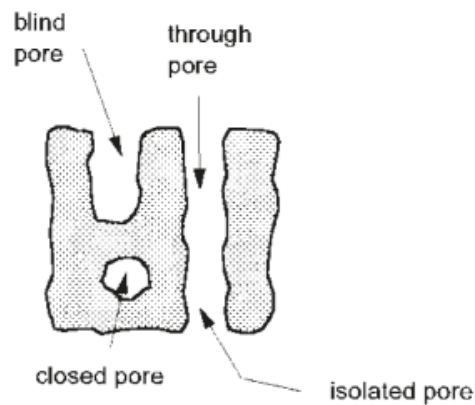


**Figure I-9: Illustration of the types of pores [35]**

The notion of porosity and specific surface area are highly correlated. In fact porosity plays an important role in the specific surface area development. The specific surface area  $S_{sp}$  represents the total surface developed by the material which is different from the apparent surface area. It is often expressed as the total surface of the sample over its total volume (see Eq.I-9). A shape factor  $\psi$  is introduced to take into account the deviation to a spherical particle.

$$S_{sp} = \frac{\psi \cdot S_{tot}}{m} \quad \text{Eq.I-9}$$

with:

$S_{sp}$ : specific surface area ( $m^2/g_{char}$ )

$\psi$ : shape factor (= 1 for spherical particle)

$S_{tot}$ : total surface ( $m^2$ )

$m$ : mass sample (g)

Analytical techniques based on adsorption of gases have been developed to estimate the specific surface area, nature and volume of the porosity. This is a well-known technique so-called BET specific surface area determination. Usually adsorption of nitrogen is performed. For each value of nitrogen partial pressures the volume of nitrogen adsorbed at the surface (at equilibrium) is determined until  $P/P_0$  equals to 1. The curve obtained is called the adsorption isotherm. The shape of the adsorption isotherm provides information about the nature of the porosity. The volume adsorbed is used to determine the specific surface area, the volume and average size of pores. More details into the technique are given in the section 2.3 of the chapter II.

This section presents the different physico-chemical properties of the biochars surface separately. To go further the potential interactions between them are presented thereafter.

#### **2.1.5. *Influence of the pyro-gasification operating conditions on the biochars physico-chemical surface properties***

The pyro-gasification operating conditions influence the biochars conversion but also its physico-chemical properties. Influence of the heating rate, temperature and gasifying agent are discussed. Pressure should also significantly impact the chars properties. However regular pyro-gasification is usually performed at atmospheric pressure.

##### **2.1.5.1. Heating rate**

During pyro-gasification process the heating rate significantly impacts the products composition. From this observation two classes of pyrolysis have been distinguished: slow pyrolysis (heating rate of about 10°C/min) and fast pyrolysis (heating rate of about 10°C/s). Di Blasi et al. [10] presented the products yields (biochars, tars and gas) versus temperature for the slow and fast pyrolysis (see Figure I-10).

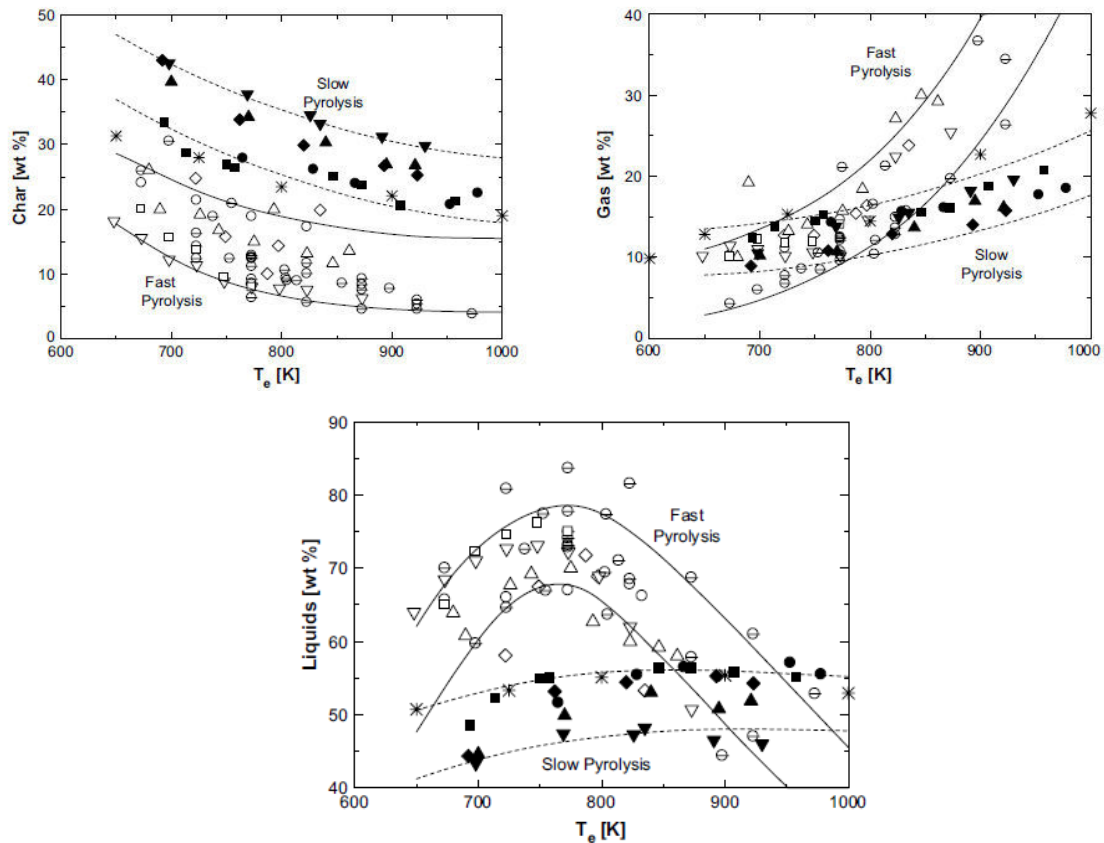


**Figure I-10: Yields of char, gas and liquid on dependence of heating temperature from fluidized-bed during fast pyrolysis (empty symbol) and slow pyrolysis (full symbol) [10]**

As an example, one can observe on Figure I-10 that at 700K (427°C) a fast pyrolysis leads to mainly produce liquid (about 65 wt%). Biochars contribution is about 25 wt% and gas 10 wt%. As for the slow pyrolysis at the same temperature, the gas production is comparable to the one of the fast pyrolysis but the biochars production is more important (about 45 wt%). Thus the fast pyrolysis tends to favor the condensable products (gas or liquid) and the slow pyrolysis the biochars formation. These differences can be explained by the fact that fast pyrolysis did not give enough time for the transformation of cellulose into a more thermo-stable molecule [15]. Literature highlighted that the biochars from fast pyrolysis was the most reactive due to the brutal release of the volatile from the solid structure which damaged the carbon matrix and created high porosity and increased potential gas-solid interactions [6].

### 2.1.5.2. Temperature

Temperature of the pyro-gasification process greatly impacts the surface properties of the biochars. Di Blasi et al. [10] highlighted that the increase of the temperature treatment, decreases the O-

containing groups concentration and favors the aromatic rings condensation (see Figure I-11). Russell et al. [26] also pointed out the increase of ordering into the graphene-like sheets with temperature: the not oriented sheets start to align face-to-face in distorted columns above 800°C, then columns coalesce to form wrinkled layers from 1600°C and a perfect alignment could be observed for temperatures higher than 2100°C (see Figure I-11). Septien et al. [15] investigated the ash composition of biochars after pyrolysis treatment at 1000 and 1400°C and highlighted that no mineral crystalline forms were detected for the former one but carbonates were present in the latter. This indicates that the mineral oxide amount and structure at the biochars surface are influenced by the temperature of pyro-gasification.

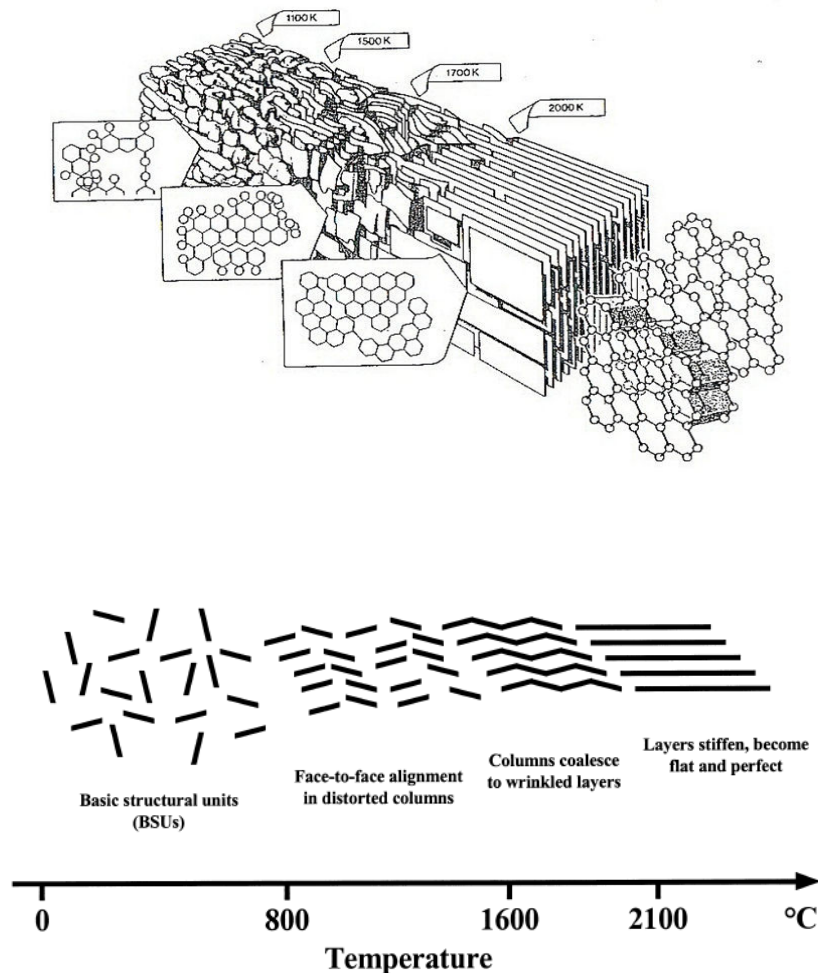


Figure I-11: Modification of the biochar carbon structure versus temperatures [42], [26]

### 2.1.5.3. Gasifying agent

Guizani et al. [43] and Klinghoffer et al. [19] investigated in details the physico-chemical properties of woody biochars after H<sub>2</sub>O and CO<sub>2</sub> pyro-gasification. They concluded that different pathways were followed during the two types of gasification leading to biochars with different physico-chemical properties. They agreed on the fact that the biochars gasified under CO<sub>2</sub> were more microporous than the one produced under steam gasification. Guizani et al. suggested that the H<sub>2</sub>O molecules would diffuse more deeply in the biochars matrix than the CO<sub>2</sub> molecules which could enhance the formation of larger pores under steam. Klinghoffer et al. performed gasification in an ESEM (Environmental Scanning Electron Microscope) up to 1000°C under different atmospheres: CO<sub>2</sub>, H<sub>2</sub>O and air. It has been highlighted that the biochars gasification was slower with CO<sub>2</sub> as a co-reactant than with air or H<sub>2</sub>O. In addition, with these two latter, at high temperature (up to 1000°C) sintering was observed (densification of the structure due to the growth and the coalescence of particles at the surface) which directly decreased the pore volume and could block the micropores. Regarding the carbon matrix, Guizani et al. stated that steam was more likely to react with small aromatic rings and induced ring condensation due to activation of the cycles by hydrogen penetration whereas graphene-like sheets were better active sites in CO<sub>2</sub> gasification. Klinghoffer et al. did not notice significant difference of O-containing groups on the two biochars. However Guizani et al. highlighted a slightly higher concentration of basic groups on biochars from CO<sub>2</sub> gasification. No significant differences about the mineral composition and concentration were depicted in correlation with the gasifying agent.

The characterization of the biochars surface properties is of great interest to understand the mechanism and the origin of the reactivity of the biochars during the pyro-gasification process. This is the topic of the next subsection.

## 2.2. Origin of the reactivity of biochars in pyro-gasification process

Reactivity of biochars towards gasification has often been investigated regarding the composition of the carbon matrix and the minerals composition.

### 2.2.1. **Carbon matrix**

The structural features evolution of biochars during pyro-gasification has been studied by several authors [44][45][46] using Raman spectroscopy in order to get insights into the interactions between the gasifying agent and the carbon structures. Asadullah et al. [31] investigated the pyro-gasification of mallee wood at 370°C in a thermogravimetric analyzer and correlated it to the characterization of the distribution of carbon structures by Raman spectroscopy. Prior to gasification a pyrolysis of the wood particles was performed between 700-900°C to obtain char particles of different sizes and carbon structure composition. They stated that amorphous aromatic rings and aliphatic chains with O-containing groups were the most reactive structures in the gasification process. They also noticed that small aromatic rings systems are dominant in the biggest particles which have been produced at low temperature (pyrolysis at 700°C). On the contrary, at higher temperature of pyrolysis, smaller particles containing preferentially larger aromatic rings systems have been produced and are less reactive towards gasification. Then gasification is a selective process in which small aromatic rings systems are the most reactive. Temperature of the heat treatment impacts the carbon structures distribution since it promotes the condensation of the aromatic rings and thus also impacts the overall biochars reactivity.

Keown et al. [47] investigated the steam gasification of cane trash biomass. They obtained similar results as Asadullah et al. [48] since they noticed that small aromatic rings were preferentially reacting and transform into large rings systems. They suggested that the initial reactions would involve the formation of chemisorbed hydrogen on the char surface which would be able to penetrate deeper into the char structure and tend to activate the carbon structure (aromatic rings) which would condense and grow.

Li et al. [49] investigated the structural features of Victorian brown coals during gasification in air at 400°C by FT-IR/Raman spectroscopy. They studied the preferred gasification reaction sites in the presence and absence of catalyst (Ca and Na). They also highlighted that small aromatic rings were preferentially consumed both in the presence or absence of the catalysts (see Figure I-12). However, in the absence of catalyst, the gasification was slower and took also place on some aliphatic chains. They noticed that the catalysts particles were rather dispersed in the small aromatic rings systems than in the large ones which seemed to be increasingly concentrated with little flexibility.

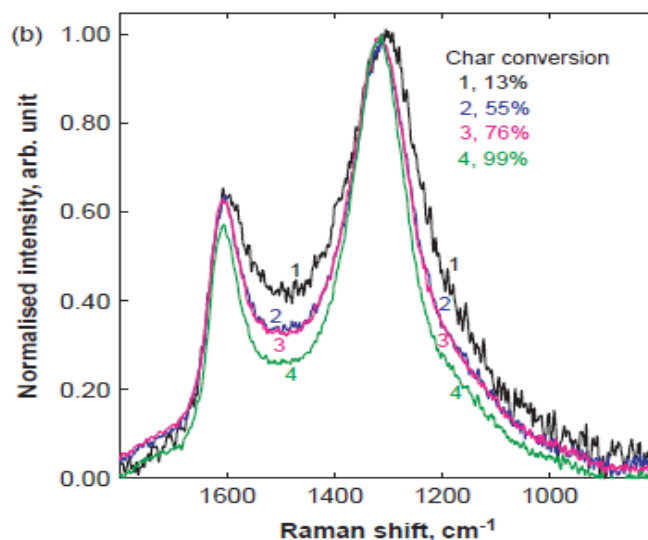


**Figure I-12: Changes in Raman spectra during the gasification of char in air at 400°C in TGA (height-normalised Raman intensity [49])**

Thus, among the different carbons structures, small aromatic rings systems and aliphatic chains seem to be the most reactive structures since they can be more easily attacked by oxygen atoms from the gasifying agent than the other structures (graphite and large aromatic rings). Minerals structures (which are active sites too) tend to be mostly dispersed into the small aromatic rings system.

### 2.2.2. Mineral content

The role of the mineral content in the pyro-gasification process has also been widely studied since they have been depicted to be catalyst of the biochars conversion. To investigate their influence, most of the studies doped (by impregnation) the biochars with the minerals of interest prior to the pyro-gasification [50]–[52]. Methods of impregnation are presented in the section 2.1.2. The activities of the Alkali and Alkaline Earth minerals (AAEMs) and the transition metals, and their deactivation are presented in the subsections below.

#### 2.2.2.1. AAEM's role

AAEMs have been highlighted to be the most efficient catalysts during the pyro-gasification processes [53]. McKee et al. [54] highlighted that the pyro-gasification reaction (with steam or CO<sub>2</sub>) occurred via the metal particles dispersed on the surface. First the gasifying molecule is dissociated on the metal sites and then oxygen atoms adsorbed on the metals diffuse over the carbon matrix to

react with carbon atoms. This observation could be correlated to the fact that small aromatic rings systems, on which mineral particles have been depicted to be dispersed are the most reactive. In fact, oxygen atoms attracted by minerals diffuse firstly into these structures and thus they are preferentially consumed.

Regarding minerals properties, concentration, elemental composition and crystalline arrangement of the biochars surface were investigated [55]–[58]. As it was described previously AAEMs are the major components in the ash composition. Potassium has been presented to be one of the most effective catalyst [58], [59]. Delannay et al. [60] investigated the role of KOH in the steam gasification of graphite. They proposed a mechanism in four steps: dissociative adsorption of water forming C-H and C-OH groups, formation of a K-O-H entity, from the reaction of KOH with the phenol group, the decomposition of the K-O-C entities to give CO, K<sub>2</sub>O and perhaps metallic potassium and the formation of KOH from K<sub>2</sub>O with water. Huttinger et al. [61] also performed water vapor gasification on graphite and coal biochars and investigated the activity and the formation of different potassium species. They found the following reactivity sequence KOH ≈ K<sub>2</sub>CO<sub>3</sub> ≈ KNO<sub>3</sub> > K<sub>2</sub>SO<sub>4</sub> > KCl. In addition they stated that the presence of KOH is a key component since all the other species are formed from it. An illustration is presented in Figure I-13. The study from Devi et al. [37] presented previously stated that below the boiling point of the metallic potassium (about 923 K or 650°C) the active species are K<sub>2</sub>O, K<sub>2</sub>CO<sub>3</sub> and KOH while at higher temperature the potassium vaporizes as metal and then interacts with the carbon surface.

The catalytic role of the other AAEM was investigated in the literature as well. Some early works on the importance of alkali catalysts in biomass pyro-gasification such as the one published by Elliott et al. [62] found that sodium, potassium and caesium carbonates were equally effective at typical pyro-gasification temperatures. Hwuang et al. [36] investigated the magnesium role in the fast pyrolysis of yellow poplar impregnated with different concentrations of MgCl<sub>2</sub>. They showed that the yield of biochars and some physico-chemical properties of biochars were directly affected by the magnesium content. The role of calcium was also investigated since it is usually the major component in the ash fraction of biochars [63]. Studies have shown that calcium species enhanced the char yield conversion however it seems to not be the most effective AAEM catalyst [58], [59], [64], [65]. However a specific role of calcium was emphasized by Jiang et al. [66], they highlighted that calcium species prevents potassium carbonate from being deactivated. A mixed carbonate K<sub>2</sub>Ca(CO<sub>3</sub>)<sub>2</sub> was identified as the active species. In fact, it is established that potassium could be deactivated by formation of a silicate. Kannan et al. [67] emphasized that the catalytic effect of potassium was reduced by its arrangement with silica to form silicate during pyrolysis. Different studies from Zhang and Zhang et al. have been reported in “A review of catalysts for the pyro-gasification of biomass

char, with some reference to coal” from Nzihou et al. [53] in which they have highlighted that the distribution in concentration of calcium, potassium, sodium and silicate play a significant role in terms of carbon reactivity (see Figure I-14). Three groups were distinguished as:

- group I is described as  $[K] + [Na] > [Ca]$
- group II:  $[Ca] > [K] + [Na]$
- group III contains a high amount of silicon

Group I was depicted to be the most effective which seems to show that inherent alkali metals are more effective than alkaline earth. The low reactivity of the group III enhances the fact that high amount of silicon deactivate potassium forming potassium silicate species.

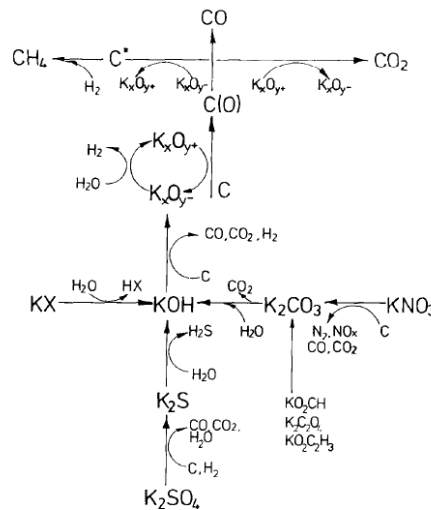


Figure I-13: General scheme of the potassium catalyzed water vapour gasification:  $K_xO_{y+}$ , and  $K_xO_{y-}$  do not necessarily mark the same species [61]

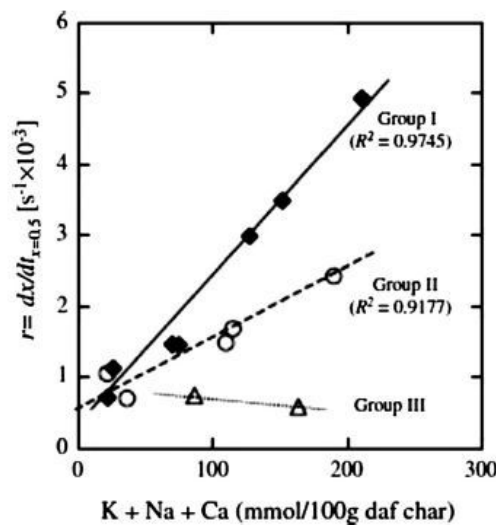


Figure I-14: Reactivity towards steam for 14 biomass biochars with respect to AAEM content Group I:  $[K] + [Na] > [Ca]$ , group II  $[Ca] > [K] + [Na]$ , group III high  $[SiO_2]$  [68]

### 2.2.2.2. Transition metals

Some studies investigated the role of the transition metals in the biomass pyro-gasification reactivity. The effect of Cu, Ni and Fe on gasification under oxygen between 300 and 500°C and CO<sub>2</sub> at 700-800°C was investigated by Gallagher and Harker [69]. They found that the efficacy is dependent on the liberation of the free metal. The comparison of the efficiency of the three same transition metals by Figueredo et al. [70] has shown that nickel and cobalt are more interesting than iron. However the transition metals represent few percents of the ash composition and are only traces at the biochars surface. The catalytic activity should not be directly or at least not only related to them.

### 2.2.2.3. Inhibition mechanism and loss of AAEMs

Deactivation or decrease in the activity of the AAEM species could be due to some arrangements of the active mineral such as potassium and calcium with silicon to form amorphous and inactive silicates. However deactivation could be due to others factors. For example the disproportionation of CO on the AAEM active sites slows down the char conversion by blocking the access to the gasifying agent. The release of AAEMs is also another key issue at high temperature. Jiang et al. [71] highlighted that the divalency of alkaline earth metal (Ca and Mg) provides a higher stability at the biochars surface because two bonds are created with the matrix rather than one of the alkali metals (K and Na). Hence alkaline earth metals are harder to vaporize during a pyro-gasification treatment. The mobility of the metal species is a crucial feature as well. Klinghoffer et al. [19] have shown that above 1000°C reactivity of biochars were drastically diminished probably due to agglomeration of the metal species. Radovic et al. [72] found that deactivation of calcium occurred due to sintering via crystallite growth. Baker et al. [73] observed that above the so-called Tammann temperature the mineral particles start to become mobile. The Tammann temperature is proportional to the melting temperature, it is usually defined as  $0.51 T_M$  (with  $T_M$  melting temperature). Figure I-15 shows the Tammann temperature for different metals. One can notice that calcium oxide has the highest Tammann temperature (1500 K) which indicates that calcium species should be prevent from agglomeration and thus deactivation at the usual pyro-gasification reaction.

Thus AAEMs have been depicted to be the major components in ashes and the most efficient catalyst sites. Some differences in efficiency in the AAEMs were highlighted the potassium seem to be the most reactive for carbon conversion during thermal treatment. KOH and K<sub>2</sub>CO<sub>3</sub> were depicted to be really efficient and KOH a key component for the formation of the other structures. However potassium suffers from volatilization up to around 780°C and from deactivation by combination with silicon to form silicate complex. The presence of calcium was described as a good protection from the

formation of potassium silicates because potassium and calcium mixed in a new structure which is still active. Also operating conditions are really important regarding the reactivity of the AAEMs since they influence their mobility, their volatilization and their predominant structures.

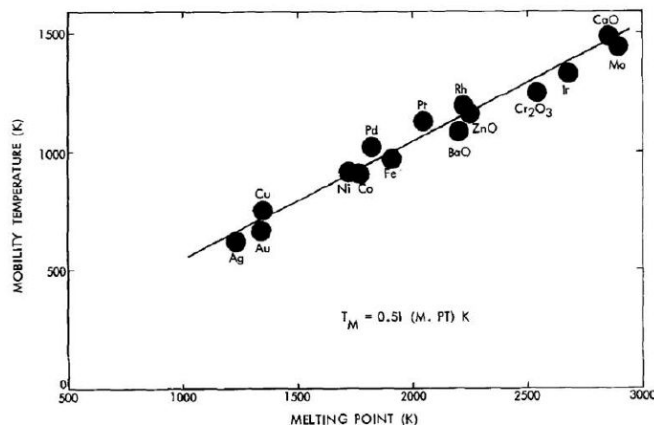


**Figure I-15: Relationship between mobility of particles supported on graphite and their bulk melting temperatures [73]**

Thus, the characterization of the surface properties of the biochars and the relationship with their reactivity gave insights into the pyro-gasification mechanism. Some studies worked in enlarging the utilization of the biochars for other applications which are presented in the following section.

### 2.3. Applications

Three main domains have been highlighted for biochars valorization: their utilization as fertilizer/soil acidity regulator, adsorbent or catalyst.

#### 2.3.1. Fertilizer/soil acidity regulation

A potential valorization of biochars is their utilization as fertilizer and soil acidity regulator [74], [75]. In fact, biochars are carbon materials containing abundant carbonaceous components, basic and organic cations. Thus they have the ability to regulate the soil acidity [76]. They are able to increase the soil pH and enhance the cation exchange capacity (CEC; capacity of the soil to hold cations). The CEC of biochars has been evaluated in the range from 10 to 69  $\text{cmol}_c.\text{kg}^{-1}$  while, for example, sandy soils CEC is about 3  $\text{cmol}_c.\text{kg}^{-1}$  [77]. In addition the incorporation of biochars with sludge composite into land application was found to significantly reduce nitrogen loss [78].

### 2.3.2. **Adsorbent**

The inherent high specific surface area of biochars is of great interest for adsorbent applications. Various studies investigated the effectiveness of biochars for removal of organic contaminants such as phenol in aqueous media [79], [80] or tetracycline [81], adsorption of dyes [82] or metal ions [83], [84]. Hot gas cleaning was also performed on biochars. For example Lizzio et al. [85] investigated the adsorption of SO<sub>2</sub> from flue gases on biochars.

### 2.3.3. **Catalyst**

The utilization of the biochars as catalyst represents a large opportunity since the demand is steadily increasing and the common commercial catalysts are really expensive due to the use of metal as active phase. In catalysis application both the surface developed by the catalyst and the functional groups at the surface are important criteria. Recent studies proposed catalytic applications for biochars. Wu et al. [86] investigated their use for catalytic reduction of nitrobenzene. Li et al. [87] investigated the NO and NO<sub>2</sub> reduction over coal chars. Dekhoda et al. [88] et Kastner et al. [89] studied the simultaneous esterification and transesterification of fatty acids over biochars. Yuan et al. [90] worked on the oxygen reduction in a microbial fuel cell over sewage sludge biochars. Lastly, El Rub et al. [20] and Klinghoffer et al. [91] investigated the use as catalyst of the biochars directly in the pyro-gasification process to catalyze the cracking of heavy and light hydrocarbons. This latter application seems to be promising. In fact, the use of biochars as catalyst for syngas cleaning presents various advantages: firstly it is an on-site valorization of the material which do not require any transportation. Secondly it could replace metal-based catalysts which are costly and deactivate quickly due to the harsh environment.

## 2.1. **Functionalization**

In order to increase the reactivity of biochars, post-gasification treatments can be performed to play on their surface physico-chemical properties.

### 2.1.1. **Oxygenation treatments**

Various methods have been proposed to oxygenate the carbon based material surface [32], [92]–[94]. These methods can be gathered into two main families: the wet impregnation and the dry treatments. Nitric acid ( $\text{HNO}_3$ ), phosphoric acid ( $\text{H}_3\text{PO}_4$ ) and hydrogen peroxide ( $\text{H}_2\text{O}_2$ ) solutions are the most common wet impregnations because they are strong oxidizing agents. The dry treatments are essentially oxygen, ozone ( $\text{O}_3$ ) and nitrous oxides ( $\text{N}_2\text{O}$ ) treatments.

Figueiredo et al. [40] investigated different oxygenation methods on commercial activated carbons:  $\text{O}_2$  and  $\text{N}_2\text{O}$  gas-phase treatments and nitric acid, hydrogen peroxide immersions. They evaluated the performances of the oxygenation and the selectivity by TPD, XPS and FTIR analyses. Regarding the efficacy of the treatment both TPD and XPS highlighted the following sequence:  $[\text{O}]_{\text{raw}} < [\text{O}]_{\text{H}_2\text{O}_2} < [\text{O}]_{\text{HNO}_3} < [\text{O}]_{\text{N}_2\text{O}} < [\text{O}]_{\text{O}_2}$ . Results also clearly emphasized that the wet methods enhanced the acidic functions desorbing into  $\text{CO}_2$  in the temperature range 100-800°C whereas gas-phase treatment tends to increase the basic functions desorbing into CO at higher temperature 400-1000°C. Jaramillo et al. [95] investigated almost the same methods of oxygenation as Figueiredo et al.:  $\text{O}_2$  and  $\text{O}_3$  treatments,  $\text{HNO}_3$  and  $\text{H}_2\text{O}_2$  wet impregnations on activated carbons but FTIR and Boehm titration were used to study the oxygenated functions. They found that the  $\text{HNO}_3$  and  $\text{O}_3$  treatments were the most efficient processes to increase the acidic oxygenated functions whereas  $\text{H}_2\text{O}_2$  and  $\text{O}_2$  treatments rather enhanced equally all the oxygenated functions. Thus according to the type of oxygenated functions targeted to be enhanced at the carbonaceous surface the chemical treatment to apply will be different.

Operating conditions such as time and temperature will impact the efficiency and the selectivity of the oxygenation as well. Xianglan et al. [92] prepared activated carbons using  $\text{HNO}_3$  and  $\text{H}_2\text{O}_2$  and performed TPD to characterize them. Activation time increased lactone functions during the  $\text{HNO}_3$  immersion and carbonyl groups during the  $\text{H}_2\text{O}_2$  treatment. Fanning et al. [96] characterized carbon black and Saran carbon after oxidation under an  $\text{O}_2/\text{N}_2$  mixture. At the early stage of the oxygenation FTIR analyses highlighted the formation of ether function. Upon further oxygenation anhydride, lactone and phenol functions were enhanced. Koch et al [97] also investigated air oxygenation of carbonaceous char by FTIR. They observed that the oxygenation was time and temperature dependent. Lactone, anhydride, carboxylic and ketone functions increased with temperature. At 280°C, quinones were enhanced continuously over the oxygenation. Anhydride, ketone and carboxyl after a strong increase due to the temperature stabilized around a constant value.

Oxygenation treatments tend to impact the other physico-chemical properties of the carbonaceous surface. The evolution of the specific surface area and porosity are usually investigated simultaneously as the enhancement of the oxygenated functions. Pradhan et al. [98] oxygenated highly microporous charcoal activated carbons by wet impregnation under nitric acid, hydrogen peroxide and ammonium persulfate ((NH<sub>4</sub>)<sub>2</sub>S<sub>2</sub>O<sub>8</sub>). The oxygenation leads to carbons with a higher amount of oxygenated functions but with a smaller porosity and specific surface area. Post oxygenation, the specific surface area and porosity have been halved. The two other treatments had a less significant impact on the textural properties. They also investigated the evolution of the structural parameters of the carbon crystallites (L<sub>a</sub>, L<sub>c</sub> and d<sub>002</sub>) by X-ray diffraction (XRD). Oxygenation brought closer the graphitic planes but did not impact the size and thickness of the crystallites. Figueiredo et al. [40] investigated the textural properties evolution according to the type of oxygenation treatments. They found that the wet impregnation did not impact the specific surface area whereas the O<sub>2</sub> gas phase treatment tends to significantly increase the micropore volume and their average width.

### 2.1.2. ***Impregnation with minerals***

Such as for the oxygenation, wet and dry techniques can be employed. Shen et al. [99] proposed a review on the utilization of biochars as adsorbents for tar elimination during pyrolysis or pyro-gasification and summarized the possible methods to increase the mineral content of biochars. The physical method consists in mechanically mixing metal oxides with biochars. The wet method is an impregnation of rather biomass particle or biomass biochars in a solution of the mineral salt. Shen et al. stated that the wet method provided a better metal particles dispersion than the physical mixing since metal with nanoparticles could also be formed inside the support. Richardson et al. [100] immersed beechwood chips into a solution of nickel nitrate aqueous solution during 3 days at room temperature. They highlighted that the oxygenated groups acted as adsorption sites for metal cations in aqueous medium which lead to a very high dispersion into the wood matrix. Transmission Electronic Microscopy (TEM) highlighted the good dispersion of the mineral at the wood biochars surface.

## 2.2. Partial conclusion

This section was dedicated to the characterization of the physico-chemical properties of the biochars, its reactivity, the possibilities to enhance its reactivity and the potential applications. Biochar is the solid residue from pyro-gasification which is highly porous and thus which developed a high specific surface area. It is a turbostratic carbon structure containing various types of amorphous structures (aliphatic chains, aromatic rings, “in plane” imperfections). Amorphous content was described to be more reactive toward pyro-gasification than well-ordered carbon. Biochar contains also functional groups at the surface such as O-containing groups and minerals. Various oxygenated functions can be identified which could have an acidic character (carboxylic acid, phenol, lactone) or basic (pyrone, quinone). Mineral content represents the inorganic part of the biochars and is usually called ash. In biochars, AAEMs represent the major concentration of the ash: calcium, potassium and magnesium. Depending on the biomass, silicon and aluminum could take part of the major components. The AAEMs have been revealed to be catalytic sites for the pyro-gasification process and most specifically potassium. The amount of silicon is an important parameter since potassium silicate can be formed which is an inactive structure. Some studies highlighted that calcium prevent from potassium silicate formation to rather form  $K_2Ca(CO_3)_2$  which is an active catalytic site.

The physico-chemical properties of the biochars are adapted for different applications such as fertilizer, adsorbent or catalyst. Recent studies investigated the utilization of biochars to adsorb pollutants from aqueous media or to catalyze hydrocarbon cracking. To get better activity and selectivity, the biochars can be functionalized prior their utilization such as adsorbent or catalyst. To enhance the oxygen content at the surface, a liquid or dry oxygenation can be performed. The dry method has been depicted to potentially enhance the porosity of the biochars and enhance the “in plane” imperfections. A wet impregnation into a mineral salt solution can also be performed to increase the mineral content at the surface. Thus different ways of valorization are possible for biochars. However the best option for different reasons seems to utilize the biochars as catalyst for hot syngas cleaning. In fact current commercial catalysts for this application are expensive and suffer from quick deactivation. Biochars could replace them such as they are already on site and for free. To ensure good catalytic performances, functionalization of the surface is an option to enhance the reactive sites at the biochar surface.

### 3. Catalytic methane cracking

The methane cracking reaction has been chosen to evaluate the catalytic activity of biochars. In fact, methane cracking is representative of the C-H bonding breakage (model molecule) which is present in hydrocarbons in general. In addition, methane is the second gaseous co-product right after carbon dioxide and its conversion leads to increase the hydrogen production and thus the syngas yield. Methane is the most stable hydrocarbon, high temperature is required to obtain an acceptable yield in the case of a pure thermal cracking. Thus, catalysts are used to obtain better yield at lower temperature. Commercial catalysts are commonly composed of an active phase (transition metals such as nickel, copper or iron) dispersed onto a support with a high specific surface area (for example alumina). However, an issue is the fast deactivation of the (expensive) active phase due to coke deposit over the reaction (chemisorption of carbon atoms from the methane molecule on the metal particle and in the pores). Carbonaceous materials and more specifically biochars (which contain inherently minerals) present a promising and cheaper alternative.

This section introduces thermodynamic considerations to justify the utilization of a catalyst in the methane cracking reaction. Then a quick presentation of the utilization of nickel based catalysts and their deactivation by coke deposit is provided to introduce the interest in the carbonaceous catalysts for this type of reaction.

#### 3.1. Thermodynamic aspects

For a given reaction, an equilibrium constant is associated which expresses the relationship between the products and reactants at the equilibrium. According to the value of the equilibrium constant rather the products or reactants will be predominant.

If the equilibrium coefficient is:

- < 1 then equilibrium favors reactants
- > 1 then equilibrium favors products

If we consider the methane cracking reaction presented in Eq.I-10, the associated equilibrium constant is defined as presented in Eq.I-11.



$$K_{eq} = \frac{(P_{H_2})_{eq}^2}{(P_{CH_4})_{eq}} \quad \text{Eq.I-11}$$

A relationship exists between the equilibrium constant and the Gibbs free energy (see Eq.I-12). At equilibrium Eq.I-12 becomes Eq.I-13. The standard Gibbs free energy of reaction could also be expressed as a function of the standard enthalpy of reaction and the standard entropy of reaction (see Eq.I-14). According to this relationship, the temperature above which the reaction becomes spontaneous can be calculated. In fact:

- if  $\Delta G^0 < 0$ : the formation of products is spontaneous
- if  $\Delta G^0 = 0$ : the reaction is at the equilibrium
- if  $\Delta G^0 > 0$ : the formation of the reactants is favored

$$\Delta G = \Delta G^0 + RT \ln (K_{eq}) \quad \text{Eq.I-12}$$

$$\Delta G^0 = -RT \ln (K_{eq}) \quad \text{Eq.I-13}$$

$$\Delta G^0 = \Delta H_r^0 - T \Delta S_r^0 \quad \text{Eq.I-14}$$

**Table I-2: Thermodynamics properties**

	units	$CH_4(g)$	$C(s)$	$H_2(g)$
$\Delta H^0$	KJ.mol <sup>-1</sup>	-74.8	0	0
$S^0$	J.K <sup>-1</sup> .mol <sup>-1</sup>	186.3	5.68	130.7

From the calculation we performed using the thermodynamics properties presented in Table I-2, we estimated that the reaction becomes spontaneous above 480°C (this was only an estimation since enthalpy and entropy were considered constant). From the literature, in which more accurate calculations have been carried out the reaction has been evaluated to become spontaneous above 550°C [101]. However, even if the formation of products is favored from about 550°C, the reaction rate is dependent from the kinetics of the reaction. The reaction rate constant can be written following Eq.I-15 which is exponentially dependent from the activation energy. Thus, a little change of the activation energy could have significant impact on the reaction rate. The goal in utilizing a catalyst is to provide an alternative route for the reaction to occur. In fact, intermediates can be

formed at the surface of the catalysts which can make the reaction mechanism more complicated but can result in lowering the energetic barrier (see Figure I-16). For example, the binding energy of the C-H bond is of  $415 \text{ kJ}\cdot\text{mol}^{-1}$  which represents the energy required to break this linkage. In fact, Muradov et al. [102] reported that for non-catalytic methane cracking the activation energy required was in the range 370-430 kJ/mol. In the following sections, one will observe that the activation energy needed using a catalyst will be lowered. In this chapter, some kinetics aspects are discussed such as the activation energy. However, the Chapter 5 is dedicated to a detailed presentation and discussion of the kinetics aspects of the reaction.

$$k = Ae^{\frac{-E_a}{RT}} \quad \text{Eq.I-15}$$

with:

$k$ : reaction rate constant

$A$ : pre – exponential factor

$E_a$ : activation energy (J/mol)

$R$ : Ideal gas constant (J/mol.K)

Thus, the utilization of a catalyst did not influence the thermodynamics equilibrium but impacts the kinetics of the reaction. Four parameters are important when dealing with catalysts: their activity, selectivity, stability and cost. Tests have to be performed to evaluate the most adapted catalyst for a type of reaction.

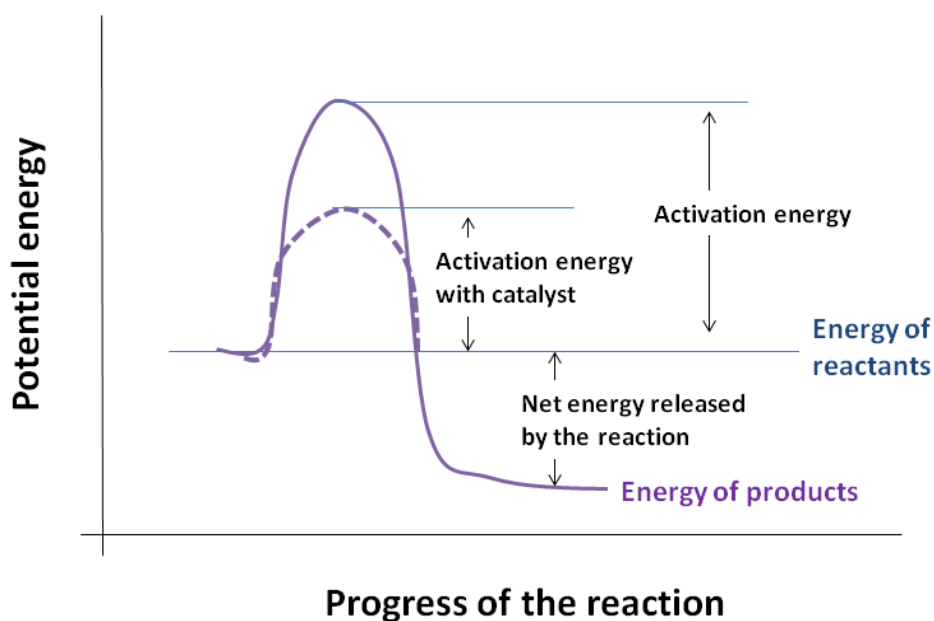


Figure I-16: Illustration of the energetic barrier in the non-catalyzed and catalyzed reactions

### 3.2. Metal supported catalysts

Transition metal supported catalysts show high reactivity toward methane cracking due to their unique 3d-orbital properties [103]. Muradov et al. [102] reported that the activation energy for transition metal-catalyzed reaction was as low as 60 kJ/mol and below. Nickel, iron and cobalt were highlighted to be the most efficient. In fact, iron is widely utilized to catalyze hydrocarbons cracking [104]. However, regarding methane cracking which is the most stable hydrocarbon nickel has been depicted to be the most interesting in terms of cost/efficacy and remains the most active phase utilized in commercial catalysts [101], [105].

During the methane cracking reaction, carbon firstly fixed on nickel particles and then diffused through the support. Deactivation process is due to the blocking of the nickel particles which are the active sites for the reaction and the clogging of pores due to carbon deposit. A tricky issue when dealing with methane cracking over nickel supported catalyst is to increase the efficacy time of the catalyst. To achieve the best performances the operating conditions play an important role. In fact an optimal temperature for methane cracking over nickel supported catalysts at 550°C was highlighted due to the equilibrium achieved between the amount of carbon deposited on nickel particles and their migration on the supports [106]. The activity of the nickel particles are also strongly correlated to their physico-chemical properties. In fact the electronic state and the dispersion of the nickel particles are of great importance. To increase the dispersion of nickel particles and thus the catalyst reactivity, nickel-based alloys such as Ni-Pt, Ni-Pd, Ni-Co, Ni-Mo and Ni-Cu were investigated [103], [107], [108].

### 3.3. Carbonaceous materials

Growing interest for the utilization of carbonaceous materials as catalyst for methane cracking can be noticed. Reviews proposed by Amin [106] and Fidalgo et al. [109] draw up the state-of-the-art regarding the use of various carbonaceous materials as catalysts. Carbonaceous catalysts can be utilized on their own or as support of the active phase.

### 3.3.1. **Comparison of carbonaceous catalyst activities**

Carbonaceous materials present interesting advantages knowing the difficulties we can encounter using metal active phases. In fact they are low cost, available and durable catalysts which are temperature resistant and sulfur tolerant as well. They produce hydrogen which is not polluted by carbon oxides and thus could mitigate the CO<sub>2</sub> emission [109]. Carbon catalyst could be used as support. In this case the textural properties of the carbonaceous material are of great importance to provide a good metal dispersion. For such kind of applications activated carbons or carbon blacks are the most adequate. However in this study, the focus is on the carbonaceous materials utilized as catalyst on their own. Literature reported methane cracking investigations in various types of carbons such as the activated carbons, carbon blacks, glassy carbons, graphite carbon, nanotubes or fullerenes and more recently on biochars [102]. Each of these carbons presents different physico-chemical properties which gives rise to different reactivity and selectivity.

Two types of catalytic tests are usually performed: isothermal cracking (at a temperature fixed between 700 and 950°C) or non-isothermal cracking (over heating with a fixed heating ramp). Tests could be carried out rather in a plug flow reactor or in a thermogravimetric balance. In fact, the catalytic performance could be estimated by measuring the methane conversion, the hydrogen production or the carbon deposit onto the catalyst since the main cracking reaction is the conversion into hydrogen and coke (see Eq.I-10). Operating conditions greatly affects the methane conversion such as temperature, methane partial pressure, flow rate and have been extensively studied in the literature.

In terms of activation energy, the value is dependent of the type of carbons. Muradov et al. [102] reported that for activated carbon  $E_a$  varied in a range of 160-201 kJ/mol (at 600-900°C), for coal derived AC it was estimated between 186-198 kJ/mol and for carbon black catalysts the measured  $E_a$  were somewhat higher (205-236 kJ/mol).

Activated carbons and carbon blacks have been the most investigated carbonaceous materials. The Suelves's team published several papers on this subject [108], [110]–[112]. Suelves et al. [113] compared the activity and stability of six commercial samples: two graphitized carbon blacks (Carbopack), three carbon blacks (Fluka) and an activated carbon (CG NORIT). Catalytic tests were performed in a fixed-bed reactor at 850°C. Figure I-17 presents the hydrogen production over time for the six commercial carbons tested.

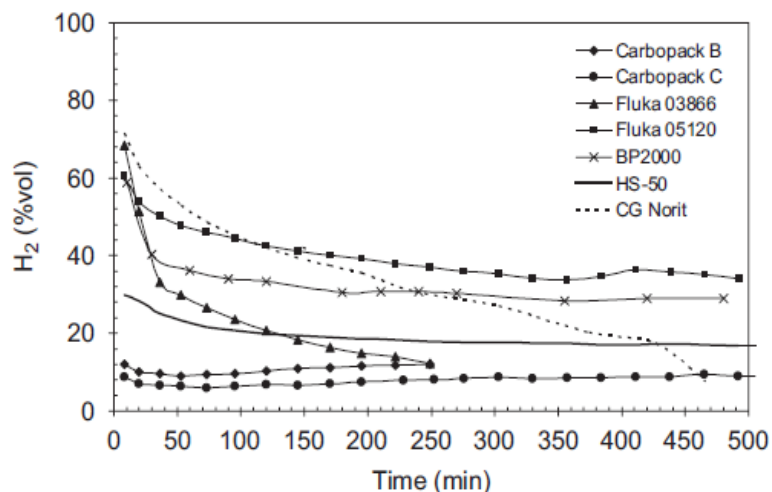


**Figure I-17: Hydrogen production (%vol) for the different catalysts tested, T:850°C, methane flow:20 mL/min [113]**

- **Initial activity:**

One can observe on Figure I-17 that the initial hydrogen production is significantly different according to the nature of the carbonaceous catalyst. Two groups are observed: graphitized carbon blacks (Carbopack) present the lowest initial activity (about 10 vol% H<sub>2</sub>) whereas carbon blacks (Fluka) and the activated carbon (NORIT) show a significant higher production (about 70%). Muradov et al. [114] observed as well that the activated carbons presented a highest initial hydrogen production than carbon blacks.

- **Deactivation:**

It is visible on Figure I-17 that the two distinct groups did not behave similarly. In fact, the activated carbon and carbon blacks are strongly deactivated during the first hour (loss of about 30 vol% of H<sub>2</sub> production). On the contrary, the graphitized carbon blacks present a quite steady production. Kim et al. [115] also investigated methane cracking on activated carbons from coconuts shell in a fixed-bed reactor. A quick deactivation within the first hour and then a stabilization was also reported. Regarding carbon blacks Lázaro et al. [110] tested three commercial carbon blacks for methane cracking at 850°C. Even if a slight deactivation in the early stages was observed, the overall hydrogen production was more constant than for the activated carbons. Fidalgo et al. [109] highlighted in their review that several research groups agreed on the observation that activated carbons presented higher initial hydrogen production than carbon blacks. However they suffered from a stronger deactivation as well in the early stages of the reaction [102], [110], [116].

Regarding the biochars activity, Klinghoffer et al. [91] investigated the catalytic cracking of methane over biochars from poplar wood pyro-gasification (gasified under steam or CO<sub>2</sub> at 750 and 920°C). Tests were performed in a thermogravimetric analyzer up to 1000°C with an heating ramp of 5°C/min. To evaluate the efficiency of the cracking reaction, the mass gain due to carbon deposit is monitored during the experiment. Figure I-18 shows the mass gain over time for the four biochars tested as catalyst for the methane cracking. The threshold temperature (from which coke starts to be deposited on biochars during the methane cracking) was about 650°C for the four biochars and a similar deposit is observed up to 800°C. At higher temperature a significant increase of the coke deposit amount was observed for the biochars produced at the 920°C under CO<sub>2</sub> during 30 minutes and under steam at 750°C during 1h. Then a decrease in the coke deposit amount is observed during the plateau for the biochars.

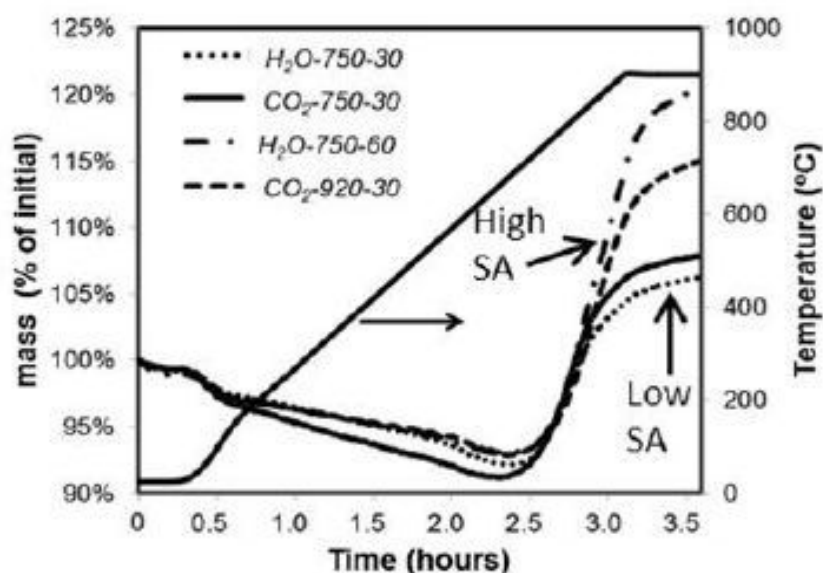


Figure I-18: Catalytic performance of different char samples for methane cracking [19]

Klinghoffer et al. further investigated the deactivation of the biochars. An additional methane cracking test was performed in the thermogravimetric analyzer. However, for this test the reaction was performed at a fixed temperature (750°C) and the coke deposit amount was recorded over the reaction (see Figure I-19). One can observe on Figure I-19 that two regions of deactivation are observed: an initial rapid deactivation and a second regime of more gradual deactivation. The deactivation rates were calculated: for regime 1 it was evaluated at  $-2.2 \times 10^{-3} \text{ mmol.gchar}^{-1}.\text{h}^{-2}$  and during the regime 2 at  $-1.1 \times 10^{-3} \text{ mmol.gchar}^{-1}.\text{h}^{-2}$ . This deactivation pattern is similar to the one observed for the activated carbons.

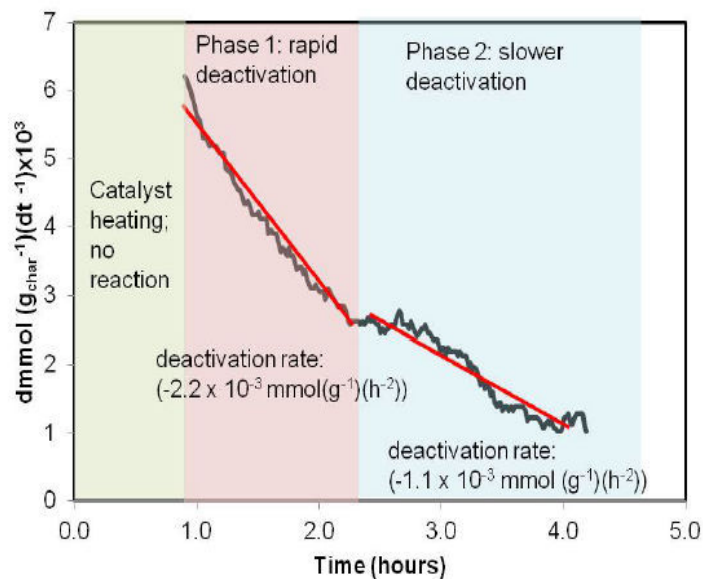


Figure I-19: Catalyst deactivation for CH<sub>4</sub> cracking reaction [19]

Thus, different behaviors have been observed according to the type of carbonaceous materials at the initial stages of the methane cracking reaction and in the long-term. To get a best understanding of the methane cracking mechanism at the carbonaceous materials surface some studies have been dedicated to investigate the role of the physico-chemical properties of the surface in the reactivity of the biochars. This is the topic of the following section.

### 3.3.2. *Correlation surface properties / reactivity*

Studies presented in the previous section questioned the difference of activity and stability of different carbonaceous materials. In order to get insights into the methane cracking mechanism, several studies worked on establishing a correlation between the methane conversion and the surface catalyst physico-chemical properties. The initial conversion and the deactivation were usually studied separately.

- **Influence of the pore volume and specific surface area**

Regarding the influence of the physical properties (specific surface area and porosity) on the initial methane conversion, several authors [111]–[113], [115], [117] agreed to say that no good correlation can be established. Regarding their influence on the long-term, Suelves et al. [112] represented the

carbon deposit per initial catalyst mass against specific surface area and total pore volume. They highlighted that a linear relationship is observed between the total pore volume and the carbon deposit whereas for close values of specific surface area different amount of coke can be deposited (see Figure I-20). In fact, it has been highlighted that coke deposit should be the mode of deactivation of the catalyst by clogging of the pores which should directly decrease the total pore volume [91]. Moliner et al. [111] performed a similar study plotting the initial methane cracking rate and amount of carbon deposit versus specific surface area of activated carbons. No correlation was observed between the initial reactivity and the specific surface area as mentioned previously. However in this case they highlighted a good relationship between the carbon deposit and the specific surface area (which diverges from the Suelves's observations) (see Figure I-21). This difference observed between the two studies could be due to the fact that only activated carbons have been compared in the Moliner's study whereas different types of carbons: activated carbons and carbon blacks have been studied. Other surface properties in the ACs and CBs could be different and thus impacted the results. Thus the textural properties seem to play a role in the deactivation process. However further researches are required to state on the pore volume and specific surface independent role.

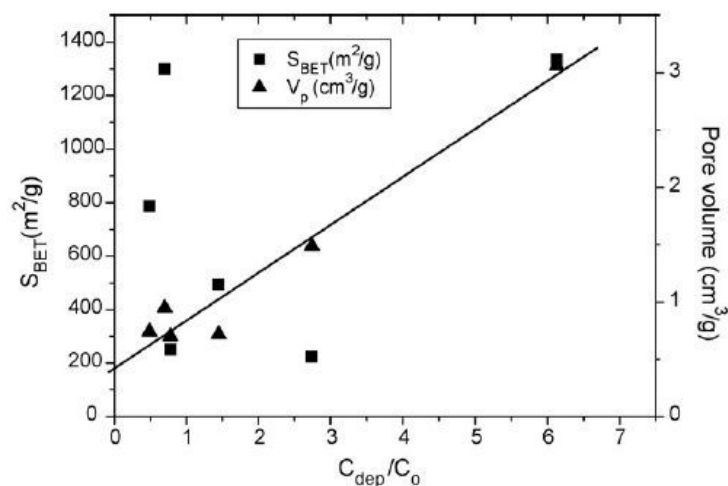


**Figure I-20: Carbon deposited per initial catalyst mass for the runs carried out at 900°C until deactivation versus surface area (left axis) and versus total pore volume (right axis) of the fresh catalyst [112]**

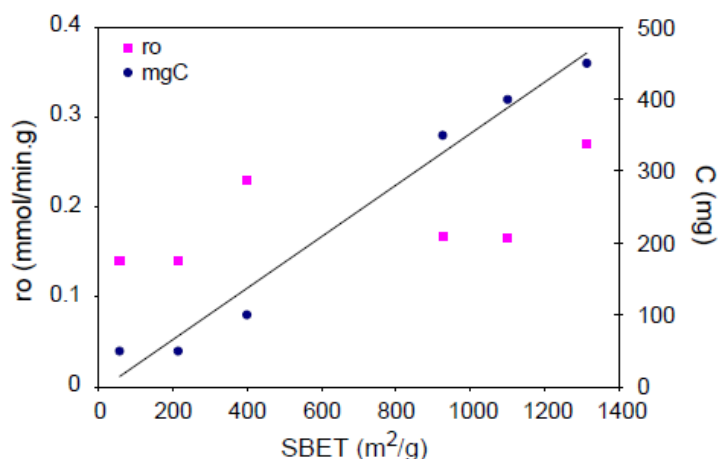


**Figure I-21: Initial activity from methane conversion and carbon accumulated as a function of the BET surface area of the fresh catalyst T=850°C [111]**

- **Influence of the O-containing groups**

Regarding O-containing groups, as it has been presented in the section 2.1.3, several oxygenated functions exist on the carbonaceous surface which are more or less stable when increasing the temperature. Acidic groups tend to be less stable than basic functions. O-containing groups could rather desorb into CO<sub>2</sub> or CO. They could affect the methane cracking in two different ways: (1) non stable groups at the methane cracking temperature (> 700°C) will desorb before the methane introduction and then let unsaturated carbons or vacancies into the carbon matrix which are potential active sites for the methane cracking. In that case O-containing groups are not directly active sites but can influence the increase of potential other active sites. In the second case, the remaining oxygenated functions could be active sites on their own. Suelves et al. [112] investigated the influence of the non-stable oxygenated groups on the methane cracking on activated carbons and carbon blacks. In fact they evaluated the amount of oxygenated groups desorbed below 850°C (methane cracking temperature) by TPD. Then they plotted the amount of CO and CO<sub>2</sub> desorbed versus initial methane cracking reaction rate (see Figure I-22). They observed that a good correlation between the amount of CO desorbed prior to the reaction and the initial decomposition rate whereas no clear relationship with the CO<sub>2</sub> amount was highlighted. In fact the activated carbon containing the highest amount of basic groups desorbing above 850°C showed the highest catalytic activity. Lazaro et al. [110] investigated the CO and CO<sub>2</sub> production over time during a methane cracking run on carbon blacks. They noticed that even if both gases productions quickly diminished the CO evolution tend to follow the methane conversion whereas CO<sub>2</sub> seems to be disconnected. Muradov et al. [102] tested the impact of oxygenated groups by comparing the activity of an

activated carbon and a N<sub>2</sub> pre-treated activated carbon. The N<sub>2</sub> treatment was carried out to remove the oxygenated functions. They compared the hydrogen and carbon monoxide production of the two catalysts. They stated that even if oxygenated functions could play a role at the early stage of the test, they should not influence the conversion in the long term. Thus several authors agree on the fact that the early stages of the methane cracking should be influenced by the O-containing groups.

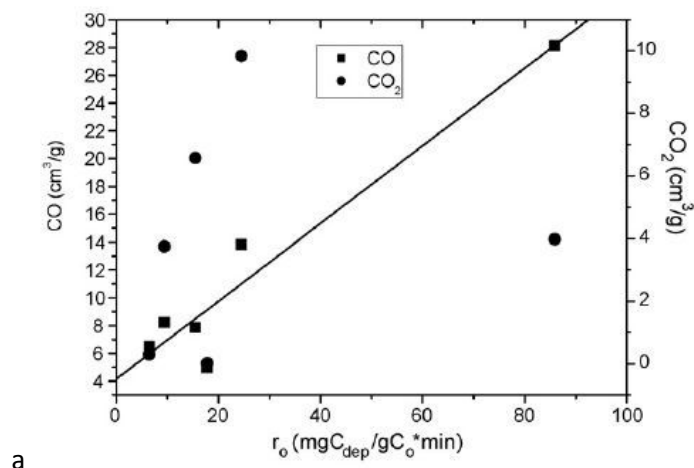


**Figure I-22: Initial decomposition rate versus amount of surface oxygenated groups desorbed in TPD runs as CO (left axis) and CO<sub>2</sub> (right axis) [112]**

- **Influence of the minerals**

The role of the ash content in the methane cracking reaction was not extensively studied. Iron was mentioned to be active for methane cracking [118]. However its content in most of the carbonaceous materials is very low. Kim et al [115] investigated the methane conversion of raw and ash-removed activated carbons from coconut. Activated carbons from coconut usually contain between 1 and 5 wt% of ashes which are mainly composed of K, Na, Si and Mg. Methane conversions were slightly impacted by the removal of the ash content but the deactivation profiles stay similar.

Klinghoffer et al. [19] compared the activities of a raw and acid washed biochars in a plug flow reactor at 700°C. They highlighted that the activity of the latter was significantly smaller than the former. These results tend to say that mineral content at the surface play a catalytic role for methane cracking. To go further in the understanding they performed the same catalytic test on pure ash of which the activity was drastically diminished compared to the char. This should mean that the interaction between ash and carbon matrix should give rise to organometallic active sites since carbon or ash taken alone show smaller activity than together (see Figure I-23). A third test has been carried out, methane cracking was performed on a pre-heated biochars (up to 1000°C). Figure I-23 compares the activities of this pre-heated biochars and the raw biochars.

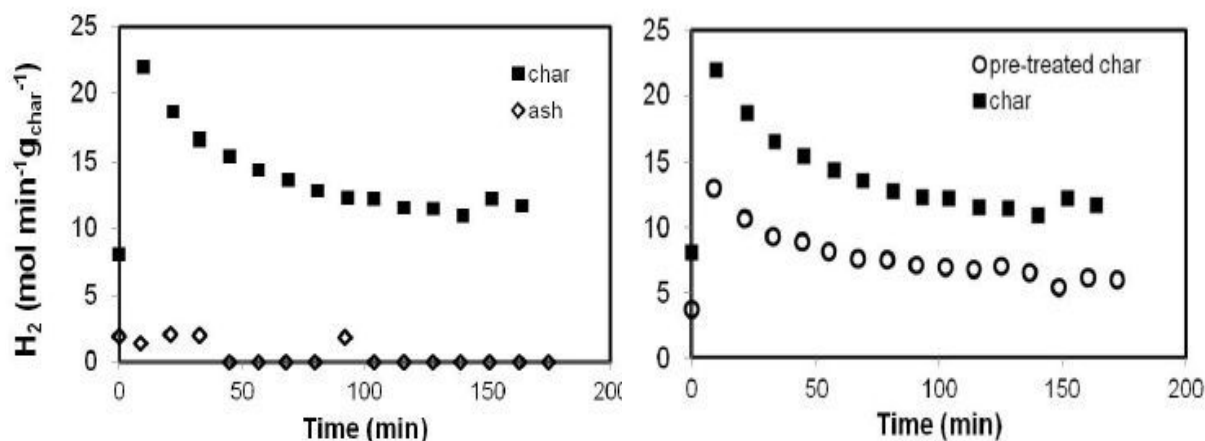


**Figure I-23: Comparison of H<sub>2</sub> productions from the catalytic cracking of methane on ash, char and char that has been heated to 1000°C prior to the reaction [19]**

On Figure I-23, one can observe that again the hydrogen production is lower with the pre-treated biochars than with the raw biochars. XPS analyses have shown that minerals tend to agglomerate at the surface on the pre-heated biochars which leads to decrease the catalytic activity. Thus the methane cracking seems to be sensitive to the dispersion of the minerals onto the biochars surface. In addition the carbon from the surface and the minerals seem to form a complex which is most reactive than each component taken alone.

- **Influence of the carbon matrix**

Regarding the carbon structures, Suelves et al. [112] and Lázaro et al. [110] investigated the crystallinity of fresh and deactivated carbons by XRD. They highlighted that coke deposit was more ordered than the catalyst carbon structure. Figure I-24.A presents the evolution of the XRD profiles as the run progressed. One can observe that the fresh catalyst was highly disordered. However, an increase in the intensity of the diffraction was observed at 27° (002) and at 78° (101) which is characteristic from ordered structure. Figure I-24.B shows the variation of the parameter,  $d_{002}$ , of the hexagonal unit cell over the reaction. It is visible that the parameter decreased from 0.385 nm for the fresh catalyst to 0.345 nm for the deactivated catalyst to tend to a value of the  $d_{002}$  close to the perfect graphite (0.3352 nm) [110]. Thus, deactivation by coke deposit tends to increase the ordering in the structure sample and then decreases its reactivity.

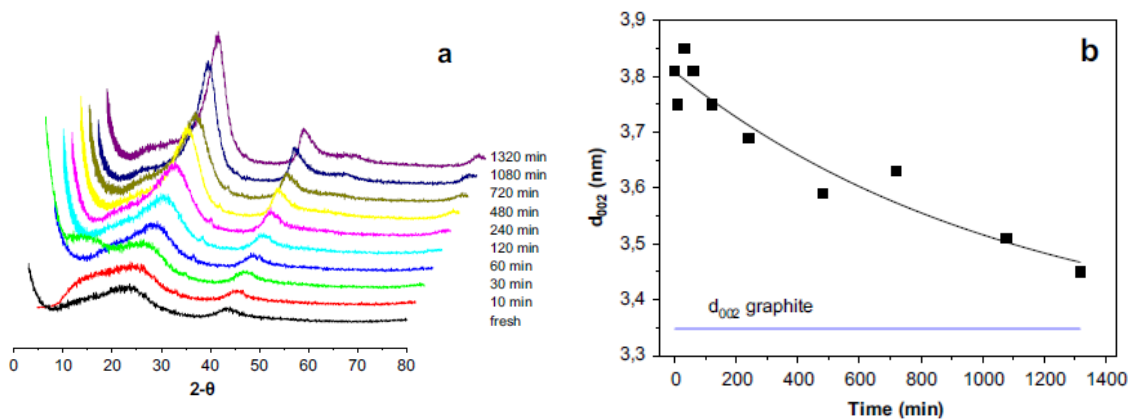


**Figure I-24: Change of the XRD pattern (a) and  $d_{002}$  (b) during the test carried out at  $T=950^{\circ}\text{C}$  and  $\text{GHSV}=360 \text{ h}^{-1}$  (gas hourly space velocity) [110]**

The different surface properties seem to be potentially involved in the reactivity of the carbonaceous materials. The chemical functions such as the oxygenated functions, the minerals content and the carbon matrix structures are important parameters for the global catalyst activity and seem to be mostly involved during the early stages of the reaction. During the reaction, the main mode of deactivation seems to be the coke deposition which blocks the access to the active sites and to the porosity. Previous researches opened discussion on the correlation between the physico-chemical properties and the reactivity. However further researches are required to improve the understanding of the mechanisms which are involved.

### 3.4. Partial conclusion

Methane cracking has been chosen for different reasons as the reference reaction for testing the performances of biochars. In fact methane is the second major gaseous co-product of pyro-gasification right after carbon dioxide. It is representative to the C-H breakage which is present in hydrocarbons. Its conversion leads to enhance the hydrogen production and thus the syngas yield.

The methane decarbonization is thermodynamically feasible from about  $550^{\circ}\text{C}$ . To decrease the energetic barrier and thus accelerate the reaction, methane cracking is usually performed on solid catalyst. In fact methane molecule is known to be the most stable hydrocarbon. Regarding metal based catalysts, transition metals are the most reactive due to their unique 3d orbital. Alloys of Ni-Cu have been depicted to be the most effective. However they suffer from quick deactivation which is a real issue due to the high cost of the commercial catalyst. A regeneration step to burn coke deposit is required for multiple utilizations of the catalysts.

Carbon based catalysts are gaining interest since they are stable and low cost catalysts. They also suffer from deactivation by coke deposition. However since they are cheaper than metal based catalyst, the utilization of fresh catalyst more frequently is not such a big issue. Some recent studies investigate the relationship between surface properties of carbonaceous materials and methane cracking activity. Most authors agree on the fact that surface chemistry influences the early stages of the methane cracking reaction and the deactivation process is mostly governed by physical properties. However further researches are required to get better insights into these correlations.

#### 4. Conclusion

This literature review has been done with the objective of a better understanding of the biochars properties, methods of production and possibilities of valorization. Biochars are the carbonaceous solid residue from the pyro-gasification of 2<sup>nd</sup> generation biomass. This process consists in converting ligno-cellulosic biomass into a high energetic valuable gas so-called syngas (composed of hydrogen and carbon monoxide) which can be further used to produce electricity, chemicals, fuels or heat. However biomass conversion is incomplete and leads to the formation of heavier organic molecules than syngas which are in gaseous, liquid and solid phases. The co-products formation raises considerable problems since they decrease the yield and purity of the syngas yield. Systems of gas cleaning have been designed, the most effective has been depicted to be the addition of a second reactor downstream the gasifier in which the hot syngas should go through a bed of metal supported catalysts. This solution is a real upgrading of the syngas however it is quite costly.

Biochar is a highly porous carbon with a turbostratic structure. It is composed of several amorphous carbons structures and inherent functional groups such as O-containing groups and minerals are present on the surface. Literature described that the biochars itself catalyses the pyro-gasification process. In fact the amorphous carbon structures are highly reactive. In addition minerals and more specifically AAEMs have been highlighted to play a catalytic role. Up to now biochars were considered to be waste and thus additional cost has to be taken into account for their disposal in landfills. However recent studies investigated potential ways of valorization since the physico-chemical properties of the biochars are interesting. Three main ways were quoted in the literature: utilization as fertilizer, adsorbent or catalyst. To achieve good activity, functionalization treatments could be performed on biochars surface to play on its physico-chemical properties. Literature is abundant regarding oxygenation treatment and wet impregnation to increase the mineral content.

The best option for the biochars valorization is to utilize them directly in the pyro-gasification process to replace the costly metal supported catalysts for the hot syngas upgrading. To use at the maximum potential the biochars for this application it is important to understand the relationship between the activity and the physico-chemical properties. As it has been described previously the co-products from pyro-gasification are multiple, thus the selection of one component to be model molecule seems to be more reasonable. Methane cracking seems to be interesting for the investigation because, in addition to be a model molecule for C-H breaking bond (present in all hydrocarbons), its conversion produces hydrogen which increases the syngas yield. It is also the second gaseous co-product (right after carbon dioxide). Transition metal supported catalysts are commonly utilized for methane cracking. However they suffer from quick deactivation. Literature reported several investigations of methane cracking on carbonaceous materials such as activated carbons, carbon blacks, coals or even biochars. Many authors who worked on this topic agreed to say the initial methane catalytic activity is in relationship with the functional groups however the deactivation is governed by the filling of the pores. Even if previous studies have highlighted good insights further investigations are required.

---

## Bibliography

- [1] C. Baskar, S. Baskar, and R. S. Dhillon, "Biomass Conversion: The interface of Biotechnology, Chemistry and Material Science," vol. 908, R. S. Dhillon, Ed. 2012, pp. 11–23.
- [2] D. Ori and C. Béral, "Comment produire de la BIOMASSE en agroforesterie," 2012.
- [3] P. Basu, *Biomass gasification and pyrolysis-Practical design and theory*. 2010.
- [4] E. Bilgic, S. Yaman, H. Haykiri-Acma, and S. Kucukbayrak, "Limits of variations on the structure and the fuel characteristics of sunflower seed shell through torrefaction," *Fuel Process. Technol.*, vol. 144, no. April, pp. 197–202, 2016.
- [5] Energy research Centre of the Netherlands, "Phyllis2, database for biomass and waste." [Online]. Available: <https://www.ecn.nl/phyllis2>.
- [6] F. Mermoud, "Gazéification de charbon de bois à la vapeur d'eau : de la particule isolée au lit fixe continu," Institut national polytechnique de Toulouse, 2006.
- [7] C. Dupont, R. Chiriach, G. Gauthier, and F. Toche, "Heat capacity measurements of various biomass types and pyrolysis residues," *Fuel*, vol. 115, pp. 644–651, 2014.
- [8] S. Salvador, *Valorisation énergétique de biomasse par voie thermochimique- Aspects théorique*. . .
- [9] E. G. Baker and L. K. Mudge, "Mechanisms of catalytic biomass gasification," *J. Anal. Appl. Pyrolysis*, vol. 6, no. 3, pp. 285–297, 1984.
- [10] C. Di Blasi, "Combustion and gasification rates of lignocellulosic chars," *Prog. Energy Combust. Sci.*, vol. 35, no. 2, pp. 121–140, 2009.
- [11] P. L. J. Walker, F. J. Rusinko, and L. G. Austin, "Gas reactions of carbon," *Adv. Catal.*, vol. 11, pp. 133–221, 1959.
- [12] A. Nzihou, G. Flamant, and B. Stanmore, "Synthetic fuels from biomass using concentrated solar energy – A review," *Energy*, vol. 42, no. 1, pp. 121–131, Jun. 2012.
- [13] J. M. Bermúdez, A. Arenillas, and J. a. Menéndez, "Syngas from CO<sub>2</sub> reforming of coke oven gas: Synergetic effect of activated carbon/Ni- $\gamma$ -Al<sub>2</sub>O<sub>3</sub> catalyst," *Int. J. Hydrogen Energy*, vol. 36, no. 21, pp. 13361–13368, Oct. 2011.
- [14] Devi, Ptasiński, V. Paasen, Bergman, and Kiel, *Catalytic removal of biomass tars; Olivine as prospective in-bed catalyst for fluidized-bed biomass gasifiers*. 2005.
- [15] S. Septien, S. Valin, M. Peyrot, C. Dupont, and S. Salvador, "Characterization of char and soot from millimetric wood particles pyrolysis in a drop tube reactor between 800 C and 1400 C," *Fuel*, vol. 121, pp. 216–224, 2014.
- [16] A. Dufour, E. Masson, P. Girods, Y. Rogeau, and A. Zoulalian, "Evolution of aromatic tar composition in relation to methane and ethylene from biomass pyrolysis-gasification," *Energy and Fuels*, vol. 25, no. 9, pp. 4182–4189, 2011.
- [17] T. A. Milne and R. J. Evans, "Biomass Gasifier 'Tars': Their Nature, Formation, and Conversion," 1998.
- [18] L. Devi, K. J. Ptasiński, and F. J. J. G. Janssen, "A review of the primary measures for tar elimination in biomass gasification processes," *Biomass and Bioenergy*, vol. 24, no. 2, pp. 125–140, 2002.
- [19] N. Klinghoffer, "Utilization of char from biomass gasification in catalytic applications," Thesis:

- Columbia University, 2013.
- [20] Z. Abu El-Rub, E. a. Bramer, and G. Brem, "Experimental comparison of biomass chars with other catalysts for tar reduction," *Fuel*, vol. 87, no. 10–11, pp. 2243–2252, Aug. 2008.
- [21] L. Lu, "Quantative X-ray diffraction analysis and its application to various coals," *Carbon N. Y.*, vol. 43, no. 39, pp. 1821–1833, 2001.
- [22] Y. J. Liou and W. J. Huang, "Quantitative Analysis of Graphene Sheet Content in Wood Char Powders during Catalytic Pyrolysis," *J. Mater. Sci. Technol.*, vol. 29, no. 5, pp. 406–410, 2013.
- [23] Y. Liu, Q. Liu, J. Gu, D. Kang, F. Zhou, W. Zhang, Y. Wu, and D. Zhang, "Highly porous graphitic materials prepared by catalytic graphitization," *Carbon N. Y.*, vol. 64, pp. 132–140, 2013.
- [24] V. A. Davydov, A. V. Rakhmanina, J. P. Boudou, A. Thorel, H. Allouchi, and V. Agafonov, "Nanosized carbon forms in the processes of pressure-temperature-induced transformations of hydrocarbons," *Carbon N. Y.*, vol. 44, no. 10, pp. 2015–2020, 2006.
- [25] A. Oberlin, "CARBONIZATION AND GRAPHITIZATION," *Carbon N. Y.*, vol. 22, no. 6, pp. 521–541, 1984.
- [26] N. V. Russell, J. R. Gibbins, and J. Williamson, "Structural ordering in high temperature coal chars and the effect on reactivity," *Fuel*, vol. 78, no. 7, pp. 803–807, 1999.
- [27] P. Pré, G. Huchet, D. Jeulin, J.-N. Rouzaud, M. Sennour, and A. Thorel, "A new approach to characterize the nanostructure of activated carbons from mathematical morphology applied to high resolution transmission electron microscopy images," *Carbon N. Y.*, vol. 2, 2012.
- [28] A. Sharma, T. Kyotani, and A. Tomita, "Quantitative evaluation of structural transformations in raw coals on heat-treatment using HRTEM technique," *Fuel*, vol. 80, no. 10, pp. 1467–1473, 2001.
- [29] D. P. Serrano, J. A. Botas, J. L. G. Fierro, R. Guil-López, P. Pizarro, and G. Gómez, "Hydrogen production by methane decomposition: Origin of the catalytic activity of carbon materials," *Fuel*, vol. 89, no. 6, pp. 1241–1248, 2010.
- [30] A. Guedes, B. Valentim, A. C. Prieto, and F. Noronha, "Raman spectroscopy of coal macerals and fluidized bed char morphotypes," *Fuel*, vol. 97, pp. 443–449, Jul. 2012.
- [31] M. Asadullah, S. Zhang, Z. Min, P. Yimsiri, and C. Z. Li, "Effects of biomass char structure on its gasification reactivity," *Bioresour. Technol.*, vol. 101, no. 20, pp. 7935–7943, 2010.
- [32] Z. Karpinski and G. S. Szymanski, "The effect of the gradual thermal decomposition of surface oxygen species on the chemical and catalytic properties of oxidized activated carbon," *Carbon N. Y.*, vol. 40, pp. 2627–2639, 2002.
- [33] F. Vautard, J. Dentzer, M. Nardin, J. Schultz, and B. Defoort, "Influence of surface defects on the tensile strength of carbon fibers," *Appl. Surf. Sci.*, vol. 322, pp. 185–193, Dec. 2014.
- [34] X. Wu, Q. Song, H. Zhao, Z. Zhang, L. Zhang, and Q. Yao, "Influence of mineral transformation on the reactivity evolution during rice straw char–NO reaction," *Fuel*, vol. 113, pp. 553–559, 2013.
- [35] S. Link, S. Arvelakis, M. Hupa, P. Yrjas, I. Külaots, and A. Paist, "Reactivity of the biomass chars originating from reed, douglas fir, and pine," *Energy and Fuels*, vol. 24, no. 12, pp. 6533–6539, 2010.
- [36] H. Hwang, S. Oh, I.-G. Choi, and J. W. Choi, "Catalytic effects of magnesium on the characteristics of fast pyrolysis products – Bio-oil, bio-char, and non-condensed pyrolytic gas fractions," *J. Anal. Appl. Pyrolysis*, vol. 113, pp. 27–34, 2015.
- [37] T. G. Devi and M. P. Kannan, "X-ray diffraction (XRD) studies on the chemical states of some metal species in cellulosic chars and the Ellingham diagrams," *Energy and Fuels*, vol. 21, no. 2,

- pp. 596–601, 2007.
- [38] I. I. Salame and T. J. Bandoz, "Surface Chemistry of Activated Carbons: Combining the Results of Temperature-Programmed Desorption, Boehm, and Potentiometric Titrations.," *J. Colloid Interface Sci.*, vol. 240, no. 1, pp. 252–258, Aug. 2001.
- [39] L.-H. Zhang and J. M. Calo, "Thermal desorption methods for porosity characterization of carbons and chars," *Colloids Surfaces A Physicochem. Eng. Asp.*, vol. 187–188, pp. 207–218, Aug. 2001.
- [40] J. L. Figueiredo, M. F. R. Pereira, M. M. A. Freitas, and J. J. M. Orfao, "Modification of the surface chemistry of activated carbons," *Carbon N. Y.*, vol. 37, pp. 1379–1389, 1999.
- [41] U. Zielke, K. J. Huttinger, and W. P. Hoffman, "Surface-oxidized carbon fibers: I. Surface structure and chemistry," *Carbon N. Y.*, vol. 34, no. 8, pp. 983–998, 1996.
- [42] I. Edwards, H. Marsh, R. Menendez, B. Rand, S. West, A. Hosty, K. Kuo, B. McEnaney, T. Mays, D. Johnson, J. Patrick, D. Clarke, J. Crelling, and R. Gray, "Introduction to carbon science," 1989.
- [43] C. Guizani, "Effects of CO<sub>2</sub> on the biomass pyro-gasification in High Heating Rate and Low Heating Rate Conditions," Thesis: Ecoles des Mines d'Albi-Carmaux, 2014.
- [44] J. McDonald-Wharry, M. Manley-Harris, and K. Pickering, "Carbonisation of biomass-derived chars and the thermal reduction of a graphene oxide sample studied using Raman spectroscopy," *Carbon N. Y.*, vol. 59, pp. 383–405, Aug. 2013.
- [45] L. Kelebopile, R. Sun, H. Wang, X. Zhang, and S. Wu, "Pore development and combustion behavior of gasified semi-char in a drop tube furnace," *Fuel Process. Technol.*, vol. 111, pp. 42–54, Jul. 2013.
- [46] T. Li, L. Zhang, L. Dong, and C. Z. Li, "Effects of gasification atmosphere and temperature on char structural evolution during the gasification of Collie sub-bituminous coal," *Fuel*, vol. 117, no. PARTB, pp. 1190–1195, 2014.
- [47] D. M. Keown, X. Li, J. Hayashi, and C.-Z. Li, "Evolution of biomass char structure during oxidation in O<sub>2</sub> as revealed with FT-Raman spectroscopy," *Fuel Process. Technol.*, vol. 89, no. 12, pp. 1429–1435, Dec. 2008.
- [48] M. Asadullah, S. Zhang, Z. Min, P. Yimsiri, and C.-Z. Li, "Importance of Biomass Particle Size in Structural Evolution and Reactivity of Char in Steam Gasification," *Ind. Eng. Chem. Res.*, vol. 48, no. 22, pp. 9858–9863, 2009.
- [49] X. Li, J. Hayashi, and C. Li, "Volatilisation and catalytic effects of alkali and alkaline earth metallic species during the pyrolysis and gasification of Victorian brown coal. Part VII. Raman spectroscopic study on the changes in char structure during the catalytic gasification in air," *Fuel*, vol. 85, no. 10–11, pp. 1509–1517, Jul. 2006.
- [50] M. Q. Jiang, R. Zhou, J. Hu, F. C. Wang, and J. Wang, "Calcium-promoted catalytic activity of potassium carbonate for steam gasification of coal char: Influences of calcium species," *Fuel*, vol. 99, pp. 64–71, 2012.
- [51] J. G. Lee, E. J. Shin, R. a. Pavelka, M. S. Kirchner, D. Dounas-Frazer, B. D. McCloskey, D. E. Petrick, J. T. McKinnon, and A. M. Herring, "Effect of metal doping on the initial pyrolysis chemistry of cellulose chars," *Energy and Fuels*, vol. 22, no. 4, pp. 2816–2825, 2008.
- [52] V. H. Rane, S. T. Chaudhari, and V. R. Choudhary, "Influence of alkali metal doping on surface properties and catalytic activity/selectivity of CaO catalysts in oxidative coupling of methane," *J. Nat. Gas Chem.*, vol. 17, no. 4, pp. 313–320, 2008.
- [53] A. Nzihou, B. Stanmore, and P. Sharrock, "A review of catalysts for the gasification of biomass char, with some reference to coal," *Energy*, vol. 58, pp. 305–317, Sep. 2013.

- [54] D. W. McKee, C. L. Spiro, P. G. Kosky, and E. J. Lamby, "Catalytic Effects of Alkali Metal Salts in the Gasification of Coal Char," *ACS spring Meet.*, 1982.
- [55] P. Lahijani, Z. A. Zainal, A. R. Mohamed, and M. Mohammadi, "CO<sub>2</sub> gasification reactivity of biomass char: Catalytic influence of alkali, alkaline earth and transition metal salts," *Bioresour. Technol.*, vol. 144, pp. 288–295, 2013.
- [56] K. Mitsuoka, S. Hayashi, H. Amano, K. Kayahara, E. Sasaoaka, and M. A. Uddin, "Gasification of woody biomass char with CO<sub>2</sub>: The catalytic effects of K and Ca species on char gasification reactivity," *Fuel Process. Technol.*, vol. 92, no. 1, pp. 26–31, 2011.
- [57] P. Nanou, H. E. Gutiérrez Murillo, W. P. M. Van Swaaij, G. Van Rossum, and S. R. a Kersten, "Intrinsic reactivity of biomass-derived char under steam gasification conditions-potential of wood ash as catalyst," *Chem. Eng. J.*, vol. 217, pp. 289–299, 2013.
- [58] D. Vamvuka, E. Karouki, and S. Sfakiotakis, "Gasification of waste biomass chars by carbon dioxide via thermogravimetry. Part I: Effect of mineral matter," *Fuel*, vol. 90, no. 3, pp. 1120–1127, 2011.
- [59] Y. Huang, X. Yin, C. Wu, C. Wang, J. Xie, Z. Zhou, L. Ma, and H. Li, "Effects of metal catalysts on CO<sub>2</sub> gasification reactivity of biomass char," *Biotechnol. Adv.*, vol. 27, no. 5, pp. 568–572, 2009.
- [60] F. Delannay, W. T. Tysoe, H. Heinemann, and G. a. Somorjai, "The role of KOH in the steam gasification of graphite: Identification of the reaction steps," *Carbon N. Y.*, vol. 22, no. 4–5, pp. 401–407, 1984.
- [61] K. J. Hüttinger and R. Minges, "The influence of the catalyst precursor anion in catalysis of water vapour gasification of carbon by potassium," *Fuel*, vol. 65, no. 8, pp. 1122–1128, 1986.
- [62] D. C. Elliott., R. T. Hallen., and S. L. John., "Alkali catalysis in biomass gasification," *J. Anal. Appl. Pyrolysis*, vol. 6, pp. 299–316, 1984.
- [63] Y. Zhang, M. Ashizawa, and S. Kajitani, "Calcium loading during the dewatering of wet biomass in kerosene and catalytic activity for subsequent char gasification," *Fuel*, vol. 87, no. 13–14, pp. 3024–3030, 2008.
- [64] S. L. Goertzen, K. D. Thériault, A. M. Oickle, A. C. Tarasuk, and H. a. Andreas, "Standardization of the Boehm titration. Part I. CO<sub>2</sub> expulsion and endpoint determination," *Carbon N. Y.*, vol. 48, no. 4, pp. 1252–1261, Apr. 2010.
- [65] R. Gopalakrishnan, F. M. J, and C. H. Bartholomew, "Catalysis of Char Oxidation by Calcium Minerals: Effects of calcium compound chemistry on intrinsic reactivity of doped spherocarb and zap chars," *Energy & Fuels*, vol. 8, pp. 984–989, 1994.
- [66] M.-Q. Jiang, R. Zhou, J. Hu, F.-C. Wang, and J. Wang, "Calcium-promoted catalytic activity of potassium carbonate for steam gasification of coal char: Influences of calcium species," *Fuel*, vol. 99, pp. 64–71, Sep. 2012.
- [67] M. P. Kannan and G. N. Richards, "Calcium catalysis in air gasification of cellulosic chars," *Fuel*, vol. 69, no. 8, pp. 999–1006, 1990.
- [68] Y. Zhanga, M. Ashizawaa, S. Kajitania, and K. Miurab, "Proposal of a semi-empirical kinetic model to reconcile with gasification reactivity profiles of biomass chars," *Fuel*, vol. 87, no. 4–5, pp. 475–481, 2008.
- [69] H. Harker, J. T. Gallagher, and a. Parkin, "Reaction of carbon with oxidizing gases: The role of unpaired electrons," *Carbon N. Y.*, vol. 4, no. 3, pp. 401–409, 1966.
- [70] J. L. Figueiredo, J. Rivera-Utrilla, and M. a. Ferro-Garcia, "Gasification of active carbons of different texture impregnated with nickel, cobalt and iron," *Carbon N. Y.*, vol. 25, no. 5, pp. 703–708, 1987.

- [71] J. Long, H. Song, X. Jun, S. Sheng, S. Lun-Shi, X. Kai, and Y. Yao, "Release characteristics of alkali and alkaline earth metallic species during biomass pyrolysis and steam gasification process," *Bioresour. Technol.*, vol. 116, pp. 278–284, 2012.
- [72] L. R. Radović, P. L. Walker, and R. G. Jenkins, "Effect of lignite pyrolysis conditions on calcium oxide dispersion and subsequent char reactivity," *Fuel*, vol. 62, no. 2, pp. 209–212, 1983.
- [73] R. Baker, "The relationship between particle motion on a graphite surface and Tammann temperature," *J. Catal.*, vol. 78, no. 2, pp. 473–476, 1982.
- [74] S. Nielsen, T. Minchin, S. Kimber, L. van Zwieten, J. Gilbert, P. Munroe, S. Joseph, and T. Thomas, "Comparative analysis of the microbial communities in agricultural soil amended with enhanced biochars or traditional fertilisers," *Agric. Ecosyst. Environ.*, vol. 191, pp. 73–82, 2014.
- [75] J. Lehmann, M. C. Rillig, J. Thies, C. A. Masiello, W. C. Hockaday, and D. Crowley, "Biochar effects on soil biota - A review," *Soil Biol. Biochem.*, vol. 43, no. 9, pp. 1812–1836, 2011.
- [76] R. Zhao, N. Coles, Z. Kong, and J. Wu, "Effects of aged and fresh biochars on soil acidity under different incubation conditions," *Soil Tillage Res.*, vol. 146, pp. 133–138, 2015.
- [77] P. Kim, A. M. Johnson, M. E. Essington, M. Radosevich, W. T. Kwon, S. H. Lee, T. G. Rials, and N. Labbé, "Effect of pH on surface characteristics of switchgrass-derived biochars produced by fast pyrolysis," *Chemosphere*, vol. 90, no. 10, pp. 2623–2630, 2013.
- [78] L. Hua, W. Wu, Y. Liu, M. B. McBride, and Y. Chen, "Reduction of nitrogen loss and Cu and Zn mobility during sludge composting with bamboo charcoal amendment," *Environ. Sci. Pollut. Res.*, vol. 16, no. 1, pp. 1–9, 2009.
- [79] N. Karakoyun, S. Kubilay, N. Aktas, O. Turhan, M. Kasimoglu, S. Yilmaz, and N. Sahiner, "Hydrogel–Biochar composites for effective organic contaminant removal from aqueous media," *Desalination*, vol. 280, no. 1–3, pp. 319–325, Oct. 2011.
- [80] W.-J. Liu, F.-X. Zeng, H. Jiang, and X.-S. Zhang, "Preparation of high adsorption capacity biochars from waste biomass.," *Bioresour. Technol.*, vol. 102, no. 17, pp. 8247–52, Sep. 2011.
- [81] P. Liu, W.-J. Liu, H. Jiang, J.-J. Chen, W.-W. Li, and H.-Q. Yu, "Modification of bio-char derived from fast pyrolysis of biomass and its application in removal of tetracycline from aqueous solution.," *Bioresour. Technol.*, vol. 121, pp. 235–40, Oct. 2012.
- [82] C. Jindarom, V. Meeyoo, B. Kitiyanan, T. Rirksomboon, and P. Rangsunvigit, "Surface characterization and dye adsorptive capacities of char obtained from pyrolysis/gasification of sewage sludge," *Chem. Eng. J.*, vol. 133, no. 1–3, pp. 239–246, Sep. 2007.
- [83] D. C. K. Ko, J. F. Porter, and G. McKay, "Optimised correlations for the fixed-bed adsorption of metal ions on bone char," *Chem. Eng. Sci.*, vol. 55, pp. 5819–5829, 2000.
- [84] D. Mohan, C. U. Pittman, M. Bricka, F. Smith, B. Yancey, J. Mohammad, P. H. Steele, M. F. Alexandre-Franco, V. Gómez-Serrano, and H. Gong, "Sorption of arsenic, cadmium, and lead by chars produced from fast pyrolysis of wood and bark during bio-oil production.," *J. Colloid Interface Sci.*, vol. 310, no. 1, pp. 57–73, Jun. 2007.
- [85] A. A. Lizzio and J. A. Debarr, "Effect of surface area and chemisorbed oxygen on the SO<sub>2</sub> adsorption capacity of activated char," *Fuel*, vol. 75, no. 13, pp. 1515–1522, 1996.
- [86] S. Wu, G. Wen, B. Zhong, B. Zhang, X. Gu, N. Wang, and D. Su, "Reduction of nitrobenzene catalyzed by carbon materials," *Chinese J. Catal.*, vol. 35, no. 6, pp. 914–921, Jun. 2014.
- [87] Y. H. Li, G. Q. Lu, and V. Rudolph, "The kinetics of NO and N<sub>2</sub>O reduction over coal chars in fluidised-bed combustion," *Chem. Eng. Sci.*, vol. 53, no. 1, pp. 1–26, 1998.
- [88] A. M. Dehkoda and N. Ellis, "Biochar-based catalyst for simultaneous reactions of

- esterification and transesterification," *Catal. Today*, vol. 207, pp. 86–92, May 2013.
- [89] J. R. Kastner, J. Miller, D. P. Geller, J. Locklin, L. H. Keith, and T. Johnson, "Catalytic esterification of fatty acids using solid acid catalysts generated from biochar and activated carbon," *Catal. Today*, vol. 190, no. 1, pp. 122–132, Aug. 2012.
- [90] Y. Yuan, T. Yuan, D. Wang, J. Tang, and S. Zhou, "Sewage sludge biochar as an efficient catalyst for oxygen reduction reaction in an microbial fuel cell.," *Bioresour. Technol.*, vol. 144, pp. 115–20, Sep. 2013.
- [91] N. Klinghoffer, M. Castaldi, and A. Nzihou, "Catalyst properties and Catalytic Performance of Char from Biomass Gasification," *Ind. Eng. Chem. Res.*, vol. 51, no. 40, pp. 13113–13122, 2012.
- [92] Z. Xianglan, D. Shengfu, L. Qiong, Z. Yan, and C. Lei, "Surface functional groups and redox property of modified activated carbons," *Min. Sci. Technol.*, vol. 21, no. 2, pp. 181–184, Mar. 2011.
- [93] D. B. Mawhinney and J. T. Jr Yates, "FTIR study of the oxidation of amorphous carbon by ozone at 300 K — Direct COOH formation," *Carbon N. Y.*, vol. 39, pp. 1167–1173, 2001.
- [94] A.-N. A. El-Hendawy, "Variation in the FTIR spectra of a biomass under impregnation, carbonization and oxidation conditions," *J. Anal. Appl. Pyrolysis*, vol. 75, no. 2, pp. 159–166, Mar. 2006.
- [95] J. Jaramillo, P. M. Álvarez, and V. Gómez-Serrano, "Oxidation of activated carbon by dry and wet methods," *Fuel Process. Technol.*, vol. 91, no. 11, pp. 1768–1775, Nov. 2010.
- [96] P. E. Fanning and M. A. Vannice, "A drift study of the formation of surface groups on carbon by oxidation," *Carbon N. Y.*, vol. 31, no. 5, pp. 721–730, 1991.
- [97] A. Kochan, A. Krzton, and G. Fingueneisel, "A study of carbonaceous char oxidation in air by semi-quantitative FTIR spectroscopy," *Fuel*, vol. 77, no. 6, pp. 563–569, 1998.
- [98] B. K. Pradhan and N. K. Sandle, "Effect of different oxidizing agent treatments on the surface properties of activated carbons," *Carbon N. Y.*, vol. 37, no. 8, pp. 1323–1332, Jan. 1999.
- [99] Y. Shen, "Chars as carbonaceous adsorbents/catalysts for tar elimination during biomass pyrolysis or gasification," *Renew. Sustain. Energy Rev.*, vol. 43, pp. 281–295, 2015.
- [100] Y. Richardson, J. Blin, G. Volle, J. Motuzas, and A. Julbe, "In situ generation of Ni metal nanoparticles as catalyst for H<sub>2</sub>-rich syngas production from biomass gasification," *Appl. Catal. A Gen.*, vol. 382, no. 2, pp. 220–230, 2010.
- [101] A. M. Amin, E. Croiset, and W. Epling, "Review of methane catalytic cracking for hydrogen production," *Int. J. Hydrogen Energy*, vol. 36, no. 4, pp. 2904–2935, 2011.
- [102] N. Muradov, F. Smith, and A. T-Raissi, "Catalytic activity of carbons for methane decomposition reaction," *Catal. Today*, vol. 102–103, pp. 225–233, May 2005.
- [103] Y. Shen and A. C. Lua, "Synthesis of Ni and Ni–Cu supported on carbon nanotubes for hydrogen and carbon production by catalytic decomposition of methane," *Appl. Catal. B Environ.*, vol. 164, pp. 61–69, 2015.
- [104] M. a. Ermakova and D. Y. Ermakov, "Ni/SiO<sub>2</sub> and Fe/SiO<sub>2</sub> catalysts for production of hydrogen and filamentous carbon via methane decomposition," *Catal. Today*, vol. 77, no. 3, pp. 225–235, 2002.
- [105] A. Rakib, "Valorisation du méthane en hydrogène par reformage catalytique," Thesis: Université du Littoral Côte d'Opale, 2013.
- [106] A. M. Amin, E. Croiset, and W. Epling, "Review of methane catalytic cracking for hydrogen production," *Int. J. Hydrogen Energy*, vol. 36, no. 4, pp. 2904–2935, Feb. 2011.
- [107] I. Alstrup, "A New Model Explaining Carbon-Filament Growth on Nickel, Iron, and Ni-Cu Alloy

- Catalysts," *J. Catal.*, vol. 109, no. 2, pp. 241–251, 1988.
- [108] Y. Echegoyen, I. Suelves, M. J. Lázaro, R. Moliner, and J. M. Palacios, "Hydrogen production by thermocatalytic decomposition of methane over Ni-Al and Ni-Cu-Al catalysts: Effect of calcination temperature," *J. Power Sources*, vol. 169, no. 1, pp. 150–157, 2007.
- [109] B. Fidalgo and J. Á. Menéndez, "Carbon materials as catalysts for decomposition and CO<sub>2</sub> reforming of methane: A review," *Chinese J. Catal.*, vol. 32, no. 1, pp. 207–216, 2011.
- [110] M. J. Lázaro, J. L. Pinilla, I. Suelves, and R. Moliner, "Study of the deactivation mechanism of carbon blacks used in methane decomposition," *Int. J. Hydrogen Energy*, vol. 33, no. 15, pp. 4104–4111, 2008.
- [111] R. Moliner, I. Suelves, M. J. Lázaro, and O. Moreno, "Thermocatalytic decomposition of methane over activated carbons: Influence of textural properties and surface chemistry," *Int. J. Hydrogen Energy*, vol. 30, no. 3, pp. 293–300, 2005.
- [112] I. Suelves, J. L. Pinilla, M. J. Lázaro, and R. Moliner, "Carbonaceous materials as catalysts for decomposition of methane," *Chem. Eng. J.*, vol. 140, no. 1–3, pp. 432–438, 2008.
- [113] I. Suelves, M. J. Lázaro, R. Moliner, J. L. Pinilla, and H. Cubero, "Hydrogen production by methane decarbonization: Carbonaceous catalysts," *Int. J. Hydrogen Energy*, vol. 32, no. 15 SPEC. ISS., pp. 3320–3326, 2007.
- [114] N. Muradov, "Catalysis of methane decomposition over elemental carbon," *Catal. Commun.*, vol. 2, no. 3–4, pp. 89–94, 2001.
- [115] M. H. Kim, E. K. Lee, J. H. Jun, S. J. Kong, G. Y. Han, B. K. Lee, T. J. Lee, and K. J. Yoon, "Hydrogen production by catalytic decomposition of methane over activated carbons: Kinetic study," *Int. J. Hydrogen Energy*, vol. 29, no. 2, pp. 187–193, 2004.
- [116] S. Y. Lee, J. H. Kwak, G. Y. Han, T. J. Lee, and K. J. Yoon, "Characterization of active sites for methane decomposition on carbon black through acetylene chemisorption," *Carbon N. Y.*, vol. 46, no. 2, pp. 342–348, 2008.
- [117] S. Krzyzynski and M. Kozłowski, "Activated carbons as catalysts for hydrogen production via methane decomposition," *Int. J. Hydrogen Energy*, vol. 33, no. 21, pp. 6172–6177, 2008.
- [118] B. L. Zongqing Bai, Haokan Chen, Wen Li, "Hydrogen production by methane decomposition over coal char," *Hydrog. Energy*, vol. 31, pp. 899–905, 2006.



## **II. Chapter 2: Materials and methods**

# Content

1. Experimental capabilities .....	65
1.1. Pyro-gasification of poplar wood under an H <sub>2</sub> O/N <sub>2</sub> mixture in a fluidized bed .....	66
1.2. Functionalization of the biochars surface .....	70
1.3. Catalytic methane cracking on a fixed bed of biochars.....	73
2. Biochars surface characterizations.....	79
2.1. Proximate and ultimate analysis .....	80
2.2. Minerals content .....	80
2.3. Textural properties.....	83
2.4. Oxygenated content .....	87
2.5. Carbon structures.....	91
3. Summary .....	97
Bibliography.....	99

This chapter is dedicated to the description of the materials and methods. It is divided into two main sections:

- 1) a presentation of the experimental capabilities for: the poplar wood pyro-gasification, the biochars functionalizations and the catalytic methane cracking tests.
- 2) a description of the analytical methods utilized for the biochars surface characterization.

Prior to presenting the experimental capabilities, a brief description of the poplar wood sample is provided. Figure II-1 shows poplar wood chips which have been gasified. This wood has been provided by Lithaspen company. Table II-1 presents the particle size distribution.



**Figure II-1: Picture of poplar wood chips**

**Table II-1: Particle size distribution of poplar wood chips**

	< 1 mm	1 < L < 2 mm	> 2 mm
		wt%	
<b>poplar wood chips</b>	2.4	44.6	53.0

## 1. Experimental capabilities

This section presents the experimental devices used for the poplar wood pyro-gasification, the functionalization of the biochars surface and the methane cracking tests.

## 1.1. Pyro-gasification of poplar wood under an H<sub>2</sub>O/N<sub>2</sub> mixture in a fluidized bed

### 1.1.3. *Experimental device*

Pyro-gasification of poplar wood has been performed in a fluidized bed at RAPSODEE centre (see Figure II-2 and Figure II-3). The fluidized bed is composed of four parts:

- reactor
- gas flow control system composed in two different sections the gas control panel and the steam generator
- heat control system
- tars and gas collection system



**Figure II-2: Picture of the fluidized bed at RAPSODEE center**

The tubular reactor made in stainless steel is 60 cm height with an internal diameter of 6 cm. The reaction zone is surrounded by a clearance zone. A quartz frit was positioned at approximately 12 cm from the bottom to hold the biomass. To ensure the biomass remains in the reactor a second frit was put at the top of the reactor. The thermal regulation of the reactor is ensured by an electrical furnace which is composed of two radiative covers. The first cover which surrounds the reaction zone



1.1.4. **Minimum fluidization velocity for poplar wood pyro-gasification**

Prior to the pyro-gasification, preliminary tests of poplar wood chips fluidization have been performed. The minimum velocity of fluidization  $U_{mf}$  corresponds to the point at which the gas flow causes the bed of particles to expand and lift into the vertical column. In this case, the hydrodynamic drag force on the bed particle matches the net gravitational forces. This also means that the pressure drop  $\Delta p$  over the length  $L_b$  of the bed is equal to the weight of the apparent density of the particles bed (see Eq.II-1).

$$\frac{\Delta p}{L_b} = (\rho_p - \rho_g) \cdot (1 - \varepsilon_b) \cdot g \quad \text{Eq.II-1}$$

where:

$\rho_p$  and  $\rho_g$ : particle and gas densities

$\varepsilon_b$ : bed particle porosity

$g$  : gravitational constant

Then, the minimum velocity of fluidization  $U_{mf}$  can either be determined by calculations or experimentally. The semi-Empirical Ergun equation is usually utilized:

$$\frac{\Delta p}{L_b} = \frac{150(1 - \varepsilon_b)^2 \cdot \mu_g \cdot U_g}{\varepsilon_b^3 \cdot d_p^2} + \frac{1.75(1 - \varepsilon_b) \cdot \rho_g \cdot U_g^2}{\varepsilon_b^3 \cdot d_p} \quad \text{Eq. II-2}$$

where:

$\mu_g$ : gas viscosity

$d_p$ : particle diameter

The minimum velocity of fluidization  $U_{mf}$  can also be determined experimentally by monitoring the pressure drop through the particle bed while increasing the fluid velocity. An illustration is provided in Figure II-4. The pressure drop keeps increasing with gas velocity while the fluidization is not reached. Once the particle bed is fluidized, the pressure drop stabilizes.

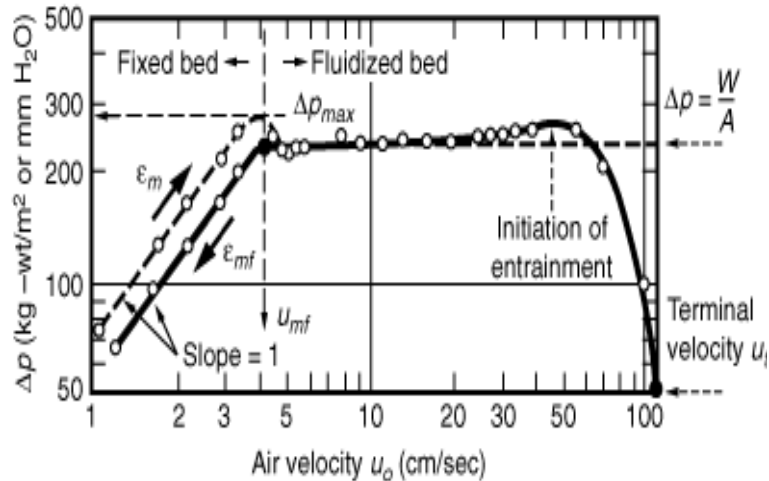


Figure II-4: The different regions of fluidization according to the gas velocity [1]

In this study, the minimum velocity of fluidization has been determined experimentally. A manometer with a liquid column (MVI 1500 type; liquid: tetra bromide) has been connected to two entrances at different height of the fluidized bed: the first one was plugged in the entrance right above the frit which maintains the biomass (18 cm from the reactor bottom) and the second one at the top of the reaction zone (40 cm from the reactor bottom). The fluidization test has been done at room temperature using 50 g of poplar wood chips under pure nitrogen. It has been experimentally found that from  $0.8 \text{ Nm}^3/\text{h}$  the bed of 50 g of wood chips is fluidized.

#### 1.1.5. *Operating conditions for poplar wood pyro-gasification*

65 g of poplar wood chips have been gasified at  $750^\circ\text{C}$  during 30 minutes with an heating ramp of  $20^\circ\text{C}/\text{min}$  into a 90 vol%  $\text{H}_2\text{O}$  / 10 vol%  $\text{N}_2$  mixture (purity: 99.5) with a total flow rate of  $1.5 \text{ Nm}^3/\text{h}$ . The poplar wood has been heated under pure nitrogen until the temperature inside the reactor was higher than  $180^\circ\text{C}$  in order to prevent steam liquefaction. Then the steam was introduced. The temperature program is presented in Figure II-5. Temperature profiles have been recorded in the reaction zone (from 4 thermocouples) during poplar wood pyro-gasification. They are presented in Figure II-6.

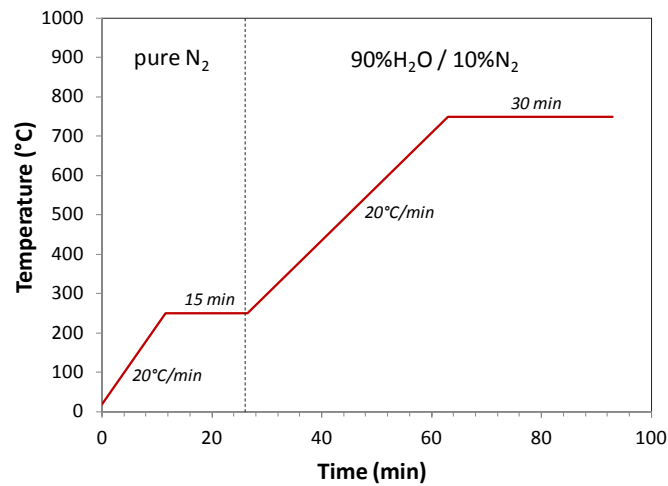


Figure II-5: Temperature profile for the pyro-gasification of poplar wood chips in the fluidized bed

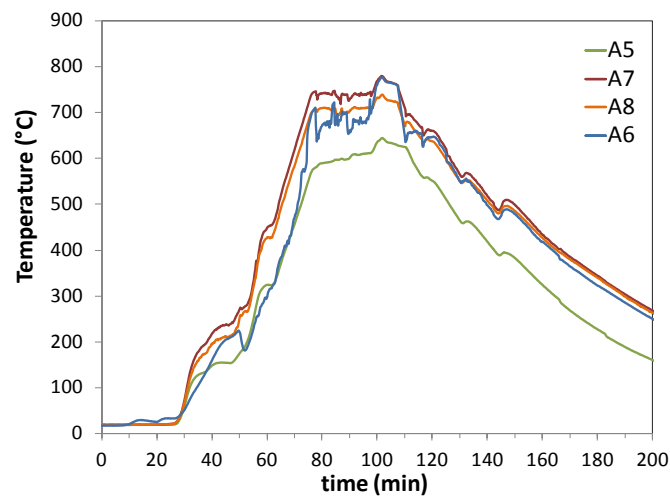


Figure II-6: Recorded temperatures in the reaction zone during the poplar wood pyro-gasification at 750°C during 30 min under a mixture of 90% H<sub>2</sub>O / 10% N<sub>2</sub>

## 1.2. Functionalization of the biochars surface

Two treatments of the biochars surface have been performed: an O<sub>2</sub> gas-phase treatment and a wet impregnation under nitrate salts solutions. Each treatment has been carried out in order to emphasize the role of a specific physico-chemical property of the biochars surface. The O<sub>2</sub> gas-phase treatment was performed to increase the amount of oxygenated functions at the biochars surface. The wet impregnation was performed to enhance the amount of minerals at the surface.

### 1.2.3. **Wet impregnation of raw poplar wood**

The goal of the wet impregnation is to enhance the concentration of mineral of interest at the biochars surface in order to evaluate the reactivity of these biochars towards methane cracking. In this study we are interested in the separate role of the calcium and potassium on the one hand and the synergic effect of their simultaneous presence on the other hand. The impregnation was carried out on the raw poplar wood prior to pyro-gasification instead of on biochars. In fact impregnation of the biochars should lead to an encapsulation of the carbonaceous bulk by the minerals and not to a homogeneous distribution of minerals at the surface.

The same protocol was followed for the three impregnations. A solution of nitrate salt containing 1 wt% of the mineral of interest was prepared. 30 mg of poplar wood were immersed in 300 mL of solution during 6 hours (Figure II-7). Regarding the simultaneous impregnation of calcium and potassium, the solution prepared contained 0.5 wt% of calcium and potassium respectively. The solution was agitated in order to favor the mass transfer. The impregnated poplar woods were dried overnight at 105°C. These three impregnated poplar woods were gasified in the same operating conditions as the raw biochar (see section 1.1) to provide impregnated biochars. The impregnated biochars are named as follows: Ca\_char, K\_char, Ca+K\_char thereafter.

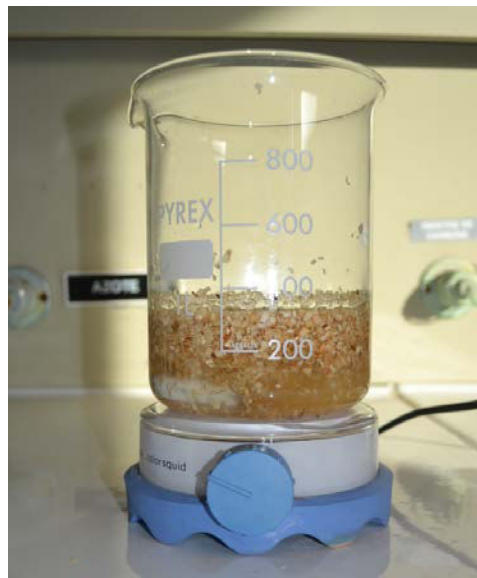


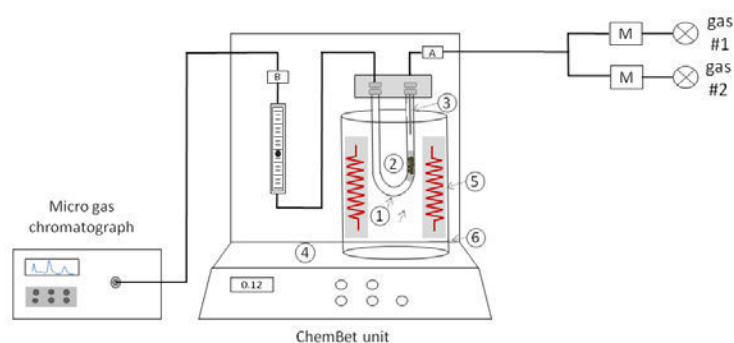
**Figure II-7: Wet impregnation of the poplar wood chips**

### 1.2.4. *O<sub>2</sub> gas-phase treatment on biochars*

An O<sub>2</sub> gas-phase treatment has been performed to enhance the oxygenated functions at the surface of biochars. The oxygenation was carried out in a micro-reactor -ChemBet Pulsar-model 05090- (Figure II-8) coupled with a gas chromatograph (Agilent 3000A). 100 mg of biochars were oxygenated under a mixture of 8 vol% O<sub>2</sub> / 92 vol% N<sub>2</sub> (ultra-high purity) and a flow rate of 45 ml/min. Various time durations (2h, 4h, 8h and 16h) at 280°C and different temperatures (340, 400°C) for 2h were tested to determine the impact of the operating conditions on the efficacy and selectivity of the oxygenation.



Figure II-8: Chembet Pulsar TPD instrument from Quantachrome company



**Captions:**

- |          |                        |          |                     |          |                      |
|----------|------------------------|----------|---------------------|----------|----------------------|
| <b>M</b> | mass flow controller   | <b>①</b> | sample cell         | <b>④</b> | furnace              |
| <b>A</b> | reference TCD detector | <b>②</b> | sample              | <b>⑤</b> | heating resistances  |
| <b>B</b> | sample TCD detector    | <b>③</b> | sample thermocouple | <b>⑥</b> | furnace thermocouple |

Figure II-9: Scheme of the plug flow reactor (Chembet instrument coupled with the micro gas chromatograph)

Sample to be oxygenated has been placed in a quartz U-tube (Figure II-9, #1) with an internal diameter of 4 mm placed into an electrical furnace (Chembet Pulsar instrument). The char bed of 75 mm length was maintained by quartz wool at the extremities (Figure II-9, #2). The Chembet furnace was equipped with two grounded thermocouples (K-type) one for control and the other one inserted into one branch of the U-tube to monitor for over-temperature conditions (Figure II-9, #3 and #6). The biochars bed was heated to the oxygenation temperature under pure nitrogen with a heating rate of 5°C/min. Once the oxygenation temperature was reached, the pure nitrogen (3.7 ultra-high purity) was replaced by the 8 vol% O<sub>2</sub> / 92 vol% N<sub>2</sub> mixture after 15 minutes (see Figure II-10). The effluent gas phase was analyzed online using a gas chromatograph (Agilent 3000A) with four different columns and TCD detectors which allow the detection of He, N<sub>2</sub>, O<sub>2</sub>, H<sub>2</sub>, CH<sub>4</sub>, CO and CO<sub>2</sub>. The oxygenated biochars are named as follows: ox2h\_280C, ox4h\_280C, ox8h\_280C, ox16h\_280C, ox2h\_340C and ox2h\_400C respectively.

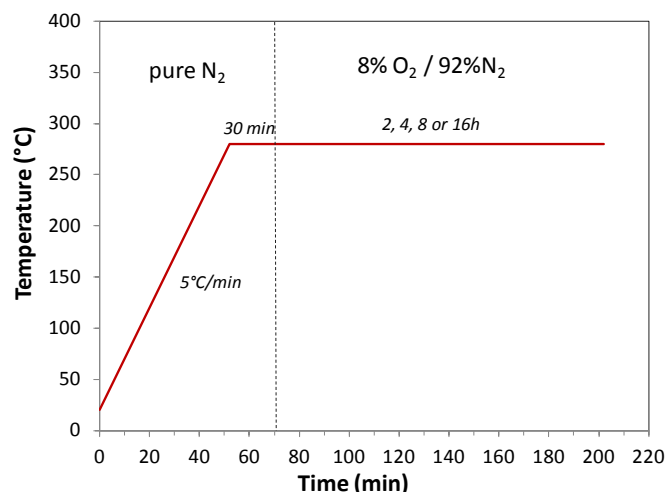


**Figure II-10: Temperature program of the oxygenation in the Chembet Reactor coupled with the micro gas chromatograph**

### 1.3. Catalytic methane cracking on a fixed bed of biochars

Reactivity of the biochars has been tested towards methane cracking reaction. Methane cracking mainly consists in hydrogen production and deposit of coke at the char surface (see Eq.II-3). Tests have been performed on two different types of reactors: a plug flow reactor and a thermogravimetric analyzer. In fact, regarding the plug flow reactor the advantage is that the reactive flow of gas should go through the entire char bed. A thermogravimetric analyzer provides the evolution of the mass over the experiments.



### 1.3.3. **Methane cracking tests in a plug flow reactor**

Two sets of methane cracking tests have been performed on the Chembet instrument (described in the functionalization by an O<sub>2</sub> treatment in the section 1.2.4): preliminary tests were carried out on raw biochars to evaluate the efficiency of the biochars as catalyst and the influence of the operating conditions on the methane cracking. Then tests investigating the role of the oxygenated functions were performed.

#### 1.3.3.1. **Preliminary parametric study of the methane cracking on raw biochar**

A first set of experiments has been carried out to investigate the efficiency of the raw biochars as catalyst for the methane cracking and to evaluate the influence of the operating conditions. Tests were performed in the Chembet instrument coupled with the gas analyzer (see Figure II-9). A sampling of the output gas phase has been done every three minutes. A mass flow controller unit from Quantachrome instrument was used to control the gas flow rates (calibrated between 0-15 mL/min for N<sub>2</sub>, 0-20 mL/min for CH<sub>4</sub>). The efficiency of the methane cracking has been evaluated through the production of hydrogen. In fact the TCD detector in the gas chromatograph is more sensitive to hydrogen than methane. Methane cracking has been performed at 700°C. However before introducing the reactive mixture, the sample was heated under pure nitrogen (research grade purity) to 900°C with an heating rate of 20°C/min and held 15 minutes before cooling down to the reaction temperature and introducing the methane. This pre-treatment has been performed to outgassing the surface of the biochars. In fact some hydrogen coming from the biochars was analyzed during the heating ramp under pure nitrogen. Thus, once the pre-treatment is achieved and the mixture of methane introduced we could assure that the analyzed hydrogen is coming from the methane conversion. The temperature program is presented in Figure II-11. Prior to test using biochars, methane cracking has been performed with an empty cell and no methane conversion into hydrogen was detected. The tests consisted in three cycles of 45 minutes of methane cracking with in between two injection cycles of pure nitrogen. This gas switching has been done to evaluate the regeneration of the biochars surface. Three parameters were investigated: the length of the biochars bed (1.6, 3.8 and 7.6 cm), the methane partial pressure (7, 14, 21%) and the total flow rate (25, 45 mL/min).

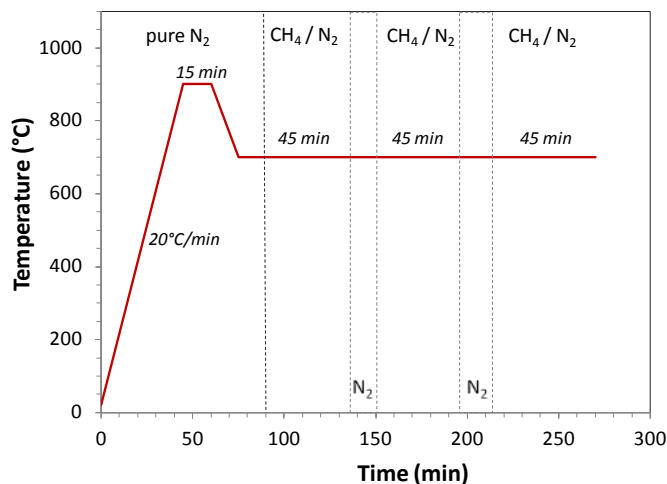


**Figure II-11: Temperature program of the preliminary methane cracking tests on raw biochars in the ChemBet instrument**

### 1.3.3.2. Methane cracking on raw and oxygenated biochars

The same device, as presented in the above section, has been used to test the reactivity of the oxygenated biochars and biochars heated up to 900°C under pure nitrogen (see Figure II-9). A flow rate of 45 mL/min of 20 vol% CH<sub>4</sub>/ 80 vol% N<sub>2</sub> mixture was injected in the reactor once the sample has been heated under pure nitrogen (research grade purity). The temperature program has been slightly modified compared to the one of the preliminary test (see Figure II-12). The sample has been directly heated to the reaction temperature (700°C) and hold for 30 minutes before introducing the methane/ nitrogen mixture (controlled by mass flow controllers TYLAN) for 2 hours. The pretreatment at 900°C has been skipped to avoid removing oxygen functional groups which are not stable above the reaction temperature. Tests have been performed using 50 mg of crushed biochars (100 < d<sub>p</sub> < 250 μm). The residence time was of 1.12 s. Tests on the raw biochars were performed at least three times. Tests were doubled on some oxygenated biochars.

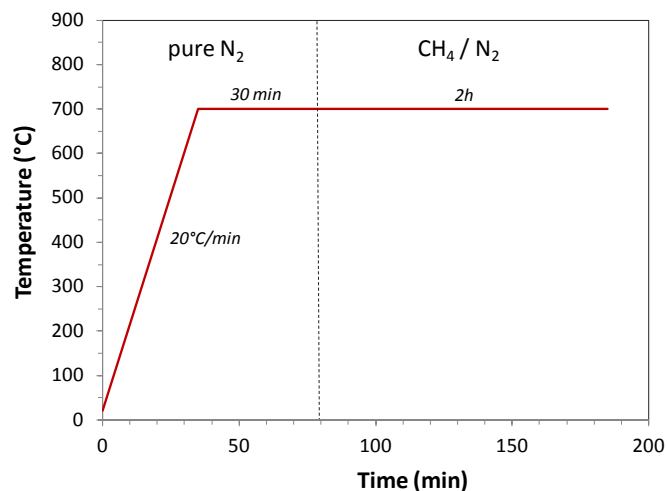


**Figure II-12: Temperature program of the methane cracking experiments**

#### 1.3.4. Methane cracking tests on the Thermogravimetric Analyzer (TGA)

A set of experiments have been performed in a Thermogravimetric Analyzer (TGA) to record the mass gain over the methane cracking reaction and correlate with the hydrogen production.

##### 1.3.4.1. 951 Dupont thermogravimetric analyzer

A thermogravimetric analyzer (951 Dupont Instrument, see Figure II-13) coupled with the gas chromatograph (Agilent 3000A) have been used to get simultaneously insights into the gas production and mass evolution over the experiment (Figure II-14). The 951 thermogravimetric analyzer from Dupont Instrument is a horizontal module composed of two separate chambers disposed on the two sides of the balance housing. A scheme of the experimental device is displayed in Figure II-14. The first chamber made of glass is sheltering the counter weight arm, the lamp and the photovoltaic cells (Figure II-14, #2 and #3). This chamber is constantly inerted in order to prevent any oxidation of the system. The secondary chamber is made of quartz, it is 206 mm long with an internal diameter of 22 mm. It is housing the quartz rod which holds the platinum pan where the sample is deposited (Figure II-14, #4). A thermocouple is positioned on the right side of the pan to record the temperature sample (Figure II-14, #5). This quartz reactor is composed of two entrances: one dedicated to the nitrogen flow rate and a second one for the methane introduction. The entire module is designed to be translated in order to place the second chamber into the external 500-watt furnace. A thermocouple located close to the furnace wall monitors furnace temperature (Figure II-14, #7 and #8).



Figure II-13: Dupont Thermogravimetric Analyzer (TGA) used for methane cracking tests over a bed of biochars

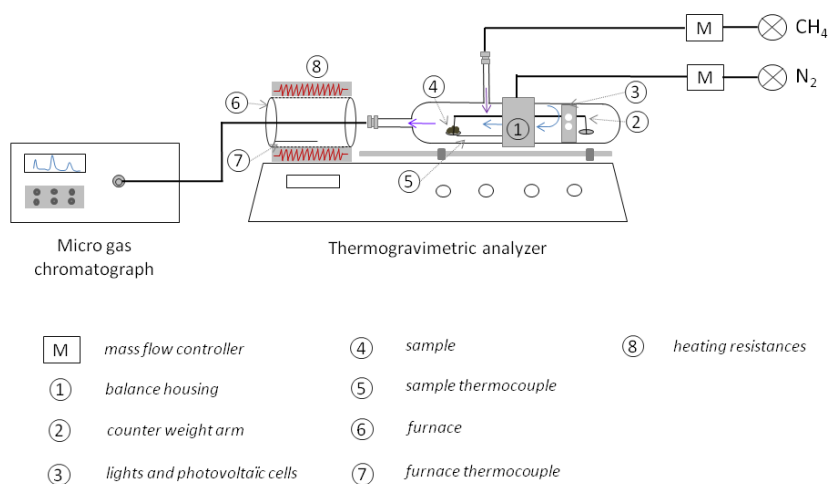
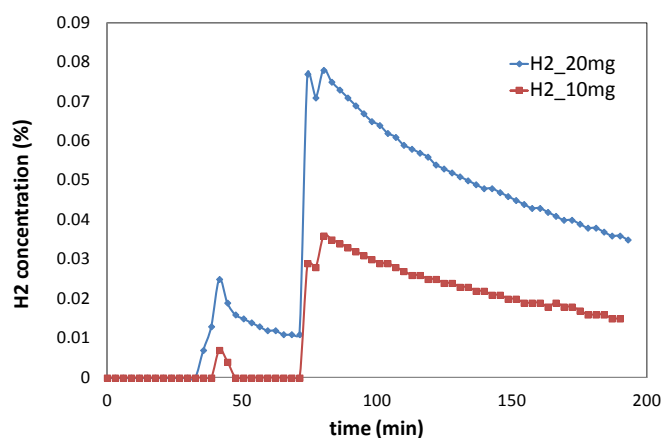


Figure II-14: Scheme of the experimental device used in the methane cracking experiments over a bed of biochars (Dupont TGA + gas chromatograph)

#### 1.3.4.2. Operating conditions for preliminary tests on raw biochars

Most of the thermogravimetric analyzers are vertical modules in which the gas is coming from the bottom of the apparatus and going up without any contact with the sample surface. Some diffusion limitations are potentially occurring. The Dupont TGA is a horizontal unit which is an advantage since the contact between the reactive gas and the sample surface is enhanced. In this configuration the gas mixture is licking the upper surface of the sample and could potentially go through the bed of chars. Some previous tests have been performed to evaluate the influence of the operating conditions on the methane cracking. To test if the gas mixture was going through the biochars bed or

only licking the surface two experiments were carried out changing the mass of biochars (10 and 20 mg). Figure II-15 shows the hydrogen productions during methane cracking at 700°C under a mixture of 10% CH<sub>4</sub>/ 90% N<sub>2</sub> and with a total flow rate of 80 mL/min for the two different mass of biochars. It has been observed that the hydrogen production was proportional to the initial mass of biochars. In fact, for an initial mass twice higher, the hydrogen production was doubled. This should indicate that the gas mixture go through the bed biochars instead of only licking the upper surface.



**Figure II-15: Hydrogen production during methane cracking in the TGA (700°C, 80 mL/min, 10% CH<sub>4</sub>/ 90% N<sub>2</sub>)**

The same temperature program as described in the section 1.3.3.2 (see Figure II-12) was performed.

#### 1.3.4.3. Operating conditions for methane cracking on impregnated biochars

20 mg of crushed biochars ( $100 < d_p < 125 \mu\text{m}$ ) were exposed to a mixture of 10 vol% CH<sub>4</sub>/ 90 vol% N<sub>2</sub> with a flow rate of 80 mL/min (flow rate controlled by mass flow controller (TYLAN). Preliminary tests using an empty crucible were performed and no methane conversion into hydrogen was detected. The same temperature program as described in the section 1.3.3.2 (see Figure II-12) was performed. Tests on the raw biochars were performed three times, some tests on minerals impregnated biochars were doubled. From the set of experiments, it has been estimated a maximal error of 7% on the hydrogen concentration measurement.

## 2. Biochars surface characterizations

The goal of this section is to present the different analytical techniques which have been utilized to characterize the biochars. The characterization was focused on the biochars surface properties since the surface is the interface where the reaction occurs in heterogeneous catalysis.

Figure II-16 and Table II-2 present a picture of the biochars chips and the particle size distribution respectively. As it has been presented in Chapter 1, biochars are amorphous carbons mainly composed of small aromatics units with heteroatoms embedded in the matrix. In terms of reactivity, four aspects of the biochars surface are important: the carbon structures, the oxygenated functions, the mineral contents and the surface/porosity properties. For each properties of the surface one or several analytical techniques have been performed:

- carbon structures were investigated using Raman spectroscopy and Transmission Electron Microscopy (TEM),
- oxygenated functions were analyzed by FTIR spectroscopy and Temperature Programmed Desorption (TPD),
- X-ray fluorescence, ESEM and XRD were performed to get insights into the content, distribution and structure of the minerals.
- porosity and specific surface area were investigated by BET analyses.



Figure II-16: Figure of biochars from poplar wood pyro-gasification

Table II-2: Particle size distribution of biochars chip

	0.25 < L < 0.5 mm	0.5 < L < 1 mm	1 < L < 2 mm
		wt%	
<b>Biochars chip</b>	35.3	40.7	24.0

## 2.1. Proximate and ultimate analysis

The proximate analysis - moisture, ash - and the ultimate analysis – C, H, O, N, S - have been carried out for the poplar wood chips and biochars. The measurements of the moisture and ash contents have been performed following the French standards: NF-M03-002 (AFNOR 1995; [2]) and NF-EN-14775 (AFNOR 2010; [3]). The ultimate analysis has been done on an elemental analyzer (CE instrument NA 2100). The determination of C, H, N, S consisted in a complete combustion in excess of air. The CO<sub>2</sub>, NO<sub>2</sub> and SO<sub>2</sub> produced have been separated by gas chromatograph column and then quantified thanks to a TCD detector. The amount of oxygen is evaluated by difference (%O= 100- %C- %H- %N- %S- %ash).

## 2.2. Minerals content

Characterization of the minerals is of great interest since they are considered to be active sites in catalytic applications. However their nature, dispersion, quantity, structure and interaction with the substrate are all the parameters which determine their efficiency. In this study we performed X-ray fluorescence to get insights into the nature and amount of each mineral component. To evaluate the minerals structure we performed X ray-Diffraction (XRD). The dispersion and interaction with the carbonaceous substrate were investigated by Environmental Scanning Electron Microscopy coupled with Energy-dispersive X-ray microanalysis (SEM+EDS).

### 2.2.1. *X-ray fluorescence (XRF)*

The X-ray fluorescence has been performed to get insights into the nature and amount of mineral elementary components in raw poplar wood and biochars.

#### 2.2.1.1. Theoretical basis

X-ray fluorescence is produced when a X-ray beam, with enough energy to take away an electron from internal layer from the electronic cloud, collides with an atom. In this situation there is a probability that an electron is ejected (with an energy  $E_0$ ) which let the atom in a very high instable state. To return in a more stable energy state the electrons from the electronic cloud will be reorganized. An electron from an upper layer ( $E_1$  or  $E_2$ ) will replace the ejected electron and will

liberate a photon energy ( $E_0 - E_1$ ) or ( $E_0 - E_2$ ). This is the X-ray fluorescence phenomenon. The energy of the emitted photon is characteristic from the element (see Figure II-17). Several rays from the different electronic orbits (K, L and M) can potentially be emitted during the transition. However the quantification is based on the more intense ray. Prior the quantification it is required to determine the matrix composition since the ray intensity is not directly proportional to the amount of the element. Results from the ultimate analysis have been used to get the stoichiometry of the matrix.

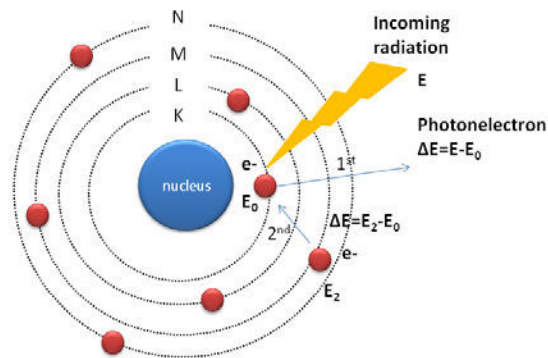


**Figure II-17: Scheme of the X-ray fluorescence phenomenon ©Copyright Amptek [4]**

#### 2.2.1.2. Experimental device

XRF have been performed using an Energy Dispersive X-ray fluorescence spectrometer (EPSILON 3XL from PANanalytical company). The instrument is composed of 3 main parts:

- the X-ray column contains a silver anode. Its electrical power is of 15W. Filters are positioned on the beam route to the sample to avoid detector saturation.
- the sample holder and sample
- the high resolution Silicium Drift SDD detector with a resolution range of 135 eV to 5.9 keV.

#### 2.2.2. X-ray Diffraction (XRD)

XRD has been performed to investigate the structure of the impregnated minerals (calcium and potassium) on the biochars surface.

### 2.2.2.1. Theoretical basis

Crystalline state is characterized by a tridimensional atomic unit shell. This well ordered distribution gives rise to parallel plan equidistant from each other and which are called "lattice plans". The distance between lattice plans is characteristic from a crystal structure and can be characterized by XRD. A monochromatic X-ray bombarding the sample with a  $\theta$  angle is diffracted with the same angle if the Bragg law is respected which means that the different diffracted beams are in phase:

$$2. d_{hkl} \sin(\theta) = n. \lambda \quad \text{Eq.II-4}$$

with:

$\theta$ : angle between the incident beam and the sample surface (rad)

$d_{hkl}$ : lattice plan distance (nm)

$\lambda$ : wavelength (nm)

### 2.2.2.2. Experimental device

XRD analyses have been performed in a Philips diffractometer (from PANalytical, X'pert Pro MPD model) with a  $\theta$ - $\theta$  Bragg-Brentano configuration, a current of 45kV and an intensity of 40 mA. The X-ray tubing is in copper, the radiation wavelength is of 1.543 Å. Diffraction peaks have been recorded in the 10- 70 degrees in  $2\theta$  and a speed of 0.042°/sec. The peak assignment was based on the JCPDS and COD databases.

### 2.2.3. ***Environmental Scanning Electron Microscopy (ESEM) coupled with Energy-dispersive X-ray microanalysis (EDS)***

Environmental Scanning Electron Microscopy (ESEM) is a well known surface analysis which is used in a wide range of scientific fields such as biology, medicine or geology. ESEM provides information on the textural properties (porosity, structure) of the analyzed sample coupled with the Energy X-ray microanalysis it also provides chemical analysis of specific zones of the surface. In this study it has been mainly utilized to investigate the dispersion and the geometry of the minerals impregnated on the biochars.

### 2.2.3.1. Theoretical basis

SEM images are produced from the interaction between a thin high energetic beam of electrons and the surface of the material. This interaction gives rise to a various type of signals: secondary electrons (SEM images), back scattered electrons, X-ray, Auger electrons, photons and heat. SEM images are built from the emission of the secondary electrons. According to their orientation the signal which is sent back to the detector will be of different intensities which provide information about the topography of the surface. To differentiate composition of material at the surface of the sample back-scattered electrons will display SEM images with contrast according to the nature of the element present. Minerals present at the biochars surface appear brighter than the organic surface.

### 2.2.3.2. Experimental device

A Scanning electron microscope is composed of 3 main parts [5]:

- an electron gun which contains a tungsten filament placed under a high vacuum to allow electrons to reach the sample without being deflected by gas molecules in the air. Once electrons are produced they are accelerated through a high voltage (20 kV).
- a system of condensers and deflection bobbins which allows one to monitor the aperture of the beam and the scanning of the surface.
- detectors which are of different types according to the type of beam and the information one wants to collect.

## 2.3. Textural properties

Methods and models to investigate the specific surface area and porosity of the biochars are presented in this section. They are evaluated from the adsorption isotherms of the sample.

### 2.3.1. Adsorption isotherms

The isotherm of adsorption is the representation of the equilibrium between the activity of a known quantity of adsorbate in a define atmosphere and the quantity of adsorbate adsorbed at the surface [6]. It is usually represented as the quantity of gas adsorbed at the surface versus  $P/P_0$ . The shape of the adsorption isotherm is characteristic from a type of porosity. Six shapes have been identified by the IUPAC. Type I isotherm is characterized by a sharp increase of the amount of adsorbate adsorbed

at the surface at low  $P/P_0$  and a horizontal plateau until  $P/P_0$  reaches one (see Figure II-18). This shape of isotherm is typical from microporous material and chemisorption over a monolayer.

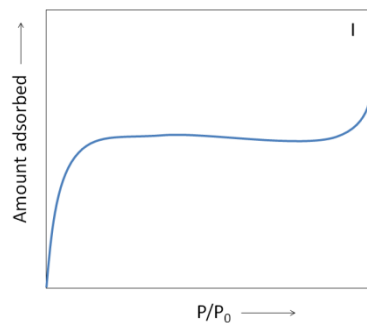


**Figure II-18: Illustration of the adsorption isotherm of type I characteristic from the microporous material according to the IUPAC classification [7]**

### 2.3.2. *Specific surface area*

Determination of the specific surface area is based on the adsorption isotherm. In fact the volume of probe adsorb at the surface is needed to get the specific surface area. Various methods have been developed to calculate the surface area but two main principles are mostly used: the Langmuir model and Brunauer, Emmett and Teller (BET) model. For a monolayer adsorption (Type I) the Langmuir model is the most adapted. Basically the Langmuir model is built on the following hypotheses:

- adsorbate molecules are adsorbed on well-defined sites of the surface
- all sites are identical in terms of energy
- only one molecule of adsorbate can settle down on a site
- the energy of one molecule is not dependent of its location on the surface

Then the Langmuir equation is based on the equilibrium between the adsorption and desorption of the adsorbate from the surface. The adsorption rate can be written as follows:

$$r_{ads} = k_{ads} \cdot P_a (1 - \theta_a) \quad \text{Eq.II-5}$$

where:

$r_{ads}$ : adsorption rate of the adsorbate on the surface ( $\text{mol} \cdot \text{m}^{-2} \cdot \text{s}^{-1}$ )

$k_{ads}$ : adsorption rate constant

$P_a$ : partial pressure of the adsorbate in the bulk phase

$\theta_a$ : fraction of the surface covered by the substrate

and the desorption rate:

$$r_{des} = k_{des} \cdot \theta_a \quad \text{Eq.II-6}$$

$r_{des}$ : desorption rate of the adsorbate from the surface ( $\text{mol} \cdot \text{m}^{-2} \cdot \text{s}^{-1}$ )

At the equilibrium:

$$r_{ads} = r_{des} \quad \text{Eq. II-7}$$

That gives the linearized following equation:

$$\frac{1}{n} \cdot \frac{P_a}{P_0} = \frac{1}{n_a} \cdot \frac{P_a}{P_0} + \frac{1}{K \cdot n_a} \quad \text{Eq.II-8}$$

where

$n_a$ : moles of adsorbate on the surface (mol)

$n$ : total moles of adsorbate (mol)

$K$ : thermodynamic equilibrium constant

$P_a$ : partial pressure of the adsorbate

$P_0$ : saturation vapour pressure

By plotting  $\frac{1}{n} \cdot \frac{P_a}{P_0}$  versus  $\frac{P_a}{P_0}$  we obtain a linear equation of slope  $\frac{1}{n_a}$  and intercept  $\frac{1}{K \cdot n_a}$ .

Once the moles of adsorbate adsorbed at the surface is known, the following equation is used to calculate the total surface area:

$$S_{tot} = \xi \cdot n_m \cdot N_A \quad \text{Eq.II-9}$$

with:

$S_{tot}$ : total surface area ( $\text{m}^2$ )

$\xi$ : adsorbate cross sectional area ( $\text{m}^2$ )

$N_A$ : Avogadro number ( $\text{mol}^{-1}$ )

Then the specific surface area is calculated by dividing the total surface area by the mass of the sample:

$$S_{sp} = \frac{\psi \cdot S_{tot}}{m_s} \quad \text{Eq.II-10}$$

with:

$S_{sp}$ : specific surface area ( $m^2/g$ )

$m_s$ : sample mass ( $g$ )

$\psi$ : shape factor (= 1 for spherical particle)

### 2.3.3. Porosity

It exists various ranges of pores diameter which are in the order of magnitude of nanometers. The IUPAC classified the pores in three families:

- macropore:  $d_p > 50$  nm
- mesopore:  $2 < d_p < 50$  nm
- micropore:  $< 2$  nm

According to the type of porosity the method to calculate the pore volume is different. Regarding micropores, the determination of the total volume is dependent of the width and shape of the pores. Different methods can be used to determine the volume such as the t-method, the Horvath-Kawazoe (HK) or the Dubinin-Stoeckli methods. In this study we used the Horvath-Kawazoe (HK) method. The idea is that the relative pressure  $P/P_0$  necessary to fill the pores is directly correlated to the interaction energy between adsorbate/adsorbent.

$$R.T. \ln \left( \frac{P}{P_0} \right)_{pores} = f(\Psi(r)_{pore}) \quad \text{Eq.II-11}$$

with:

$R$ : ideal gas constant

$T$ : temperature

$\Psi(r)_{pore}$ : interaction potential of Lennard – Jones type

From the analysis of the adsorption isotherm this is possible to get insights into the specific surface area and porosity. The next section presents the experimental devices which have been used to obtain the adsorption isotherm.

#### 2.3.4. **Experimental device**

BET analyses have been done on an ASAP 2010 apparatus from Micromeritics. Adsorption of argon has been monitored at 77 K until a relative pressure of 1. Argon has been chosen rather than nitrogen because its molecular overcrowding is lower than the nitrogen which is more adapted to characterize our sample. Prior to argon adsorption a degassing step of 30 h under high vacuum at 200°C has been performed. Specific surface area has been determined by application of the Langmuir model. Pore size and pore volume have been evaluated using the Horvath-Kawazoe model. BET analyses were performed twice for the raw biochar.

### 2.4. **Oxygenated content**

In this study two techniques have been employed: Fourier Transform Infrared Spectroscopy (FTIR) and Temperature Programmed Desorption (TPD) to characterize the oxygenated content.

#### 2.4.1. **FTIR**

Fourier Transform InfraRed (FTIR) takes part in the family of the spectroscopic analyses. FTIR is a non-destructive and fast analysis which gives insights into the carbon-oxygen bonds and functional groups. This technique is a powerful tool to quickly estimate if the oxygenation has been efficient and get insights into the type of functional groups which have been enhanced.

##### 2.4.1.1. **Theoretical basis**

FTIR theory is based on the interactions between light and matter. An infrared source (400-4000  $\text{cm}^{-1}$ ) is used to bomb the sample. If the wavelength of the light source is closed to the vibration energy of the molecule, the molecule will absorb the energy and the transmitted or reflected light will be diminished. Not all vibrations give rise to an absorption, it is depending on the geometry and more particularly the symmetry of the molecule. For a given geometry, it is possible to determine the active modes in the infrared domain by referring to the group theory. Oxygen- carbon bonds are responding in FTIR, two main domains are visible: C=O bonds are visible in the 1600-1800  $\text{cm}^{-1}$  region, C-O linkages in the 1000-1300  $\text{cm}^{-1}$  region. The Table II-3 present the characteristic oxygen-carbon bonds detected in FTIR.

**Table II-3: FTIR peak assignments (adapted from [8])**

Type of bonding	Wave number (cm <sup>-1</sup> )	Functional group
C=O	1850-1786	Anhydrides
	1740,1724	Lactones (C=O)
	1710-1680	Carboxylic (C=O)
	1670-1660	Quinone or conjugated keton
C-O	1440	Carboxylic (O-H)
	1264	Lactones (C-O-C)
	1250-1235	Ether bridges between rings
	1162-1114	Phenol (C-O) and (O-H bend/stretching)
	1076-1014	Alcohol (C-O)

#### 2.4.1.2. Experimental device

Prior to FTIR analyses samples have been finely ground in a mortar and mixed in KBr. Spectra have been obtained from a Nicolet Impact 400D spectrometer by adding 32 accumulations at a resolution of 8 cm<sup>-1</sup>.

#### 2.4.2. Temperature Programmed Desorption (TPD)

Temperature programmed desorption has been used to get insights into the type and amount of oxygenated groups at the surface. It is a dynamic analysis which consists in slowly heating the sample into an inert atmosphere with a constant heating rate. During the heating CO<sub>2</sub> and CO are produced. According to the literature, the temperature of gas desorption provides information about the nature of the oxygenated functions.

##### 2.4.2.1. Experimental device

TPD of 50 mg of raw and oxygenated biochars have been performed in the ChemBet Pulsar instrument under a 25 ml/min of helium from 25°C to 1100°C with a heating rate of 5°C/min. The same experimental device as for the oxygenation or methane cracking tests was used (see 1.2.4 and Figure II-9). Gas production was monitored by both the TCD detector from the ChemBet Instrument and by a 3000a gas chromatograph from Agilent with four different columns and TCD detectors

which allow the detection of He, N<sub>2</sub>, O<sub>2</sub>, H<sub>2</sub>, CH<sub>4</sub>, CO and CO<sub>2</sub>. Tests on the raw biochar were carried three times, some tests on oxygenated biochars were doubled.

#### 2.4.2.2. Deconvolution

There is controversy in the literature over the assignment of the different peaks during TPD analyses. However some global trends have been established in previous studies [9]–[11]. The CO<sub>2</sub> desorption is resulting from carboxylic acid desorption at low temperature and lactones desorption at high temperature. Carboxylic anhydrides produce both CO and CO<sub>2</sub>. Peroxides should produce a CO<sub>2</sub> peak at 550-600°C. Hydroxyl and phenols desorb into CO in the 600-800°C temperature range and hydroxyl should be produced first. Pyrone-type structure and quinone (carbonyls) have been identified at the highest temperature. In addition quinone desorb before pyrone-type structure. An illustration of the desorption peaks of the oxygenated functions versus temperature is provided in Figure II-19.

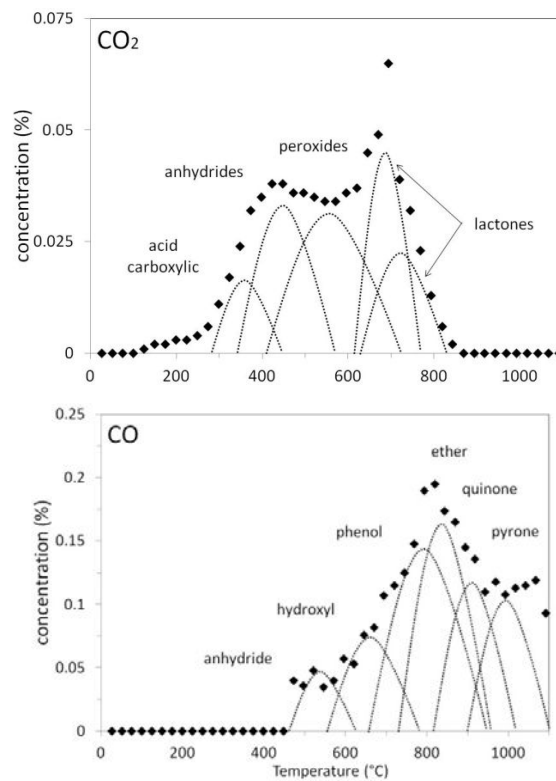


Figure II-19: Scheme of CO and CO<sub>2</sub> peak assignments desorption versus temperature (from gas chromatograph analyses)

Table II-4: O-containing groups temperature desorption

Functions	Temperature desorption (°C)	Desorbed into:
Carboxylic acid	390	CO <sub>2</sub>
Anhydride	450	CO <sub>2</sub>
	590	CO
Peroxide	530	CO <sub>2</sub>
Lactone	660	CO <sub>2</sub>
	720	CO <sub>2</sub>
Hydroxyl	620	CO
Phenol	750	CO
Ether	844	CO
Quinone	880	CO
Pyrone	973	CO

The TCD signal is the sum of all the species which desorbed during the TPD analyses. The deconvolution has been performed on the TPRWin software furnished with the ChemBet Pulsar instrument. Results from micro GC have been a support to carry out the deconvolution. From the literature and the micro GC results, the signal has been deconvoluted using Gaussians functions. The peaks related to O-containing groups desorption are presented in Table II-4. Peak temperatures were bound by +/- 50°C and the Half Width at Half Maximum (HWHM) was kept constant.

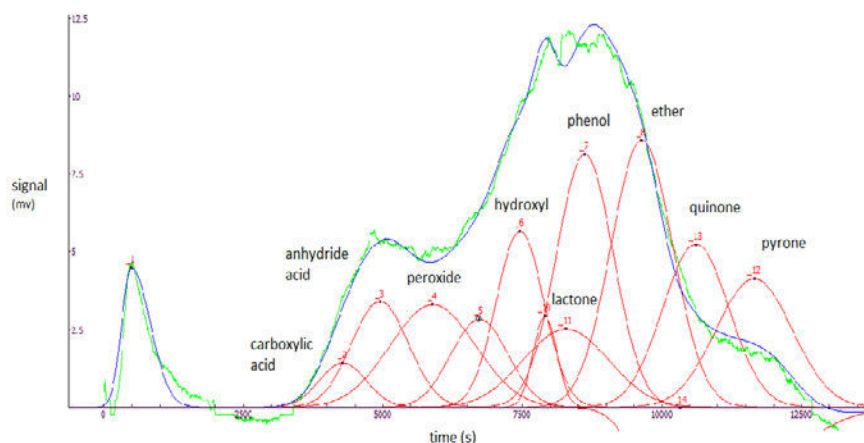


Figure II-20 : Example of Curve-fitting of the TCD signal during TPD (TPR Win Software® Pulsar)

## 2.5. Carbon structures

The biochars carbon structures have been studied using two types of analysis: Raman spectroscopy, and Transmission Electron Microcopy (TEM).

### 2.5.1. *Raman spectroscopy*

Raman spectroscopy has been widely used to characterize carbon based materials and more specifically biochars from pyro-gasification. As it has been mentioned in the introductory part of this section, biochars are highly disordered carbons. Different sources of disorder are contributing: insertion of heteroatoms such as oxygen into the carbon rings, different orientations between well-ordered graphitic structures, different size of aromatic rings or presence of unsaturated carbon and aliphatic chains. Information about the type and relative amount of the different structures can be determined by Raman spectroscopy.

#### 2.5.1.1. Theoretical basis

Raman spectroscopy as all the spectroscopic techniques is based on the interaction between light and matter. In this case the analysis is based on the inelastic scattering phenomenon. Photons from a monochromatic light (most of the time a laser) which have been absorbed by the sample are reemitted with a different energy (shift up or down). Depending if the molecule has a Raman-active mode, the frequencies of the reemitted photon will be different (see Figure II-21) [12]:

- If a photon with an initial frequency of  $\nu_0$  is absorbed by a molecule with no Raman-active mode, the molecule will be excited but will return to its initial ground state since it did not reach any excited states. Then the molecule will emit a photon with the same frequency than the initial one. This interaction is called an elastic Rayleigh scattering.
- If a photon with an initial frequency of  $\nu_0$  is absorbed by a molecule with a Raman-active mode, and the molecule is in the ground state, the absorption of the incident photon will propel the molecule to an excited vibrational state. Part of energy of the photon has been used to activate the Raman mode which could be named  $\nu_a$ . The reemitted photon will have a lower frequency equal to  $\nu_0 - \nu_a$ . This is called a Stokes interaction.
- If a photon with an initial frequency of  $\nu_0$  is absorbed by a molecule with a Raman-active mode, and the molecule is already in an excited vibrational state, the absorption of the incident photon will cause an excessive energy of the Raman mode. The molecule will return

to a ground state and the scattered light will have a frequency of  $\nu_0 + \nu_a$ . This mode is an Anti-Stokes interaction.

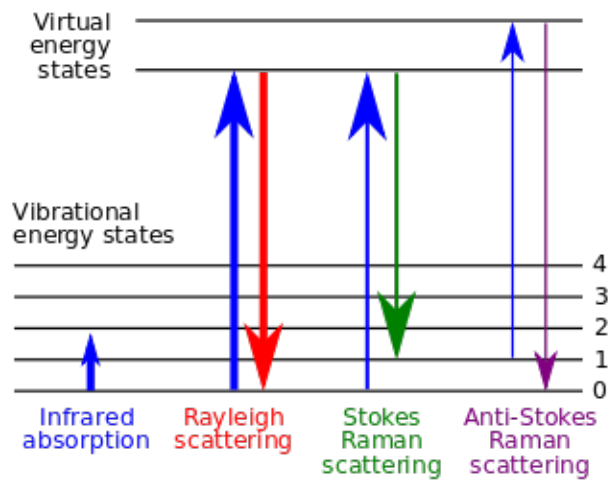


**Figure II-21: Raman active modes [13]**

For a Raman analysis, only the Stokes and Anti-Stokes interactions will provide information about the fingerprint of the sample. Inelastic scattering is a weaker signal than the Rayleigh one, thus specific experimental conditions are needed to obtain a proper Raman spectra. The equipment used in this study is presented in the following section.

### 2.5.1.2. Experimental device

Basically to perform Raman analysis, four devices are required:

- excitation source (laser)
- light
- filter
- detector

In this study a Confocal RAMAN – AFM Witec Alpha 300AR microscope equipped with a CCD camera detector in the range  $175\text{-}4000\text{ cm}^{-1}$  and a Nd-YAG excitation laser at  $532\text{ nm}$  was used to investigate the carbonaceous structures at room temperature. Ten analyses have been performed at different locations of the biochar surface. As mentioned in Chapter I, a Raman spectrum of a carbonaceous material provides 10 peaks referring to the carbon structures. However these peaks are superimposed in the  $800\text{-}2000\text{ cm}^{-1}$  zone of Raman shift. The discussion of the carbon structures requires the post treatment of the spectra. Once Raman spectra have been collected, the deconvolution has been performed to get the relative amount of each carbonaceous structure.

### 2.5.1.3. Deconvolution of a spectrum

#### Peak assignment

The region of interest in the Raman spectrum of an amorphous carbonaceous material is the 800-2000  $\text{cm}^{-1}$ . Typically one can observe two main peaks located at 1320 (D band) and 1590  $\text{cm}^{-1}$  (G band) which are surrounded by minor peaks. The simultaneous presence of the D and G bands are representative of the duality in the composition of the biochars surface. In fact highly disordered structures which are assigned to the D peak are mixed with sheets of graphene-like carbons (G peak) which consist of carbon rings very well organized. These two bands are observable on the Figure II-22. The D peak is more specifically representative of the large aromatic rings systems ( $\geq 6$  rings). Other amorphous structures respond in Raman spectroscopy which explains the presence of other peaks. For example the overlap which is visible between the D and G band is due to three peaks: the  $G_r$  band at 1540  $\text{cm}^{-1}$ , the  $V_l$  band at 1465  $\text{cm}^{-1}$  and the  $V_r$  band at 1380  $\text{cm}^{-1}$  (see Figure II-22). They represent mainly aromatic semi-quadrant ring breathing for aromatic ring systems having more than two fused benzene rings [14]. These peaks are usually considered as one entity which represents the small aromatic rings with 3-5 rings. On Figure II-22 four peaks at lower wavenumber than the D band are represented. The S band at 1185  $\text{cm}^{-1}$  is assigned to the  $\text{sp}^2\text{-sp}^3$  carbonaceous structures in biochars. The  $S_l$  band at 1230  $\text{cm}^{-1}$ , the  $S_r$  band at 1060  $\text{cm}^{-1}$ , and the R band at 800-960  $\text{cm}^{-1}$  are representative of the contributions of ether and benzene related structures. At higher wavenumber than the G band, the  $G_l$  band at 1700  $\text{cm}^{-1}$  is assigned to carbonyl structure. The  $G_l$ ,  $S_r$ ,  $S_l$  and R bands are considered as minor bands which allow the reduction of widths of the main bands in performing the spectral curve-fitting [14]. The assignments of the ten peaks are summarized in Table II-5.

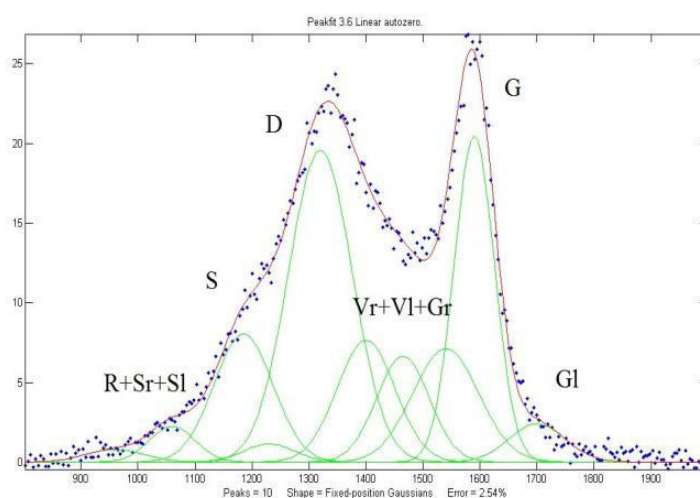


Figure II-22: Example of Raman spectrum deconvolution using the Peakfit program on Matlab®

**Table II-5: Raman peak assignment from [14]**

Band name	Band position (cm <sup>-1</sup> )	Description	Bond type
G <sub>i</sub>	1700	Carbonyl group C=O	sp <sup>2</sup>
G	1590	Graphite E <sup>2</sup> <sub>2g</sub> ; aromatic ring; quadrant breathing; alkene C=C	sp <sup>2</sup>
G <sub>r</sub>	1540	Aromatics with 3-5 rings; amorphous carbon structures	sp <sup>2</sup>
V <sub>i</sub>	1465	Methylene or methyl group; semi circle breathing of aromatic rings; amorphous carbon structures	sp <sup>2</sup> , sp <sup>3</sup>
V <sub>r</sub>	1380	Methyl group; semi-circle breathing of aromatic rings; amorphous carbon structures	sp <sup>2</sup>
D	1300	D band on highly ordered carbonaceous materials; C-C between aromatic rings and aromatics with not less than 6 rings	sp <sup>2</sup> , sp <sup>3</sup>
S <sub>i</sub>	1230	Aryl-alkyl ether; para-aromatics	sp <sup>2</sup> , sp <sup>3</sup>
S	1185	C <sub>aromatic</sub> -C <sub>alkyl</sub> ; aromatic (aliphatic) ethers; C-C on hydroaromatic rings; hexagonal diamond carbon sp <sup>3</sup> ; C-H on aromatic rings	sp <sup>2</sup> , sp <sup>3</sup>
S <sub>r</sub>	1060	C-H on aromatic rings; benzene (ortho-di-substitued) ring	sp <sup>2</sup>
R	960-800	C-C on alkanes and cyclic alkanes; C-H on aromatic rings	sp <sup>2</sup> , sp <sup>3</sup>

### Curve-fitting method and treatment of the results

The curve fitting has been performed on the Matlab® software using the Peakfit program. Peak positions have been fixed and band widths have been restricted. A least square refinement was performed to provide the optimal solution according to the parameters conditions. Curve fitting results provide bands areas. Four ratios have been calculated to be able to conclude on the relative distribution of the main carbon structures:  $I_G/I_{tot}$ ,  $I_D/I_{tot}$ ,  $I_{G+I_{V_i}+I_{V_r}}/I_{tot}$ ,  $I_s/I_{tot}$ . The  $I_G/I_{tot}$  represents the contribution of the graphitic structure in the carbon matrix. The  $I_D/I_{tot}$  is assigned to the large aromatic rings and the “in-plane” imperfections structure. The  $I_{G+I_{V_i}+I_{V_r}}/I_{tot}$  ratio is an indicator of the presence of small aromatic rings and the  $I_s/I_{tot}$  is the representation of the unsaturated carbons such as in the aliphatic chains. Table II-6 summarized the interpretation of the four calculated ratios. Three other ratios could be of great interest:  $I_D/I_G$ ,  $I_D/(I_{G+I_{V_i}+I_{V_r}})$  and  $(I_{G+I_{V_i}+I_{V_r}})/I_G$ . The ratio  $I_D/I_G$  is a direct comparison of the amorphous and highly ordered structures. The  $I_D/(I_{G+I_{V_i}+I_{V_r}})$  is highlighting the predominance of rather the large rings or the smallest ones. Then the last one is a good indicator of biochar surface graphitization. The three peaks  $I_{G+I_{V_i}+I_{V_r}}$  are also called the “valley”.

**Table II-6: Ratios definition for the interpretation of RAMAN spectra**

ratio	description
$I_G/I_{tot}$	graphitic structure
$I_D/I_{tot}$	aromatic rings systems ( $\geq 6$ rings) « in-plane » defects
$(I_{Gr}+I_{Vr}+I_{Vr})/I_{tot}$	small aromatic rings systems (3-5 rings)
$I_S/I_{tot}$	$sp^2$ - $sp^3$ carbonaceous structures
$I_D/I_G$	amorphous over highly ordered structures
$I_D/(I_{Gr}+I_{Vr}+I_{Vr})$	large rings ( $\geq 6$ rings) over small aromatic rings (3-5 rings)
$(I_{Gr}+I_{Vr}+I_{Vr})/I_G$	indication of surface graphitization

### 2.5.2. *Transmission Electron Microscopy (TEM)*

Transmission Electron Microscopy (TEM) has been performed in addition to the Raman spectroscopy on some biochars: the raw and three oxygenated biochars (ox2h\_280C, ox8h\_280C and ox2h\_400C) to get better insights into the carbon nanostructure. During a TEM analysis, Selected Area Electron Diffraction (SAED) patterns can be performed as well to discriminate nanocrystalline from amorphous phases at specific location of the surface (such as EDS during ESEM analysis). In addition, High-Resolution TEM images were recorded to observe graphene-like sheets organization at the nano-scale.

#### 2.5.2.1. **Theoretical basis**

Electron microscopy allows one to obtain images at the nano-scale of thin slices of material which is not possible with light microscope due to limitations by the wavelength of the photons. A transmission microscope is composed of three main parts (see Figure II-23):

- the electron source and electron beam
- condenser lenses, objective lens and objective aperture
- projector lenses

Electrons are sent from the top of the column (from the source), go through the sample and the resulting pattern of electron absorption and transmission is magnified onto a viewing screen.

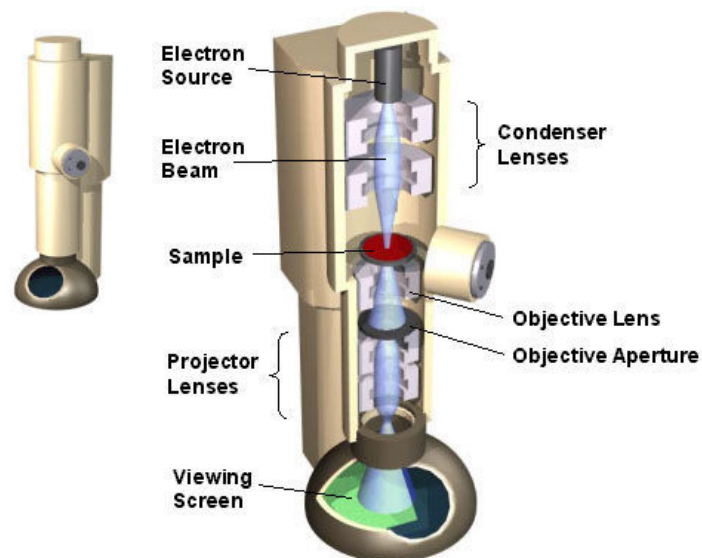


**Figure II-23: Illustration of the different parts of a Transmission Electron Microscope**

TEM images are provided by the transmitted electrons which went through the thin layer of the sample analyzed. A fraction of the electron beam is scattered to particular angles, determined by the crystal structure of the sample. The SAED patterns are formed from these diffracted electrons. Regarding the High-Resolution TEM, the image is formed by the interference of the diffracted beam with the direct beam (phase contrast). In HRTEM analyses, precautions have to be taken to limit the impact of the lenses aberrations (astigmatism, spherical and chromatic) which reduce image quality [15].

#### **2.5.2.2. Experimental device**

Samples were prepared by ultramicrotomy using a LEICA Ultracut R Ultramicrotome. The resulting ~100 nm thick layers were transferred onto 300 square mesh gold grids (Agar Scientific). TEM characterization was performed using a FEI Tecnai F 20 ST TEM, operated at 200kV, with a field electron gun (FEG) as the electron source. Bright field imaging enabled to observe the carbonaceous structure of the chars and selected area electron diffraction (SAED) patterns were recorded on the corresponding areas. The 002 lattice fringe mode - referred later to as high resolution (HR) - was used to image the profile of the aromatic layers (extent and shape) on the thinnest parts of the samples. The HRTEM images were acquired with drastic care at a magnification of 700 000 times, and at about the Scherzer optimum underfocus (-55.88 nm) to obtain reliable data with a spatial resolution of 0.28 nm.

### 3. Summary

This chapter presented the experimental capabilities which have been utilized to perform the pyro-gasification of poplar wood, the characterization and the functionalization of the biochars and their utilization as catalyst for methane conversion into hydrogen. The pyro-gasification has been performed at the RAPSODEE centre in a fluidized bed at 750°C under a mixture of 90 vol% H<sub>2</sub>O / 10 vol% H<sub>2</sub>O. Then two functionalizations of the biochars surface have been performed: an O<sub>2</sub> gas-phase treatment with the main objective to increase the oxygen content at the surface and a wet impregnation into nitrate salts of potassium and calcium to enhance their concentration at the biochars surface. The names of the functionalized biochars and the analytical techniques utilized to characterize their physico-chemical properties are summarized in Table II-7 and Table II-8 respectively. Lastly, the raw and functionalized biochars have been tested as catalyst for methane cracking. The set of experiments has been performed at the Catalysis and Combustion Laboratory at the City College of New York (USA).

**Table II-7: Summary of the names of the functionalized biochars**

#	Abbreviation	Description
1	raw_char	biochars directly recovered from the poplar wood pyro-gasification
2	ox2h_280C	biochars oxygenated during 2 h at 280°C (O <sub>2</sub> gas-phase treatment)
3	ox4h_280C	biochars oxygenated during 4 h at 280°C (O <sub>2</sub> gas-phase treatment)
4	ox8h_280C	biochars oxygenated during 8 h at 280°C (O <sub>2</sub> gas-phase treatment)
5	ox16h_280C	biochars oxygenated during 16 h at 280°C (O <sub>2</sub> gas-phase treatment)
6	ox2h_340C	biochars oxygenated during 2 h at 340°C (O <sub>2</sub> gas-phase treatment)
7	ox2h_400C	biochars oxygenated during 2 h at 400°C (O <sub>2</sub> gas-phase treatment)
9	Ca-char	biochars from pyro-gasification of poplar wood impregnated during 6h in a (0.5 wt%) calcium nitrate solution
10	K-char	biochars from pyro-gasification of poplar wood impregnated during 6h in a (0.5 wt%) potassium nitrate solution
11	Ca+K-char	biochars from pyro-gasification of poplar wood impregnated during 6h in a (0.25 wt%) potassium nitrate and (0.25 wt%) calcium nitrate solution

**Table II-8: Summary of the physico-chemical properties which have been characterized, the analytical instrument and the information provided**

<b>Physico-chemical properties</b>	<b>Type of analysis</b>	<b>Information</b>
<b>carbon structure</b>	RAMAN	Distribution of carbon structures
	TEM	Nanostructure
<b>Oxygenated functions</b>	FTIR	Nature of oxygenated functions
	TPD	Quantification
<b>Minerals content</b>	XRF	Elemental analysis
	XRD	Mineral structure
	ESEM+EDS	Distribution and interaction with support
<b>Textural properties</b>	Gas adsorption	Specific surface area
		Porosity

---

## Bibliography

- [1] K. Daizo and O. Levenspiel, *Fluidization Engineering*. 1991.
- [2] AFNOR, *Combustible minéraux solide: détermination de l'humidité*. France, 1995, p. 10.
- [3] AFNOR, *Biocombustible slides: méthode de la détermination de teneur en cendres*. France, 2010, p. 13.
- [4] AMPTEK, "What is XRF ?," 2015. [Online]. Available: <http://www.amptek.com/xrf/>. [Accessed: 01-Jan-2015].
- [5] C. CNRS, "Microscopie Electronique à transmission," 2002. [Online]. Available: <http://www.crhea.cnrs.fr/crhea/cours-caract.htm>. [Accessed: 01-Jan-2015].
- [6] N. T. E. Mines Albi, "Science et technologie des poudres," 2008. [Online]. Available: [http://nte.mines-albi.fr/STP/co/partie\\_C.html](http://nte.mines-albi.fr/STP/co/partie_C.html). [Accessed: 01-Jan-2015].
- [7] H. Z. Berlin, "Gas sorption measurements," 2015. [Online]. Available: [https://www.helmholtz-berlin.de/forschung/oe/ee/solare-brennstoffe/analytische-methoden/gassorptionsmessungen\\_en.html](https://www.helmholtz-berlin.de/forschung/oe/ee/solare-brennstoffe/analytische-methoden/gassorptionsmessungen_en.html). [Accessed: 01-Jan-2015].
- [8] A.-N. A. El-Hendawy, "Variation in the FTIR spectra of a biomass under impregnation, carbonization and oxidation conditions," *J. Anal. Appl. Pyrolysis*, vol. 75, no. 2, pp. 159–166, Mar. 2006.
- [9] Z. Karpinski and G. S. Szymanski, "The effect of the gradual thermal decomposition of surface oxygen species on the chemical and catalytic properties of oxidized activated carbon," *Carbon N. Y.*, vol. 40, pp. 2627–2639, 2002.
- [10] J.-H. Zhou, Z.-J. Sui, J. Zhu, P. Li, D. Chen, Y.-C. Dai, and W.-K. Yuan, "Characterization of surface oxygen complexes on carbon nanofibers by TPD, XPS and FT-IR," *Carbon N. Y.*, vol. 45, no. 4, pp. 785–796, Apr. 2007.
- [11] U. Zielke, K. J. Huttinger, and W. P. Hoffman, "Surface-oxidized carbon fibers: I. Surface structure and chemistry," *Carbon N. Y.*, vol. 34, no. 8, pp. 983–998, 1996.
- [12] Princeton Instruments, "Raman spectroscopy basics." [Online]. Available: [http://web.pdx.edu/~larosaa/Applied\\_Optics\\_464-564/Projects\\_Optics/Raman\\_Spectroscopy/Raman\\_Spectroscopy\\_Basics\\_PRINCETON-INSTRUMENTS.pdf](http://web.pdx.edu/~larosaa/Applied_Optics_464-564/Projects_Optics/Raman_Spectroscopy/Raman_Spectroscopy_Basics_PRINCETON-INSTRUMENTS.pdf). [Accessed: 01-Jan-2015].

- [13] (licensed under CC-BY-SA2.5) User:Pavlina2.0, "Creative Commons Raman Energy Levels," 2006. [Online]. Available: [https://en.wikipedia.org/wiki/Raman\\_spectroscopy](https://en.wikipedia.org/wiki/Raman_spectroscopy).
- [14] M. Asadullah, S. Zhang, Z. Min, P. Yimsiri, and C. Z. Li, "Effects of biomass char structure on its gasification reactivity," *Bioresour. Technol.*, vol. 101, no. 20, pp. 7935–7943, 2010.
- [15] ETH, "Image Modes in TEM-Lattice Images (HRTEM)." [Online]. Available: [http://www.microscopy.ethz.ch/TEM\\_HRTEM.htm](http://www.microscopy.ethz.ch/TEM_HRTEM.htm). [Accessed: 09-Oct-2015].

### **III. Chapter 3: Characterization of the raw and functionalized biochars**

## Content

1. Raw biochar surface properties .....	101
1.1. Oxygenated functions of the raw biochar .....	102
1.2. Mineral content of the raw biochar .....	104
1.3. Carbon matrix of the raw biochar .....	107
1.4. Specific surface area and porosity of the raw biochar .....	109
1.5. Partial conclusion on the physico-chemical properties of the raw biochar .....	110
2. Oxygenated biochars surface properties .....	111
2.1. Oxygenated functions on the oxygenated biochars.....	113
2.2. Mineral content of the oxygenated biochars.....	120
2.3. Carbon matrix of the oxygenated biochars.....	121
2.4. Specific surface area and porosity of the oxygenated biochars.....	128
2.5. Partial conclusion on the physico-chemical properties of the oxygenated biochars.....	130
3. Impregnated biochars surface properties.....	132
3.1. Oxygenated functions of the impregnated biochars.....	135
3.2. Mineral content of the impregnated biochars.....	136
3.3. Carbon matrix of the impregnated biochars.....	143
3.4. Specific surface area and porosity of the impregnated biochars.....	145
3.5. Partial conclusion on the physico-chemical properties of the impregnated biochars....	146
4. Conclusion on the characterization of the raw and functionalized biochars.....	148
Bibliography.....	150

This chapter describes the characterization of the raw and functionalized biochars. Four physico-chemical properties were investigated: the oxygenated functional groups, the mineral content, the textural properties and the carbon structure. As it has been described in the literature review, in Chapter I, these physico-chemical properties impact the catalytic activity of the biochars. Two functionalization treatments were performed: an oxygenation to enhance the oxygenated functions (O<sub>2</sub> gas-phase treatment) and an impregnation into a nitrate salts solution to increase the concentrations of AAEMs at the biochars surface (wet impregnation). Post-treatment, the nature and amount of the added chemical functions at the biochars surface were evaluated. In addition, the other physico-chemical properties of the functionalized biochars were characterized. In fact, it has been highlighted in the literature, that the functionalization treatments could also have impacted the textural properties and carbon matrix structure. Thus, it becomes necessary to characterize the whole physico-chemical surface properties of the raw and functionalized biochars.

This chapter is divided into three sections related to the raw biochar, the oxygenated biochars and the mineral impregnated ones. Each section describes the four physico-chemical properties quoted before.

## 1. Raw biochar surface properties

Raw biochar has been characterized immediately after the poplar wood gasification at 750°C under a mixture of 90 vol% H<sub>2</sub>O/ 10 vol% N<sub>2</sub> during 30 min. This section presents the characterization of:

- the oxygenated functions by Fourier Transform Infrared spectroscopy (FTIR) and Temperature Programmed Desorption (TPD) analyses,
- the minerals composition, structure and dispersion by X-ray Diffraction (XRD), X-ray fluorescence (XRF) and Environmental Scanning Electron Microscopy + Energy Dispersive Microscopy (ESEM-EDS),
- the carbon structures distribution by Raman spectroscopy,
- the specific surface area and pore volume by BET analyses

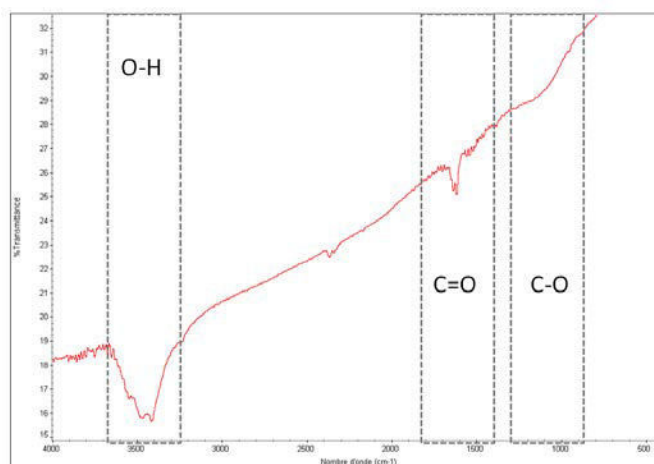
Prior to characterizing the surface properties of the biochar, the proximate and ultimate analyses (see Table III-1) have been performed on the raw biochar following the procedure described in the section 2.1 of chapter II. The raw biochar is mainly composed of carbon (82 wt%) and oxygen (10 wt%) functions and contains in minor concentration hydrogen (2 wt%) and nitrogen (0.5 wt%). The ash content and moisture are of 3.8 wt% and 6.18 wt% respectively. The global chemical composition of the raw biochar is similar to results for other biochars presented in the literature [1], [2].

**Table III-1: Proximate and ultimate analyses of raw biochar**

	C	H	N	S	O	ash	moisture
	wt%, dry					wt%, dry	wt%
<b>Raw biochar</b>	82.54	2.16	0.55	0	10.93	3.82	6.18

### 1.1. Oxygenated functions of the raw biochar

Oxygen is the second element in the raw biochar composition (see Table III-1). As described in the section 2.1.3 of the chapter I, various functions have been identified at the surface of carbonaceous materials. FTIR and TPD analyses have been performed to determine the type and amount of the oxygenated functions. Figure III-1 presents the FTIR spectrum for the raw biochar. Three bands are observable: the band assigned to the O-H stretching mode of hydroxyl and bound water molecules [3] and bands related to the single and double carbon-oxygen linkages [4]. A band with two sharp peaks around  $1600\text{-}1750\text{ cm}^{-1}$  is visible which indicates that lactone, carboxylic and quinone functions should be present at the surface. The broad band between  $1000\text{-}1200\text{ cm}^{-1}$ , not well defined, is assigned to C-O stretching from lactone, ether and phenol functions (the detailed band assignment is provided in the section 2.4 of the chapter II).

**Figure III-1: FTIR spectrum of the raw biochar**

FTIR gives insights into the type of oxygenated functions present at the biochar surface. However, the quantitative analysis is not straightforward. For this purpose, TPD analysis was performed on biochar surface to quantify the different oxygenated groups. Results of the analysis are presented in Figure III-2. They confirm the presence of carboxylic acid, lactone, phenol, ether and quinone/pyrone

structures. However, according to the literature review, other functions have been identified at the surface of the biochar. For example peroxide and hydroxyl have been assigned to the CO<sub>2</sub> production at 450°C and the CO production at 600°C [5].

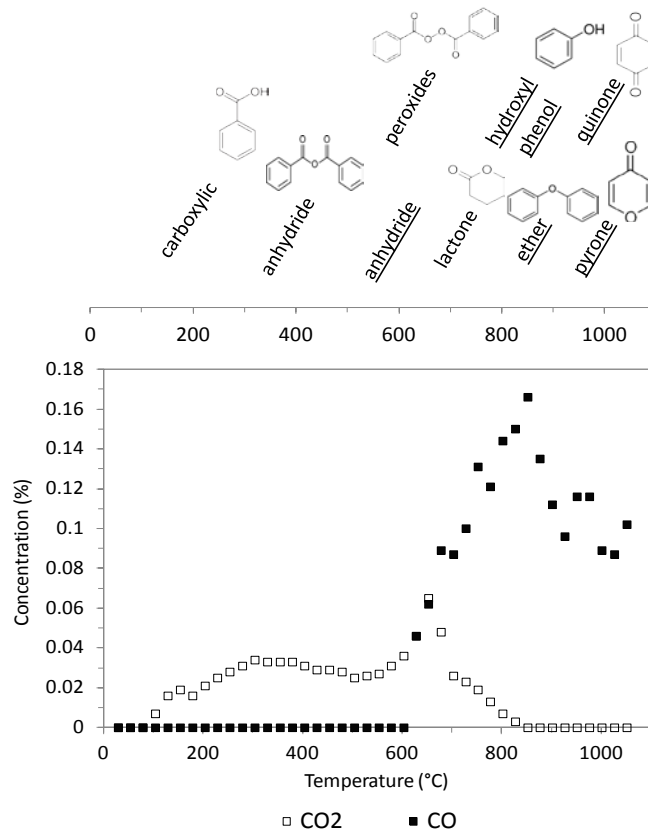


**Figure III-2: TPD analysis of the raw biochar (empty symbol CO<sub>2</sub>; full symbol CO) and corresponding temperature ranges of oxygenated functions (underlined text: functions desorbing into CO; not underlined text: functions desorbing into CO<sub>2</sub>)**

The total amount of the oxygen functions has been evaluated by integration of the area under the curve of the CO<sub>2</sub> and CO production (presented in Figure III-2). The total amount of O-containing groups at the raw biochar surface has been evaluated at 3.05 mmol/g<sub>char</sub> with a predominance of the basic functions (producing CO at high temperature when they desorb). Deconvolution of the TPD signal provides the distribution of the oxygenated functions which are presented in Figure III-3. It confirms the predominance of basic functions such as pyrone, quinone and ether functions. Carboxylic acids which are the strongest acids account for 12% of the oxygenated functions. The other O-containing groups present at the surface are mostly weak acids such as phenol, hydroxyl and lactone. Thus, various types of oxygenated functions are present at the surface of the raw biochar.

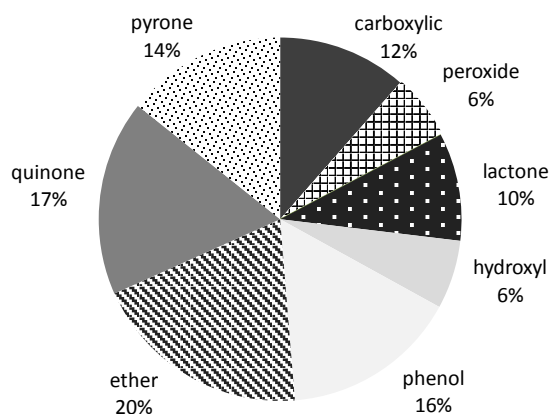


Figure III-3: Distribution of the oxygenated functions at the raw biochar surface

## 1.2. Mineral content of the raw biochar

From the proximate analysis, it has been shown that ash represents 3.8 wt% of the raw biochar. The X-ray fluorescence has been performed to determine the chemical composition of the inorganics part. Table III-2 shows the elemental composition of the minerals in the raw biochar. As it has been depicted in the literature review, the Alkali and Alkaline Earth Minerals (AAEMs) are the major components. Calcium and potassium have the highest contents representing 0.586 and 0.639 wt% of the total mass of the biochar respectively. Magnesium percentage is about three times lower with a concentration of 0.18 wt%. Silicon, chlorine, phosphorus, sulfur and iron were also detected with concentrations between (0.09 and 0.02 wt%).

Table III-2: Elementary composition of the main mineral components in the raw biochar (wt%; traces of Al and Zn  $\leq$  0.001 wt%; maximum standard deviation 0.04 wt%)

	Ca	K	Mg	Si	Cl	P	S	Fe
Raw biochar	0.586	0.639	0.182	0.090	0.080	0.078	0.051	0.021

In addition to X-ray fluorescence, X-ray diffraction analysis has been carried out to investigate the crystalline structures of the minerals present at the raw biochar surface. Figure III-4 shows the X-ray pattern of the raw biochar. The large and flat peak at 25° is characteristic from the peak of the plane (002) of the graphite carbon. The other peaks are related to carbonate or oxide forms of minerals. Orthorhombic calcium carbonates, monoclinic potassium carbonate and cubic magnesium oxide were identified.

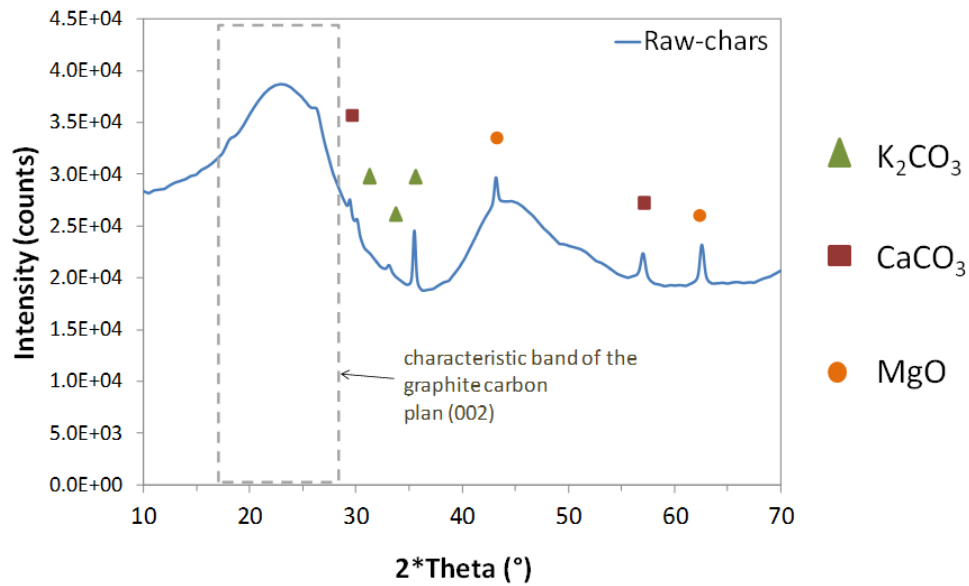


**Figure III-4: X-ray diffraction pattern of the raw biochar**

The dispersion of the mineral particles at the biochar surface has been investigated using ESEM. Figure III-5 presents some ESEM images taken at different locations of the surface to draw a mapping of the mineral dispersion. Indeed bright spots on Figure III-5 are minerals agglomerates. EDS analysis has been performed on minerals visible on Figure III-5.B and Figure III-5.C. The agglomerate visible on Figure III-5.B is complex and contained various minerals: Ca, K, Na, Si, Fe, Ni, Cl. The mineral on Figure III-5.C contains calcium and potassium. Thus, minerals in the raw biochar are randomly dispersed at the surface. Some regions are more concentrated in minerals than other ones. Complex agglomerates composed of several minerals are observed.

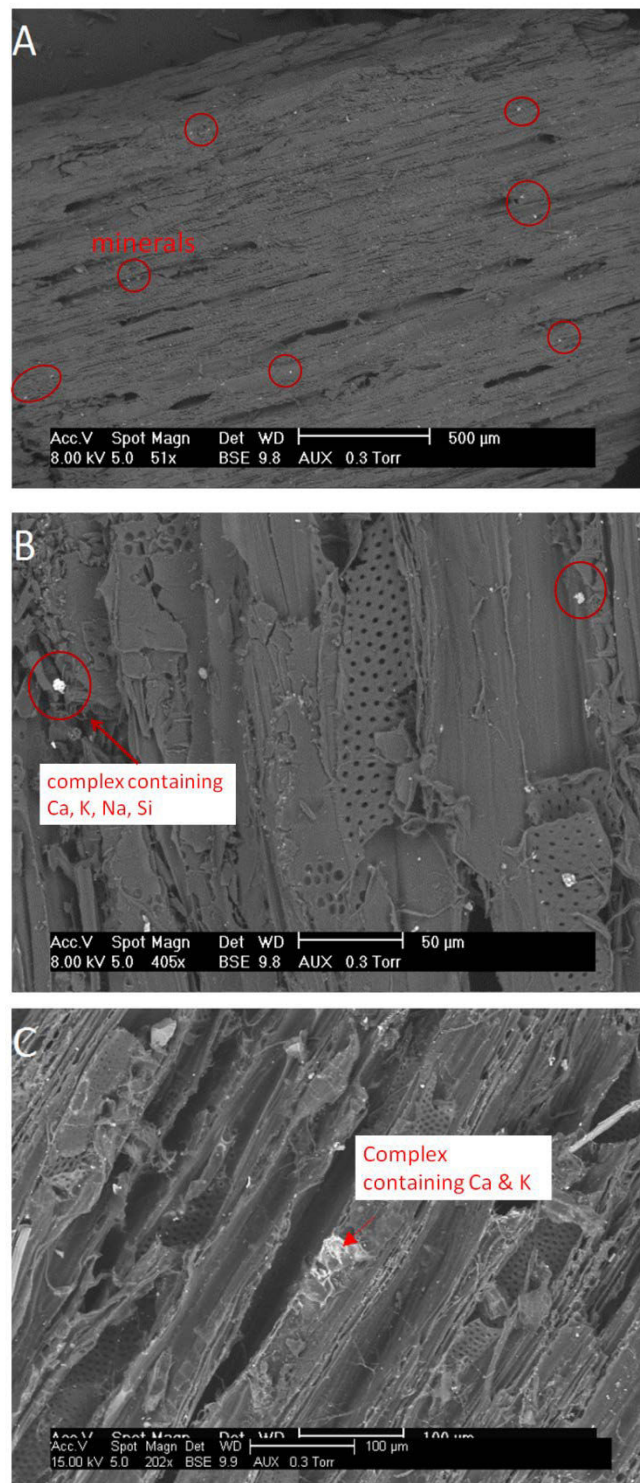


**Figure III-5: ESEM pictures of the minerals dispersion at different locations of the raw biochar surface and with different magnitudes**

### 1.3. Carbon matrix of the raw biochar

Raman analysis has been used to characterize the distribution of the different carbon structures in the raw biochar. In fact, it is possible to evaluate the type of carbon structure in a sample according to its Raman spectrum. For example, the spectrum of well-known ordered carbons: graphene-like sheets (only one layer of hexagonal close-packed lattice of carbons) and graphite (multiple layers) are presented in Figure III-6. In the first order region ( $800\text{-}2000\text{ cm}^{-1}$ ) only the sharp peak G (representative to the Graphite) is observable.

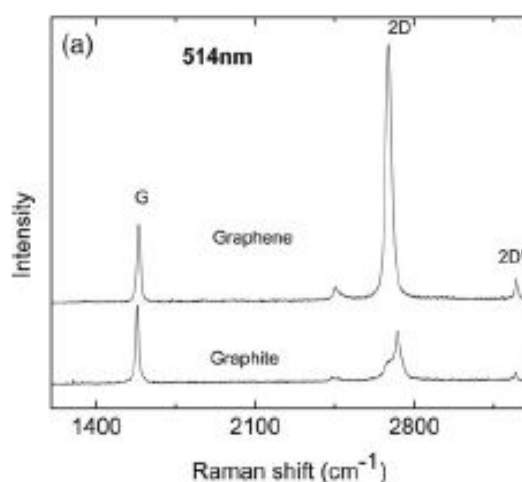


**Figure III-6: Illustration of Raman spectra of ordered structures: graphene and graphite [6]**

Average Raman spectrum of the raw biochar is displayed in Figure III-7 (representative of the ten points analysis at different locations of the surface). One can observe that the spectrum is broader than the one of the graphite. The G band is observable such as for graphite but other bands overlap. In fact, biochar are highly amorphous carbons. As described in the chapter II, the main structures in an amorphous carbon are:

- graphene-like cycles which represent the ordered features,
- disordered structures which can be of a different nature such as small and large aromatic rings cycles, aliphatic chains and lattice point defects in the graphite cycles.

Deconvolution of the Raman spectrum into 10 peaks gave insights into the relative amount of each structures described above. Figure III-7 is an illustration of the deconvolution of a Raman spectrum of the raw biochar in the region  $800\text{-}2000\text{ cm}^{-1}$ . Assignment of the ten peaks has been described in the section 3.2.1 of the chapter II. However, the discussion will be mainly focused on the evolution of the

four main families of structures which are: graphite (G band), large aromatic rings systems and “in-plane defects” (D band), small amorphous structures (Vr +VI +Gr bands) and aliphatic chains (S band) (you can refer to the table II.7 in the chapter II).

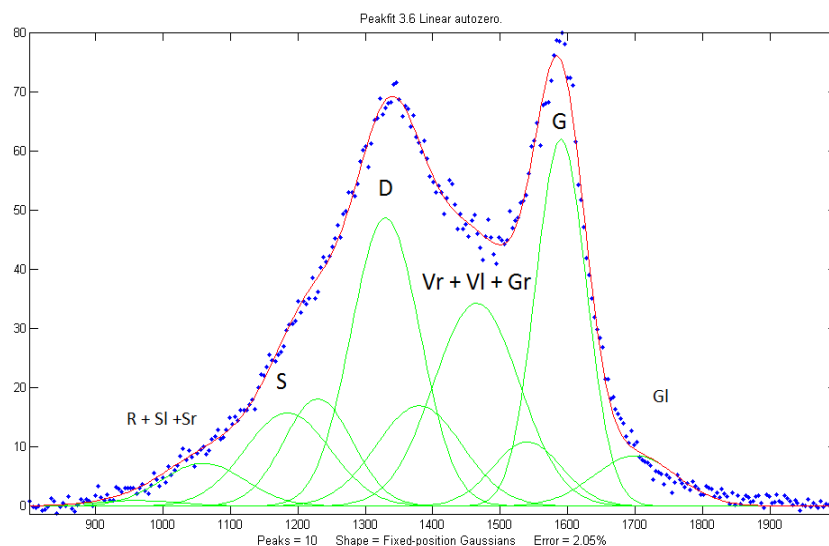


**Figure III-7: Illustration of a Raman spectrum deconvolution of the raw biochar into 10 peaks using the Matlab® software**

On Figure III-7, it is observable that the D and G bands are respectively at 1330 and 1590  $\text{cm}^{-1}$ . The G band is slightly higher than the D band revealing a relative high amount of graphene-like structures. However the intensity of the D band combined with the fact that the spectrum is broad highlight the high disorder in the biochar skeleton and the variety of defects nature.

Figure III-8 represents the distribution of the four main families of carbon structures, and graphitic structure, large and small aromatic rings are equally distributed with a percentage of 26, 25, 27% respectively. The aliphatic chains account for 9% of the carbon skeleton (see Figure III-8). In addition, three ratios were calculated to evaluate the predominance of rather the “in-plane” imperfections and large aromatic cycles over the graphite ( $I_D/I_G$  ratio), the small aromatic rings systems over the graphite ( $I_{(Vr+VI+Gr)}/I_G$  ratio) and the large aromatics systems over the small ones ( $I_D/I_{(Vr+VI+Gr)}$  ratio). These three ratio values are obviously closed to 1 for raw biochar (0.99, 1.11 and 0.97 respectively). However, these relative ratios will be of great interest for further modifications of biochar surfaces to better discuss the evolving of carbon structures.

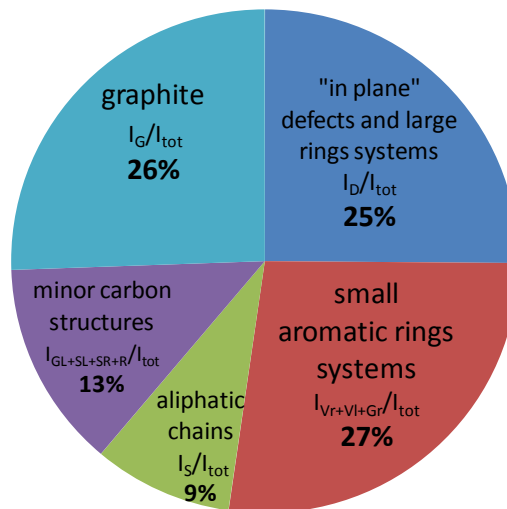


Figure III-8: Distribution of main carbon structures in the raw biochar

#### 1.4. Specific surface area and porosity of the raw biochar

The specific surface area and porosity have been determined from the adsorption isotherm of argon at the temperature of the liquid nitrogen (77 K). Argon has been chosen rather than nitrogen because its molecular overcrowding is the lowest. Figure III-9 shows the adsorption isotherm for the raw biochar. A drastic increase (up to 150 cm<sup>3</sup>/g STP) is observable at low relative pressure and a plateau is clearly visible from a relative pressure of 0.3. This adsorption isotherm is of type I (one can refer to the Figure.II.17 of the section 3.2.1 of the chapter II) which highlights that the raw biochar is microporous.

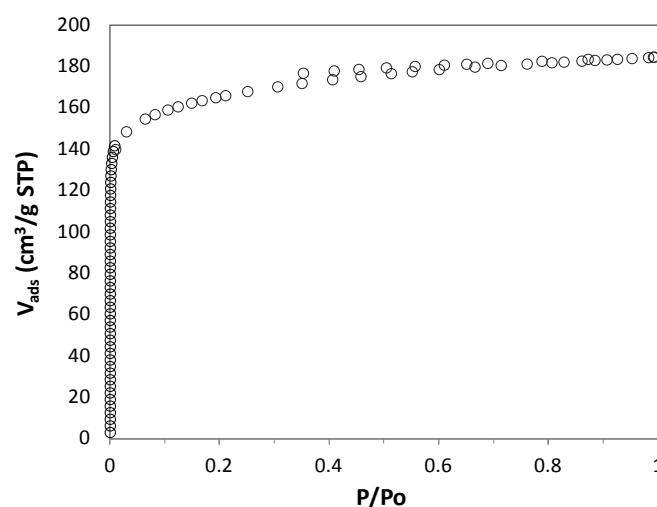


Figure III-9: Adsorption isotherm of argon on raw biochar (at 77 K after 20h of outgassing at 200°C)

As explained in the section 3.2 of the chapter II, in the case of a microporous material from which an adsorption isotherm of type I is observed, the Langmuir model is the most adapted to evaluate the specific surface area. To determine the total volume and average diameter size of the micropores the Horvath-Kawazoe model has been applied. Thus, the specific surface area and total pore volume have been evaluated at 662 m<sup>2</sup>/g and 0.22 cm<sup>3</sup>/g respectively. The specific surface area of the raw biochar is in a middle range of the carbonaceous materials specific surface areas: it is higher than some carbon blacks of which the specific surface areas are between 100 and 250 m<sup>2</sup>/g [7] but lower than some activated carbons which have specific surface areas of about 1000 m<sup>2</sup>/g [8]. This difference could be attributed to the different experimental conditions processed to obtain the biochar.

### **1.5. Partial conclusion on the physico-chemical properties of the raw biochar**

The raw biochar is an amorphous carbon of which related structures to graphene-like sheets are the major components. This biochar can be qualified of turbostratic carbon since these graphene-like sheets are far away from long range well ordered carbon sheets. They are sprinkled of “in-plane imperfections” such as vacancies or insertions of hetero atoms. Various amorphous structures are also present such as small and large aromatic rings systems or aliphatic chains. Regarding oxygenated functions, various types of O-containing groups have been identified such as strong acids groups (carboxylic acids), weak acids (lactones, peroxides, phenols, hydroxyls) and basic groups (ether, quinone or pyrone) which are the predominant functions at the surface. Ash is mainly composed of AAEMs such as calcium, potassium and magnesium. Silicon, phosphorous, sulfur and iron were found in a minor percentage. Three structures were detected by XRD: calcium and potassium carbonate and magnesium oxide. Regarding the textural properties, the adsorption isotherm is of type I which let one conclude that the biochar is highly microporous with a total micropore volume of 0.22 cm<sup>3</sup>/g and a specific surface area of 662 m<sup>2</sup>/g. Figure III-10 sums up the characterization of the physico-chemical properties of the raw biochar.

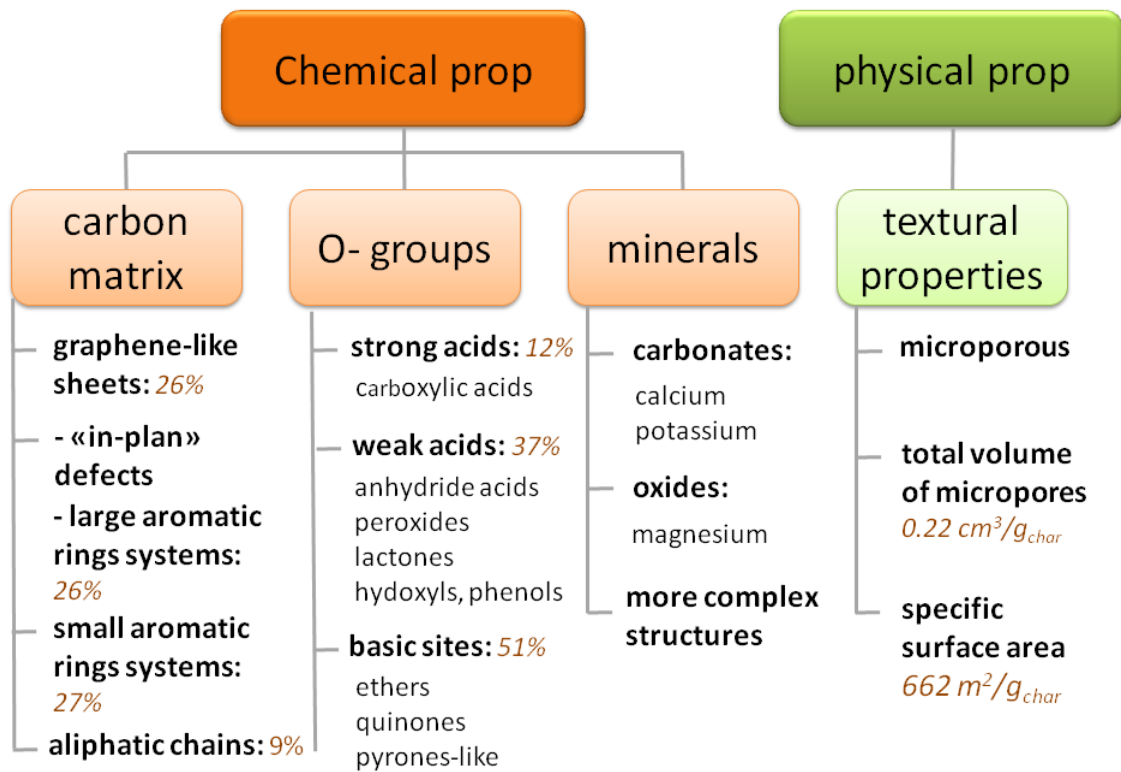
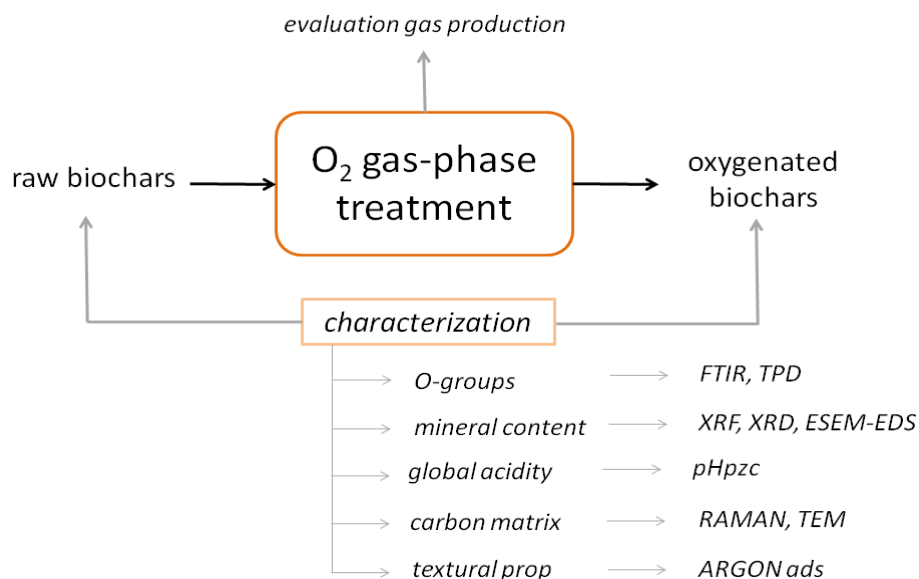


Figure III-10: Scheme to sum up the physico-chemical surface properties of the raw biochar

## 2. Oxygenated biochars surface properties [14]

This section presents the oxygenation by an  $O_2$  gas-phase treatment and its impact on the evolution of the biochars physico-chemical surface properties. The oxygenation was performed varying the time and the temperature to investigate their impact on the efficiency and selectivity of the oxygen chemisorption. At  $280^\circ\text{C}$ , biochars were oxygenated for 2, 4, 8 and 16 h. Then two temperatures of oxygenation were additionally tested for two hours of oxygenation at  $340$  and  $400^\circ\text{C}$ . The evolution of the gas production over the oxygenation is first discussed. Then, the characterization of the surface properties is presented in the following sequence: oxygenated functions, mineral content, carbon matrix and textural properties. Figure III-11 sums up the characterization which have been done during and post  $O_2$  gas-phase treatment.



**Figure III-11: Scheme of the characterizations which have been performed during and post O<sub>2</sub> gas-phase treatment**

The oxygenation process was composed of two steps: the heating was performed under pure nitrogen, then, after 20 minutes of stabilization at the reaction temperature, the O<sub>2</sub>/N<sub>2</sub> mixture was introduced. During the oxygenation, the output gas phase was sampled every 4 minutes and analyzed. The oxygenation was performed in those conditions to be able to identify and quantify the oxygenated functions which are not stable at the reaction temperature. Figure III-12 shows the gas production during the heating under inert gas and the gas production during the oxygenation at 400°C. One can observe on Figure III-12.A a CO<sub>2</sub> production which corresponds to the desorption of some carboxylic acid functions which are not stable at the oxygenation temperature [5]. The same trend was observed at the other oxygenation temperatures.

The second reason to heat the biochars under pure nitrogen was to desorb all the non-stable oxygenated groups (at the oxygenated temperature) before starting the oxygenation. Thus, by employing this method, we ensure that the gases analyzed in the second part of the oxygenation (when O<sub>2</sub> is introduced) are coming from the reaction. In fact, Figure III-12.B shows that CO<sub>2</sub> and CO are produced as soon as O<sub>2</sub> is introduced in the reactor at 400°C which highlights that combustion occurs. At 340°C, both CO<sub>2</sub> and CO were produced during the oxygenation but in a lower extent. At 280°C, only CO<sub>2</sub> was produced. Table III-3 compares the amount of CO<sub>2</sub> and CO produced during the oxygenation at the three oxygenation temperatures. The O<sub>2</sub> chemisorbed at the surface has been evaluated by TPD analysis in the following paragraph.

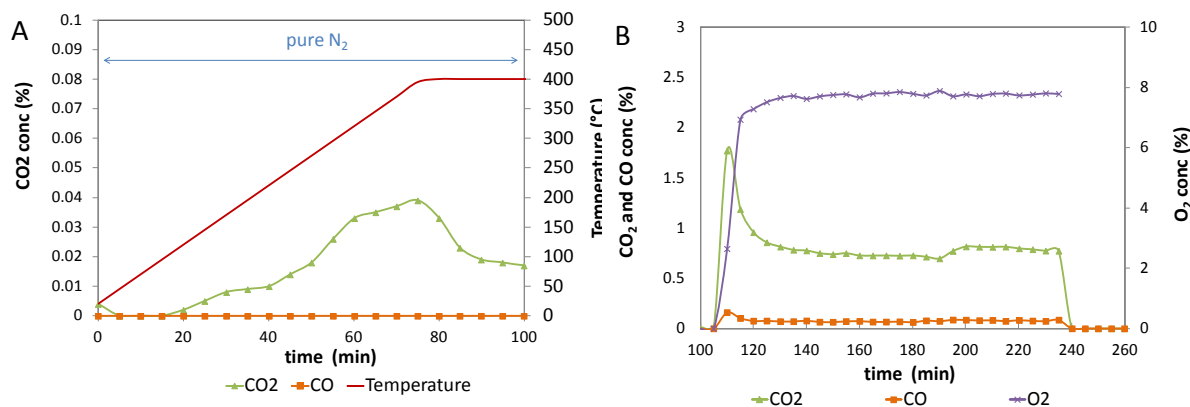


**Figure III-12: Gas production during the oxygenation at 400°C during 2h: (A) CO<sub>2</sub> gas production during the heating under inert atmosphere up to the oxygenation temperature; (B) CO<sub>2</sub> and CO productions during the oxygenation**

**Table III-3: CO<sub>2</sub> and CO produced (due to combustion) during the oxygenation of 100 mg of biochars for 2h at 280, 340 and 400°C**

	CO <sub>2</sub>	CO	total
	mol	mol	mol
Ox_2h_280°C	6.08e <sup>-5</sup>	-	6.08e <sup>-5</sup>
Ox_2h_340°C	1.33e <sup>-4</sup>	3.74e <sup>-4</sup>	5.07e <sup>-4</sup>
Ox_2h_400°C	1.83e <sup>-4</sup>	1.90e <sup>-3</sup>	2.08e <sup>-3</sup>

Out-put gas-phase analyses showed that some oxygenated functions were lost during the heating prior to the oxygenation since they were not stable. In addition, it highlighted that combustion was in competition with oxygen chemisorption. Above 500°C, only ash was recovered at the end of the process.

## 2.1. Oxygenated functions on the oxygenated biochars

To investigate the evolution of the O-containing groups at the biochars surface FTIR and TPD were performed. FTIR was first carried out to quickly evaluate if the oxygen chemisorption was successful. In fact, TPD analyses are more complicated to interpret since a deconvolution of the signal is required. Figure III-13 shows FTIR spectra for the raw and all the oxygenated biochars.

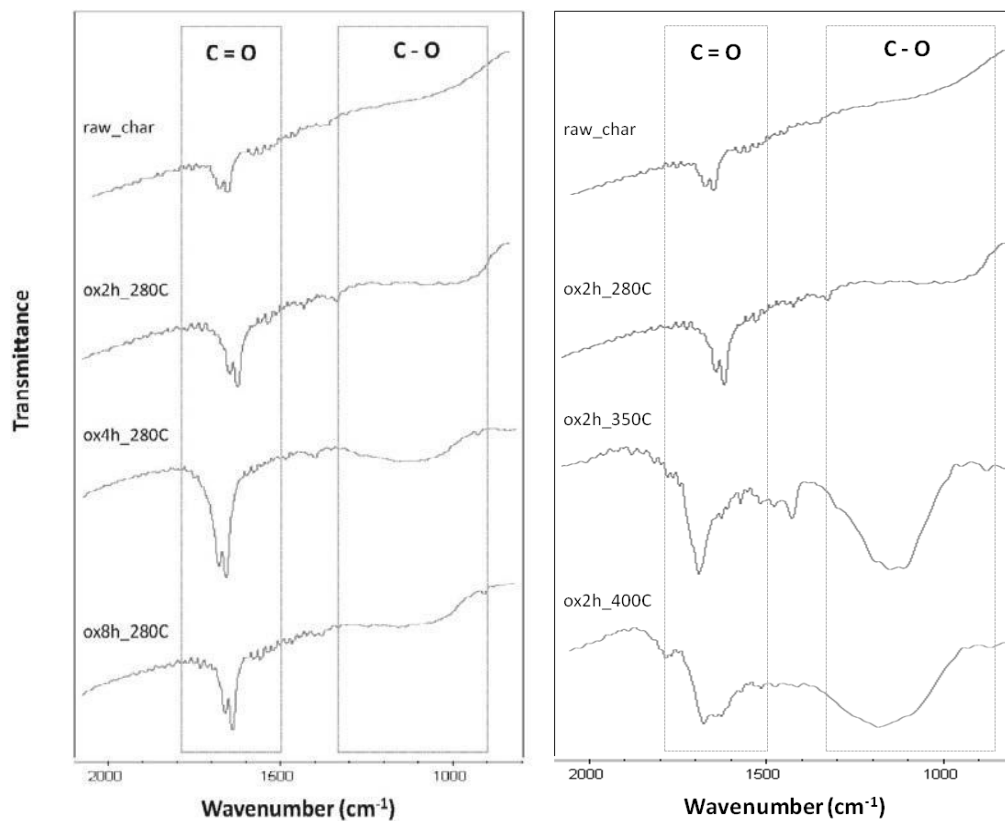


**Figure III-13: FTIR spectra of the raw and oxygenated biochars**

On Figure III-13, bands in the regions of 1600-1800 and 1000-1300  $\text{cm}^{-1}$  such as the raw biochar are visible for the oxygenated biochars. Regarding the biochars oxygenated at 280°C, shapes of the peaks are very similar to those of the raw biochar. However, they are more pronounced for the oxygenated biochars which highlights that the oxygen atoms chemisorbed at the surface. Several functions containing rather only C=O or C-O or both seem to have been enhanced. As for the biochars oxygenated at 340 and 400°C, drastic increase of the bands intensities correlated to the C-O linkages are observed. The band in the 1000-1300  $\text{cm}^{-1}$  became broader and more intense. The band at 1500-1700  $\text{cm}^{-1}$  is also becoming more intense and the two peaks clearly visible for the raw biochars are not well differentiated anymore due to the overlap of the peaks. FTIR spectra show that the oxygenation at 340 and 400°C should have been even more efficient than at 280°C. However FTIR did not provide quantitative information. In order to get better insights into the efficacy and the selectivity of the oxygen chemisorption TPD analyses have been performed. Time and temperature influences are discussed in two different sections.

### 2.1.1. Role of the oxygenation time

To confirm and get better insights into the evolution of the O-containing groups, TPD analyses have been performed on the raw biochar and biochars oxygenated at 280°C. Figure III-14 shows the TPD profiles.

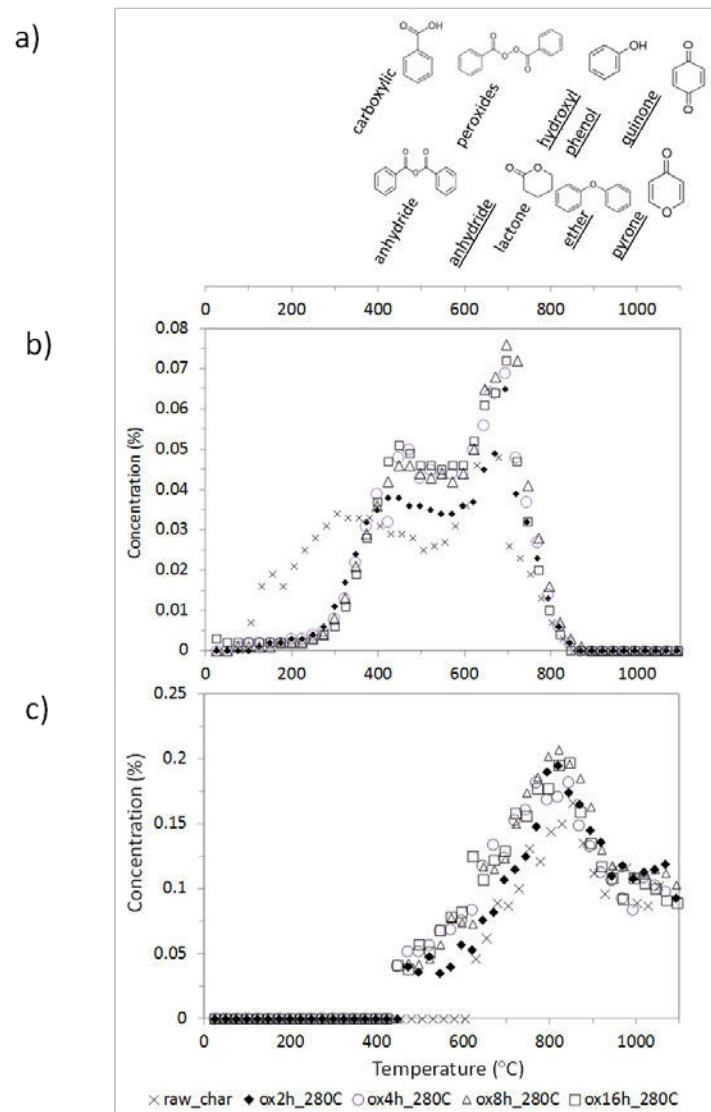


**Figure III-14: TPD profiles of the raw and oxygenated biochars at 280°C for 2, 4, 8 and 16h: a) peak assignment (underlined text: functions desorbing into CO; not underlined text: functions desorbing into CO<sub>2</sub>); b) CO<sub>2</sub> desorption; c) CO desorption**

On Figure III-14, one can observe that the productions of CO<sub>2</sub> and CO have been enhanced between 400 and 800°C. Above 800°C, the CO production is similar for all the samples. Below 400°C less CO<sub>2</sub> is produced for the oxygenated chars. It is explained by the loss of a part of the carboxylic acids which were not stable at 280°C. The CO<sub>2</sub> and CO productions are very similar for the biochars oxygenated at

4, 8 and 16h. These results highlight the saturation of the surface by oxygen atoms after four hours of treatment. Koch et al. [9] oxygenated coal char under a mixture of air and observed a saturation of the surface after an increase of the oxygenated functions as well.

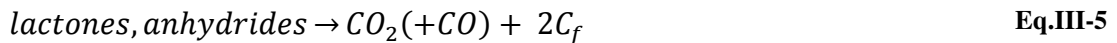
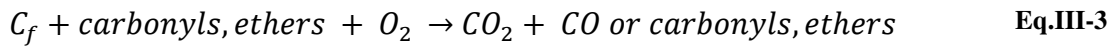
Table III-4 shows the CO<sub>2</sub>, CO, total production and CO<sub>2</sub>/CO ratio for the raw and oxygenated biochars calculated from the integration under the curve of the TPD profiles. The total amount of oxygenated groups has been increased by a factor of 1.5 after 4h of treatment and remains stable for biochars oxygenated during a longer time. Regarding the CO<sub>2</sub>/CO ratio it decreases from 0.42 to 0.30 after two hours of treatment and remains stable for longer times. This is due to the loss of carboxylic acids.

**Table III-4: Comparison of CO<sub>2</sub>, CO and total production for raw and functionalized chars oxygenated at 280°C for different duration times (from the integration of the area under the curve of Figure III-14)**

	CO <sub>2</sub>	CO	total	CO <sub>2</sub> /CO
	mmol/g <sub>char</sub>			
raw_char	0.9	2.1	3.0	0.42
ox_2h	0.8	3.0	3.8	0.28
ox_4h	1.0	3.3	4.3	0.30
ox_8h	1.0	3.5	4.5	0.29
ox_16h	1.0	3.4	4.4	0.29

Deconvolution of the TPD analyses provides quantitative information about the oxygenated groups. In decreasing order, hydroxyl, peroxide, phenol, ether and lactone concentrations have been increased 2.6, 2.1, 1.7, 1.3 and 1.2 times while quinone and pyrone amounts were not impacted. Anhydride function was formed during the oxygenation. In fact, the raw biochar did not seem to contain this type of functions according to FTIR analyses. In addition, literature claimed that anhydride groups desorbed in both CO<sub>2</sub> and CO at 450°C and 580°C respectively. CO production only started above 620°C during the TPD of the raw biochar. One can observe that the CO light-off temperature is lower for the oxygenated biochars rather than for the raw biochar. The formation of anhydride function could be explained by the following scheme proposed by Figueiredo et al. [10]:





This scheme indicates that ether, quinone, pyrone and phenol functions already present at the biochars surface (in a higher concentration than the other functions) reacted with the oxygen molecules during the oxygenation to form more complex oxygenated functions such as anhydride or lactone groups leading to a new equilibrium at the biochars surface.

Figure III-15 compares the distribution of the oxygenated functions at the raw biochar surface and biochars oxygenated during 8 hours. After the oxygenation, the difference of concentration between the O-containing groups has been diminished at the biochars surface. Even if ether and phenol remain the main functions (18%), the other O-containing groups represent about 10 mol% respectively of the overall oxygen content. However, the amount of carboxylic acids which were not stable at the oxygenation temperature has been drastically diminished.

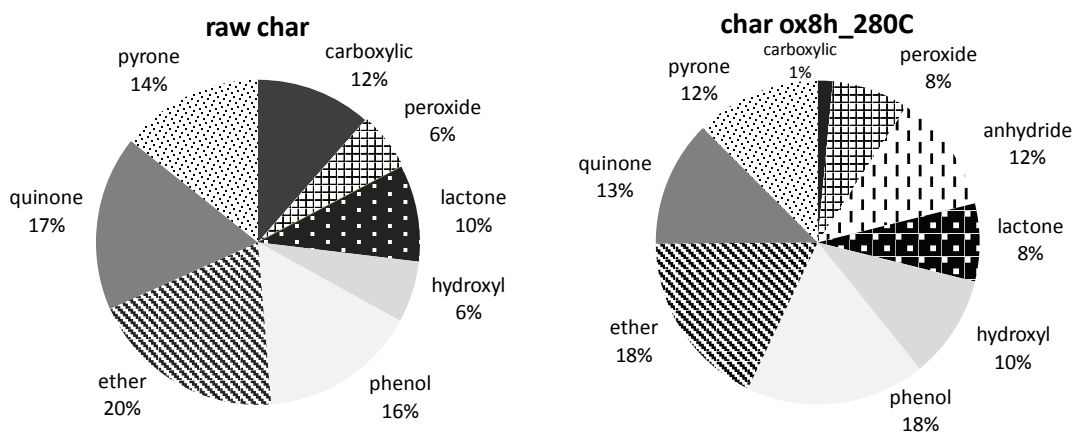
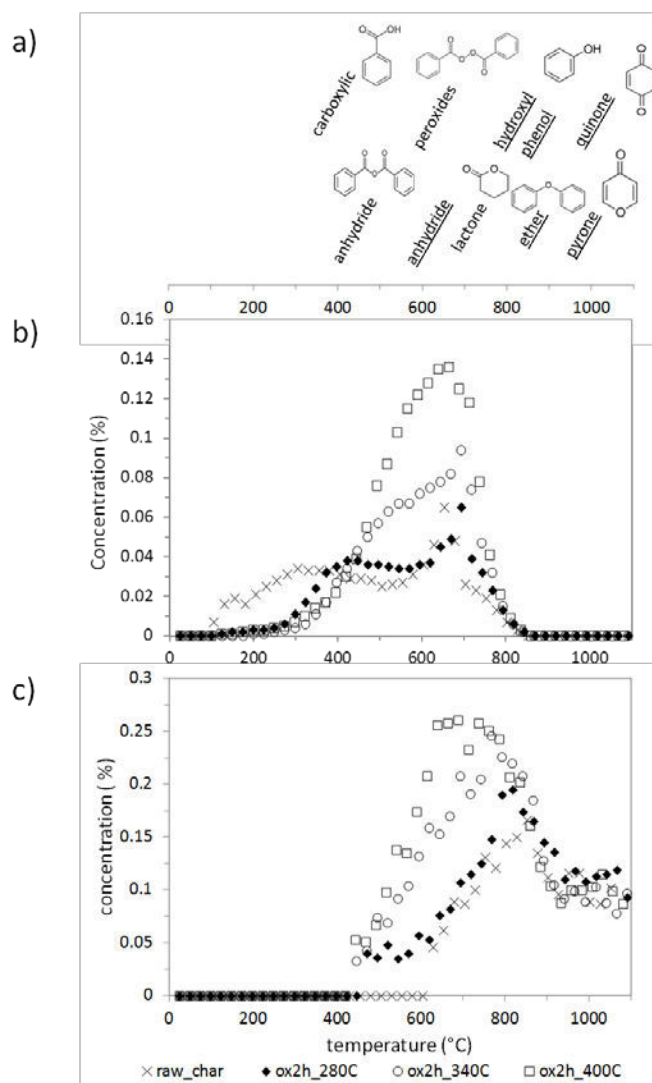


Figure III-15: Distribution of the oxygenated functions (mol%) for the raw biochar (left) and biochar oxygenated at 280°C during 8h (right)

### 2.1.2. Role of the oxygenation temperature

In the literature review (see section 2.1.3 of the chapter 1) temperature was observed to play an important role in the oxygen chemisorption. In addition, Figure III-13 highlighted drastic increased in intensity of bands related to C-O and C=O bondings in FTIR spectra. Figure III-16 presents the TPD profiles of the same oxygenated biochars.



**Figure III-16: TPD profiles of the biochars oxygenated at 280, 340 and 400°C for 2h: a) peak assignment (underlined text: functions desorbing into CO; not underlined text: functions desorbing into CO<sub>2</sub>); b) CO<sub>2</sub> desorption; c) CO desorption**

The first observation is that the shapes of the CO<sub>2</sub> and CO production curves are different for the oxygenated chars from those of the raw biochar. In particular the CO<sub>2</sub> curve in which two peaks were noticeable for the raw biochar (at 420 and 700°C) became a single peak more intense centered at 650°C. The same observation is applicable for the CO curve production. At 340 and 400°C, the same functions seemed to have been enhanced. However the efficiency was higher at 400°C. Deconvolution of the TPD curves were performed to provide quantitative results of the different O-containing groups. Hydroxyl, peroxide, phenol and lactone were enhanced 7.0, 4.6, 2.1 and 2.0 times respectively after the oxygenation at 400°C. Carboxylic acids were totally removed while quinone and pyrone-like structures concentrations remain stable.

Figure III-17 presents the distribution of the O-containing groups at the surface of the biochars oxygenated at 340 and 400°C. Hydroxyl and phenol functions become the main functions (21%) which is coherent with the drastic increase of the band at 1000-1300  $\text{cm}^{-1}$  in the FTIR spectrum. The other O-containing groups are almost equally distributed and represent about 10 mol% respectively of the total amount of the oxygen content.

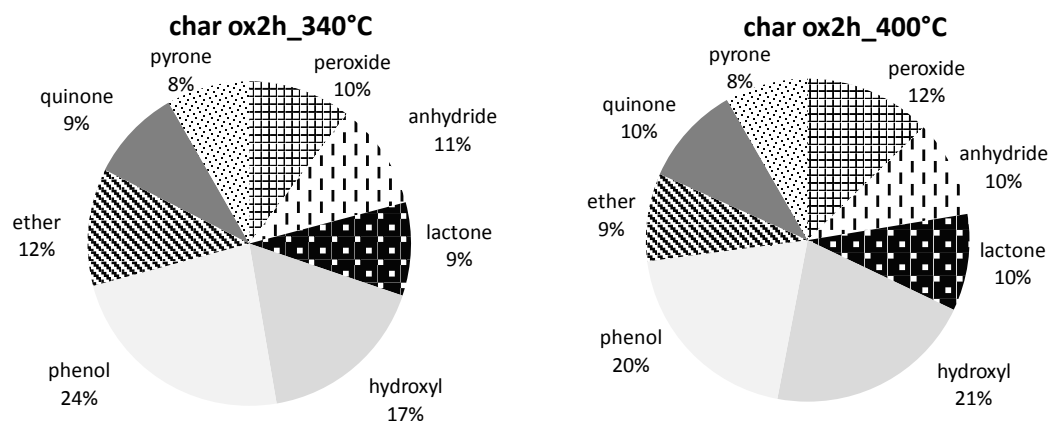


**Figure III-17: Distribution of the oxygenated functions (mol%) for the biochars oxygenated at 340°C (left) and 400°C (right)**

Table III-5 provides the  $\text{CO}_2$ , CO, total productions and  $\text{CO}_2/\text{CO}$  ratio for the raw biochar and oxygenated biochars at the different temperatures. Oxygenations at 340 and 400°C were effectively more efficient than at 280°C since the total oxygen content at the biochars surface has been increased 1.9 and 2.1 times respectively instead of 1.3. The  $\text{CO}_2/\text{CO}$  ratio has also been decreased after the three oxygenations compared to the initial ratio for the raw biochars. It reached 0.26, 0.29 and 0.37 at 280, 340 and 400°C respectively instead of 0.42 for the raw biochar. This should be due, in part, to the carboxylic functions removal. The drastic increase of phenolic functions should also contribute to decrease the  $\text{CO}_2/\text{CO}$  ratio since they desorbed into CO. However, the enhancement of the lactone and anhydride functions concentrations (desorbing into  $\text{CO}_2$ ) should have counterbalanced the loss of carboxylic functions at 340 and 400°C. In fact, the ratio value is higher at these two temperatures than at 280°C.

**Table III-5: Comparison of CO<sub>2</sub>, CO and total production of raw\_char, ox2h\_280C, ox2h\_340C, ox2h\_400C obtained (from the integration of the area under the curve of Figure III-16)**

	tot CO <sub>2</sub>	tot CO	total	CO <sub>2</sub> /CO
	mmol/g <sub>char</sub>			-
<b>raw_char</b>	0.9	2.1	3.0	0.42
<b>ox2h_280C</b>	0.8	3.0	3.8	0.26
<b>ox2h_340C</b>	1.2	4.0	5.2	0.29
<b>ox2h_400C</b>	1.7	4.6	6.3	0.37

Thus, FTIR and TPD analyses highlighted that the oxygenations under the different operating conditions increased the oxygen content and lead to characterize the type and amount of oxygenated functions present on the raw and oxygenated biochars.

## 2.2. Mineral content of the oxygenated biochars

The minerals functions at the raw biochar surface were characterized in the section 1.2. X-ray diffraction pattern highlighted that the minerals were in carbonate and oxide forms (oxidized form). Thus, the oxygenation process should not have drastically modified their oxidation state. However, in order to verify that no rearrangements happened during the functionalization, XRD analysis has been performed on one of the oxygenated biochars. Figure III-18 shows the comparison of the X-ray patterns of the raw biochars and the biochars oxygenated 2h at 340°C. Magnesium oxide, calcium and potassium carbonates which were identified in the raw biochar are still present in the oxygenated biochar. The two X-ray diffraction patterns are similar which should indicate that minerals structures were not drastically impacted by the oxygenation process.

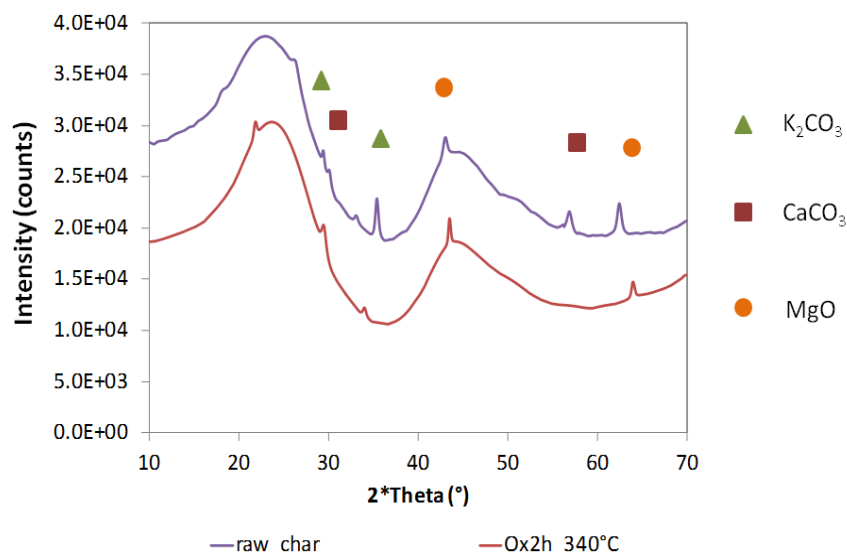


**Figure III-18: X-ray patterns of the oxygenated biochars**

Thus, an XRD analysis has been performed to verify that the minerals structures were not impacted by the oxygenation treatment. X-ray pattern confirmed that the minerals forms were not modified during the treatment. This observation should be applicable for all oxygenated biochars. Regarding the dispersion of the minerals particles at the surface, the temperature was not enough high during the oxygenation treatment to consider that minerals could have migrate (see discussion about the Tammann temperature in the section 2.2.2 of the Chapter. I).

### 2.3. Carbon matrix of the oxygenated biochars

The carbon structures distribution in the raw biochar has been presented in the section 1.3. It was highlighted that graphene-like sheets, small and large amorphous aromatic rings and imperfections in the matrix were equally distributed and represented about 25% of the carbon skeleton.

According to the section 2.1, the oxygenations under the different operating conditions increased the oxygen concentration at the biochars surface due to chemisorption of oxygen atom which should have modified, at least locally, the carbon matrix structure. In addition, combustion and desorption of non-stable carboxylic acids should have impact the carbon structure as well. Oxygen chemisorption, O-groups desorption and combustion could have differently impacted the carbon skeleton structure. Chemisorption could happen at the edges of the carbon rings or on the unsaturated carbons of the aliphatic chains. It could also lead to deeper interaction with insertion in

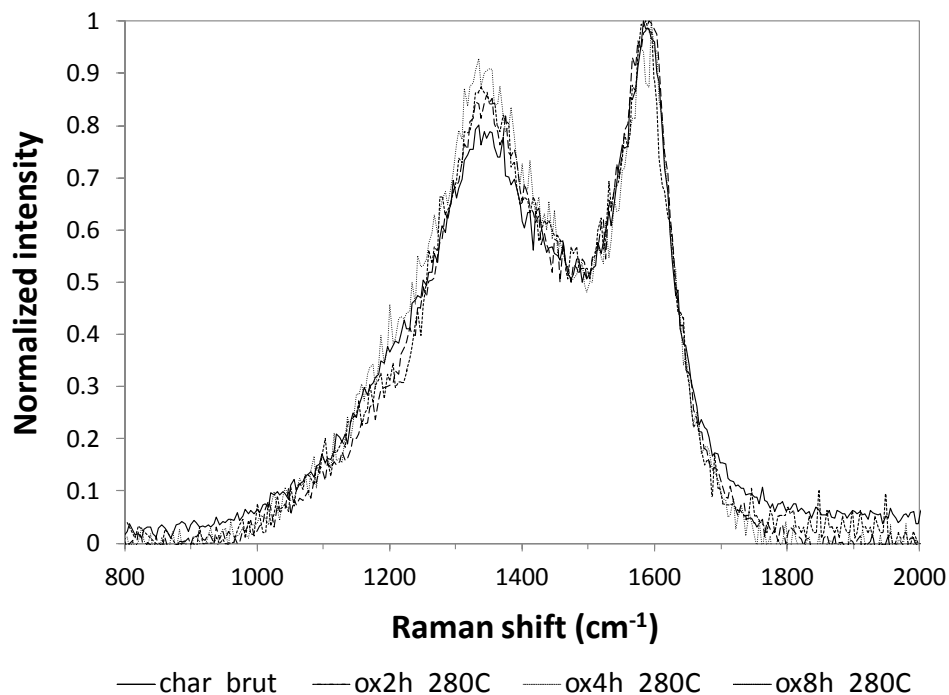
the carbon rings. Desorption of O-containing groups and combustion should have created vacancies in the carbon matrix. Combination of these three reactions should increase the disorder in the carbon matrix and thus modify the carbon structures distribution.

A publication from Keown et al. [11] investigated the oxidation at 400°C in air of biochars from pyrolysis of sugarcane trash. They performed Raman analysis in order to get better insights into the carbon/O<sub>2</sub> interaction during gasification. They stated that small aromatic rings systems and aliphatic chains were preferentially consumed during the oxygenation. Another study proposed by Vautard et al. [12] characterized carbon materials after various oxidation treatments. They investigated the oxidation of carbon fibers to correlate the loss of the mechanical properties with the generation of surface defects. Results have shown that the oxygenation process enhanced disorder in the structure due to an erosion of the crystallites and create edge plans.

In this study Raman spectroscopy has been performed on biochars oxygenated at 280°C during 2, 4 and 8h and on those oxygenated at 340 and 400°C for 2h. Results are presented and discussed following the same plan as the previous section. We first investigated the oxygenation time impact and then the temperature influence on the evolution of the carbon skeleton. In addition, Transmission Electron Microscopy (TEM) has been performed on some samples (raw biochar, ox2h\_280C, ox8h\_280C and ox2h\_400C) to get better insights into the nanostructure.

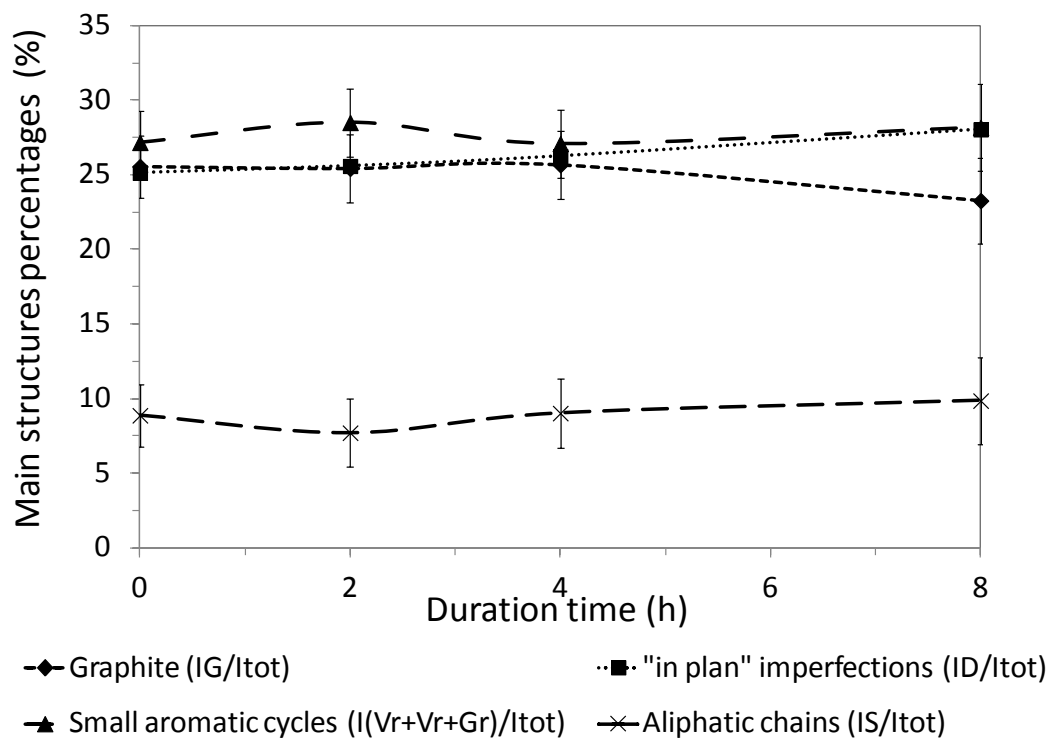
### 2.3.1. ***Impact of the oxygenation time***

Figure III-19 presents the Raman spectra of the raw and oxygenated biochars (they have been normalized by the G peak intensity). Shape of the four spectra is very similar suggesting that the carbon skeleton was not drastically impacted. However one can notice that the D band intensity increases slightly over the process.



**Figure III-19: Raman spectra of the raw biochars and the biochars oxygenated at 280°C for 2, 4 and 8h**

Deconvolution of the spectra gave insights into the evolution of the carbon matrix composition over time at 280°C. Figure III-20 shows the distribution of the graphene-like sheets, small aromatic rings systems, aliphatic chains and large aromatic rings for the raw and oxygenated biochars. These ratios have been calculated from the band area obtained after deconvolution. Results of the curve fitting confirmed the trend observed on the raw Raman spectra. No significant changes were observed in the distribution of the structures. However after 8 hours of treatment, an increase of the amount of large and small aromatic rings systems ( $I_D/I_{tot}$  and  $I_{VR+VL+GR}/I_{tot}$ ) and a decrease of the graphene-like structures ( $I_G/I_{tot}$ ) were observed. In fact graphene-like structures, small aromatic rings and large aromatic rings + imperfections in the graphene-like structures represented 26, 27 and 25 % of the raw biochars surface respectively. The new distribution in the biochars oxygenated at 280°C was 22, 28 and 28% respectively. Regarding the aliphatic chains, their amount remained stable (around 10%) during the process.



**Figure III-20: Evolution of the main carbon structures over the oxygenation at 280°C**

Carbon structure modifications should be correlated to the variation of the oxygen content during the oxygenation. We observed that at 280°C, after 4 hours of treatment the surface became saturated by oxygen atoms. Anhydride, ether and lactone which are functions with an oxygen atom inserted in a carbon ring have been formed. Thus, oxygen atom have entered more deeply in the carbon rings and were inserted into graphene-like sheets and amorphous structures increasing the amount of "in-plane imperfections" ( $I_D/I_{tot}$ ) and aromatic rings systems ( $I_{VR+VL+GR}/I_{tot}$ ). We also noticed that most of the carboxylic acids were removed. This should have created vacancies in the carbon matrix and enhancing the point defects in the graphene-like structure ( $I_D/I_{tot}$ ). Thus, oxygenation at 280°C did not drastically modify the biochars carbon skeleton. However, chemisorption of oxygen atoms combined with carboxylic acids desorption and combustion led to more disordered biochars. Disorder corresponding to "in-plane" defects and amorphous content were both enhanced. Ratios to compare disordered and ordered structures were calculated to evaluate the predominance of the former ones. The ratio  $I_D/I_G$  which represents "in-plane" imperfections + large aromatic rings systems over graphene-like sheets was calculated. It slightly increased from 0.99 in the raw biochars to 1.21 in the biochars oxygenated during 8 hours at 280°C. A second ratio which compare small aromatic rings system and graphene-like sheets ( $I_{VR+VL+GR}/I_G$ ) was calculated. It increased by 10% after the longest oxygenation time at 280°C.

### 2.3.2. Impact of the oxygenation temperature

Figure III-21 presents the Raman spectra of the raw biochars and biochars oxygenated for 2 hours at 280, 340 and 400°C. On the contrary to the spectra of the biochars oxygenated at 280°C, those of the biochars obtained at 340 and 400°C are significantly different from the one of the raw biochars. A first observation is an inversion in the highest peak. For the raw biochars the G band is the highest one, for the biochars oxygenated at 340 and 400°C the D band was intensified. In addition, structures from which Raman bands surround the D and G peaks were drastically diminished. These structures gather the aliphatic chains, the small aromatic rings cycles and the minor structures such as the  $sp^3$ - $sp^2$  rich functions. Deconvolution of these spectra led to quantify the modification in the carbon matrix.

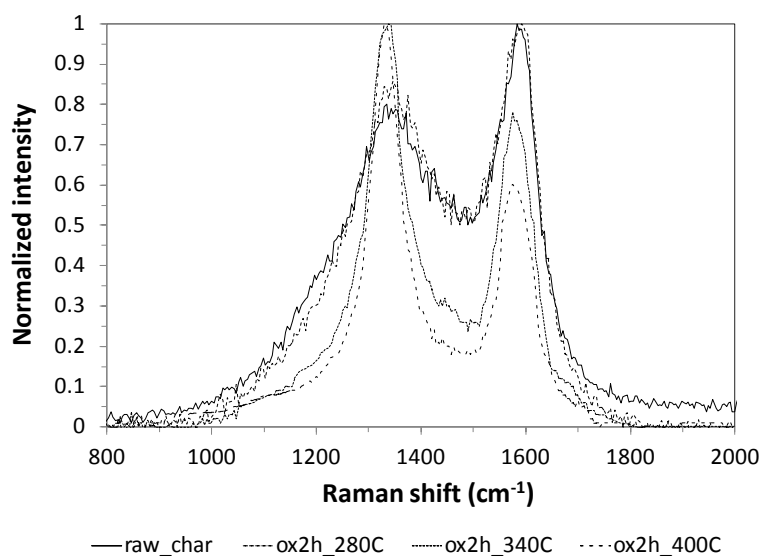


**Figure III-21: Raman spectra of the raw biochars and biochars oxygenated for 2h at 280, 340 and 400°C**

Figure III-22 presents the evolution of the main carbon structures for the raw and oxygenated biochars at different temperatures. At 340°C, significant modifications were already noticeable. However, they were even more important at 400°C. As expected, the small aromatic rings systems amount was decreased by 40 % after the oxygenation at 400°C. The aliphatic chains amount was also diminished, it represents 75% of the initial value. The large aromatic rings systems and point defects in the graphene-like structures (D band) represented about 25% in the raw biochars structure, they reached 39% after two hours at 400°C. The same ratios as in the previous paragraph were calculated to evaluate the part of a type of disorder in the carbon skeleton. The “in-plane” imperfections and large aromatic rings over graphitic structures ratio has been increased by 42% after the oxygenation

at the highest temperature. The small amorphous rings systems over graphite and aliphatic chains over graphite ratios were decreased by 49% and 20% respectively.

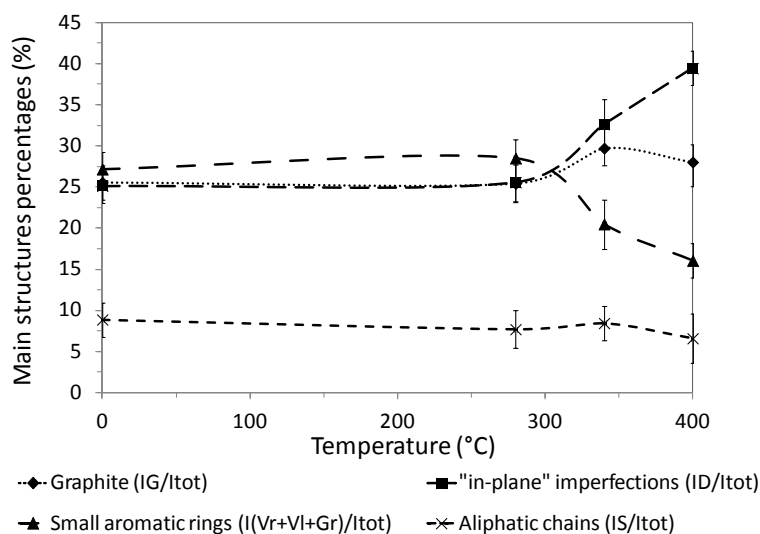


**Figure III-22: Evolution of the main carbon structures for raw biochar and biochars oxygenated at 280, 340 and 400°C for 2 hours**

These observations are in accordance with the results obtained by Keown et al. [11] and briefly presented at the beginning of the paragraph 2.3. Oxygenation at 340 and 400°C led to a significant decrease of amorphous content leading to biochars more ordered but with more scattered imperfections in the graphene-like structures. According to the literature review, the reactivity of carbon materials is due to the presence of disordered structures in the matrix. Thus, these biochars should be more reactive. However, the concentrations of the different types of disordered structures have been also modified. In fact, the biochars oxygenated at high temperature (340 and 400°C) contained higher amount of “in-plane” defects than the raw biochar. On the contrary, they lost small amorphous rings systems. The comparison of these different biochars for methane cracking will give insights into the reactivity of these two types of disordered structures.

### 2.3.3. *Impact on the nanostructure*

Transmission Electron Microscopy analyses (TEM) have been performed on some biochars (raw, ox2h\_280C, ox8h\_280C and ox2h\_400C) to go further in the investigation of the carbon matrix nanostructure. Figure III-23 shows bright field TEM images of the different samples and the corresponding Selected Area Electron Diffraction (SAED) patterns. The four biochars presented a

porous microstructure with a non-uniform density and lamellar edges. Diffuse ring SAED patterns have been observed for the four biochars, which is indicative of a short-ordered isotropic structure. The SAED ring dimensions correspond to inter-reticular distances of 0.35-0.40 nm, 0.21 nm and 0.12 nm and these reflections may originate respectively from the (002), (101), and (110) + (112) atomic planes of a graphitic structure.

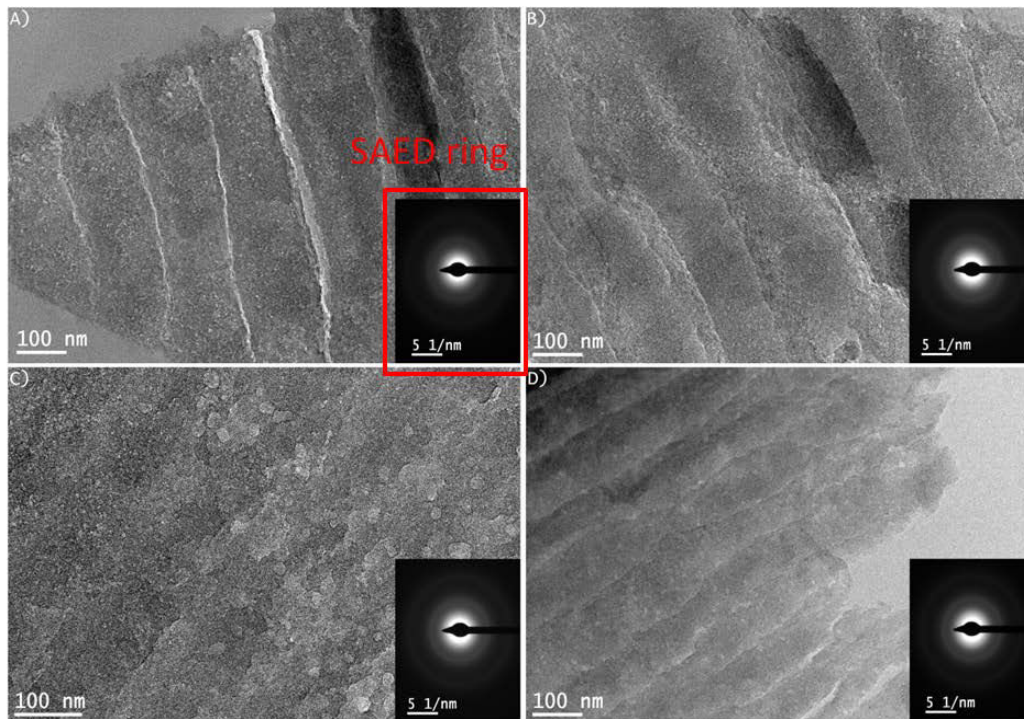


**Figure III-23: Bright field TEM images of samples (A) raw\_char, (B) ox2h\_280C, (C) ox2h\_400C, and (D) ox8h\_280C. Insets: corresponding SAED patterns.**

High Resolution Transmission Electron Microscopy (HRTEM) images are presented in Figure III-24 and reveal the graphene layer short-order isotropic organization. These images reinforce the observations from the Raman analyses, the biochars are turbostratic structures. This means that graphene sheets are ordered in a short-range but numerous defects can be observed in the structure. This is traduced by a prevalence of the D band (representing the disordered structure in the graphite) in the Raman spectrum. One can observe on Figure III-24 that graphene sheets are displayed in all the directions and especially in the raw biochar structure (Figure III-24.A). In the three oxygenated biochars, at some locations (close to the edges; red square in Figure III-24), some concentric graphene-like sheets organization can be observed. This should be the result of restructuration of the carbon matrix during the oxygenation process.

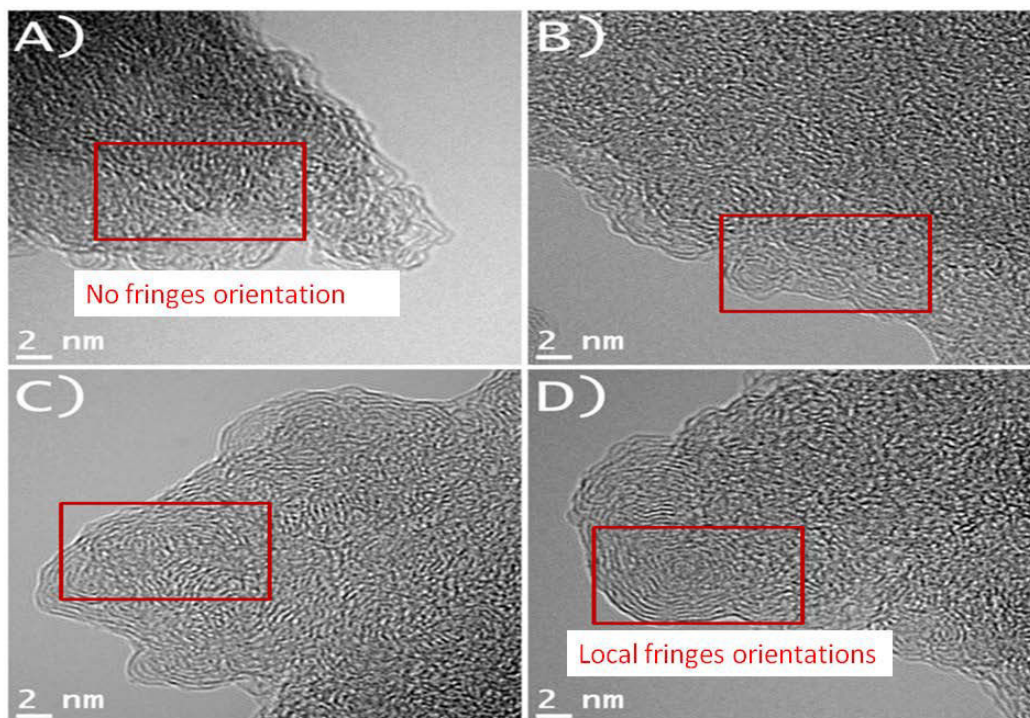


**Figure III-24: HRTEM images of samples raw\_char (A), ox2h\_280C (B), ox2h\_400C (C), and ox8h\_280C**

Thus, Raman spectroscopy and TEM images confirmed that the biochars were turbostratic structures. The oxygenation tended to increase the disorder in the carbon matrix. At high temperature, aliphatic chains and amorphous rings were burnt which let a carbon structure containing more graphene-like sheets (but sprinkled of defects).

#### 2.4. Specific surface area and porosity of the oxygenated biochars

The specific surface area and porosity of the oxygenated biochars have been determined with the same method as for the raw biochars. Adsorption isotherms for all the oxygenated biochars were of type I. Thus, the oxygenation did not change the type of porosity, oxygenated biochars remained microporous. Table III-6 shows the specific surface area, the total volume and the average diameter of micropores for the raw and oxygenated biochars. At 280°C, the specific surface area as well as the total volume of pores tended to decrease with the time of oxygenation. These observations emphasize that, oxygen atoms chemisorbed at the surface, filled the pores over the process which could have blocked the pores or make them collapse. Saturation of the surface by oxygen atoms after 4 hours of treatment (discussed in the section 2.1.1) had consequences on the evolution of the

specific surface area and total volume of micropores. The specific surface area was decreased by 6.0, 12.7% and the total pores volume by 1.4 and 5.4% at 2 and 4h. At 8h of treatment, the specific surface area and the total micropore volume were close to the ones of the biochars oxygenated 4h (see Table III-6). At 340 and 400°C, the evolutions of the specific surface area and the total volume of micropores were different from the observations at 280°C. In fact, both have been significantly increased. The specific surface area was enhanced by 22 and 30% at 340 and 400°C respectively. The volume of micropores gained 37.9 and 47.4% at 340 and 400°C.

This difference in the evolution of the textural properties at 280, 340 and 400°C could be explained by the competition between combustion and chemisorption of oxygen at the surface. In fact, the numbers of moles of oxygen atoms chemisorbed at the surface during the oxygenation (calculated from the TPD analyses) and the moles of carbon burned (due to combustion) have been compared for the different operating conditions. At 280°C the chemisorption and combustion were in the same order of magnitude (about  $1.0 \times 10^{-5}$  mol). However at 340 and 400°C the moles of carbon burned were ten times higher than the moles of oxygen chemisorbed at the surface which should explain the significant increase of the surface area.

**Table III-6: Specific surface area, total volume and average diameter of micropores for the raw and oxygenated biochars**

Biochars	Specific surface area (m <sup>2</sup> /g)	Total volume of micropores (cm <sup>3</sup> /g)	Average diameter of pores (Å)
Raw biochars	662	0.22	5
Ox_2h_280°C	622	0.22	8
Ox_4h_280°C	578	0.21	6
Ox_8h_280°C	564	0.21	6
Ox_2h_340°C	808	0.30	8
Ox_2h_400°C	859	0.32	8

## 2.5. Partial conclusion on the physico-chemical properties of the oxygenated biochars

An O<sub>2</sub> gas-phase treatment was performed on biochars for various times and temperatures. During the process chemisorption of oxygen atoms at the biochars surface occurs while carbons were burnt due to combustion. Both oxygen chemisorption and combustion are time and temperature-dependent.

Regarding the oxygen chemisorption, the longer the oxygenation time, the higher the oxygen atoms chemisorbed at the surface until reaching the saturation of the surface. The temperature had a higher impact than the oxygenation time since the oxygen atom chemisorption was increased by a factor 2.1 at 400°C and was only enhanced 1.5 after 8h at 280°C. Whatever the operating conditions, weak acids functions such as anhydride, lactone and phenol groups were mostly added at the surface. Carboxylic acids which are the strongest acids functions were removed during the oxygenation since they were not stable. However, basic O-containing groups such as quinone and pyrone-like groups remained at the surface.

The O<sub>2</sub> gas-phase treatment impacted the other physico-chemical properties of the biochars. Distribution of the carbon structures and textural properties were both modified after the oxygenation. The predominance of oxygen chemisorption or combustion will dictate the evolution of the carbon structure and textural properties. At 280°C we have seen that the oxygen chemisorption and combustion were in the same order of magnitude. The carbon structures distribution remained quite unchanged after the oxygenation at 280°C. Above 8h of treatment a slight increase of the small amorphous rings content was noticed certainly due to the insertion of O-atoms in the rings. In addition, the level of graphitization was slightly decreased due to the increase of the “in-plane” defects which could be due to the O-atoms insertion or vacancy due to carbon removal. The textural properties were slightly modified. The volume of pores and specific surface areas were decreased by 14 and 6% respectively.

At 340 and 400°C, the combustion yield was 10 times higher than the oxygen chemisorption which leads to significant modifications of the carbon matrix and textural properties. Combustion burned almost all the amorphous content such as small aromatic rings and aliphatic chains. The carbon structure distribution was then completely modified. The amount of graphene-like sheet concentration increased but the large aromatic rings systems and “in-plane” defects were the predominant functions. Regarding the porosity and specific surface area, they were drastically

enhanced. The micropore volume of the biochars oxygenated at 400°C was twice higher than the one of the raw biochars which also increased by 30 % the specific surface area.

Hence the oxygenation process, whatever the operating conditions, increased the oxygenated groups concentration at the biochars surface and enhanced the weak acids formation without removing the basic functions. These functionalized biochars could be utilized for NO<sub>x</sub> reduction (with NH<sub>3</sub>) [13]. The other physico-chemical properties were also modified. However, according to the predominance of the combustion on the oxygen chemisorption, the evolution of the carbon matrix and textural properties were not the same. Thus, the biochars oxygenated at 280°C and those treated at 340 or 400°C have finally physico-chemical properties significantly different. An illustration of the physico-chemical properties modifications over the oxygenation process for different times and temperatures is presented on Figure III-25 and Figure III-26. The study of the catalytic methane cracking for the different oxygenated biochars should give precious insights into the physico-chemical properties which enhance the reactivity. This point will be discussed in the chapter IV. This work on the oxygenated biochars characterization has been published in the journal Fuel [14].

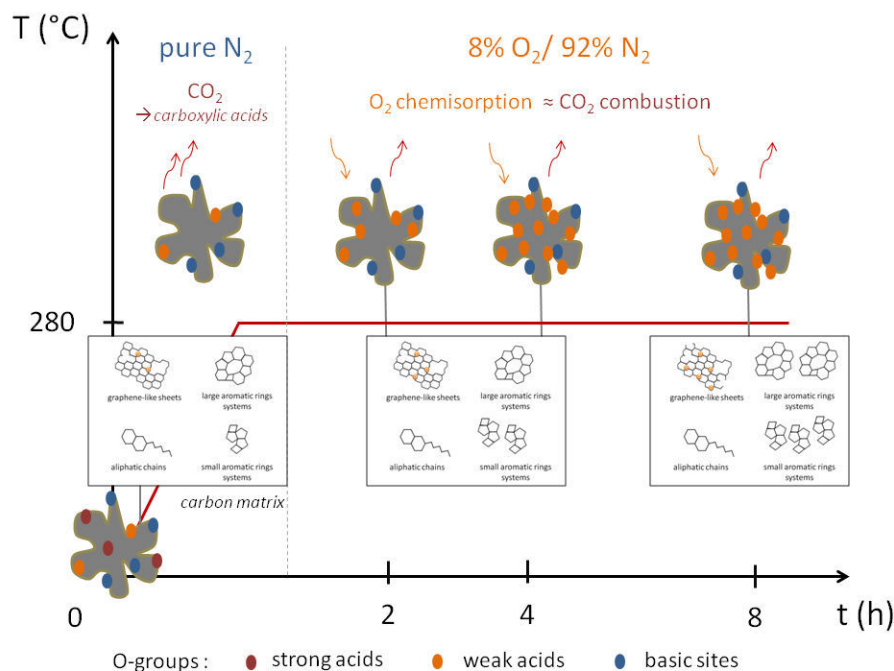


**Figure III-25: Illustration of the physico-chemical properties modifications over the oxygenation process for different times at 280°C**

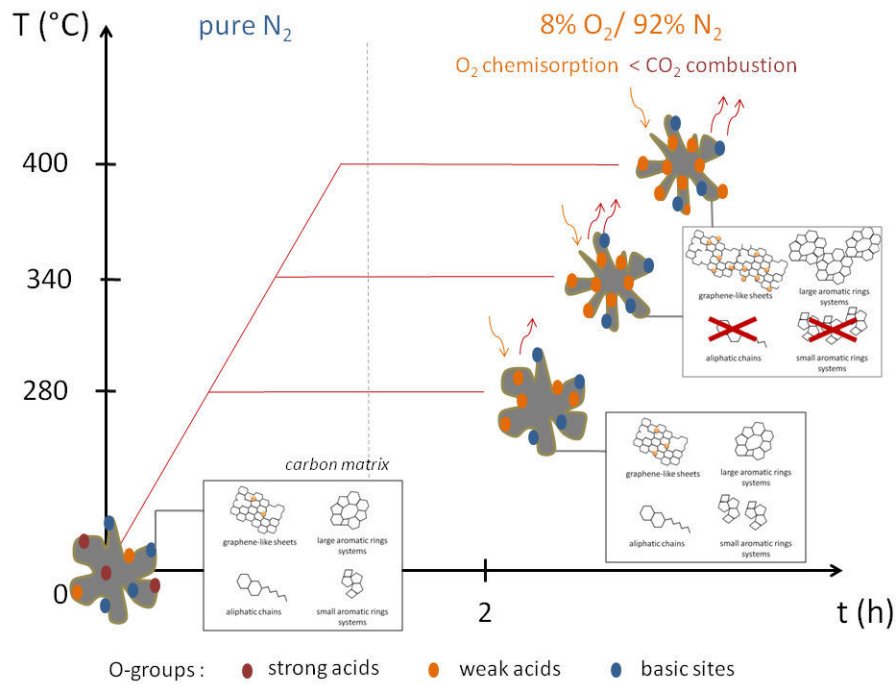


**Figure III-26: Illustration of the physico-chemical properties modifications over the oxygenation process at different temperatures**

### 3. Impregnated biochars surface properties

The second functionalization treatment consisted in a wet impregnation of biochars into a nitrate salts solution. It has been carried out to enhance rather the calcium or potassium content at the biochars surface. The impregnation has been performed on the raw poplar wood prior to the pyro-gasification. Then, the impregnated wood chips were gasified under the same conditions as for the raw poplar wood. Figure III-27 sums up the method which was followed to obtain the mineral impregnated biochars. Even if the discussion will be centered on the characterization of the biochars surface properties - since this information is required to understand the biochars reactivity towards methane cracking- characterizations of the poplar wood impregnated minerals content are first briefly presented. In a second time, the overall characterization of the impregnated biochars surface properties is discussed in the following sequence:

- O-groups
- mineral content
- carbon matrix
- specific surface area and porosity

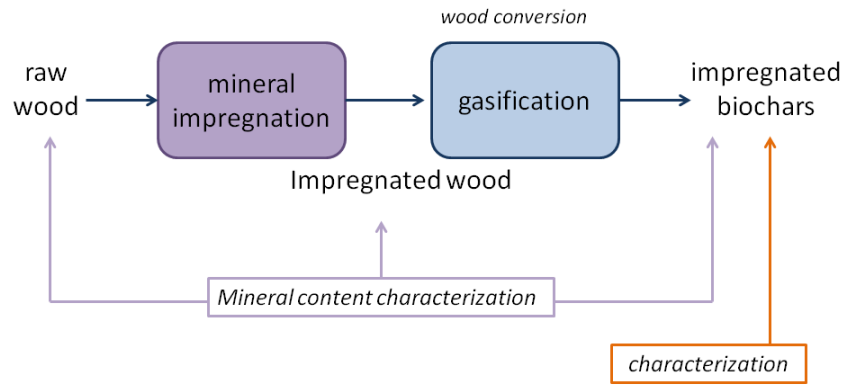


**Figure III-27: Scheme of the different characterizations which have been performed on the raw, mineral impregnated woods and mineral impregnated biochars**

Prior to characterization of the impregnated biochars, mineral content of the raw and impregnated poplar woods have been carried out. The elemental analysis of the ash was performed by X-ray fluorescence and presented in the Table III-7. As it was depicted in the literature, AAEMs (calcium, potassium and magnesium) were the major components of the raw poplar wood [15]. Silicon also took part in the major element with an equal percentage as the potassium. Minor components such as chlorine, phosphorus, sulfur and iron were detected. Post-impregnation calcium content is increased four times in the Ca-wood. As far as the potassium is concerned in the K-wood, its concentration was enhanced ten times. Calcium and potassium are present in an equivalent percentage in the Ca+K-wood (around 0.5%). Regarding the impact of the impregnation on the other elements, the amount of magnesium was halved in the three impregnated woods. The same trend is observable for the silicon and the chlorine in the K-wood, the sulfur and the phosphorus in the Ca-wood and K-wood. This decrease of the other minerals should be due to their leaching during the impregnation.

**Table III-7: Elemental composition of the major minerals in the poplar wood (wt%; traces of Na, Al, Cr, Mn, Zn, Ni, Cu  $\leq$  0.001 wt%; maximum standard deviation 0.04 wt%)**

	Ca	K	Mg	Si	Cl	P	S	Fe
<b>Raw wood</b>	0.25	0.13	0.11	0.13	0.01	0.06	0.02	<0.01
<b>Ca-wood</b>	1.08	0.02	0.04	0.08	0.01	0.03	0.01	<0.01
<b>K-wood</b>		1.25	0.04	0.06	0.01	0.02	0.01	<0.01
<b>Ca+K-wood</b>	0.55	0.42	0.05	0.09	0.08	0.03	0.02	<0.01

ESEM/EDS analyses have been performed at different locations of the raw and impregnated woods surfaces. Approximately the same quantity of bright spots (characteristic of the minerals) can be observed on the surfaces of the impregnated woods than on the surface of the raw biochars. However, EDS analyses performed on a zone of the surface presented in Figure III-28 highlighted the presence of calcium on the Ca-wood surface and the presence of potassium on the K-wood surface.

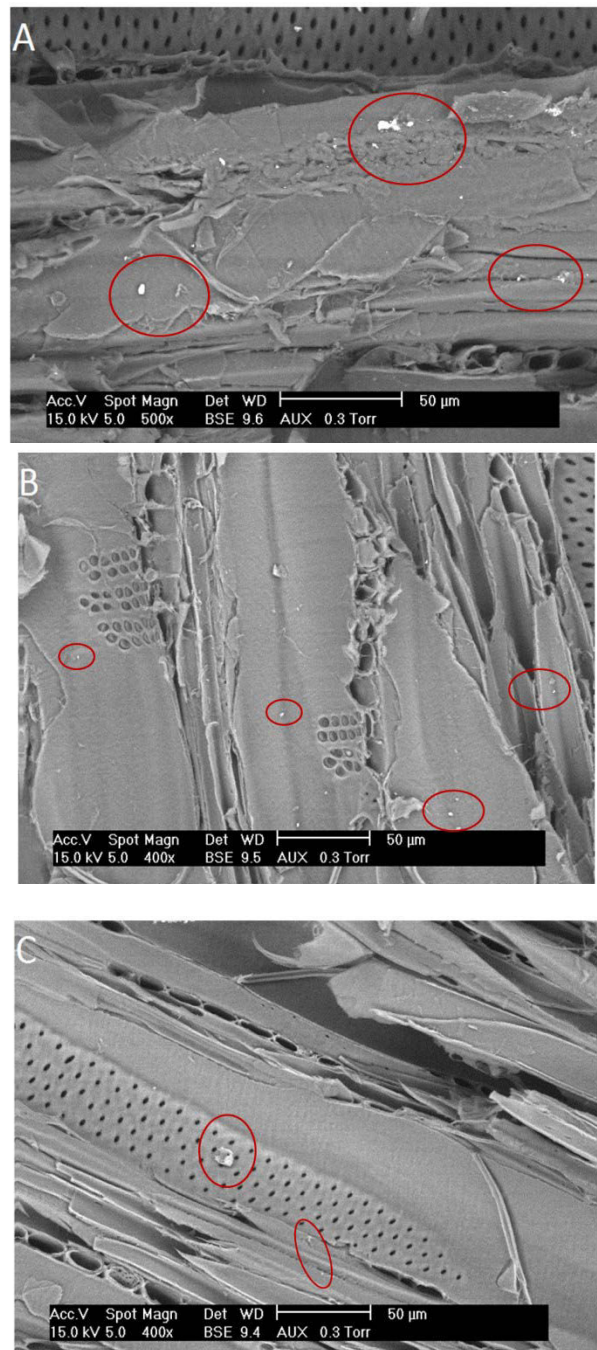


Figure III-28: ESEM pictures of the: (A) raw poplar wood, (B) Ca-wood, (C) K-wood

This paragraph was dedicated to a brief characterization of the impregnated woods mineral content. However the core of the topic is the characterization of the impregnated biochars physico-chemical properties. This is the topic of the four following sections, which approached the characterization of the oxygen functions, the mineral content, the carbon structure and the textural properties of the mineral impregnated biochars.

### 3.1. Oxygenated functions of the impregnated biochars

The investigation of the O-containing groups at the mineral impregnated biochars surface revealed to be highly tricky. In fact, from the XRD results minerals are mainly in carbonates or oxides forms which mean a high content of inorganic oxygen. Common techniques employed to study the O-containing groups cannot be employed in this case. FTIR spectroscopy cannot give information about the nature of the O-containing groups since the bands corresponding to the C=O ( $\approx 1500-1700\text{ cm}^{-1}$ ) and C-O ( $\approx 1000-1300\text{ cm}^{-1}$ ) will disappear into the one of the potassium and calcium carbonates. In fact Yuh et al. [16] presented FTIR spectrum of  $\text{K}_2\text{CO}_3$  in a study dealing with the potassium impact on the coal chars gasification. Sharp bands are visible at 1650 and 1300  $\text{cm}^{-1}$  corresponding to potassium carbonate. El-Sheik et al. [17] showed that strong and broad bands related to calcium carbonate were detected at 1054 and 1400-1440  $\text{cm}^{-1}$ . Regarding TPD analysis, the  $\text{CO}_2$  and CO desorption could be rather from the O-containing groups or the carbonates/oxides functions. Huttinger et al. [18] recorded the  $\text{CO}_2$  and CO desorption during the heating of carbon samples impregnated with various potassium structures. They emphasize that both  $\text{CO}_2$  and CO were desorbed at different stages of the heating according to the potassium structure. Hence, this analysis will not give reliable results to get insights into the nature and amount of oxygenated groups at the carbon surface.

According to the literature, oxygen functions at the biochars surface should have been active sites for the minerals insertion on the carbon matrix [19]. Kannan et al. [20] stated that phenol and carboxylic acids groups were active sites for ion exchange and adhesion of minerals. Thus, oxygenated functions at the biochars surface should not be the same anymore after the mineral impregnation. Even if we are not able to investigate the nature and amount of oxygenated functions at the impregnated biochars surface, we keep in mind that oxygenated function could be present at the surface but should be in minor concentration than the oxides and carbonates functions.

### 3.2. Mineral content of the impregnated biochars

Three characteristics of the minerals content in biochars were investigated: their elemental composition, their structure and their dispersion. X-ray fluorescence (XRF), X-ray diffraction (XRD) and Scanning Electron Microscopy (SEM) analyses were performed for the characterization.

#### 3.2.1. *Elemental composition of the ash*

Table III-8 presents the elemental composition of the minerals from the raw and impregnated biochars determined by X-ray fluorescence. For the three impregnated biochars, the targeted mineral(s) (Ca and K) to increase were significantly enhanced. The amount of calcium in the Ca-chars was 8 times higher than in the raw biochar. The same trend is observed for the potassium content in the K-chars. In the Ca+K-chars, an equal content of calcium and potassium was found which were five times higher than in the raw biochars. An interesting fact is that the content of potassium in the Ca-chars is smaller than in the raw chars (decreased by a factor 6) which should be due to a leaching during the impregnation. This is also observable for the calcium content in the K-chars but in a lesser extent (it was only halved). Regarding magnesium, its concentration is globally the same in the four chars (about 0.1 wt%). The silicon content in the raw biochars, the K-chars and Ca+K-chars is in the same concentration as magnesium (about 0.1 wt%). However, in the Ca-chars the amount is significantly higher (0.326 wt%). Regarding chlorine, phosphorus and sulfur, their amounts remained the same for the four biochars and were lower than the AAEMs ones. The iron content is different according to the biochars: in the raw biochars its content is of 0.021 wt%. It was decreased in the Ca-chars and Ca+K-chars (0.008 and 0.005 wt%) and increased three times in the K-chars (0.057 wt%).

**Table III-8: Elemental composition of the major minerals in the biochars (wt%) (traces of Na, Al, Cr, Mn, Zn, Ni, Cu ≤ 0.001 wt%; maximum standard deviation 0.04 wt%)**

	Ca	K	Mg	Si	Al	Cl	P	S	Fe	Ash
<b>Raw chars</b>	0.59	0.64	0.18	0.09	traces	0.08	0.08	0.05	0.02	3.82
<b>Ca-chars</b>	5.06	0.10	0.12	0.33	0.007	0.08	0.05	0.04	0.01	17.60
<b>K-chars</b>	0.25	4.97	0.14	0.12	traces	0.09	0.05	0.04	0.06	20.86
<b>Ca+Kchars</b>	2.15	2.24	0.12	0.07	traces	0.05	0.06	0.05	0.01	18.02

Complementary EDS analyses (presented in the following section) have been performed at different locations of the biochars surface to compare and verify the results obtained by X-ray fluorescence analyses.

### 3.2.2. Dispersion and crystalline structure of the minerals onto the biochars surface

Minerals dispersion at the biochars surface has been studied by coupling ESEM and EDS analyses. In addition, XRD analyses have been carried out to provide insights into the crystalline structure of the minerals and get a better understanding on the mineral embedding in the carbon matrix.

#### 3.2.2.1. Ca-chars

Figure III-29 presents ESEM pictures of the Ca-chars at different locations and different magnitudes. On each picture one can notice the good dispersion of the calcium particles. Different shapes of structures are visible. For example, on Figure III-29.B a zone has been analyzed by EDS which highlights that these structures seem to be calcium silicate. On Figure III-29.C a rectangular-shape particle is observable. The EDS analysis of this structure indicates the presence of calcium. It should be a calcium carbonate or oxide particle.

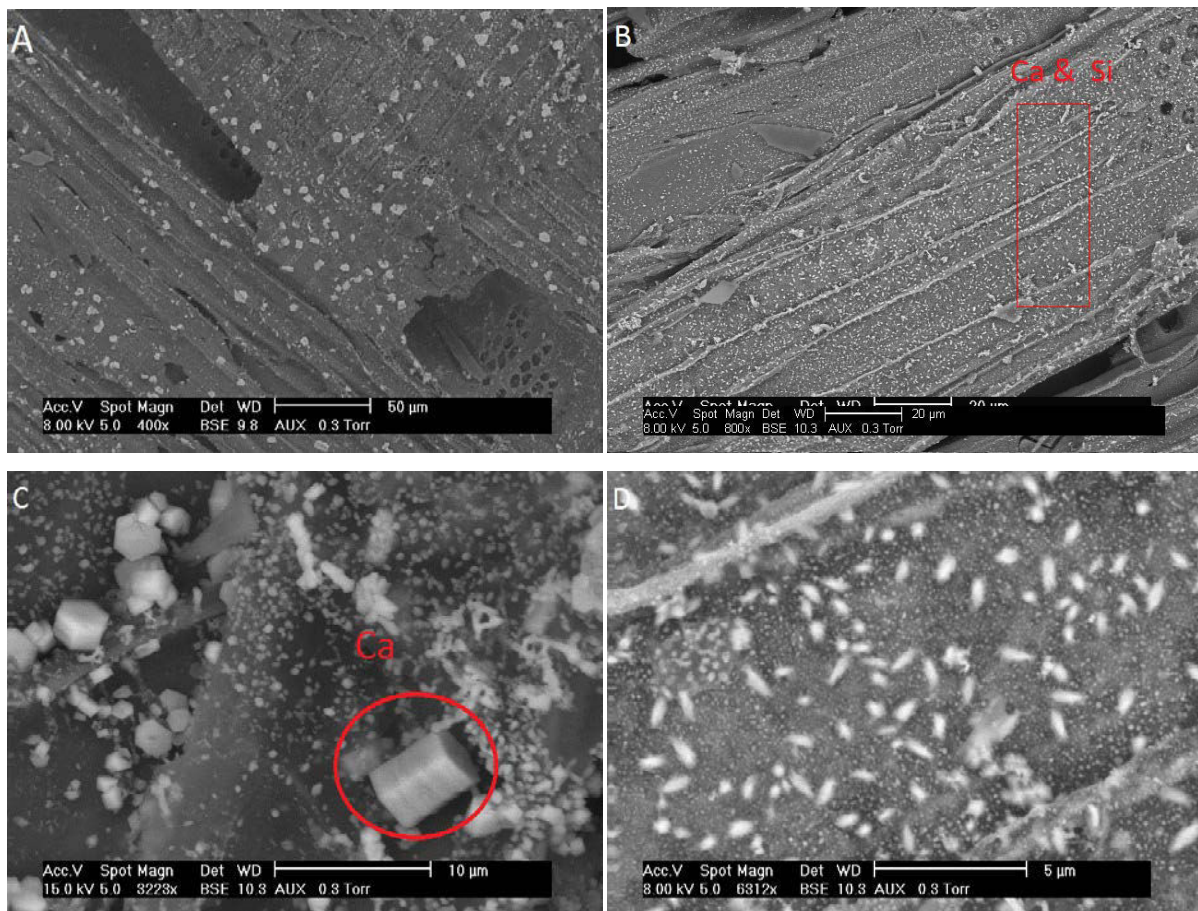
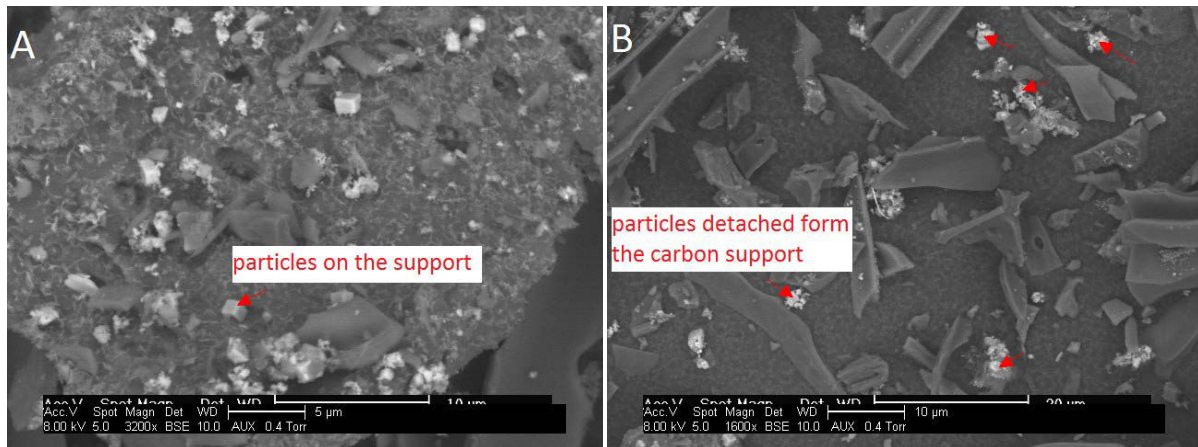
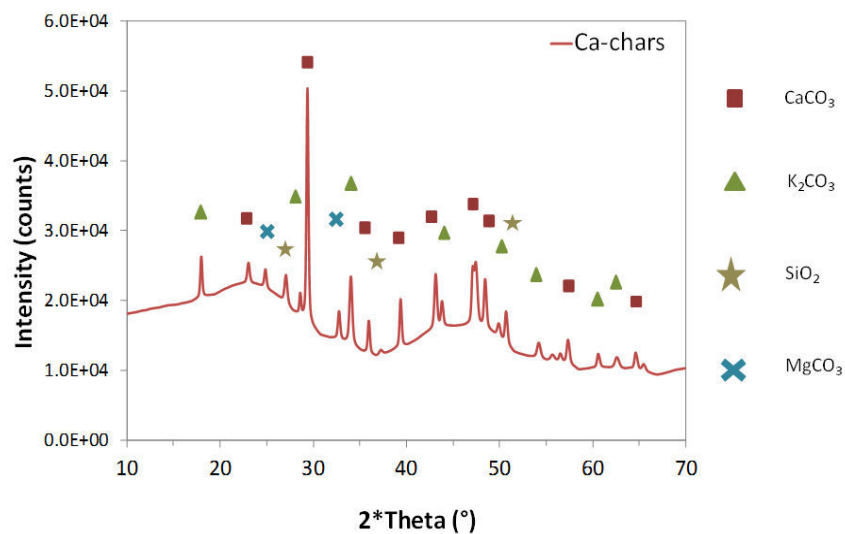


Figure III-29: ESEM pictures of the Ca-chars at different locations of the surface and with different magnitudes: (A) x400, (B) x800, (C) x3200, (D) x6312

Figure III-30 presents ESEM pictures of Ca-chars which were crushed. An interesting observation is that some of the calcium structures remained stuck on the carbon matrix (Figure III-30.A) and some others were detached (Figure III-30.B). On Figure III-30.A, a rectangular-shape particle is observable as we previously observed on Figure III-29.C. On Figure III-30.B the form of the particle is singular with no real geometry. EDS analyses showed that both of these structures contained calcium.



**Figure III-30: ESEM pictures of the crushed Ca-chars chips (a) minerals remain stuck on the carbon matrix (b) calcium oxides did not belong anymore on the carbon surface**



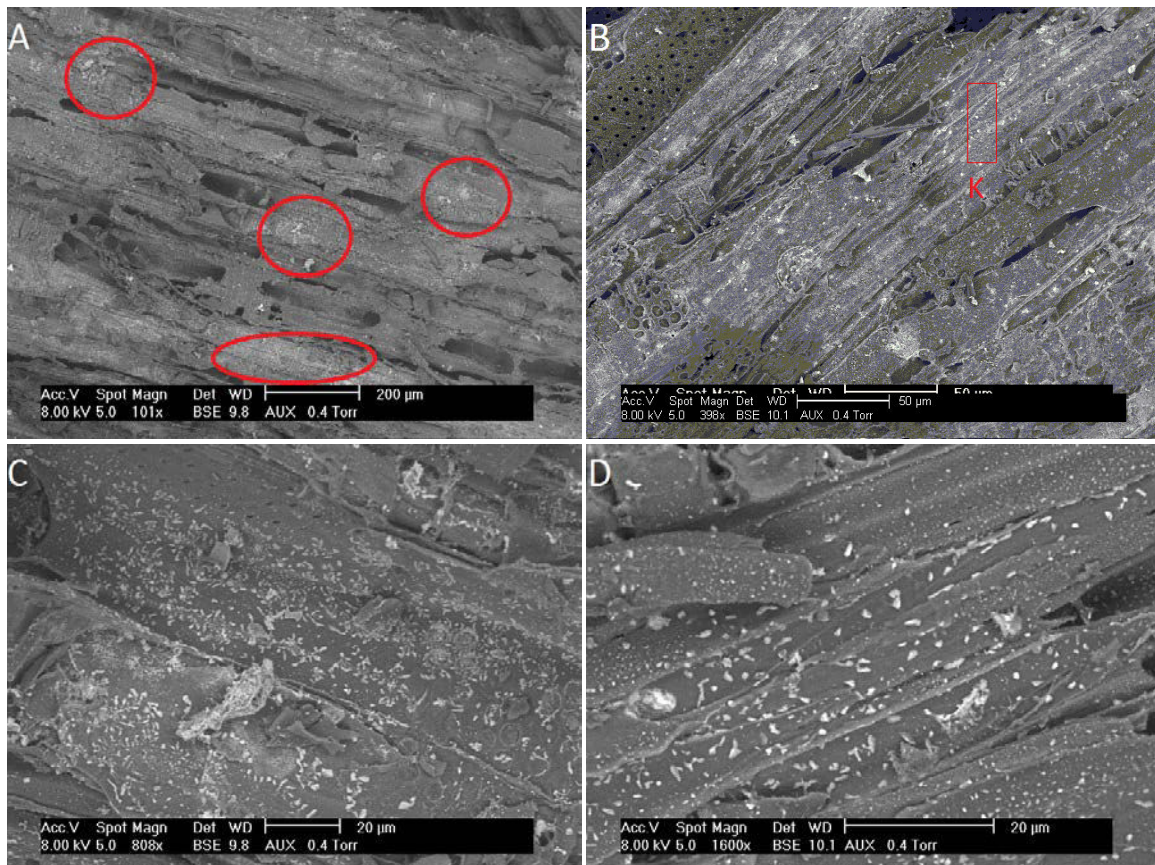
**Figure III-31: X-ray diffraction pattern of the Ca-chars**

Figure III-31 presents the X-Ray diffraction pattern of the Ca-chars. As it was observed for the raw biochar, the Ca-chars contains monoclinic potassium carbonate and rhombohedral calcium carbonate. Silicon dioxide with a hexagonal structure and monoclinic magnesium carbonates were also analyzed. The detachment of the calcium particles from the carbon surface could be explained by the rhombohedral structure of calcium carbonate of which one of the angle of the unit cell is not

equal to  $90^\circ$ . Thus its embedding in the carbon structure could be more complex than for a hexagonal or cubic structure.

### 3.2.2.2. K-chars

Figure III-32 shows the ESEM pictures of the K-chars at different locations of the surface and for different magnitudes. As for the K-char, particles of potassium are well dispersed at the surface. However their shapes are not geometrical. Huang et al. [19] observed the same type of structures on potassium impregnated fir powder. EDS analysis has been performed on a zone which is represented on the Figure III-32.B. Potassium has been detected and it should be in a potassium carbonate mineral.



**Figure III-32: ESEM pictures of K-chars at different locations of the surface and different magnitudes: (A) x101, (B) x308, (C) x808, (D) x1600**

Figure III-33 presents the ESEM pictures of the crushed K-chars surface. On the contrary to the Ca-chars, one can observe that the minerals stay on the carbon matrix. No minerals were detected out of the biochars surface. EDS analyses highlighted the presence of potassium on particles presented on Figure III-33. This difference of adhesion on the carbon matrix is of great importance because it will play a role in term of reactivity. Previous studies highlighted the interaction created between

potassium salt and the carbon structures. Yuh et al. [16] stated that a C-O-K bonding should have been formed in the impregnated carbon they studied. Delannay et al. [21] also proposed a mechanism of the reaction of KOH loaded on graphite powder involving K-O-C entity formation.

X-ray diffraction has also been performed on the K-chars. The X-ray pattern is displayed on Figure III-34. Calcium carbonate and silicon dioxide were analyzed with the same crystalline structures as for the Ca-chars. In addition, potassium hydrogen carbonate (KHCO<sub>3</sub>) and a complex of CaMgSiO<sub>4</sub> (monticellite) were identified. The potassium hydrogen carbonate presents an hexagonal structure which is appropriate to stick on hexagonal graphite carbon. This observation can explain the difference in the cohesion between the mineral and the carbon matrix of the Ca-chars and K-chars. Thus, the crystalline form of the mineral at the carbon surface is of great importance in term of adhesion of the minerals onto the matrix.

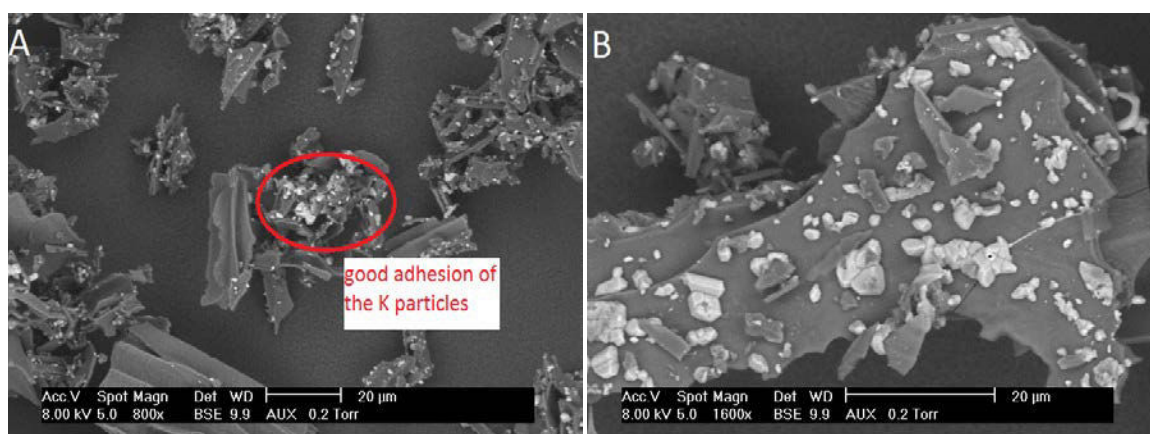


Figure III-33: ESEM pictures of minerals on the crushed K-chars at different locations of the surface and different magnitudes (A) x800, (B) x1600

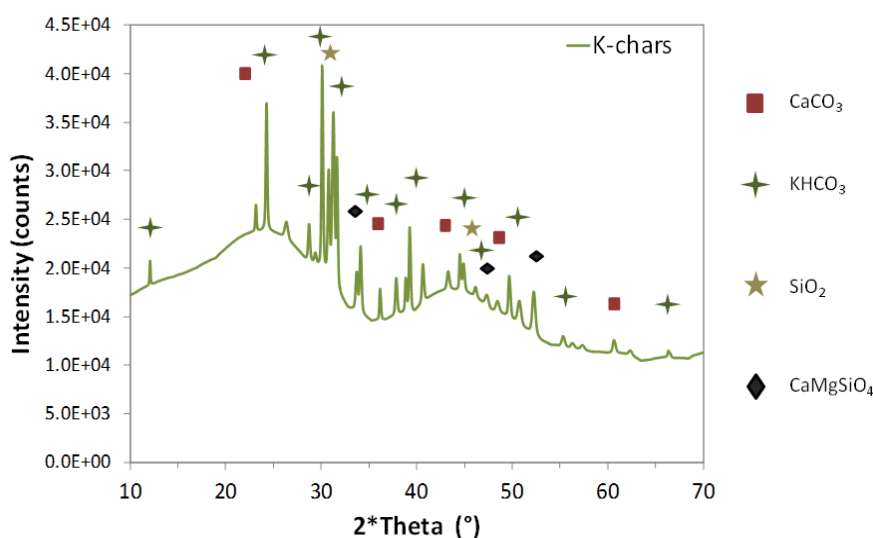
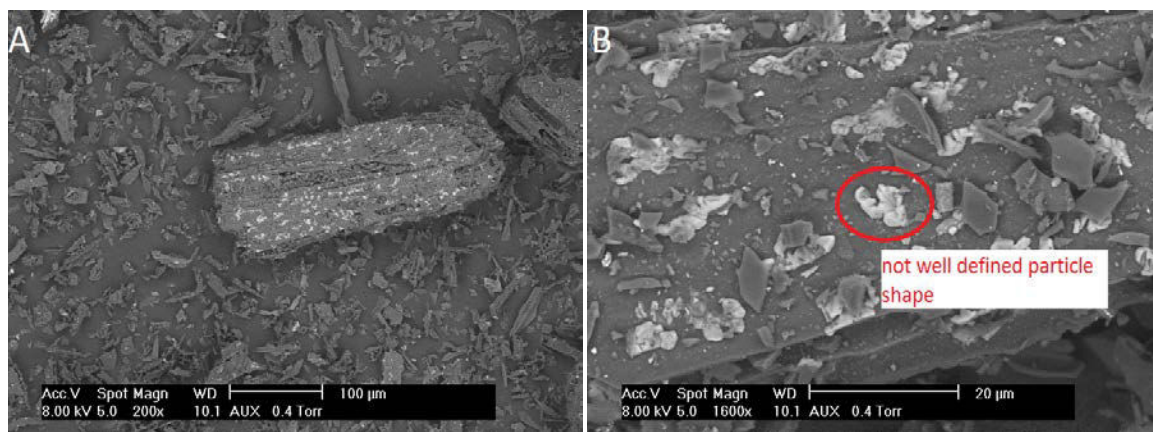


Figure III-34: X-ray diffraction pattern of K-chars

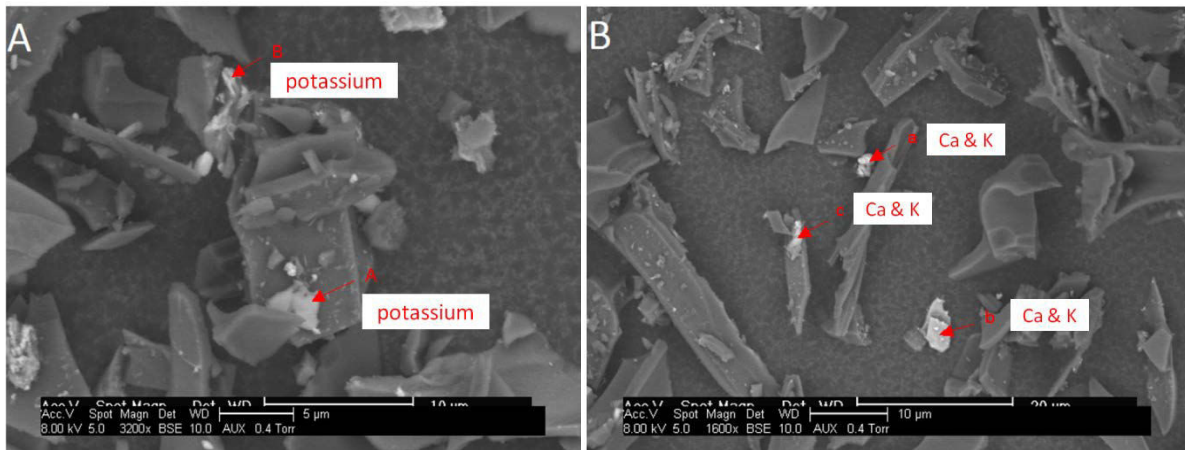
### 3.2.2.3. Ca+K-chars

Figure III-35 shows the distribution of the minerals particle of calcium and potassium through the Ca+K-chars surface. Minerals are identified at several locations of the surface. The geometry of the particles is not well defined but they are well dispersed on the biochars surface.



**Figure III-35: ESEM pictures of the Ca+K-chars at different locations of the surface and with different magnitudes: (A) x200, (B) x1600**

Figure III-36 presents the ESEM images of the crushed Ca+K-chars particles. On Figure III-36.A, the EDS analyses showed that the “A mineral” is only composed of potassium which could be potassium oxide or carbonate, the B mineral is composed of calcium and potassium. It could be a complex such as  $K_2Ca(CO_3)_2$  which has been depicted in the literature review to be an active sites in gasification process [22]. On Figure III-36.B, three mineral structures have been analyzed and seem to be  $K_2Ca(CO_3)_2$  as well. The three structures contain both calcium and potassium. Regarding the adhesion of the minerals on the carbon substrate, some inorganics particles which not belong anymore on the biochars surface were observable (Figure III-36.B). However, the dispersion out of the carbon matrix was in a lower extent than for the Ca-chars. Potassium should have retained calcium particles. Figure III-37 presents the X-ray diffraction pattern of the Ca+K-chars. Calcium carbonate and potassium hydrogen carbonate with the same structures as in the Ca-chars and K-chars were identified. As it was suggested from the EDS analyses, the complex  $K_2Ca(CO_3)_2$  and calcium hydroxide ( $Ca(OH)_2$ ) were detected as well at the surface of the Ca+K-chars.



**Figure III-36: ESEM pictures of the crushed Ca+K-chars at different locations and with different magnitudes: (A) x 3000, (B) x 1600**

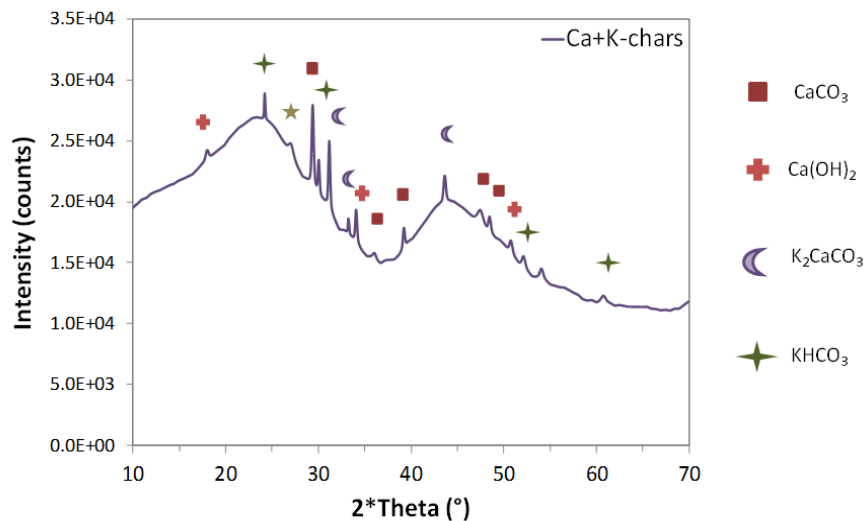


**Figure III-37: X-ray pattern of the Ca+K chars**

Thus, minerals onto the three impregnated biochars were well dispersed at the surface. However, some differences of adhesion of the minerals onto the carbon matrix were observed and seem to be linked to the crystalline structure of the minerals. In fact, XRD analyses have shown that the main crystalline forms onto the Ca-chars surface were rhombohedral calcium carbonate. This structure which is not composed of three 90° angles seemed to show a lower adhesion strength than hexagonal crystalline form (which is composed of 3 90° angles). In fact, the K-chars of which the potassium is mainly into potassium hydrogen carbonate form presented a very good adhesion of the mineral onto the carbon surface, certainly due to the hexagonal form of  $\text{KHCO}_3$ . The Ca+K-chars is in between the two others impregnated biochars in term of mineral adhesion. Rhombohedral  $\text{K}_2\text{CaCO}_3$

tended to detached from the carbon surface whereas hexagonal  $\text{Ca}(\text{OH})_2$  and  $\text{KHCO}_3$  remained stuck on the surface.

### 3.3. Carbon matrix of the impregnated biochars

Raman analyses have been performed on surfaces of  $5 \times 5 \mu\text{m}$  for the mineral impregnated biochars. The goal was to identify a zone potentially containing minerals and carbon structures. For this type of analysis, it is possible to make the software search for two different families and obtain two spectra. Once the two spectra obtained the user should be able to determine if the two families identified are actually chemically different. For the Ca-chars and K-chars, zones containing both structures (minerals and carbons) were identified. However, we did not manage to obtain one spectrum representing the minerals and another one characteristic of the carbon matrix. This indicates a good mixing of the minerals onto the surface which has been already highlighted by ESEM analyses. Figure III-38 is an illustration of the Raman image treatment for the K-chars. Two families have been identified on the zone analyzed. However the associated spectra clearly show that minerals and carbon structures are present on both families. In fact, sharp peaks in the  $800\text{-}1200 \text{ cm}^{-1}$  region which are characteristic of minerals structures can be observed on the red and blue spectra. The broad band representative of amorphous carbon is also visible in the  $800\text{-}2000 \text{ cm}^{-1}$  region. However the mineral peak is more intense in the red section whereas in the blue zone the carbon band is the predominant family.

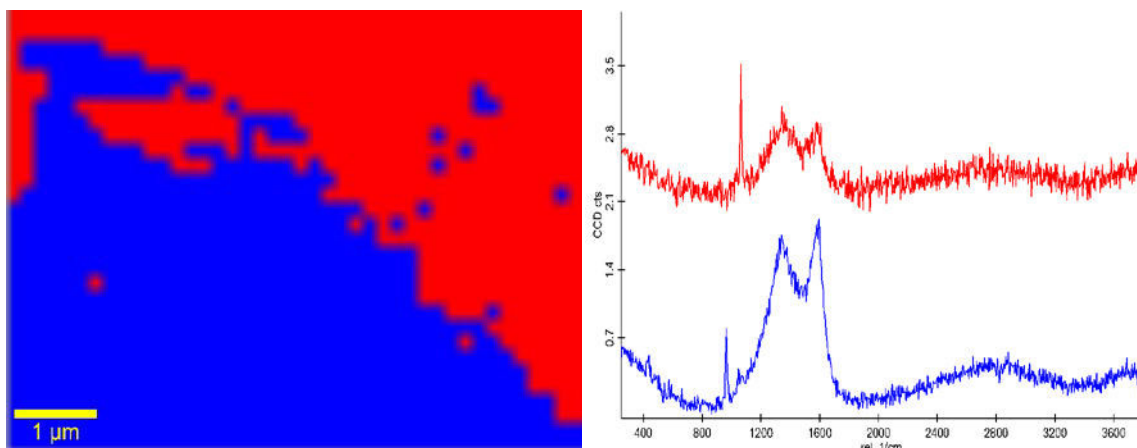
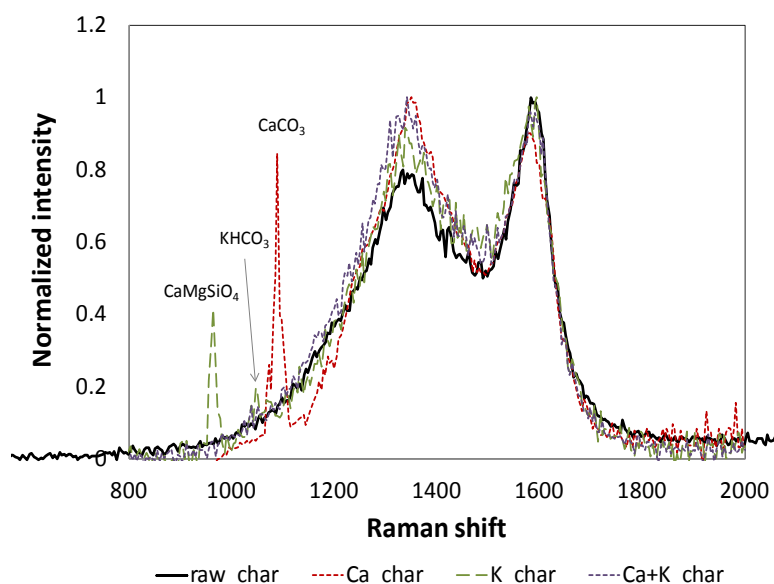


Figure III-38: Cluster image and spectra related to the two different zones (red and blue)

Figure III-39 presents the comparison of the Raman spectra of the raw and mineral impregnated biochars normalized by their highest peak. Minerals peaks are visible on the 800-1100  $\text{cm}^{-1}$  region for the Ca-chars and K-chars. However a clear differentiation between the peaks assigned to minerals and carbons structures is possible due to the fact that mineral peaks are very sharp. Peaks observed in Raman are related to mineral structures identified by XRD analyses such as calcium carbonate for the Ca-chars and bicarbonate potassium for the K-chars. The zone analyzed for the Ca+K-chars seems to not contain minerals structures. Regarding the carbon matrix, one can observe that the mineral impregnation impacted the different carbon families distribution. The D band and the valley (overlap between the D and G bands) seem to be more intense. The Ca-chars presents the highest carbon structures distribution modification followed by the Ca+K-chars. In fact, for these two biochars the D peak becomes the highest peak.



**Figure III-39: Raw Raman spectra of the raw and mineral impregnated biochars**

Deconvolution of the Raman spectra has been performed and confirmed the different trends observed. The impregnation tended to increase the disorder in the carbon matrix which was predictable. In fact, the insertion of the mineral particles into the carbon graphene sheets enhanced the concentration of heteroatoms in the matrix and, at the same time, they should have also destroyed surrounding carbon structures. Table III-9 presents the carbon structures distribution in the raw and mineral impregnated biochars obtained from the deconvolution of the Raman spectra presented in Figure III-39. The graphene-like sheets and the small aromatic cycles amounts have been decreased in favor to the increase of the “in-plane” imperfections structure (D bands). The ratios evaluating the contribution of the disordered structures versus graphite ( $I_D/I_G$  and  $I_{Vr+Vl+Gr}/I_G$ ) and the

one evaluating the contribution of “in-plane” imperfections over small aromatic rings systems ( $I_D/I_{Vr+VI+Gr}$ ) led to go further in the interpretation. In fact, it is observable that the  $I_D/I_G$  which was equal to 0.99 for the raw biochars reached 1.28 for the K-chars and 1.43 for the two other impregnated biochars. The  $I_D/I_{Vr+VI+Gr}$  was also increased by 30, 38 and 51% for the K-chars, Ca+K-chars and Ca-chars which means that impregnation favored the creation of “in-plane” imperfections but did not enhance the small amorphous cycles formation. In fact, the  $I_{Vr+VI+Gr}/I_G$  remains really close to 1.1 for the three impregnated biochars which was the ratio value for the raw biochars.

**Table III-9: Carbon structures distribution in the raw and mineral impregnated biochars (obtained from the deconvolution of the Raman spectra presented in Figure III-39; maximum standard deviation 2.5%)**

	Raw_char	K-char	Ca-char	Ca+K-char
<b>Graphite</b>	26	24	23	22
<b>“In-plane” defects + large aromatic rings</b>	25	30	33	31
<b>Small amorphous structures</b>	27	24	22	23

The increase of disordered structures at the biochars surface should increase their reactivity towards methane cracking. The specific enhancement of a type of disordered structure will be interesting to highlight if they are the active sites for methane cracking.

### 3.4. Specific surface area and porosity of the impregnated biochars

The specific surface area and porosity were investigated for the three mineral impregnated biochars. Their adsorption isotherms are of type I which shows that these biochars are microporous. Table III-10 presents the specific surface area, total volume and average diameter of micropores of the raw and mineral impregnated biochars. One can observe that the specific surface area was decreased for all the impregnated biochars. However, according to the added minerals, the decrease in the specific surface area is significantly different. Regarding the calcium impregnated biochars, the specific surface area was slightly decreased of 6.5% whereas the specific surface areas of the potassium and potassium+calcium impregnated biochars were diminished by 33 and 48% respectively.

The trend of the micropore volume evolution is different according to the mineral impregnated at the surface. The biochars impregnated with both minerals follows the trend of the potassium

impregnated one. The micropore volume was decreased of 33 and 47% for these two biochars. The calcium impregnated biochar shows a different behavior since its micropore volume has been slightly increased of 10%. As the average pores diameter is concerned, the Ca-biochar stays close to the raw biochars with an average diameter of 5.0 Å. The two other biochars show an average diameter twice higher than the raw biochars.

Thus, the Ca-biochars textural properties remain close to the one of the biochars. The K-chars properties are significantly different since the specific surface area and total volume of micropores were decreased by one third. However, the micropores average diameter was increased by a factor 2. This difference of the impregnation impact on the textural properties should be due to the more or less strong interaction between the carbon matrix and the minerals. In fact, ESEM pictures highlighted that the calcium particles tend to stand out from the carbon surface whereas the potassium remains on it. The Ca+K-chars specific surface area and porosity were the smallest certainly due to the formation of more complex and larger particles which have been highlighted by EDS.

**Table III-10: Specific surface area, total volume and average diameter of micropores of the raw and mineral impregnated biochars**

Biochars	Specific surface area (m <sup>2</sup> /g)	Total volume of micropores (cm <sup>3</sup> /g)	Average diameter of pores (Å)
Raw biochars	662	0.22	5
Ca-char	619	0.24	5
K-char	446	0.15	10
Ca+K-char	346	0.12	10

### 3.5. Partial conclusion on the physico-chemical properties of the impregnated biochars

Three mineral impregnations have been performed with the two major minerals detected in the raw biochars ash: calcium and potassium. They have been chosen because they were depicted in the literature to be active sites in the gasification process. The goal is to determine if they are reactive too for methane cracking. The first impregnation was carried out in a calcium nitrate solution, the second in a potassium nitrate one and the third in a stoichiometric mixture of calcium and potassium. X-ray fluorescence results highlighted that the raw biochars contained the same amount of calcium

and potassium (about 0.5 wt%). The calcium content was increased 8.6 times in the Ca-chars compared to the raw biochars. The same behavior for potassium is observable in the K-chars (x7.7). Regarding the Ca+K-chars, the two minerals are in equal amounts (2.15 and 2.23 wt%).

Biochars contained inherently carbonate forms. Post calcium impregnation, XRD analysis shows that the calcium is still in a carbonate structure ( $\text{CaCO}_3$ ). The potassium impregnation leads to form potassium bicarbonate ( $\text{KHCO}_3$ ). In the Ca+K-chars, calcium carbonate and potassium bicarbonate were also detected. However, calcium hydroxide ( $\text{Ca(OH)}_2$ ) and the complex (Fairchildite  $\text{K}_2\text{Ca(CO}_3)_2$ ) were also present. ESEM-EDS analysis confirmed a good dispersion of the mineral particles at the surface. However, the ESEM pictures revealed a stronger interaction between the potassium agglomerate and the carbon matrix than the one between the calcium particles and the substrate. The stronger interaction should have also led to a higher filling of the porosity since both micropore volume and specific surface area were decreased more significantly for the K-chars than for the Ca-chars. The Ca+K-chars had the smallest specific surface area, it could be explained by the fact that larger agglomerates were formed and thus filled even more the porosity than in the K-chars.

The distribution of the carbon structures in the mineral impregnated biochars has been modified. In fact, a significant increase of the structures containing “in-plane” imperfections has been noticed. The raw biochar contains about 26% of these structures whereas the mineral impregnated biochars were composed of about 31% of this type of disordered structures respectively. This is due to the insertion of the minerals crystals into the graphene-like sheets.

Regarding the oxygenated functions, the techniques previously utilized such as TPD and FTIR could not provide accurate information on the O-containing groups of the mineral impregnated biochars. In fact, in the raw and oxygenated biochars, even if mineral components were present they were significantly less concentrated than the oxygen functions at the surface. As for the mineral impregnated biochars, responses in both TPD and FTIR techniques could be of either oxygenated functions or minerals content. Thus it was not possible to evaluate the oxygen content at the surface of the mineral impregnated biochars.

#### 4. Conclusion on the characterization of the raw and functionalized biochars

Two treatments have been performed in order to enhance rather the oxygenated content at the surface of the biochars or the mineral concentration. Both processes were successful since they increased the content of the targeted chemical function. Oxygenation enhanced by 1.2, 1.7 and 2.1 the total oxygen content at the surface at 280 (during 8h), 340 and 400°C (for 2h) respectively. The impregnation led to a concentration of calcium 8 times higher in the Ca-chars, 7 times higher for potassium in the K-chars and 4 times higher for both calcium and potassium in the Ca+K-chars. In addition, one can notice that both treatments were selective. In fact, the oxygenation increased mostly weak acids (anhydride, lactone, phenol, hydroxyl), removed strong acid functions (carboxylic acids) but did not modify basic groups. The mineral impregnation either with calcium or potassium favored the carbonate forms formation.

Both processes impacted the whole physico-chemical properties. Regarding the specific surface area, the wet impregnation of minerals tends to decrease the porosity and then the specific surface area. It should be a function of the size of the agglomerates formed at the surface and the strength of the interaction between the minerals and the matrix. The biochars oxygenated at 280°C tend also to have a slightly smaller specific surface area due to oxygen chemisorption at the surface. At 340 and 400°C, the predominance of the combustion on the oxygen chemisorption significantly increased the micropore volume and specific surface area.

Regarding the carbon structures, the oxygenation increased globally the disorder in the carbon matrix. However, according to the operating conditions, not the same types of defects were enhanced. At 280°C, the increase of both “in-plane” defects and amorphous aromatic rings was highlighted. At the highest temperatures (340 and 400°C), the aliphatic chains and small aromatic rings were mostly burnt and let a biochars with more graphene-like sheets in which the “in-plane” imperfections such as heteroatoms inserted, vacancies were significantly enhanced. As for the mineral impregnated biochars are concerned, the increase of “in-plane” imperfections due to the minerals crystals embedding has been highlighted. Thus, the evolution of the physico-chemical properties over the two treatments is summarized in Table III-11. The physico-chemical properties characterization will serve as a basis in the discussion of the biochars reactivity toward methane cracking in the chapter IV.

Table III-11: Summary of the physico-chemical properties of the raw and functionalized biochars

	Carbon matrix			Oxygenated groups		Minerals		Textural properties	
	Graphite %	« in-plane » Defects %	Amorphous aromatic+aliphatic chains %	Total Increase	Nature of functions increased	Amount	Structure	$S_{spe,area}$ $m^2/g_{char}$	$V_{micropores}$ $cm^3/g_{char}$
Raw-chars	26	25	27	-	-	[Ca]≈ [K]	CaCO <sub>3</sub> K <sub>2</sub> CO <sub>3</sub>	662	0.22
Ox_2h_280°C	25	26	29	1.2*[O] <sub>rc</sub>	weak acids	≈ rc	≈ rc	622	0.22
Ox_4h_280°C	26	26	27	1.5*[O] <sub>rc</sub>	weak acids	≈ rc	≈ rc	578	0.21
Ox_8h_280°C	23	28	28	1.5*[O] <sub>rc</sub>	weak acids	≈ rc	≈ rc	564	0.21
Ox_2h_340°C	30	33	20	1.5*[O] <sub>rc</sub>	weak acids	≈ rc	≈ rc	808	0.30
Ox_2h_400°C	28	39	16	1.2*[O] <sub>rc</sub>	weak acids	≈ rc	≈ rc	859	0.32
Ca-chars	23	33	22	-	-	4*[Ca] <sub>rc</sub>	CaCO <sub>3</sub>	619	0.24
K-chars	24	30	24	-	-	10*[K] <sub>rc</sub>	KHCO <sub>3</sub>	446	0.15
Ca+K-chars	22	31	23	-	-	2*[Ca] <sub>rc</sub> 5*[K] <sub>rc</sub>	CaCO <sub>3</sub> Ca(OH) <sub>2</sub> KHCO <sub>3</sub> K <sub>2</sub> CaCO <sub>3</sub>	346	0.12

## Bibliography

- [1] C. Guizani, F. J. Escudero Sanz, M. Jeguirim, R. Gadiou, and S. Salvador, "The effects of textural modifications on beech wood-char gasification rate under alternate atmospheres of CO<sub>2</sub> and H<sub>2</sub>O," *Fuel Process. Technol.*, vol. 138, pp. 687–694, 2015.
- [2] M. Milhé, L. Van De Steene, M. Haube, J. M. Commandré, W. F. Fassinou, and G. Flamant, "Autothermal and allothermal pyrolysis in a continuous fixed bed reactor," *J. Anal. Appl. Pyrolysis*, vol. 103, pp. 102–111, 2013.
- [3] B. K. Pradhan and N. K. Sandle, "Effect of different oxidizing agent treatments on the surface properties of activated carbons," *Carbon N. Y.*, vol. 37, no. 8, pp. 1323–1332, Jan. 1999.
- [4] D. B. Mawhinney and J. T. Jr Yates, "FTIR study of the oxidation of amorphous carbon by ozone at 300 K — Direct COOH formation," *Carbon N. Y.*, vol. 39, pp. 1167–1173, 2001.
- [5] J.-H. Zhou, Z.-J. Sui, J. Zhu, P. Li, D. Chen, Y.-C. Dai, and W.-K. Yuan, "Characterization of surface oxygen complexes on carbon nanofibers by TPD, XPS and FT-IR," *Carbon N. Y.*, vol. 45, no. 4, pp. 785–796, Apr. 2007.
- [6] A. C. Ferrari, "Raman spectroscopy of graphene and graphite: Disorder, electron-phonon coupling, doping and nonadiabatic effects," *Solid State Commun.*, vol. 143, no. 1–2, pp. 47–57, 2007.
- [7] I. Suelves, M. J. Lázaro, R. Moliner, J. L. Pinilla, and H. Cubero, "Hydrogen production by methane decarbonization: Carbonaceous catalysts," *Int. J. Hydrogen Energy*, vol. 32, no. 15 SPEC. ISS., pp. 3320–3326, 2007.
- [8] S. Fujita, H. Watanabe, A. Katagiri, H. Yoshida, and M. Arai, "Nitrogen and oxygen-doped metal-free carbon catalysts for chemoselective transfer hydrogenation of nitrobenzene, styrene, and 3-nitrostyrene with hydrazine," *J. Mol. Catal. A Chem.*, vol. 393, pp. 257–262, Nov. 2014.
- [9] A. Kochan, A. Krzton, and G. Fingueneisel, "A study of carbonaceous char oxidation in air by semi-quantitative FTIR spectroscopy," *Fuel*, vol. 77, no. 6, pp. 563–569, 1998.
- [10] J. L. Figueiredo, M. F. R. Pereira, M. M. A. Freitas, and J. J. M. Orfao, "Modification of the surface chemistry of activated carbons," *Carbon N. Y.*, vol. 37, pp. 1379–1389, 1999.
- [11] D. M. Keown, X. Li, J. Hayashi, and C.-Z. Li, "Evolution of biomass char structure during oxidation in O<sub>2</sub> as revealed with FT-Raman spectroscopy," *Fuel Process. Technol.*, vol. 89, no. 12, pp. 1429–1435, Dec. 2008.

- 
- [12] F. Vautard, J. Dentzer, M. Nardin, J. Schultz, and B. Defoort, "Influence of surface defects on the tensile strength of carbon fibers," *Appl. Surf. Sci.*, vol. 322, pp. 185–193, Dec. 2014.
- [13] J. L. Figueiredo and M. F. R. Pereira, "The role of surface chemistry in catalysis with carbons," *Catal. Today*, vol. 150, no. 1–2, pp. 2–7, Feb. 2010.
- [14] M. Ducouso, E. Weiss-Hortala, A. Nzihou, and M. J. Castaldi, "Reactivity enhancement of gasification biochars for catalytic applications," *Fuel*, vol. 159, no. x, pp. 491–499, 2015.
- [15] A. Nzihou, B. Stanmore, and P. Sharrock, "A review of catalysts for the gasification of biomass char, with some reference to coal," *Energy*, vol. 58, pp. 305–317, Sep. 2013.
- [16] S. J. Yuh and E. E. Wolf, "FTIR studies of potassium catalyst-treated gasified coal chars and carbons," *Fuel*, vol. 62, no. 2, pp. 252–255, 1983.
- [17] A. H. El-sheikh, A. P. Newman, H. K. Al-daffae, S. Phull, and N. Cresswell, "Characterization of activated carbon prepared from a single cultivar of Jordanian Olive stones by chemical and physicochemical techniques," *J. Anal. Appl. Pyrolysis*, vol. 71, pp. 151–164, 2004.
- [18] K. J. Hüttinger and R. Mingos, "The influence of the catalyst precursor anion in catalysis of water vapour gasification of carbon by potassium," *Fuel*, vol. 65, no. 8, pp. 1122–1128, 1986.
- [19] Y. Huang, X. Yin, C. Wu, C. Wang, J. Xie, Z. Zhou, L. Ma, and H. Li, "Effects of metal catalysts on CO<sub>2</sub> gasification reactivity of biomass char," *Biotechnol. Adv.*, vol. 27, no. 5, pp. 568–572, 2009.
- [20] M. P. Kannan and G. N. Richards, "Potassium catalysis in air gasification of cellulosic chars," *Fuel*, vol. 69, no. 8, pp. 999–1006, 1990.
- [21] F. Delannay, W. T. Tysoe, H. Heinemann, and G. a. Somorjai, "The role of KOH in the steam gasification of graphite: Identification of the reaction steps," *Carbon N. Y.*, vol. 22, no. 4–5, pp. 401–407, 1984.
- [22] M. Q. Jiang, R. Zhou, J. Hu, F. C. Wang, and J. Wang, "Calcium-promoted catalytic activity of potassium carbonate for steam gasification of coal char: Influences of calcium species," *Fuel*, vol. 99, pp. 64–71, 2012.



**IV. Chapter 4: Biochars reactivity towards methane cracking and the relation with their physico-chemical properties**

# Content

1.	Comparison of the activities of the raw and functionalized biochars for methane cracking .	154
1.1.	Activity of the mineral impregnated biochars.....	155
1.2.	Activity of the oxygenated biochars.....	157
1.3.	Partial conclusion on the activities of the raw and functionalized biochars.....	159
2.	Interaction between the biochars reactivity and their physico-chemical properties.....	160
2.1.	Initial conversion .....	161
2.2.	Deactivation by carbon deposit.....	179
3.	Conclusion .....	184
	Bibliography.....	188

The literature review highlights that carbonaceous materials can be used as catalysts for methane cracking and that their mineral content, oxygenated functions, carbon matrix and textural properties play a role [1]. This chapter investigates the reactivity of the raw and functionalized biochars towards this reaction. Previous characterizations (presented in the Chapter III) highlighted the diversity of surface properties present in these biochars. Importantly for a similar surface property, subgroups exist with different features which could present different reactivity towards methane cracking. For example, oxygenated groups could be acidic (carboxylic acids or phenol), neutral (ether) or basic (quinone, pyrone). Literature reports have emphasized that the basic functionality should be the most reactive for dehydrogenation [2]. However the other oxygenated functions could also enhance the global reactivity due to their desorption which create new active sites at the surface (unsaturated carbons). Regarding the carbon matrix, different types of structures were identified which are classified into very well ordered (graphite) and disordered structures (structures with “in-plane” defects, aromatic rings, and aliphatic chains). The reactivity of these carbon structures are different and are dependent on the reaction considered. Minerals were highlighted to be active sites in gasification but their role in the methane cracking was less extensively studied. Klinghoffer et al. [3] emphasized that biochar reactivity was lowered when ashes were removed from the carbon structure. However, their catalytic role is not well understood yet. Thus, further research is required to get better insights into the reactivity of the different surface properties towards methane cracking. In addition, literature highlighted that methane cracking involved carbon deposits at the surface which could block the access of the active sites. However the mechanism is not well understood yet.

To perform the study, biochars have been functionalized ( $O_2$  gas-phase treatment and mineral impregnation, Chapter III) in order to enhance the concentration of chemical groups at the surface (oxygenated functions and minerals). In Chapter III, it has been highlighted that the functionalization that was done modified the other physico-chemical properties (carbon matrix, textural properties) as well. In this chapter, the hydrogen productions (due to methane cracking) of the different functionalized biochars are compared to that of the raw biochar in order to evaluate the performances of the functionalization treatment. Then, the biochars' activities are discussed in relation to their four physico-chemical properties to get better insights into the role of the different surface properties. In this chapter, the first section is dedicated to the comparison of the functionalized biochars activities with the one of the raw biochars. The second section discusses the interaction between the surface physico-chemical properties and the reactivity.

## 1. Comparison of the activities of the raw and functionalized biochars for methane cracking

Seven biochars have been tested for methane cracking: the raw, the mineral impregnated, and three oxygenated biochars. These oxygenated biochars have been selected since they are representative of catalysts with different physico-chemical properties. In fact, their carbon structure distribution, textural properties and oxygenated content are significantly different (see Chapter III). However the relationship between these surface properties and the reactivity will be further discussed in the section 2 of this chapter. In this present part, the overall activity of the different functionalized biochars is presented and compared to the one of the raw biochars. The first section (1.1) is dedicated to the mineral impregnated biochars and the second (1.2) to the oxygenated biochars.

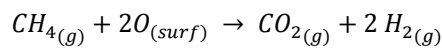
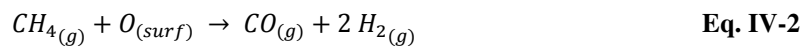
**Table IV-1: Names of the 7 biochars which have been tested for catalytic methane cracking reaction**

Type	Names
<b>Raw</b>	Raw_biochar
<b>Oxygenated</b>	ox2h_280C
	ox8h_280C
	ox2h_340C
<b>Mineral impregnated</b>	Ca-chars
	K-chars
	Ca+K-chars

Methane cracking experiments were carried out at 700°C for 2h for the seven biochars shown in Table IV-1. A preliminary test which consisted of performing the reaction in an empty reactor has been carried out to evaluate the light-off temperature of the thermal cracking. Under these conditions, hydrogen started to be produced at temperature above 850°C. Thus, the catalytic experiments were performed at 700°C to ensure that the catalytic reaction was the only source of hydrogen production. The activities of the different biochars were discussed based on the quantity of hydrogen production. In fact, the main reaction is the conversion of methane into two moles of hydrogen and one mole of solid carbon (see Eq.IV-1).



Some other reactions should occur since some carbon monoxide and carbon dioxides were detected in the output gases. These two gases should come from the reaction of the carbon atom from the methane with some oxygen functions of the surface following Eq. IV-2. However their concentrations were significantly lower than the one of the hydrogen.



This first section is dedicated to a comparison of the hydrogen productions from the methane cracking reaction on the raw and functionalized biochars (mineral impregnated and oxygenated biochars). The main goal of this part is to present a global vision of the reactivity results and to introduce the different point of discussion regarding the differences of reactivity. However, these curves of hydrogen productions are further discussed in the section 2 in relation with the physico-chemical properties presented in the Chapter III to get a better understanding of the reaction.

### 1.1. Activity of the mineral impregnated biochars

Figure IV-1 presents the hydrogen productions (normalized by the mass of char and the moles of methane introduced) of the mineral impregnated biochars: Ca-char (Ca: 5 wt%), K-char (K: 4.9 wt%) and Ca+K-char (Ca: 2.1 wt%, K: 2.2 wt%) compared to the one of the raw biochar.

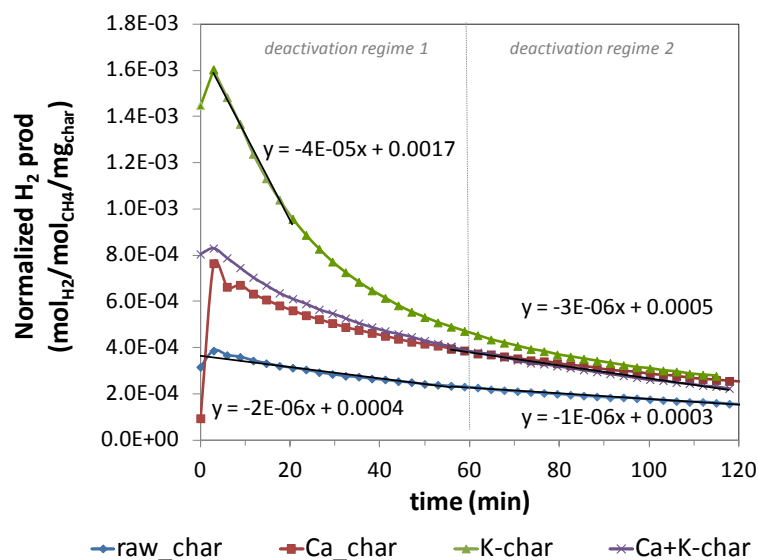


**Figure IV-1: Comparison of the hydrogen production from the methane cracking at 700°C, 10%CH<sub>4</sub> on the raw and mineral impregnated biochars**

One can observe on Figure IV-1 that the initial hydrogen production for the three mineral impregnated biochars has been significantly enhanced compared to the raw biochars. Thus, the increase of minerals amount at the biochars surface impacted clearly the methane cracking although other physico-chemical properties would be involved in. The K-chars exhibits the highest initial reactivity which is four times higher than the one of the raw biochars. The Ca+K-char and the Ca-char show a similar production at the early stages of the reaction and during the two hours of reaction. Their initial hydrogen production is twice higher than the one of the raw biochars. Thus, hydrogen production has been significantly enhanced at early stages of the reaction certainly due to the presence of the mineral as the specific surface area was decreased during the functionalization treatment.

However, for the four biochars, the highest hydrogen production is observable at the initial point. Then, over the reaction the production diminishes which should be due to surface deactivation since the operating conditions remain unchanged during the experiments. Many factors can contribute to the reduction in activity. However, they are all likely related to surface interactions. Two different regimes of deactivation are observed: during the first hour a strong decrease in the hydrogen production is visible for the four biochars. Then, a more stable hydrogen production is observed during the second hour. The K-chars which presented the highest initial hydrogen production suffered from the strongest deactivation. The Ca+K-chars deactivation is similar to the Ca-chars and is not as strong as the K-chars deactivation. Deactivation rates for the hydrogen production on the four biochars and for the two regimes have been evaluated from a fitting of the experimental data.

Some of the fit equations are presented on Figure IV-1. During the first hour, the deactivation rate of the hydrogen production on the raw biochar is equal to  $2 \times 10^{-6} \text{ mol}_{\text{H}_2}/(\text{mol}_{\text{CH}_4} \cdot \text{mg}_{\text{char}} \cdot \text{min}^{-1})$  while for the Ca-char (and Ca+K-char) and the K-char it is of  $6 \times 10^{-6}$  and  $4 \times 10^{-5} \text{ mol}_{\text{H}_2}/(\text{mol}_{\text{CH}_4} \cdot \text{mg}_{\text{char}} \cdot \text{min}^{-1})$  respectively. This means that the deactivation is 3 to 20 times stronger for the mineral impregnated biochars than for the raw biochar during the early stages of the reaction. In fact, after 1 hour of treatment, the K-chars, the Ca-chars and the Ca+K-chars lost 70, 55 and 50% of activity respectively while the raw biochars reached 45% of its initial activity.

During the second hour of the experiment, one can observe a progressive stabilization of the hydrogen production. In fact, the deactivation rate has been lowered for the four biochars. Regarding the raw biochar, it has been halved compared to the deactivation rate in the regime 1. As far as the mineral impregnated biochars are concerned, the deactivation rate is equal to  $3 \times 10^{-6} \text{ mol}_{\text{H}_2}/(\text{mol}_{\text{CH}_4} \cdot \text{mg}_{\text{char}} \cdot \text{min}^{-1})$ . Their deactivation rate remains three times higher than the one of the raw biochars. However, their hydrogen production is still higher too during the 2<sup>nd</sup> hour of reaction (1.8 times higher). If the test was performed for a longer time, the hydrogen production for the four biochars should converge at the same value which indicates that the advantage of the mineral impregnation should be lost over the reaction. This should be due to the coke deposit onto the mineral particles which cannot react anymore.

The mineral impregnation successfully increased the methane conversion into hydrogen. This indicates that potassium and calcium should be active sites for this reaction. The highest gain of activity was observed at the initial stages of the reaction and then a continuous diminution was observed due to deactivation of the biochars surface. However, the impregnated biochars presented different reactivities which highlighted that the cracking mechanism differed according to the type of mineral. The dispersion and the structure of mineral should influence their activity. In order to get better insights into the mechanism and to evaluate if the gain of activity is only due to mineral amount enhancement or also to modifications of the other physico-chemical surface properties, the hydrogen production has been discussed in function of the four physico-chemical properties in the section 2 of this chapter.

## 1.2. Activity of the oxygenated biochars

Figure IV-2 presents the hydrogen productions recorded during methane cracking experiments at 700°C on the raw and oxygenated biochars (ox2h\_280C, ox8h\_280C and ox2h\_340C). The hydrogen productions have been normalized by the mass of the chars and the moles of methane introduced.

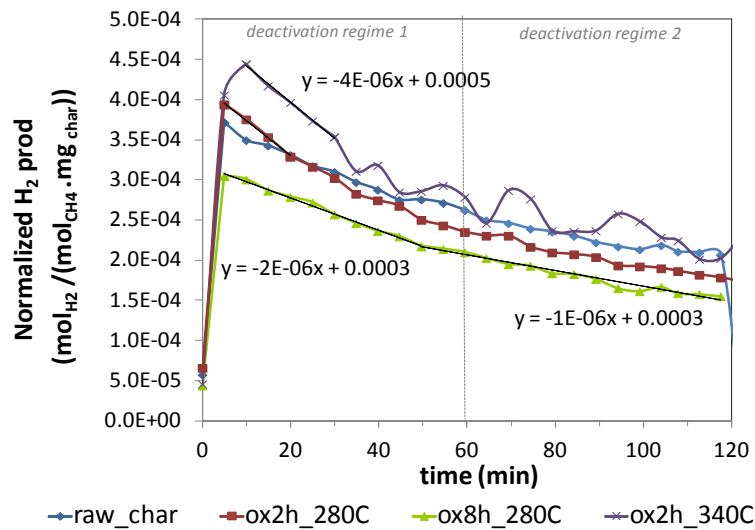


**Figure IV-2: Comparison of the hydrogen production during the methane cracking at 700°C, 20% CH<sub>4</sub> for the raw and oxygenated biochars**

The impact of the O<sub>2</sub> gas-phase treatment on the biochars reactivity is not as clear as the mineral impregnation. In fact, a distinct trend is not observable on Figure IV-2. This indicates that the reactivity of the O-containing groups should not be as strong as the one of the mineral. The activity should not be dependent only on the quantity of O-containing groups at the surface but also on other surface properties. However, such as discussed in the previous section, two deactivation regimes are visible during the two hours of reaction.

The biochars oxygenated at 340°C for 2h shows the highest initial and long-term activity. The hydrogen production is 1.5 times compared to the raw biochar at the early stages and after the 2 hours treatment. The deactivation rate during the phase 1 is twice higher than the one of the raw biochar. Its better efficacy could be due to its higher specific surface area (22% higher than the raw biochars), total pore volume (47% higher than the raw biochars) and amount of oxygenated functions (1.73 higher than the raw biochars). However, its production is more irregular than the other biochars in this second hour of reaction. This observation will be further discussed in the section 2.2.2 in comparison to the oxygenated groups behavior and the production of carbon monoxide.

The biochars oxygenated during 2h at 280°C presents a higher initial hydrogen production but also a stronger deactivation than the raw biochars in the early stages. Its initial deactivation rate is twice higher than the one of the raw biochar. After 1 hour of treatment, this biochar has been deactivated 10% more than the raw biochars. However, during the deactivation regime 2, its deactivation rate is equal to the one of the raw biochars. Characterizations presented in Chapter III, highlighted that the

amount of oxygenated functions was higher for this biochar (1.26 times higher than the raw biochars). However, its specific surface area was slightly smaller (622 compare to 662 m<sup>2</sup>/g<sub>char</sub> for the raw biochars). Thus, the higher initial hydrogen production could be explained by the higher amount of oxygenated functions. Once the oxygenated functions have been deactivated, the smaller specific surface area of the biochars oxygenated 2h at 280°C led to a faster deactivation.

The hydrogen production on the biochars oxygenated at 280°C during 8h is smaller than the raw biochars since the beginning of the reaction. The deactivation reaction rates during the phases 1 and 2 are similar to the deactivation rates on the raw biochars. Characterizations highlighted that the specific surface area (578 m<sup>2</sup>/g<sub>char</sub>) and pore volume (0.20 cm<sup>3</sup>/g) of this biochars were significantly lower than the one of the raw biochars (662 m<sup>2</sup>/g and 0.219 cm<sup>3</sup>/g). Regarding its amount of oxygenated functions, TPD analyses revealed that a higher amount of oxygen was chemisorbed after 8h than 2h. However Raman analyses highlighted that these oxygenated functions were inserted more deeply in the carbon structures. Thus, these oxygen functions might not be available to react with methane particles.

Hence, the reactivity of the oxygenated biochars seems to be dependent on the oxygenated functions amount at the surface but also from the other physico-chemical properties of the biochars and notably the textural ones. The biochar oxygenated at 340°C is the most interesting material since the initial hydrogen production and stability were both increased.

### 1.3. Partial conclusion on the activities of the raw and functionalized biochars

The raw and functionalized biochars successfully catalyzed methane cracking to produce hydrogen. However a reduction of the production was observed over the reaction for all the biochars certainly due to a deactivation of the surface by coke deposit. The functionalized biochars showed a better reactivity than the raw biochars and especially the mineral impregnated ones. They managed to increase the initial hydrogen production by a factor of 2 to 4 and by a factor 1.8 in the long-term. The biochars oxygenated at 340°C for 2h also presented good performances at the early stages and over the reaction whereas biochar oxygenated at 280°C did not show a good enhancement of the activity which is likely due to their lower textural properties. These observations indicate that all the physico-chemical properties: oxygenated content, mineral, carbon matrix and textural properties play a role in the catalytic methane cracking reaction. This section presented the hydrogen production in function of the chemical properties which has been enhanced by the functionalization treatment.

Then it would be of great interest to compare the hydrogen production versus the four physico-chemical properties of the biochars to get insights into their individual influence. This is the topic of the next section.

## 2. Interaction between the biochars reactivity and their physico-chemical properties

The goal of this section is to investigate the role of the surface properties of the biochars towards methane cracking. Literature highlighted that the physical and chemical properties of the carbonaceous materials could play a distinct role in the methane cracking reaction [4], [5]. In fact, the chemical functions present at the surface of the fresh catalyst should govern the initial stages of the reaction. Over the reaction, carbon deposit (from the cracking of the methane molecule) blocked the access to these functional groups until a complete cover of the surface. Then, over the reaction, the accumulation of the carbon deposit layers tends to fill the pores and diminish the pore volume and the specific surface area (see Figure IV-3). Thus, the activity over the process should be related to the evolution of the textural properties (specific surface area and pore volume). The section is divided into two subsections: the first one discusses the relationship between the surface properties and the initial hydrogen production. The second section is focused on the activity over the reaction and the causes of deactivation.

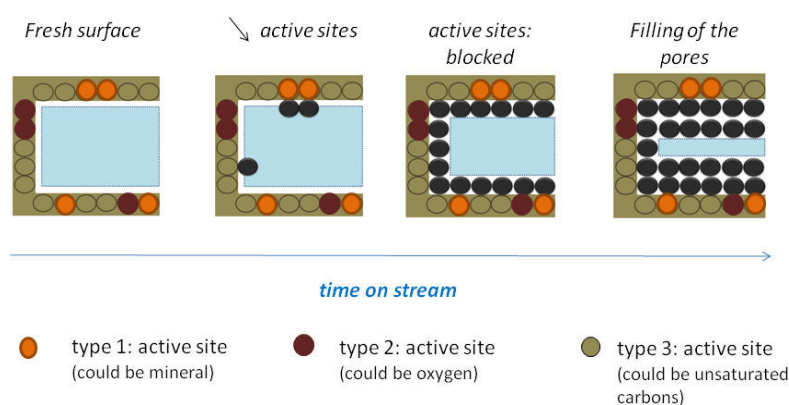


**Figure IV-3: Illustration of the initial active sites role and the potential clogging by carbon deposit**

## 2.1. Initial conversion

In a first part, the focus is put on the interaction between the initial hydrogen production and the physico-chemical properties of the biochars. To compare the activity of the different biochars the initial hydrogen productions from curves presented in Figure IV-1 and Figure IV-2 have been plotted versus the four physico-chemical properties which have been characterized for the seven biochars: the oxygenated functions, the mineral content, the carbon matrix and the textural properties (see Figure IV-4).

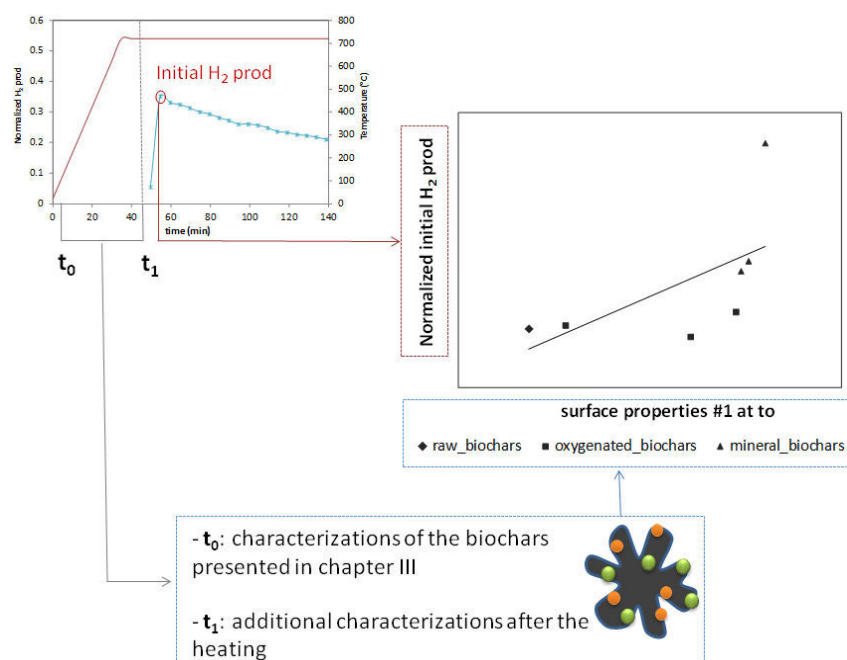


**Figure IV-4: Relation between the surface properties and the initial hydrogen production**

Results of characterization (at  $t_0$  on Figure IV-4) presented in the chapter III have been utilized to perform the study. In addition, some complementary characterizations such as ESEM and XRD (at  $t_1$  on Figure IV-4) were carried out to get information on the impact of the heating under pure nitrogen (prior to the methane introduction) on the chemical groups present at the biochars surface.

### 2.1.1. ***Impact of the textural properties on the initial hydrogen production***

Literature highlighted that the initial conversion of methane into hydrogen did not seem to be correlated to the textural properties [6] but rather to the chemistry of the surface. In this study the influence of the specific surface area, the total pore volume and the average pore diameter on the initial hydrogen production were investigated. It has been highlighted in Chapter III that the functionalized biochars present different textural properties. In fact, the impregnation tends to decrease the specific surface area and the pore volume whereas the oxygenation at 340°C significantly increases them.

Figure IV-5 presents the normalized hydrogen production ( $\text{mol}_{\text{H}_2}/\text{mol}_{\text{CH}_4}/\text{mg}_{\text{char}}$ ) versus the three textural properties. The initial hydrogen production is presented versus the specific surface area, pore volume and mean pore diameter in the Figure IV-5.A, B and C respectively. The different types of biochars (raw, oxygenated or mineral impregnated) are represented with different symbols. If one observes the overall set of data no interaction between the specific surface area, the total pore volume, the average pore diameter and the hydrogen production can be highlighted. For example, a similar hydrogen production ( $8 \times 10^{-4} \text{ mol}_{\text{H}_2}/\text{mol}_{\text{CH}_4}/\text{mg}_{\text{char}}$ ) was highlighted for two different specific surface areas (340 and  $620 \text{ m}^2/\text{g}_{\text{char}}$ ). For similar values of pore volume ( $0.11$  and  $0.14 \text{ cm}^3/\text{g}_{\text{char}}$ ), two hydrogen initial productions can be observed ( $8.3 \times 10^{-4}$  and  $16.0 \times 10^{-4} \text{ mol}_{\text{H}_2}/\text{mol}_{\text{CH}_4}/\text{mg}_{\text{char}}$ ). For two different pore diameters (5 and 10 Å), a similar hydrogen production could be observed ( $8 \times 10^{-4} \text{ mol}_{\text{H}_2}/\text{mol}_{\text{CH}_4}/\text{mg}_{\text{char}}$ ). However, these different observations mostly concerned the mineral impregnated biochars. If we focused on the raw and oxygenated biochars, it is possible to observe a trend between the textural properties and the hydrogen production. In fact, the higher the specific surface area, the total pore volume and the pore diameter, the higher the hydrogen production. It seems that the textural properties play a role in the initial reactivity of the oxygenated biochars whereas in the mineral impregnated biochars the loss of activity due to the decrease of specific surface area is counterbalanced by the high reactivity of the minerals. It could be possible that the access to the minerals at the surface is easier than the oxygenated functions.

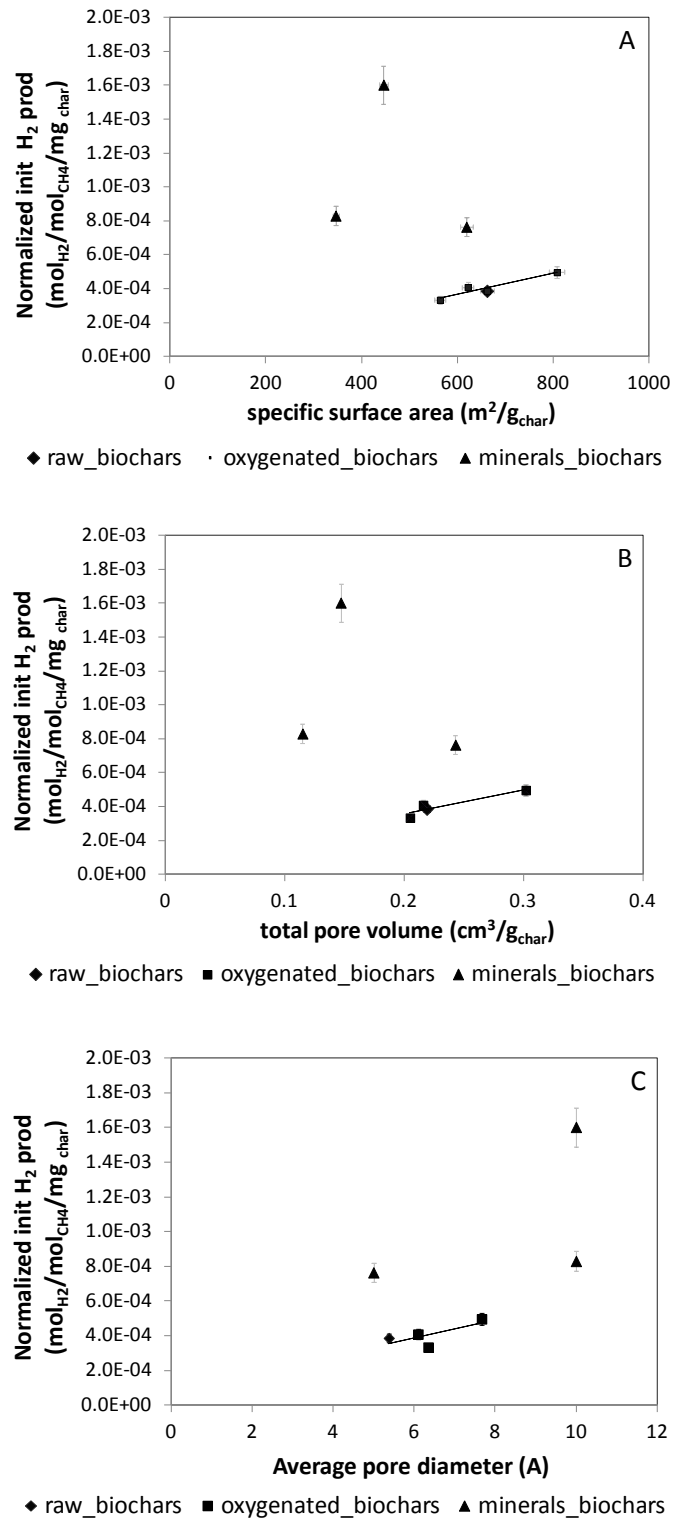
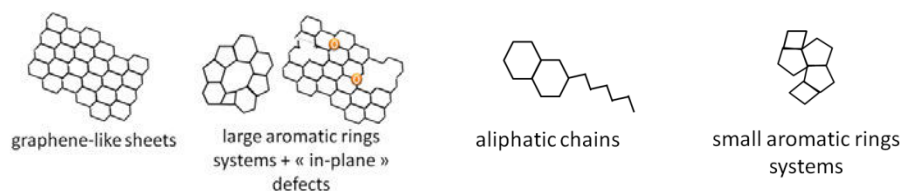


Figure IV-5: Normalized initial hydrogen production (mol<sub>H<sub>2</sub></sub>/mol<sub>CH<sub>4</sub></sub>/mg<sub>char</sub>) versus textural properties (A) specific surface area, (B) total pore volume and (C) average pore diameter of the biochars at t<sub>0</sub> (which have been characterized in the Chapter III)

### 2.1.2. **Impact of the carbon matrix on the initial hydrogen production**

The carbon matrix is a mix of well-ordered short range structures (graphene-like sheets) and disordered structures such as aromatic rings systems of various cycle size, aliphatic chains and structures containing “in-plane” defects such as heteroatoms or vacancies Figure IV-6. The literature highlighted that aromatic rings systems are the most reactive carbon structures towards gasification [7]. Regarding methane cracking, disordered structures have also been highlighted to be more active than well-ordered graphite likely due to the lower constraint on the carbon atoms. However “in-plane” imperfections have been emphasized to be the most reactive [8]. In fact methane cracking consists in a series of dehydrogenations. Unsaturated dangling carbons (close to vacancies or edge carbons) in the turbostratic biochars could potentially attract the hydrogen atoms from the methane molecule and manage to break the C-H bonding.



**Figure IV-6: Carbon structures at the biochars surface**

Both of the functionalization treatments tend to enhance the amount of structures which are represented by the D-band on a Raman spectrum. This band gathers a large variety of structures such as the defects contained in the graphene-like sheets but also the large aromatic rings and the diamond structures (definition in Chapter 2, section 2.5). The concentrations of the other disordered structures were not impacted in the same manner according to the treatment and the operating conditions. Regarding the oxygenated biochars, oxygenation at 280°C tends to slightly increase the amount of amorphous structures due to the oxygen insertion in the carbon rings. However at 340°C, the combustion of a part of the carbon matrix during the oxygenation tends to drastically diminish this type of structures. Regarding the mineral impregnated biochars, the treatment only increased the amount of structures containing “in-plane” imperfections ( $I_D$ ) due to the minerals embedding and thus the concentrations of the other structures have been lowered compared to the raw biochars.

Initial hydrogen productions were plotted versus amount of graphitic structures ( $I_G/I_{tot}$ ) however no trend was observed. In fact, for a similar value of the ratio (about 24%) different hydrogen productions were observed ( $3.0 \times 10^{-4}$ ,  $7. \times 10e^{-4}$  and  $16.0 \times 10^{-4}$  mol<sub>H<sub>2</sub></sub>/mol<sub>CH<sub>4</sub></sub>/mg<sub>char</sub>). The initial hydrogen production was then plotted versus the amount of structures containing “in plane” imperfections ( $I_D/I_{tot}$ ) in Figure IV-7. The data points seem to show that the amount of “in-plane”

defects into the carbon matrix increases the initial hydrogen production (see Figure IV-7). In fact, the increase of disorder in the graphene-like sheets should increase the amount of active sites. However the D band gathers a large variety of structures, their distribution in the different functionalized biochars could differ and thus some precautions have to be taken in the interpretation.

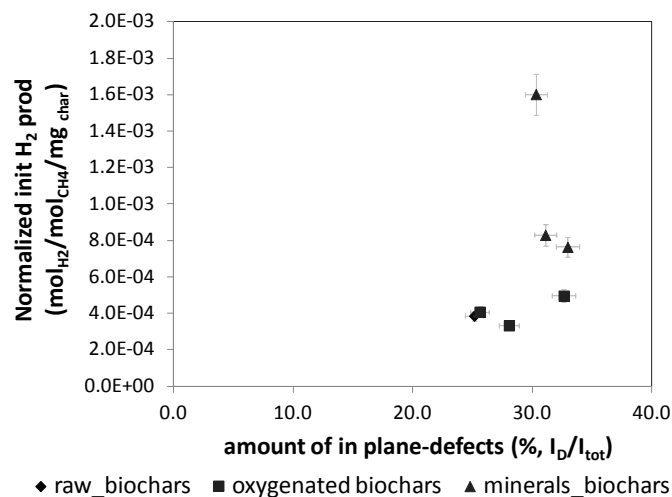


**Figure IV-7: Normalized initial hydrogen production versus "in-plane" defects amount in the carbon matrix of biochars at  $t_0$**

To go further and determine if the "in-plane" imperfections structures are the main active sites, the hydrogen production has been plotted versus ratios of the "in-plane" defects amount over the other main carbons structures: graphitic structures ( $I_D/I_G$ ), small aromatic rings ( $I_D/I_{VI+Vr+GI}$ ) and aliphatic chains ( $I_D/I_S$ ). Figure IV-8 presents the initial hydrogen production versus ratios of "in-plane" defects over: (A) graphite, (B) small aromatic rings and (C) aliphatic chains. The three graphs show that the highest the "in-plane" imperfections amounts over the other carbons structures, the highest the hydrogen production. Figure IV-8.A, Figure IV-8.B and Figure IV-8.C show that the structures containing "in-plane imperfections" are more reactive than the graphite, amorphous rings and aliphatic chains. One data point (triangular symbol) is always out of range which corresponds to the K-chars. ESEM analyses of its surface shown a special shape of potassium particles on that chars which should be highly reactive and could explain the difference in reactivity compared to the other biochars. This is further discussed in the section 2.1.4.

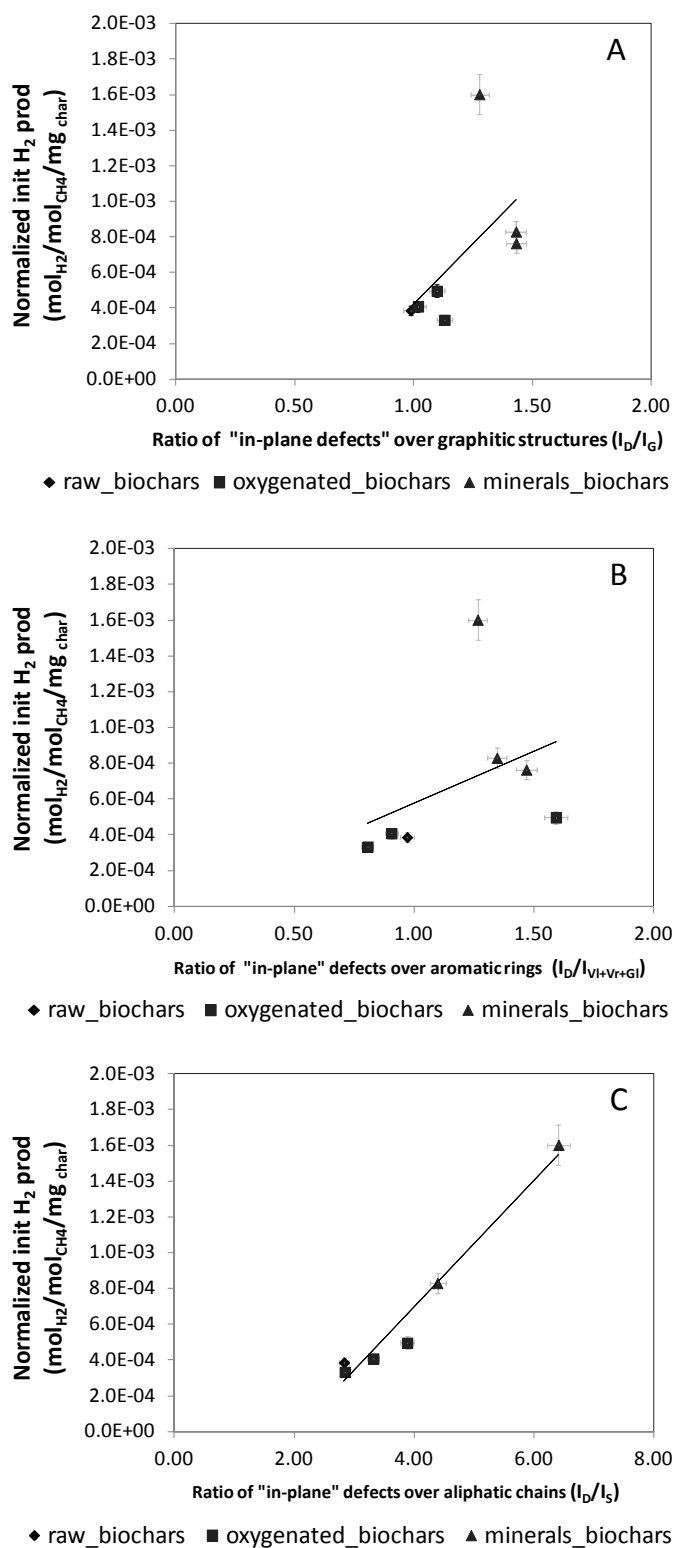


**Figure IV-8: Normalized initial H<sub>2</sub> production versus ratios of "in-plane" defects over the different others main carbon structures: (A) graphite, (B) small aromatic rings and (C) aliphatic chains of the biochars at t<sub>0</sub>**

These observations support that disordered structures in the graphene-like sheets such as the “in-plane” defects (unsaturated carbons close to vacancies) are the most attractive structures for hydrogen atoms capture and this highlights that saturation of carbon atoms in the matrix is an important parameter for dehydrogenation of the methane [9]–[11]. In structures containing defects such as vacancies, neighbor carbon atoms of the vacancy could be charged negatively and thus attract hydrogen atoms from the methane molecule. In graphite and amorphous aromatic rings, carbons atoms are not saturated (so a double bond can potentially be replaced by a simple bond and a bond with an hydrogen atom) however carbon atoms are strongly bonded to other carbons in benzene rings. In small aromatic rings cycles, even if carbon atoms are strongly bonded, heteroatoms (especially at carbon edges) can potentially be active sites. The aliphatic chains seem to be the least attractive which is coherent since the carbons are saturated and cannot form additional linkages (see Figure IV-8.C).

### 2.1.3. ***Impact of the oxygenated functions on the initial conversion***

Oxygenated functions could impact the initial methane conversion by two different mechanisms. The first assumption is that the desorption of the non-stable oxygenated groups at the reaction temperature (700°C) increases the number of unsaturated carbons at the biochars surface which have been highlighted to be active sites for methane cracking in the previous section and in the literature [10]. As example, an illustration of the consequences on the carbon structure of the lactone desorption is provided in Figure IV-9. One can observe that the removal of lactone creates polarization of the remaining carbons and thus could increase their reactivity towards methane cracking. This phenomenon is similar for the other oxygenated functions. The second hypothesis is that the oxygenated functions which remain at the surface could be active sites on their own. In fact, remaining oxygenated functions at the surface above 700°C are mainly basic functions such as quinone or pyrone. They have been depicted to be active site for dehydrogenation reaction [2]. Quinone are composed of 2 C=O functional groups at the edge carbons of benzene rings and represents a Lewis base [12]. A lone pair from an oxygen atom of the quinone function could attract an hydrogen from a methane molecule and activate the C-H breaking (see Figure IV-10).

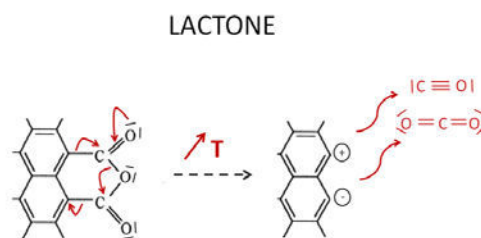


**Figure IV-9: Scheme of the possible mechanism of lactone desorption during heating and the remaining charged carbon structures**

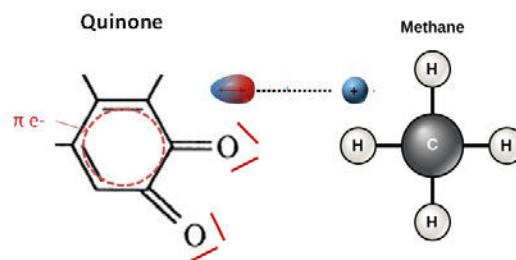


**Figure IV-10: Scheme of the quinone attraction of the hydrogen atom from the methane molecule**

The two possibilities are discussed in this section. First the influence of CO and CO<sub>2</sub> desorption during the heating and thus the role of unsaturated carbons is discussed. For the seven biochars, production of CO and CO<sub>2</sub> has been observed during the heating. Regarding the oxygenated biochars, these gases are coming from the desorption of the non-stable oxygenated functions (such as observed in the TPD analysis). However for the mineral impregnated biochars, such as for the oxygenated biochars, the origin of the CO<sub>2</sub> and CO production could be the desorption of the organic O-containing groups activated by the minerals. However it could come from the transformation of inorganic matter as well (discussed more in detailed further in this paragraph). Figure IV-11 presents the CO<sub>2</sub> and CO productions over the heating for the raw and oxygenated biochars. One can see that the gases production is higher for the oxygenated biochars than for the raw biochars. This is in agreement with the results of TPD presented in Chapter III. In fact, the O<sub>2</sub> gas-phase treatment mostly increased weak acid functions on the biochars surface which desorb in the 300-800°C temperature range. Thus, these functions, previously added by the O<sub>2</sub> gas-phase treatment, desorbed during the heating prior to the methane introduction. In Chapter III, it has been shown that the oxygenated functions concentration at the biochars surface followed this sequence: ox2h\_340°C > ox8h\_280°C > ox2h\_280°C > raw\_char. On Figure IV-11, one can observe that the amount of desorbed oxygenated function followed the same sequence: ox2h\_340°C > ox8h\_280°C > ox2h\_280°C > raw\_char. This means that most of the added functions were not stable at the reaction

temperature and were removed prior to the reaction. Thus the increase of the amount of unsaturated carbons at the biochars surface follows the same order.

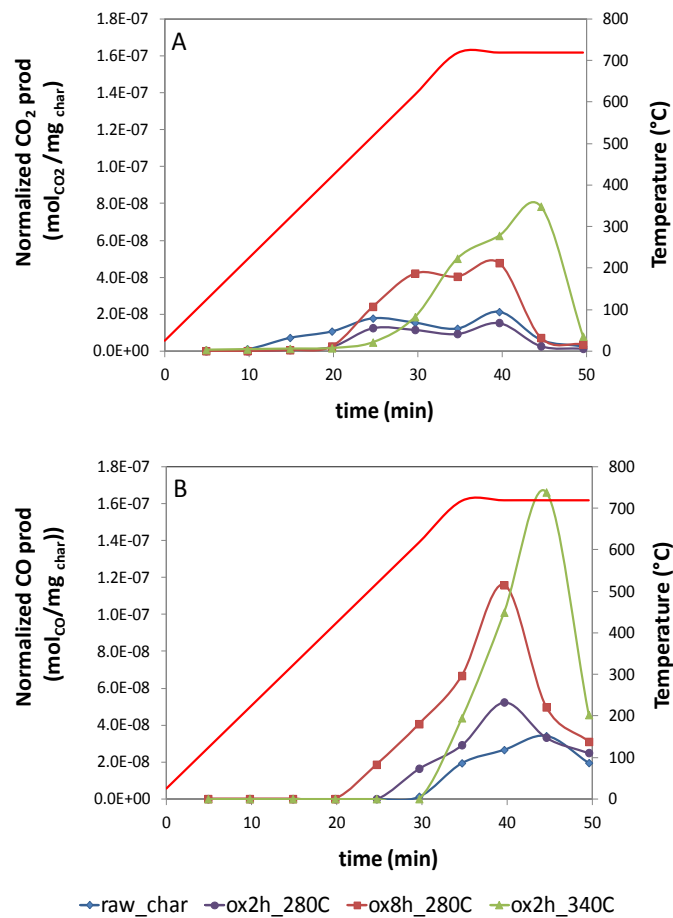


**Figure IV-11: Normalized moles of (A) CO<sub>2</sub> and (B) CO produced during the heating of the raw and oxygenated biochars up to the reaction temperature at 700°C with 20°C/min**

Figure IV-12 presents the CO<sub>2</sub> and CO productions over the heating for the raw and mineral impregnated biochars. Both gases produced are enhanced for the mineral impregnated biochars. This is in agreement with the literature which highlighted that minerals catalyze the organic devolatilization. XRD analyses have been performed on the mineral impregnated biochars at  $t_1$  (after the heating and prior to methane introduction) to determine the minerals composition (they are presented in the section 2.1.4). From these analyses, the differentiation between the different sources of gas production (organic and inorganic) was possible. It has been highlighted that the CO<sub>2</sub> production at 200°C for the K-chars and the CO<sub>2</sub> produced at 700°C for the Ca-chars came from the minerals transformation (further discussed in the section 2.1.4). However, the carbon dioxide and carbon monoxide produced during the heating at higher temperature than 200°C for the K-char and at lower temperature than 700°C for the Ca-char should come from the organic devolatilization

catalyzed by the presence of the minerals. Thus the hydrogen productions for the seven biochars were plotted versus the amount of CO<sub>2</sub> and CO (coming from the organic non stable oxygenated groups) to evaluate the relation.

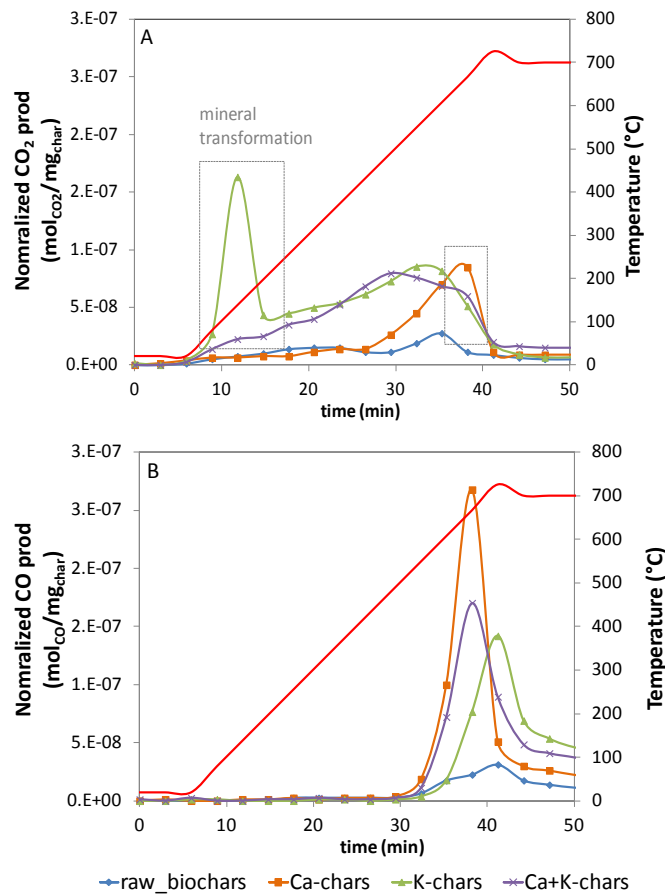


**Figure IV-12: Normalized (A) CO<sub>2</sub> and (B) CO productions (mol/mg<sub>char</sub>) during the heating up to 700°C prior to methane cracking on the raw and functionalized biochars**

Figure IV-13 presents the initial hydrogen production as function of the organic oxygenated functions desorbed during the heating of the biochars prior to the introduction of the methane mixture. One can observe a trend between the CO<sub>2</sub> and CO productions during the heating and the initial hydrogen production. The higher the oxygenated groups desorption, the higher initial hydrogen production. However, a significant amount of oxygenated function should have been desorbed to observe an impact on the methane cracking. In fact, an increase of the hydrogen production is only observable for the biochars oxygenated at 340°C during two hours and for the mineral impregnated biochars. This observation reinforces the conclusion that unsaturated carbons are active sites for methane cracking. In fact, the desorption of these groups causes electronic disorder in the carbon matrix. This leaves some carbon atoms with an excess of electrons and some others with a deficit. This duality of

sites is appropriate for dehydrogenation. In fact, Szymanski et al. [12] reported that dehydrogenation of alcohols is due to the presence of both Lewis acid and base. The base attracts the hydrogen atoms while the acid reacts with the alcoholate.

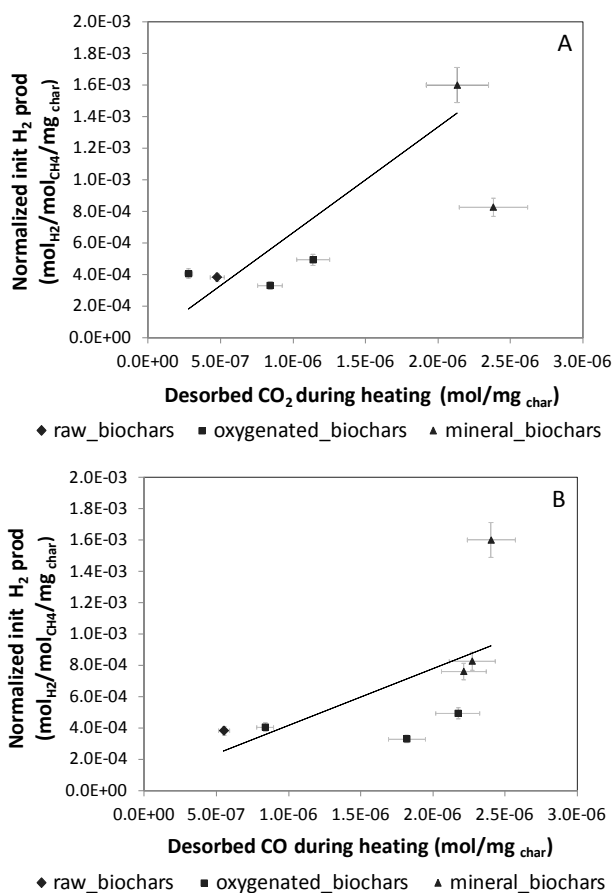


**Figure IV-13: Normalized hydrogen production versus oxygenated functions desorbed during the heating prior to methane introduction (A) CO<sub>2</sub>, (B) CO**

The stable oxygen functions at the biochars surface at 700°C are ether, quinone and pyrone. Only the ether concentration has been enhanced on the oxygenated biochars. Figure IV-14 presents the TPD results for the raw and oxygenated biochars (already presented in section 2 of Chapter III) and highlights the O-containing groups which are non stable at 700°C (red lines). The amount of quinone and pyrone remain the same as on the raw biochars. The oxygen atoms of these functions have lone pair of electrons which could attract hydrogen atoms from the surface. This could explain the better hydrogen production of the biochars oxygenated 2h at 340°C. However another phenomenon seems to be possible. Some carbon monoxide has been detected at the early stages of the methane cracking reaction (see Figure IV-15). The simultaneous production of carbon monoxide during the hydrogen production indicates that remaining oxygenated functions at the surface could be active sites. It should come from the reaction between carbon from the methane molecule and oxygen

from the biochars surface. Carbon monoxide was also produced during the methane cracking on functionalized biochars. The same initial concentration was detected which could indicates that pyrone and quinone functions are the active sites for this reactions. In fact, literature highlighted their catalytic role in dehydrogenation reactions [2].

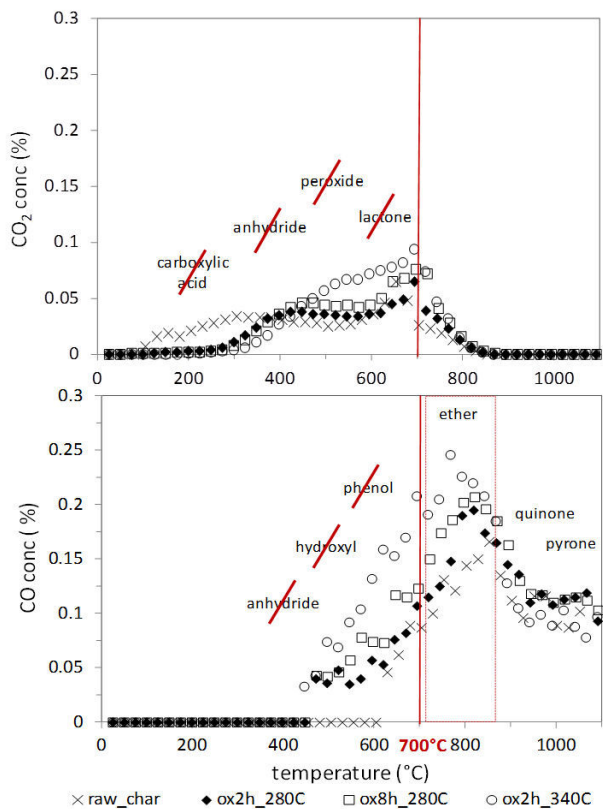


**Figure IV-14: Comparison of the TPD curves of the raw biochars and biochars oxygenated at 280°C (2 and 8h) and at 340°C 2h and the remaining oxygenated functions at 700°C**

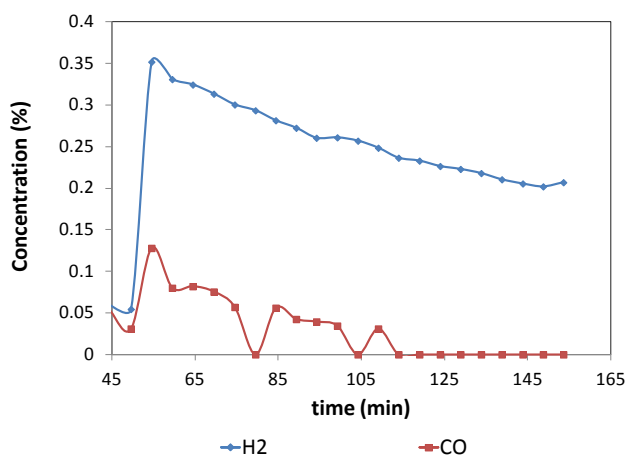


**Figure IV-15: Hydrogen and carbon monoxide productions during the methane cracking at 700°C, 20% CH<sub>4</sub> on the raw biochars**

Thus, the desorption of the non-stable oxygenated groups seem to impact positively the hydrogen production since it increases the number of unsaturated carbons at the surface which have been depicted to be active sites in the literature. Ether and basic oxygenated functions should be reactive as well for methane cracking. In fact, the production of carbon monoxide during the methane cracking indicates that carbons from the methane molecule react with oxygen from the biochars surface.

#### 2.1.4. *Impact of the minerals on the initial conversion*

The influence of the presence of calcium and potassium at the biochars surface on the methane conversion into hydrogen has been investigated. These minerals components were highlighted to be catalysts in char gasification [13][14]. Metal particles dispersed at the chars surface are considered as active sites where a gasifying agent first dissociates. For example Wigmans et al. [15] proposed a mechanism of steam gasification in which water molecules decomposed on carbonate crystals followed by spill-over of oxygen-containing radicals. Potassium has been depicted to be the most reactive AAEMs, especially KOH and  $K_2CO_3$  chemical forms. In addition Hüttinger et al. [16] stated that non-stoichiometric oxide  $K_xO_y$  ( $y < x$ ) was the active specie which acts as dissociation center for water and transfers the oxygen to the carbon surface. However the activity of the minerals is dependent from the dispersion and the size of the minerals particles, their structure and their intercalation between the graphene-like sheets. Regarding methane cracking, the key point is the activation of the C-H bonding. AAEM carbonates and oxides are ionic crystals which are composed of cations (charged positively) and superoxydes  $O^{2-}$  or carbonate ions (both charged negatively). Thus the attraction of hydrogen atoms and the activation of the C-H bonding should be enhanced with the increase of the minerals at the biochars surface.

Figure IV-16 shows the initial hydrogen production versus the mass percentage of the loaded mineral for the Ca-chars, K-chars and Ca+K-chars. The Ca-chars and the K-chars contain approximately the same amount of added mineral component. Indeed, calcium represents 5.8 wt% in the Ca-chars and potassium 6.1% in the K-chars. However one can observe on Figure IV-16 that the initial hydrogen production is twice higher for the K-chars than for the Ca-chars. As for the Ca+K-chars is concerned, its initial hydrogen production is of  $8.3 \times 10^{-4} \text{ mol}_{H_2}/\text{mol}_{CH_4}/\text{mg}_{char}$ . Calcium and potassium are present in the same concentration (2.5 wt%) at the biochars surface which represents half of their concentrations in the Ca-chars and K-chars. If the reactivity of the calcium and potassium were independent, the activity of the Ca+K-chars should be an average of the activities of the Ca-chars and K-chars and should reach  $12 \times 10^{-4} \text{ mol}_{H_2}/\text{mol}_{CH_4}/\text{mg}_{char}$ . If the addition of these two minerals had a

positive synergy, the activity should have been higher than  $12 \times 10^{-4} \text{ mol}_{\text{H}_2}/\text{mol}_{\text{CH}_4}/\text{mg}_{\text{char}}$ . However results highlighted that the activity of the Ca+K-chars was lower.

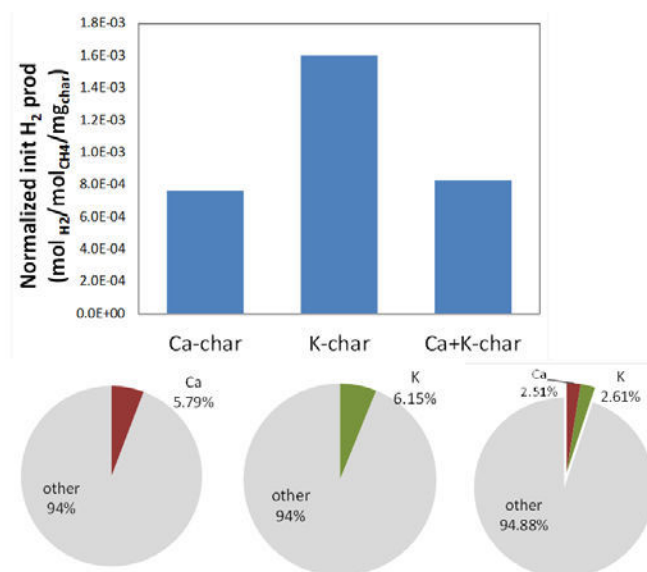


**Figure IV-16: Comparison of the initial hydrogen productions ( $\text{mol}_{\text{H}_2}/\text{mol}_{\text{CH}_4}/\text{mg}_{\text{char}}$ ) of the different mineral impregnated biochars in function of their calcium and potassium loading (wt%)**

Several observations can explain the lower activity of calcium compared to potassium. Regarding their mineral structure, it has been observed that during the heating (prior methane cracking) carbon monoxide and carbon dioxide were produced which is due to the organic devolatilization in one hand and on the other hand to minerals structures transformations. For example, the  $\text{CO}_2$  produced at  $200^\circ\text{C}$  during the heating of the K-chars should come from the transformation of potassium hydrogen carbonate (desorbed from the biochars surface) into carbonate potassium following (see Figure IV-17) [16]. The second broad peak on Figure IV-17 at  $600^\circ\text{C}$  should come from the devolatilization of organics groups since the transformation of potassium carbonate into potassium oxide ( $\text{K}_2\text{O}$ ) is happening at temperature higher than  $1200^\circ\text{C}$ . Regarding the Ca-char, calcium carbonate decomposes into calcium oxide and carbon dioxide at about  $700^\circ\text{C}$  (see Figure IV-17). This transformation usually occurs at about  $800^\circ\text{C}$ . However, the presence of a carbon support could lowered the temperature reaction [17]. XRD analyses have been performed on the mineral impregnated biochars after the heating under nitrogen up to  $700^\circ\text{C}$  to confirm these minerals structures transformations. In fact, calcium oxide was detected instead of calcium carbonate in the Ca-chars. Some calcium hydroxide was also identified which should come from the reaction at the surface between the calcium oxide and some oxygenated groups such as phenol. Regarding the K-chars, potassium carbonate was identified. Thus, after the heating up to  $700^\circ\text{C}$  under nitrogen,

calcium was not in carbonate structure anymore but in oxide and hydroxide forms whereas potassium is mainly in carbonate form. A first explanation of the lower activity of the Ca-chars than the one of the K-chars could be that one of the calcium forms is not reactive towards methane cracking. Calcium oxide which is a Lewis base should be active for methane cracking since the superoxide ion ( $O_2^-$ ) should attract hydrogen atoms. However calcium hydroxide could also be reactive since this is a ionic crystal and thus the  $(OH)^-$  group is also a potential active site.

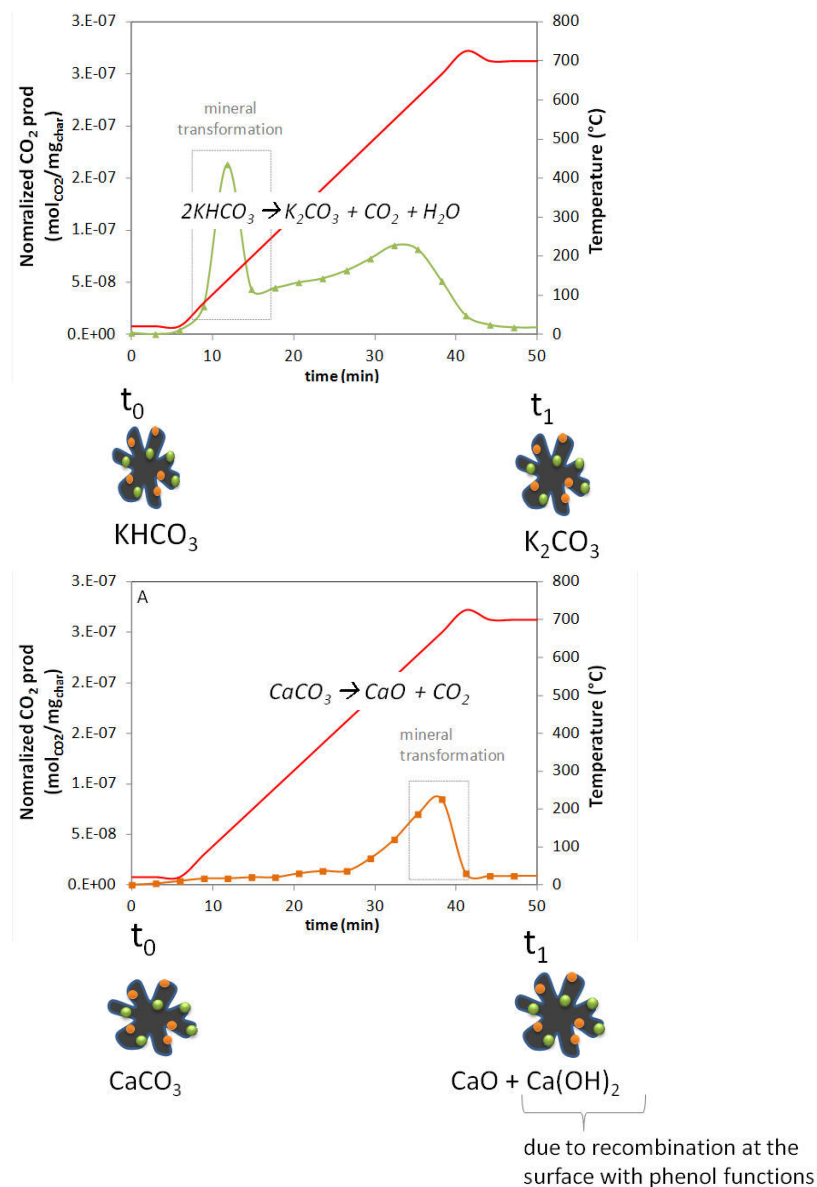


**Figure IV-17: Minerals transformations during the heating for K-chars and Ca-chars and the minerals composition at  $t_0$  and  $t_1$**

The difference in reactivity could also be explained by the dispersion and the shape of the minerals onto the biochars surface. Figure IV-18 presents ESEM pictures at different locations of the K-chars surface after heating under nitrogen at 700°C (prior to methane cracking introduction).

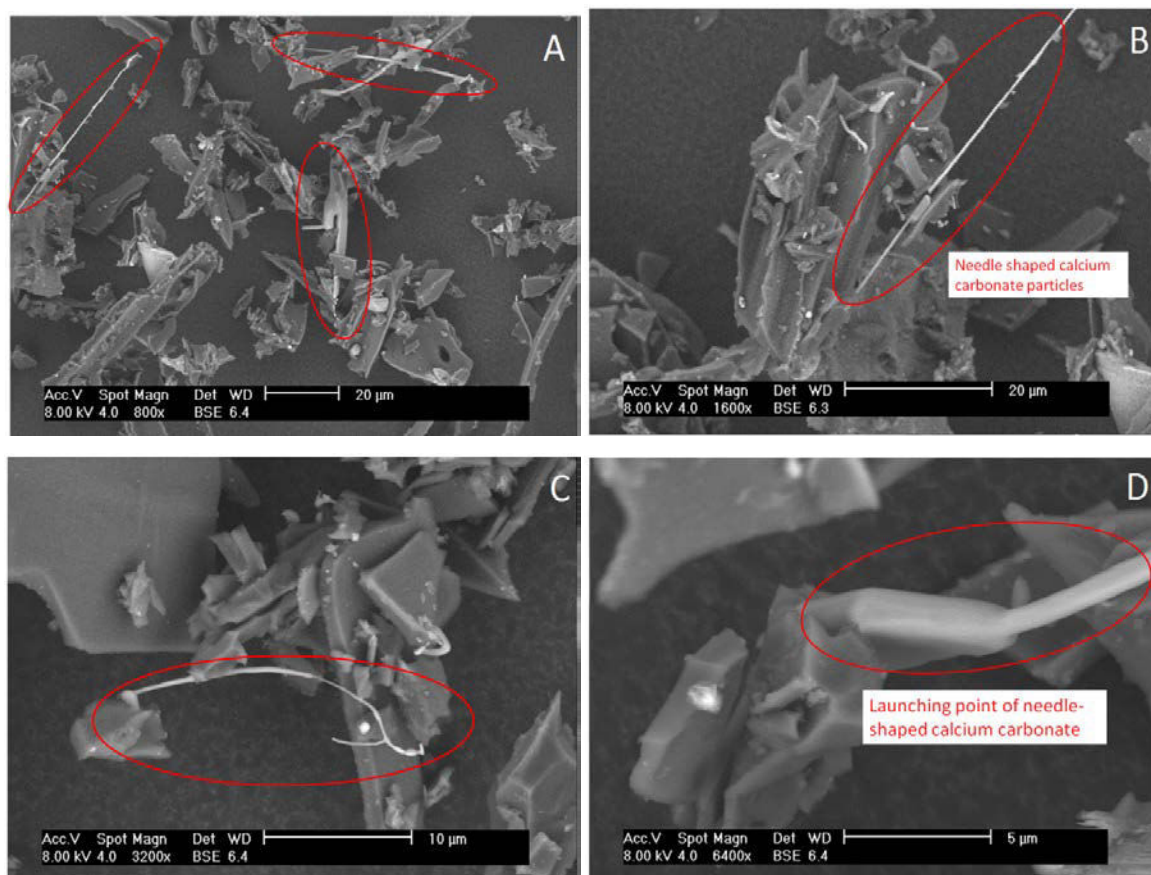


**Figure IV-18: ESEM pictures of the needle-shaped  $K_2CO_3$  crystals on the K-chars surface at different locations of the surface and for different magnitudes: (A) x800, (B) x1600, (C) x3200, (D) x 6400 at  $t_1$**

On Figure IV-18, one can observe long needle-shaped crystals coming from the base of the crystals at the char's surface. In fact, at this temperature ( $700^\circ C$ ) potassium starts to evaporate, it could react in the gas-phase with the  $CO_2$  (coming from the devolatilization of the organic matter and the decomposition of the potassium carbonate) and recrystallize into this needle-shaped structures. Perander et al. [18] reported similar crystal shape of potassium carbonate on potassium loaded spruce wood char gasified up to  $850^\circ C$  under  $CO_2$ . This particular shape of crystal offers a high exchange surface. In addition, they are first expose to the methane molecule since they are salient structures. Thus, this observation could explain the difference in reactivity of the Ca-chars and K-chars.

A second observation can also provide insights into the better reactivity of the K-chars. Figure IV-19 presents ESEM pictures of the Ca-chars and K-chars surface for the same magnitude. The comparison of the two pictures highlights the difference in mineral particle size and their dispersion. In fact, the potassium carbonate particles are much smaller than the calcium ones which should explain their better cohesion on the char surface. The potassium particles surface also seems to be soft whereas

calcium crystals are more granular and coarse. Calcium particles seem to be an agglomerate. Thus less mineral particles are active on the Ca-chars surface since no contact can be established with the methane molecules for calcium particles which are in the core of the agglomerate. In addition silicate calcium forms were detected at the Ca-chars surface by EDS analyses (which are known to be inactive structures) whereas no such complex were identified at the K-chars surface. In fact, the amount of silicon on the Ca-chars is higher than on the K-chars. X-ray fluorescence has shown that silicon represents 0.32 and 0.11 wt% in the Ca-chars and K-chars respectively. Thus the agglomeration of the particles and the formation of silicates should have decreased the reactivity of calcium towards methane cracking. On the contrary the high dispersion and the needle-shaped  $K_2CO_3$  particles should have favored the hydrogen production on the K-chars.

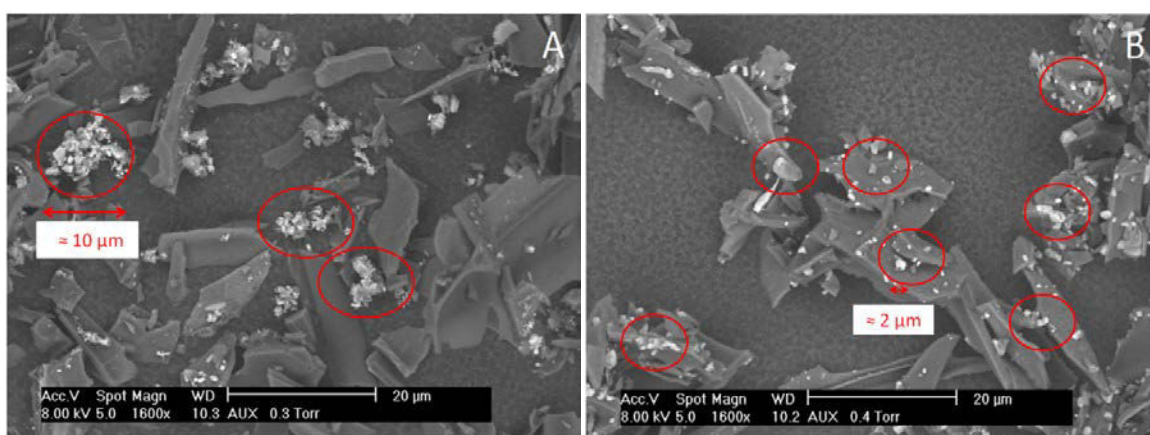


**Figure IV-19: ESEM images of (A) Ca-chars and (B) K-chars for a magnitude x1600 at  $t_1$**

Regarding the Ca+K-chars, XRD analyses were performed after heating (at  $t_1$ ) and highlighted that  $K_2Ca(CO_3)_2$  was still present at the surface. The activity of this mineral structure should be lower than the structures containing only potassium or calcium since the hydrogen production for the Ca+K-chars was lower than the expecting mathematical average of the Ca-chars and K-chars. Regarding the shape and dispersion of the particles, they are similar to the potassium carbonate structures observed on the K-chars (see Figure IV-20). They are small (size of about 5  $\mu m$ ) well dispersed and with a smooth surface. Hence, the loss of activity did not seem to be due to particle agglomeration. It should be due to a lower reactivity of this structure.

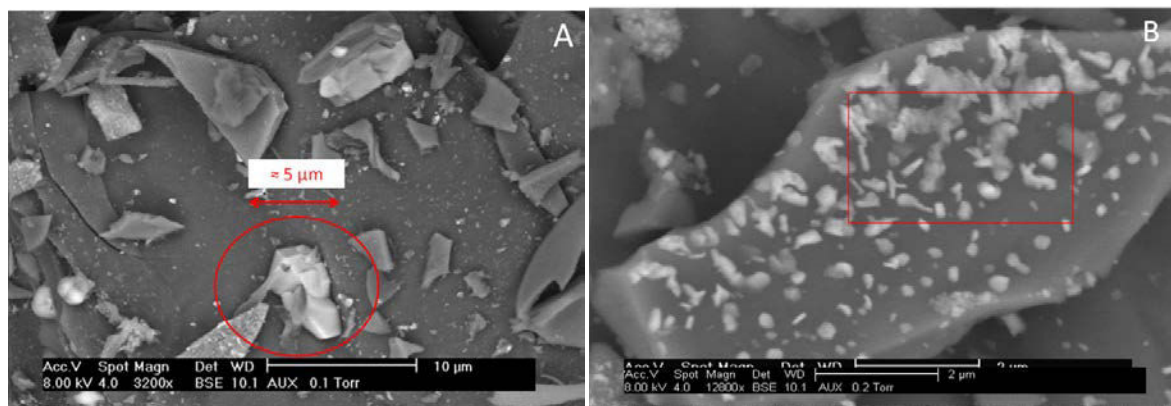


Figure IV-20: ESEM pictures at different locations of the Ca+K-chars at  $t_1$

### 2.1.5. *Partial conclusion on the interaction between the physico-chemical properties of the biochars and the initial hydrogen production*

This section highlighted that the initial hydrogen production is dependent from the different physico-chemical properties of the biochars surface. Minerals have been depicted to be the most reactive structures since an increase of their concentration at the biochars surface leads to a significant enhancement of the hydrogen production. Potassium has shown the best performances (hydrogen production 4 times higher than the raw biochars) which should be due to the needle-shaped potassium carbonate particles which have been formed during the heating and offer a large surface of exchange. The calcium particles also showed a high reactivity (enhancement of the hydrogen production by 2). However the agglomeration of the particles should have decreased its reactivity. The complex formed ( $K_2Ca(CO_3)_2$ ) in the Ca+K-chars showed a reactivity lower than the structures containing only calcium or potassium from the Ca-chars and K-chars. Regarding the oxygenated functions, ether and basic group such as quinone and pyrone are the only stable functions at 700°C and seem to be involved in the methane cracking. In fact, carbon monoxide was detected simultaneously as hydrogen production which should come from the reaction of carbon atoms from the methane molecule with the O-containing groups of the surface. The desorption of the acids functions during the heating leads to increase the amount of unsaturated carbons which also seemed to be active sites such as “in-plane” defects structures containing heteroatoms and vacancies. The textural properties play a role on the initial activity as well, especially for the raw and oxygenated biochars. In fact, for the mineral impregnated biochars, the high reactivity of the AAEMs particles seemed to have counterbalanced the loss of specific surface area.

Over the reaction, a diminution of the hydrogen production has been observed for the all set of methane cracking experiments. This decrease should be due to the surface deactivation. The next section discusses the deactivation of the surface and the consequences on the hydrogen production.

## 2.2. Deactivation by carbon deposit

Deactivation of the catalyst can be of different nature: poisoning, sintering, coke deposit (or fouling) or attrition. Poisoning and coke deposit are classified into the chemical deactivations. In fact, in the two cases, the number of active sites at the surface of the catalyst decreases over the reaction due to the chemisorption of species on them. For example, sulfur poisoning is an issue in catalytic processes utilizing reduced metals as the active phase. Even at very low concentrations, sulfur may cause significant deactivation due to the strong metal-S bonds formation. Regarding coke deposition, it consists of a carbonaceous material accumulation at the surface of the catalysts coming from the condensation of aromatic compounds which are secondary products in tars reforming reaction [19]. It represents a technological bottleneck as well since coke can be deposited on the catalyst surface but also all over the vessel clogging the reactor and causes fouling. Sintering and attrition are physical degradation mechanisms of the catalyst. Sintering consists in a reduction of the porosity followed by a loss of specific surface area due to the diffusion and agglomeration of the particles from the material with increase of temperature or pressure. Attrition represents a loss of the mechanical strength of the catalyst and causes detachment of some pieces which reduces the efficacy. It is often encountered in the fluidized bed reactors due to collision and abrasion of the catalysts particles.

Literature reported that catalysts in the methane cracking reaction are deactivated due to carbon deposit and loss of specific surface area during the experiments [1], [20]. In fact, sintering and attrition are not the main potential deactivation process since experiments were performed in fixed bed (attrition is often occurring in fluidized bed) and at not too high temperature (effects of sintering are observable on chars above 1000°C). Regarding sulfur poisoning, no sulfur compounds are present in the gas phase. In this section, the deactivation of the different physico-chemical properties of the biochars and the consequences on the hydrogen production over the reaction is discussed. Thus additional characterizations have been performed on biochars after the methane cracking (at  $t_f$  see Figure IV-21).

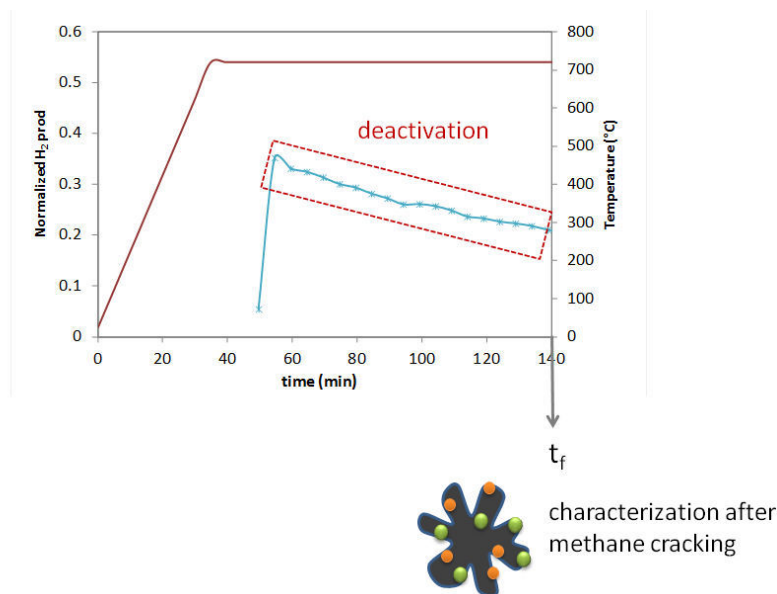


**Figure IV-21: Interaction between deactivation and modification of the surface properties**

### 2.2.1. *Deactivation of minerals*

Methane cracking tests have been performed in a thermogravimetric analyzer to record the mass evolution during the methane cracking on biochars. Figure IV-22 presents the hydrogen cumulated production and the mass gain recorded during the methane cracking on minerals impregnated biochars at 700°C in a thermogravimetric analyzer. One can observe that catalysts start gaining mass when methane is introduced in the reactor and hydrogen is produced. After 2 hours on stream, the raw biochars gained 6% in mass, the Ca-chars and Ca+K-chars 9% and the K-chars 11% (the bump in the K-char curve is not real). The higher the mass gain, the higher the hydrogen cumulated production. This should indicate that the mass gain is due to carbon deposit on the catalyst during the conversion of methane into gaseous hydrogen and solid carbon. Thus, the deactivation of the catalyst should be due to this carbon deposit.

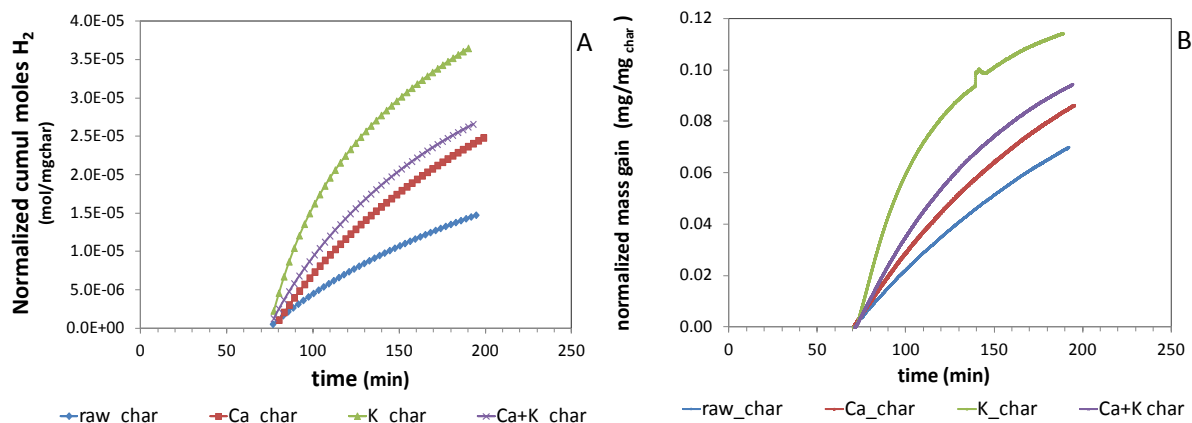


**Figure IV-22: Methane cracking reaction on raw and minerals impregnated biochars in a thermogravimetric analyzer: (A) cumulative hydrogen production, (B) mass gain**

ESEM pictures have been performed on the deactivated biochars to evaluate the minerals dispersion and shape modifications over the reaction. Regarding the K-chars, no needle-shaped  $K_2CO_3$  crystals were detected anymore after 1 hour of methane cracking. This should indicate that these structures quickly reacted with methane molecules. In fact, they were salient, they offered a large surface area of exchange and were the first structures the methane molecules encountered approaching the surface catalyst. However they should be very fragile and may be destroyed while reacting. Regarding the shape and dispersion of other minerals structures, they did not seem to have been impacted by the reaction. Similar minerals particles were observed on the surface of the biochars prior to and after the methane cracking. However on some minerals a thin layer of organic material can be detected (see Figure IV-23). This should be carbon deposit but EDS analyses cannot give insights into the chemical composition of these structures since they are too thin. However they clearly blocked the access to the minerals they are into.

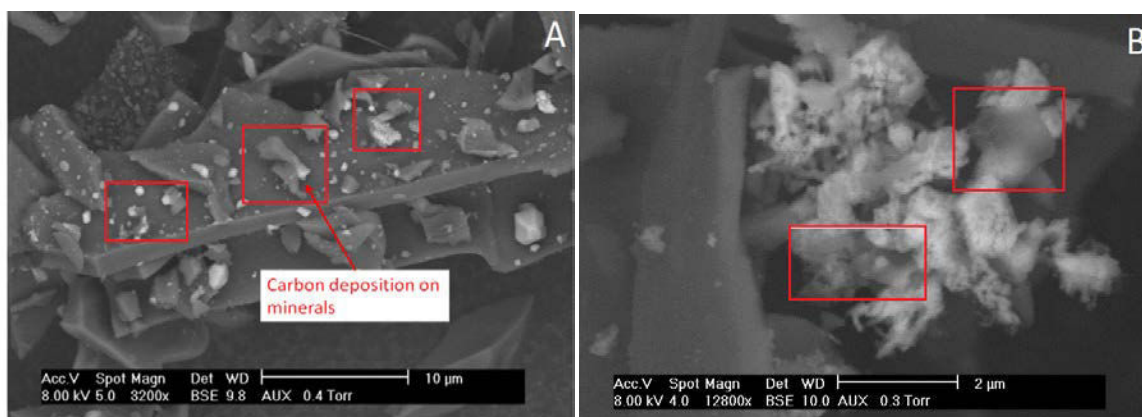


**Figure IV-23: ESEM pictures of the carbon deposit at the surface of the (A) Ca-chars and (B) Ca+K-chars after 2h (at  $t_r$ ) of methane cracking at 700°C**

### 2.2.1. *Deactivation of the carbon surface*

ESEM analyses have been performed on the deactivated raw biochars (see Figure IV-24). At some locations of the carbon surface, a specific roughness was highlighted such as a thin film of particle which covers the surface. It can make one think of carbon deposit layers onto the carbon structures. This indicates that such as for the other chemical species, carbon structures are not active anymore due to carbon deposit.

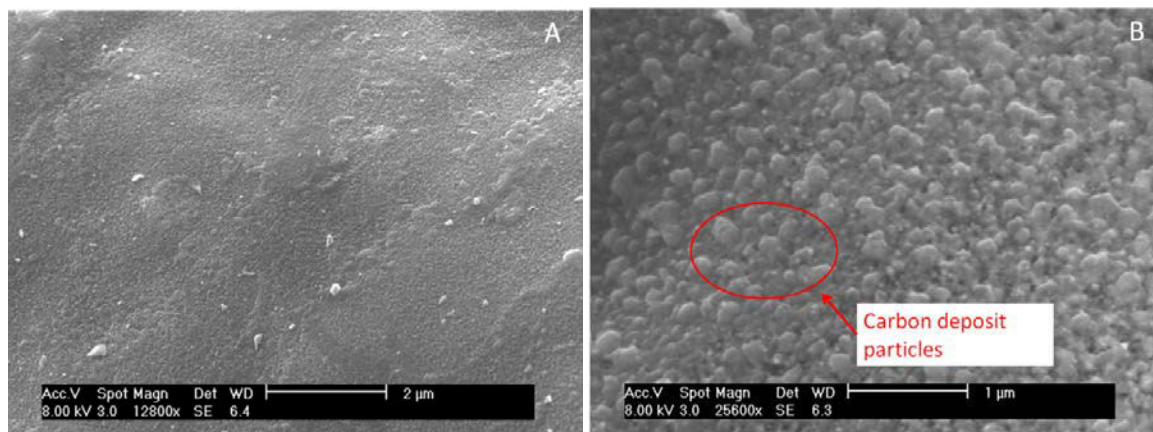


**Figure IV-24: ESEM pictures of the raw biochars after 2h (at  $t_f$ ) of methane cracking at 700°C**

Regarding the structure of the carbon deposit, one can observe on Figure IV-24 that the carbon film seems to be amorphous. This differs from what it is observed on metal-based commercial catalysts. For example, on nickel supported catalysts, filament of carbon nanotubes (which are very well-ordered structures) are usually observed on metal particles after methane cracking reaction [21], [22]. However literature highlighted that the carbon deposit structure is dependent from the catalyst it is chemisorbed into. On carbonaceous catalyst, different types of structure were observed such as nanofilament or amorphous carbon deposit [1]. Abbas et al. [23] claimed that carbon deposit produced from the decomposition of methane should be turbostratic carbon which means that it is more ordered than amorphous carbons but less than graphite. This observation can make one think that the carbon deposit could be reactive to crack other methane molecules over the reaction. In fact, it has been highlighted that disordered carbons could be reactive towards methane cracking. However its reactivity should be lower than the active sites of the catalyst since the activity keeps decreasing over the reaction.

### 2.2.2. Role of oxygenated functions in the deactivation

Hydrogen production on the oxygenated biochars was also decreasing over time. The deactivation pattern was similar to the raw biochars which should indicate that a carbon deposit deactivates the active sites on the surface. However, the hydrogen curves of the biochars oxygenated at 340°C during 2 hours slightly differs from the one of the other biochars. It seems to be irregular and correlated to the carbon monoxide production. Figure IV-25 presents the carbon monoxide and hydrogen productions for the raw biochars and biochars oxygenated 2 hours at 340°C. In Figure IV-25.A, during methane cracking on the raw biochars, carbon monoxide is recorded during the first hours and then no production is detected anymore. As for the biochars oxygenated at 340°C, carbon monoxide is produced for the entire reaction. The hydrogen production decreases steadily during the 30 minutes and then continues to diminish but more irregularly. The hydrogen productions shape is very similar to the carbon monoxide one. An explanation could be that some phenol groups -which have been significantly more increased by the oxygenation at 340°C than at 280°C and which desorb between 700°C-800°C- are desorbing during the methane cracking and lead to liberate unsaturated carbons which directly react with methane molecule. Thus this progressive desorption of oxygenated groups leads to liberate some active sites over the reaction and deactivation process seems to be slowed down.

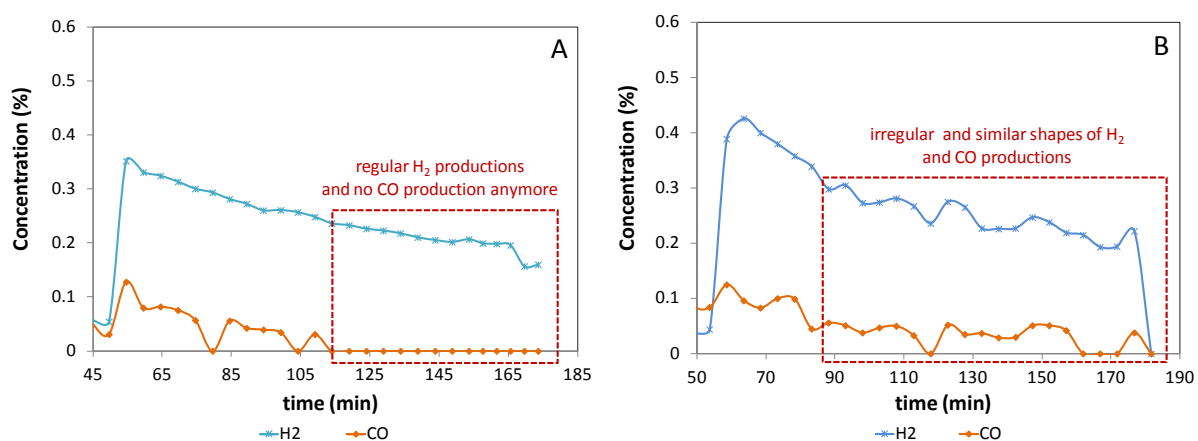


**Figure IV-25: Comparison of the hydrogen and carbon monoxide productions for the (A) raw chars and (B) biochars oxygenated 2h at 340°C during the methane cracking for 2h at 700°C**

### 2.2.3. Reduction of the specific surface area and total pore volume

Catalytic methane cracking tests performed in the Thermogravimetric Analyzer highlighted that the biochars gained 6 wt% due to carbon deposit after 2 hours of methane cracking reaction. From the

amount of carbon deposit a calculation was carried out to evaluate the ratio of the surface occupied by the carbon deposit if we assume a monolayer adsorption (the carbon particle radius is equal to 70 pm). We found that about 10% of the surface should be recovered after the experiments. A previous study performed by Klinghoffer et al. [24] highlighted that the specific surface area and pore volume were diminished by 20% and 30% respectively after methane cracking at 700°C during 3 hours on the same biochars. This indicates that coke deposition quickly blocked the biochars pores and thus the active sites.

#### 2.2.4. ***Partial conclusion on the deactivation of the surface properties and the consequences on the hydrogen production over the reaction***

Partial deactivation occurred during the methane cracking on raw and functionalized biochars due to coke deposit on active sites. Chemical functional groups either minerals or oxygenated functions were deactivated during the first hour of the reaction. The strongest deactivation was recorded on the mineral impregnated biochars and notably on the K-chars due to the destruction of the highly reactive needle-shaped potassium carbonates particles. The Ca and Ca+K-chars also suffered from a quick deactivation. ESEM analyses showed the deposit of a thin layer of carbon on some mineral particles. The oxygenated biochars 2 hours at 280 and 340°C also showed a quicker deactivation than the raw biochars and the biochars oxygenated 8 hours. It should be due to the oxygen removal during the reaction (production of carbon monoxide) and the deposit of carbon. After one hour of treatment, the deactivation patterns were similar for the raw and functionalized biochars which should indicate that the chemical groups at the surface were not the predominant function governing the reaction but rather the textural properties and the filling of the pores.

### **3. Conclusion**

This chapter approached the activity of the raw and functionalized biochars towards methane cracking and the relationship with their physico-chemical properties. Methane cracking at 700°C during two hours was performed on seven biochars: the raw, the minerals impregnated and three oxygenated biochars (which presented different physico-chemical properties: ox2h\_280C, ox8h\_280C and ox2h\_340C). All these biochars have different surface properties which have been characterized in the Chapter III. The functionalized biochars presented a higher reactivity than the

raw biochars. Minerals were depicted to be the most efficient. However all the biochars suffered from deactivation due to carbon deposit. The initial and activities during the two hours were correlated to the physico-chemical properties of the biochars.

Literature highlighted that the initial reactivity should be a function of the surface chemical species whereas the long-term activity should be rather govern by the textural properties [1]. Results of this study highlighted that the chemical species played a prevalent role in the early stages of the reaction, notably the minerals. However the textural properties were also depicted to be involved, especially during the cracking on the oxygenated biochars. Chemical species such as minerals (carbonate and oxide), “in-plane” imperfections, unsaturated carbons and basic oxygenated functions have been identified to be the active sites. They were all found to be Lewis bases which means they are able to break a C-H bonding by attracting the hydrogen atoms with their lone pair of electrons. The presence of Lewis acid sites close to the Lewis bases is also interesting which is the case, for example, in the ionic crystal structure. In fact, Szymanski et al. [12] claimed that the presence of both Lewis base and acid sites accelerated the alcohol dehydrogenation. Results have shown that minerals ionic structures were the most efficient active sites since the activity of the three mineral impregnated biochars were higher than the one of the raw and oxygenated biochars. The K-chars was revealed to be the most reactive. The presence of needle-shaped potassium carbonates due to the evaporation of some potassium particles at the reaction temperature enhanced the reactivity. These specific shapes of crystal offered a high surface area of exchange, are salient and should be part of the first structures that the methane molecule encountered before reaching the biochars surface. Calcium particles were also active, even if their activity was halved compared to the potassium. The simultaneous addition of potassium and calcium at the biochars surface (Ca+K-chars) did not present a synergetic effect. The complex which has been formed ( $K_2Ca(CO_3)_2$ ) did not show a high reactivity. Carbon structures containing “in-plane” imperfections and unsaturated carbons confirmed results presented by Serrano et al. [25] to be the most active carbon structures. In addition, the desorption of non-stable oxygenated groups during the heating (prior to the methane introduction) enhanced the amount of defects and unsaturated carbons at the biochars surface and increased the reactivity of the biochars. Basic oxygenated functions and ether (which are the only O-containing groups remaining at the surface at the reaction temperature) should play a catalytic role since some carbon monoxide was identified at the early stages of the reaction and the hydrogen production was enhanced for the biochars oxygenated 2 hours at 280 and 340°C. The textural properties, notably for the oxygenated biochars played a role in the initial stages. In fact, the biochars oxygenated 8h at 280°C did not showed a reactivity higher than the raw biochars since its specific surface area and pore volume were significantly smaller.

As for the performances of the functionalization processes are concerned, the O<sub>2</sub> gas-phase treatment at 340°C and mineral impregnation lead to increase the hydrogen production. However the mineral impregnation seems to be the most interesting treatment for two main reasons: the minerals have been highlighted to be the most reactive and notably potassium, and their catalytic effect on the organic devolatilization during the heating increases the amount of unsaturated carbons at the surface which have been depicted to be active sites. Hence, the potassium impregnation is the most efficient treatment. The deactivation of its active sites is due to carbon deposit, the investigation of a regeneration process to clean the surface should lead to extend the gain in efficacy of the catalyst.

Regarding the deactivation process, it seemed to be the same for all the biochars and due to a carbon deposit onto the catalyst surface such as presented in the literature for other carbonaceous materials. The deactivation of the chemical groups seemed to be quick and strong (during the first hour of the reaction). In fact, the deactivation rates (during regime 1) of the mineral impregnated biochars and oxygenated biochars (2h at 280C and 340C) were from 2 to 10 times higher than the one of the raw biochar. During the phase 2, the hydrogen production was still higher for the functionalized biochars (1.8 times) than for the raw biochar. However, their deactivation rates (for the three mineral impregnated biochars and ox2h\_340°C) were significantly lowered and were all close to twice higher than the deactivation rate of the raw biochar. ESEM pictures showed the presence of a thin film of carbon deposit on minerals and carbon surface. The carbon deposit seemed to be amorphous or turbostratic but not well-ordered (it could be active sites for methane cracking but with a low reactivity). Due to this carbon deposit, the reactivity of minerals decreased over time. In fact, at the early stages of the reaction the hydrogen production on the minerals impregnated biochars was 2 to 4 times higher than the one of the raw biochars. After one hour of treatment, it stabilized and was 1.5 times higher than the raw biochars. Regarding the oxygenated biochars, the two biochars treated at 280°C presented a lower long-term activity than the one of the raw biochars certainly due to their lower textural properties. The biochars oxygenated two hours at 340°C showed better performances than the raw biochars over the reaction which should be due to its higher specific surface area and pore volume and its higher amount of oxygenated functions desorbing in the 700-800°C range. In fact, the oxygenation at 340°C drastically increased the phenol functions which normally desorbed around 700-750°C. It is possible that phenols progressively desorbed during the reaction and let unsaturated carbons which are active sites. Thus, the decrease of hydrogen production is mainly due to chemical species access clogging by carbon deposit at the catalyst surface. Hence, the textural properties became the prevalent property for the stable activity. An

illustration which sums up the main conclusions on the interaction between the physico-chemical properties and the biochars reactivity is presented in Figure IV-26.

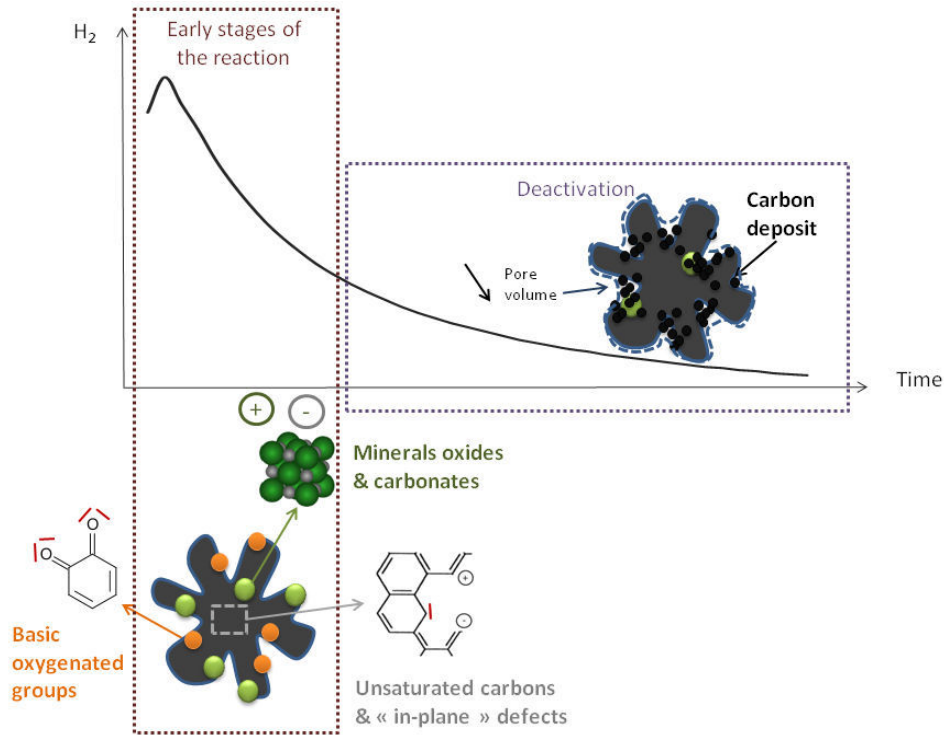


**Figure IV-26: Illustration of the main conclusions on the interaction between the physico-chemical properties and the biochars reactivity**

## Bibliography

- [1] B. Fidalgo and J. Á. Menéndez, "Carbon materials as catalysts for decomposition and CO<sub>2</sub> reforming of methane: A review," *Chinese J. Catal.*, vol. 32, no. 1, pp. 207–216, 2011.
- [2] J. L. Figueiredo and M. F. R. Pereira, "The role of surface chemistry in catalysis with carbons," *Catal. Today*, vol. 150, no. 1–2, pp. 2–7, Feb. 2010.
- [3] N. Klinghoffer, M. Castaldi, and A. Nzihou, "Catalyst properties and Catalytic Performance of Char from Biomass Gasification," *Ind. Eng. Chem. Res.*, vol. 51, no. 40, pp. 13113–13122, 2012.
- [4] A. Dufour, A. Celzard, V. Fierro, F. Broust, C. Courson, A. Zoulalian, and J. N. Rouzaud, "Catalytic conversion of methane over a biomass char for hydrogen production: deactivation and regeneration by steam gasification," *Appl. Catal. A Gen.*, vol. 490, pp. 170–180, 2015.
- [5] I. Suelves, J. L. Pinilla, M. J. Lázaro, and R. Moliner, "Carbonaceous materials as catalysts for decomposition of methane," *Chem. Eng. J.*, vol. 140, no. 1–3, pp. 432–438, 2008.
- [6] R. Moliner, I. Suelves, M. J. Lázaro, and O. Moreno, "Thermocatalytic decomposition of methane over activated carbons: Influence of textural properties and surface chemistry," *Int. J. Hydrogen Energy*, vol. 30, no. 3, pp. 293–300, 2005.
- [7] D. M. Keown, J. I. Hayashi, and C. Z. Li, "Drastic changes in biomass char structure and reactivity upon contact with steam," *Fuel*, vol. 87, no. 7, pp. 1127–1132, 2008.
- [8] D. P. Serrano, J. A. Botas, J. L. G. Fierro, R. Guil-López, P. Pizarro, and G. Gómez, "Hydrogen production by methane decomposition: Origin of the catalytic activity of carbon materials," *Fuel*, vol. 89, no. 6, pp. 1241–1248, 2010.
- [9] L. Huang, E. E. Santiso, M. B. Nardelli, and K. E. Gubbins, "Catalytic role of carbons in methane decomposition for CO- and CO<sub>2</sub>-free hydrogen generation.," *J. Chem. Phys.*, vol. 128, no. 21, p. 214702, 2008.
- [10] A. Dufour, A. Celzard, V. Fierro, E. Martin, F. Broust, and A. Zoulalian, "Catalytic decomposition of methane over a wood char concurrently activated by a pyrolysis gas," *Appl. Catal. A Gen.*, vol. 346, no. 1–2, pp. 164–173, Aug. 2008.
- [11] F. Vautard, J. Dentzer, M. Nardin, J. Schultz, and B. Defoort, "Influence of surface defects on the tensile strength of carbon fibers," *Appl. Surf. Sci.*, vol. 322, pp. 185–193, Dec. 2014.
- [12] G. S. Szymański and G. Rychlicki, "Importance of oxygen surface groups in catalytic dehydration and dehydrogenation of butan-2-ol promoted by carbon catalysts," *Carbon N. Y.*, vol. 29, no. 4–5, pp. 489–498, Jan. 1991.
- [13] M. Q. Jiang, R. Zhou, J. Hu, F. C. Wang, and J. Wang, "Calcium-promoted catalytic activity of potassium carbonate for steam gasification of coal char: Influences of calcium species," *Fuel*, vol. 99, pp. 64–71, 2012.
- [14] M. P. Kannan and G. N. Richards, "Potassium catalysis in air gasification of cellulosic chars," *Fuel*, vol. 69, no. 8, pp. 999–1006, 1990.
- [15] T. Wigmans, H. Haringa, and J. a. Moulijn, "Nature, activity and stability of active sites during alkali metal carbonate-catalysed gasification reactions of coal char," *Fuel*, vol. 62, no. 2, pp. 185–189, 1983.
- [16] K. J. Hüttinger and R. Mingos, "The influence of the catalyst precursor anion in catalysis of water vapour gasification of carbon by potassium," *Fuel*, vol. 65, no. 8, pp. 1122–1128, 1986.
- [17] M. P. Kannan and G. N. Richards, "Calcium catalysis in air gasification of cellulosic chars," *Fuel*, vol. 69, no. 8, pp. 999–1006, 1990.

- 
- [18] M. Perander, N. DeMartini, a. Brink, J. Kramb, O. Karlström, J. Hemming, a. Moilanen, J. Konttinen, and M. Hupa, "Catalytic effect of Ca and K on CO<sub>2</sub> gasification of spruce wood char," *Fuel*, vol. 150, pp. 464–472, 2015.
- [19] R. M. Heck and R. J. Farrauto, *Catalytic air pollution control*. Wiley Interscience, 2002.
- [20] V. Shilapuram, N. Ozalp, M. Oschatz, L. Borchardt, S. Kaskel, and R. Lachance, "Thermogravimetric analysis of activated carbons, ordered mesoporous carbide-derived carbons, and their deactivation kinetics of catalytic methane decomposition," *Ind. Eng. Chem. Res.*, vol. 53, no. 5, pp. 1741–1753, 2014.
- [21] A. M. Amin, E. Croiset, and W. Epling, "Review of methane catalytic cracking for hydrogen production," *Int. J. Hydrogen Energy*, vol. 36, no. 4, pp. 2904–2935, 2011.
- [22] B. Rêgo De Vasconcelos, N. D. Tran, D. Pham Minh, A. Nzihou, and P. Sharrock, "Synthesis of carbon nanotubes/hydroxyapatite composites using catalytic methane cracking," *Compos. Interfaces*, vol. 22, no. 7, pp. 673–687, 2015.
- [23] H. F. Abbas and W. M. a W. Daud, "Deactivation of palm shell-based activated carbon catalyst used for hydrogen production by thermocatalytic decomposition of methane," *Int. J. Hydrogen Energy*, vol. 34, no. 15, pp. 6231–6241, 2009.
- [24] N. Klinghoffer, "Utilization of char from biomass gasification in catalytic applications," Thesis: Columbia University, 2013.
- [25] D. P. Serrano, J. a. Botas, and R. Guil-Lopez, "H<sub>2</sub> production from methane pyrolysis over commercial carbon catalysts: Kinetic and deactivation study," *Int. J. Hydrogen Energy*, vol. 34, no. 10, pp. 4488–4494, 2009.



## **V.Chapter 5: Kinetics, mass transfer and modeling at the pore scale**

## Content

1.	Determination of the kinetics parameters and fitting of the deactivation equation .....	193
1.1.	Mass balance in the plug-flow reactor and initial kinetics parameters determination..	193
1.2.	Initial kinetics parameters determination: experimental results.....	195
1.3.	Deactivation of the biochars surface.....	197
2.	Model of H <sub>2</sub> production at the pore scale.....	199
2.1.	Introduction to heterogeneous reaction.....	199
2.2.	Description of the hydrogen concentration evolution into a micropore.....	203
2.3.	Results .....	214
3.	Conclusion .....	222
	Bibliography.....	224

In the previous chapter, some insights into the involvement of the surface properties in the biochars reactivity toward methane cracking reaction were provided. These results should help in future works to select the appropriate functionalization treatment to apply on biochars to optimize their efficiency. This work took part in the experimental physico-chemical characterization of the solid. However, from an overall chemical and reaction engineering perspective, some aspects required some investigations such as mass transfer and kinetics phenomena into the catalytic reactor. In catalysis, a notion of great importance is the rate of the reaction. The utilization of a catalyst has two main impacts: on the one hand it could reduce the temperature of the reaction if the energetic barrier to overcome is significantly smaller in presence of the catalyst. On the other hand, the rate of the reaction should be enhanced if the catalyst is efficient for the reaction targeted. A kinetics study provides expression of the reaction rate as a function of the different parameters which influence the reaction. This kind of study is usually based on experimental results which have been performed in a reactor at the laboratory scale. A kinetics study (global kinetics) at the reactor scale leads to the determination of an expression of the reaction rate as a function of the macroscopic parameters such as the temperature, pressure and reactant concentration. These kinetics parameters are the reaction rate coefficient which estimates the speed of the reaction and the activation energy which is the energetic activation required to make the reaction occurs. The investigation of the influence of the macroscopic parameters on the reaction is of great interest since it provides insights into the impact of parameters which could be directly controlled by the user (temperature, partial pressure). However, the reaction rate could also be influenced by phenomena at a smaller scale than the reactor such as the particle or the pore scales (see Figure V-1). For example, the mass transfer through and into the particle and the reaction/deactivation are phenomena which occur into the particle and at the biochars surface. In previous chapters, some insights on the interactions between the surface properties and their deactivation during the methane cracking have been provided. However the mechanism is not completely understood yet. To get a better understanding, the phenomena should be studied at those scales. The development of a model could be a possibility.

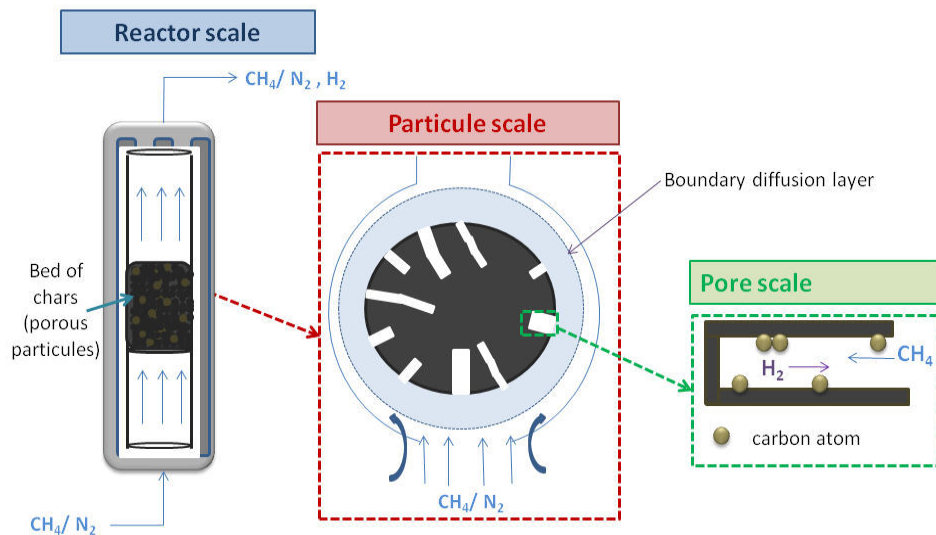


**Figure V-1: Different scales for modeling**

In this chapter, a first study at the reactor scale is presented which consists in determining the initial apparent kinetics parameters for the raw biochars. The main goal of this first work was to determine the apparent activation energy to compare to other carbonaceous materials and evaluate the performance of the biochars. In fact, the activation energy gives insights into the energy required to initiate the reaction. The lower the activation energy, the better the catalyst. Then, experimental data of the stable conversion for the raw biochars were fitted using a coke deposition model to confirm that this is the mode of deactivation of the biochars surface. However the fit did not provide information on the mechanism of coke deposit. The model will be then used for this purpose.

In a second part, a pore scale model which predicts the hydrogen concentration evolution in space and time into a pore and the surface deactivation due to coke deposition is presented. The goal of this study is to give insights into the coke deposit mechanism at the surface and its impact on the hydrogen production. The idea is to compare the hydrogen production deactivation pattern at the output of the pore to the experimental data.

## 1. Determination of the apparent initial kinetics parameters and fitting of the deactivation equation

In the case of an heterogeneous reaction where the surface of the catalyst is deactivated, the reaction rate at any time  $r(t)$  can be expressed as the product of the initial reaction rate  $r_0$  (which represents the highest activity of the fresh catalyst) and a time-dependent function  $a(t)$  (representing the deactivation of the surface over the reaction) (see Eq.V-1). Results of a parametric study performed in the plug flow reactor (ChemBet reactor) on the raw biochars were fitted to determine the initial kinetics parameters and the deactivation expression.

$$r(t) = a(t) \cdot r_0 \quad \text{Eq.V-1}$$

### 1.1. Mass balance in the plug-flow reactor and initial kinetics parameters determination: Power Law

The methane cracking experiments have been performed in a plug flow reactor (ChemBet Instrument) on a fixed bed of 50 mg of raw biochars and for a fixed total flow rate of 15 mL/min. The mass balance on a volume segment ( $dV$ ) of the plug flow reactor is described following Eq.V-2 and Eq. V-3, where  $F_{CH_4,x}$  and  $F_{CH_4,x+dx}$  represent the input and output methane molar flow rates in the volume  $dV$  (see Figure V-2).

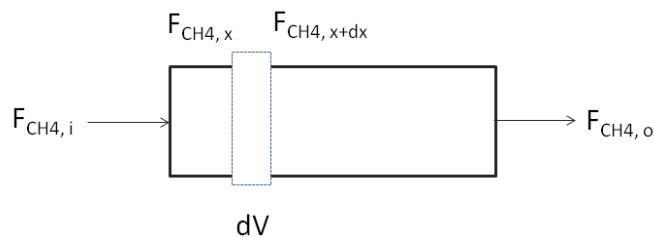


Figure V-2: Mass balance on a section  $dV$  of the plug flow reactor

$$F_{CH_4,x} - F_{CH_4,x+dx} - r dV = 0 \quad \text{Eq.V-2}$$

$$V = F_{CH_4,i} \int_{X_{CH_4,i}}^{X_{CH_4,o}} \frac{dX_{CH_4}}{r} \quad \text{Eq. V-3}$$

In a plug flow reactor, the conversion of the reactant is not constant through the volume. According to the position into the reactor a different conversion is observed. However, for low conversion (<10%), the conversion could be considered as a constant over the reactor (differential reactor). Then, the reaction rate can be expressed following Eq.V-4:

$$r = \frac{X_{CH_4,i} \cdot F_{CH_4,i}}{V} \quad \text{Eq.V-4}$$

Methane cracking is performed on a chemically heterogeneous catalyst. Therefore the global reaction rate should be a sum of several reactions. However according to the literature the main reaction of methane cracking at the initial stage is:



Experimentally, the methane conversion can be evaluated from the hydrogen concentration measurement  $C_{H_2,0}$  provided by the micro gas chromatograph. The expression of the methane conversion is presented in Eq.V-6.

$$X_{CH_4,0} = \frac{C_{H_2,0}}{2C_{CH_4,0}} \quad \text{Eq.V-6}$$

Then the initial value of reaction rate  $r_0$  can be experimentally obtained. The Power law expression for the initial reaction rate  $r_0$  is provided in Eq.V-7 with  $k_0$  the reaction rate constant,  $C_{CH_4,0}$  the initial methane concentration and  $\alpha$  the methane partial order.

$$r_0 = k_0 \cdot C_{CH_4,0}^\alpha \quad \text{Eq.V-7}$$

To determine the methane partial order ( $\alpha$ ) and the initial reaction rate constant ( $k_0$ ) presented in Eq.V-7, the differential method can be applied using experimental data (see Eq.V-8).

$$\ln(r_0) = \alpha \ln(C_{CH_4,0}) + \ln(k_0) \quad \text{Eq.V-8}$$

In fact, from the mass balance on the plug flow reactor, an expression of the initial reaction rate  $r_0$  dependent from the initial methane flow rate  $F_{CH_4,0}$  has been expressed (see Eq.V-4). Thus by plotting  $\ln(r_0)$  versus  $\ln(C_{CH_4,0})$ , it is possible to obtain the value of the methane partial pressure ( $\alpha$ : slope) and the reaction rate constant ( $\ln k_0$ : y-intercept).

In addition, the reaction can be described using the Arrhenius law (see Eq.V-9). Hence, from the determination of the value of  $k_0$  at different temperature, the activation energy  $E_a$  could be determined. Indeed, by plotting  $\ln(k_0)$  in function of  $1/T$ , the slope is  $-E_a/R$  and the y-intercept is  $\ln(A)$ .

$$k_0 = A \cdot e^{-E_a/RT} \quad \text{Eq.V-9}$$

where  $A$  is the pre-exponential factor and  $E_a$  the activation energy.

A set of experiments carried out at various temperatures and methane concentrations will let us validate the Arrhenius law and determine the kinetics parameters. The next section presents the experimental results performed in order to determine the initial kinetics parameters.

## 1.2. Initial kinetics parameters determination: experimental results

Methane cracking experiments have been performed in a plug flow reactor using a methane partial pressure of 0.07, 0.15 and 0.21 atm at 700°C. Then, three additional experiments for a methane partial pressure of 0.07 atm at 650, 700 and 800°C were carried out (thermal cracking only occurs at temperature higher than 850°C). Figure V-3.A shows the hydrogen production for the three methane partial pressures and the Figure V-3.B is for the three different temperatures. One can observe that the higher the methane partial pressure and the greater the temperature, the higher the hydrogen production. According to the previous section, the global reaction is clearly affected by the methane concentration (as in power law, see Eq.V-7) and the temperature (as in Arrhenius law, Eq.V-9). The initial hydrogen concentrations were utilized to determine the initial kinetics parameters: the methane partial order, the reaction rate constant and the activation energy.

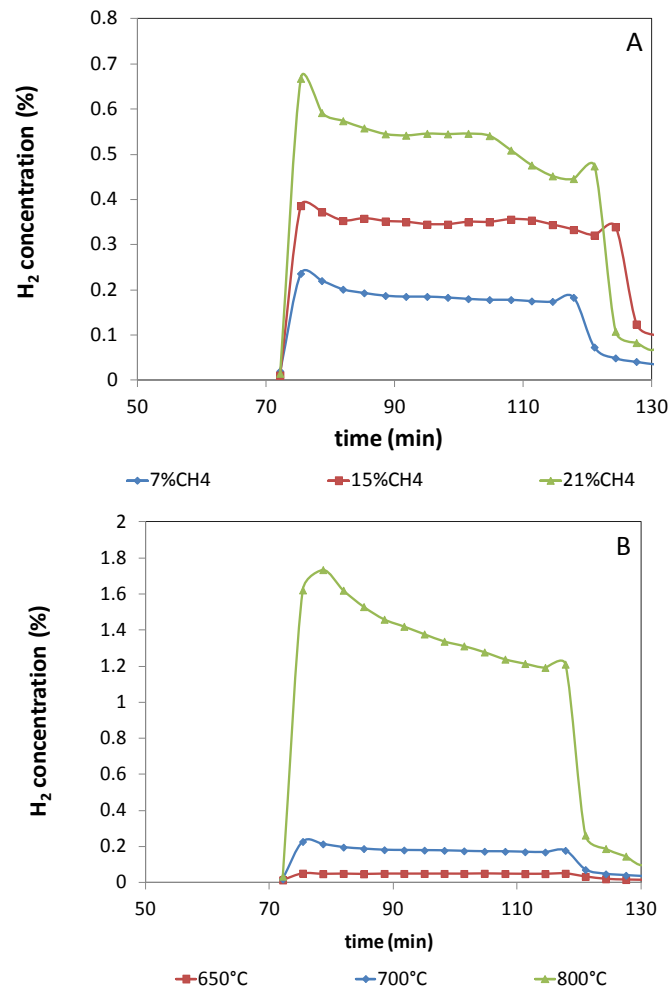


**Figure V-3: Comparison of the hydrogen production in function of (A) the methane partial pressure (0.07, 0.15 and 0.21 bar) and (B) the temperature (650, 700 and 800°C) for 50 mg of biochars (residence time 1.8 s) and a total flow rate of 15 mL/min**

Figure V-4 and Figure V-5 presents the plots of  $\ln(r_0)$  versus  $\ln(C_{CH_4,0})$  and  $\ln(k_0)$  in function of  $1/T$  for the experimental data obtained for the raw biochars. The methane partial order  $\alpha$  has been evaluated at 0.94 which can be approximate as 1 (see Figure V-4). Thus, the reaction rate expression is of pseudo first-order. The reaction rate constant and activation energy were estimated at  $32 \text{ s}^{-1}$  and 192 kJ/mol from Figure V-5 respectively. Muradov et al. [1] presented the activation energies of activated carbons and carbon blacks. Their activation energies were evaluated to be in the following ranges: 160-201 and 205-236 kJ/mol respectively. One can observe that the activation energy of raw biochars is in good agreement with values obtained with other carbonaceous materials.

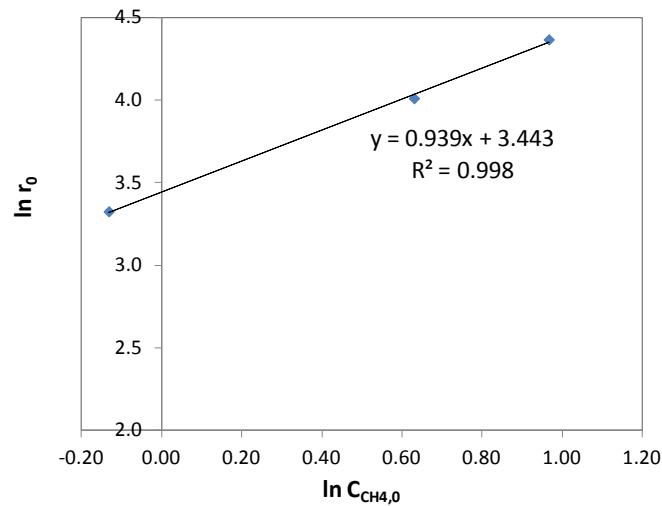


**Figure V-4: Plot of  $\ln(r_0)$  in function of  $\ln(C_{CH_4,0})$  for the determination of the methane partial pressure ( $\alpha$ ) and the reaction rate constant ( $k_0$ )**

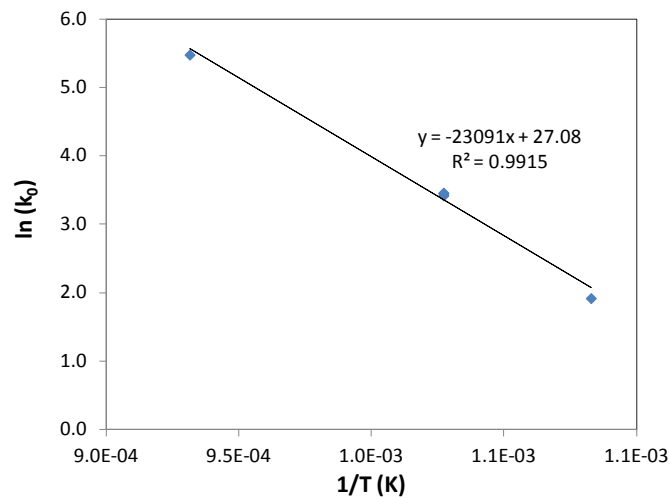


**Figure V-5: Plot of  $\ln(k_0)$  in function of  $1/T$  to determine the activation energy ( $E_a$ )**

Thus, from the parametric study, the global initial apparent kinetics parameters have been determined which correspond to the parameters for the fresh surface of the catalyst. The second part of this section is dedicated to the study of the deactivation of the surface.

### 1.3. Deactivation of the biochars surface

Deactivation has been depicted to be mainly due to coke deposit on the biochars surface. A typical empirical formula: the Voorhies correlation expresses the amount of coke deposit at the surface ( $C_c$ ; in  $g \cdot m^{-2}$ ) to a power of time on stream [2]:

$$C_c = E \cdot t^m \quad \text{Eq. V-10}$$

where:  $E$  and  $m$ : coking parameters

Methane cracking in a TGA instrument on the raw biochars has been performed to monitor the mass gain over time (presented in Figure IV.24 of the Chapter IV). The comparison of the cumulated hydrogen production and the mass gain over the reaction highlights that the mass gain is directly correlated to the deposition of the carbon atoms at the surface. Thus, a fit of the mass gain experimental data has been carried out to check if the coke deposition expression given in the literature was appropriate. Figure V-6 presents the fit of the mass gain monitored during two hours of methane cracking at 700°C on raw biochars.

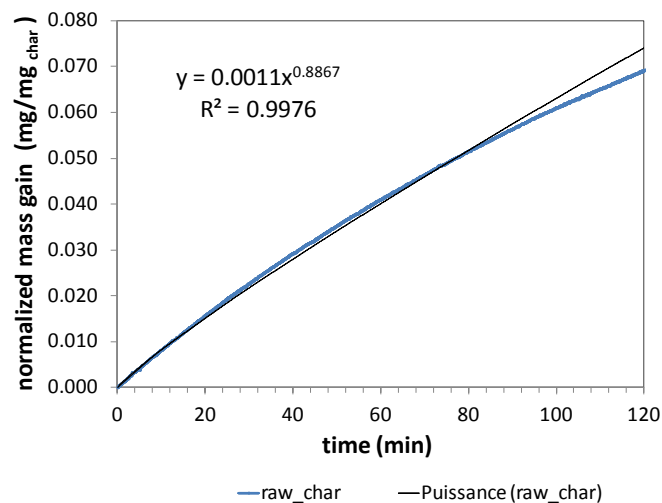


**Figure V-6: Fit of the mass gain over time during the methane cracking on raw biochars at 700°C during 2h ( 80 mL/min, 10% CH<sub>4</sub>/90%N<sub>2</sub>)**

A global conveyable fit was obtained during the first 100 min which reinforces the conclusion that coke deposit is the main deactivation process occurring during methane cracking on biochars. The expression of the coke concentration over time is presented in Eq.V-11. However above 100 minutes, the experimental data slightly diverge from the model. This means that the coke deposition should be dependent on different parameters which themselves evolve over the reaction.

$$C_c(t) = 0.0011 \cdot t^{0.89} \quad \text{Eq.V-11}$$

Thus, this fit supports the idea that the coke deposit is the main deactivation process. However it did not provide insights into the mechanism and the relationship with surface properties since the parameters  $E$  and  $m$  do not have any physical sense. In addition the divergence between the fit and the experimental data above 100 minutes should indicate that the deactivation cannot be modeled by only one equation for the overall reaction time. It would be interesting to go deeper into the understanding of the coke deposit mechanism at the surface and try to incorporate the surface parameters modification into the equation of the hydrogen deactivation. The next section presents a model at the pore scale which discusses the impact of the deactivation surface on the hydrogen concentration evolution into the pore.

## 2. Model of $H_2$ production at the pore scale

A 2-dimensional model representing the evolution of the hydrogen concentration in space and time into a pore and the impact of the deactivation of active sites at the pore walls on the hydrogen concentration is proposed in this section. First, an introduction to the basis of heterogeneous reaction is provided to present the transport phenomenon into micropore and the methane reaction at the pore walls. Then the model is presented and discussed.

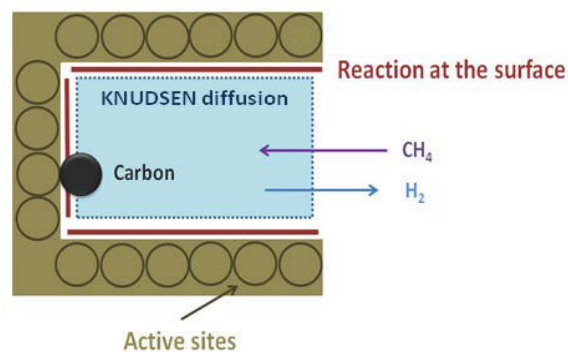


**Figure V-7: Illustration of the methane reaction at the pore wall which produces hydrogen and coke deposit**

### 2.1. Introduction to heterogeneous reaction

A quick presentation of the theoretical basis in heterogeneous catalysis is provided in order to highlight the influence of the transport phenomena in this type of reaction. In heterogeneous catalysis, the reaction occurs at the interface between two phases (at the surface of the catalyst in a

gas/solid reaction). Thus the reactant should first be transported to the surface of the catalyst to react and then products should diffuse in the reverse direction. An illustration of the main steps in a gas/solid heterogeneous reaction is provided in Figure V-8. The mechanism could be detailed according to the different phases:

- 1) Diffusion of the reactant from the bulk phase to the external surface of the catalyst
- 2) Diffusion of the reactant into the pores of the catalyst (intraparticle diffusion)
- 3) Adsorption of the reactant on the inner catalytic surface
- 4) Reaction at the specific active sites on the catalyst surface
- 5) Desorption of the products from the inner surface
- 6) Diffusion of the products into the pores
- 7) Diffusion of the products from the external particle surface to the bulk fluid.

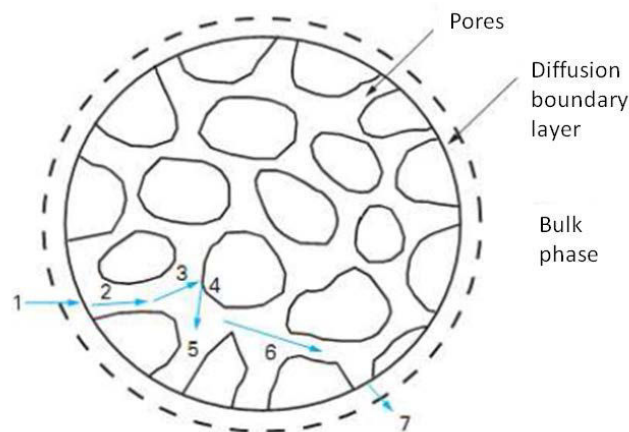


**Figure V-8: Scheme of the reaction process in a porous catalyst [3]**

### 2.1.1. Knudsen diffusion into micropore

Inside the particle, the transport of the reactant molecules only occurs by diffusion. According to the pores size the expression of diffusion coefficient differs. In fact, in macro and mesopores ( $d_{\text{pore}} > 20$  nm) the molecular diffusion coefficient expressed by the Chapman-Enskog equation is utilized. However into micropores the free mean path is longer than the pore size diameter. Hence the gas particles collide more frequently with the pore walls than between each other which slows down their diffusion. This type of diffusion is called the Knudsen diffusion. The Knudsen diffusion coefficient  $D_{\text{Knud}}$  expression into a micropore is presented in Eq.V-12. From the literature, it is in the order of magnitude of  $1.10^{-6} \text{ m}^2/\text{s}$  [3] [4].

$$D_{Knud} = \frac{2 \cdot r_{pore}}{3} \sqrt{\frac{8 \cdot R \cdot T}{\pi M}} \quad m^2 \cdot s^{-1} \quad \text{Eq.V-12}$$

where:

$r_{pore}$ : pore radius (m)

$R$ : gas constant ( $J \cdot mol^{-1} \cdot K^{-1}$ )

$T$ : temperature (K)

$M$ : molar mass (kg/mol)

If we want to calculate the effective Knudsen diffusion  $D_{Knud,eff}$  inside the entire particle, the particle porosity  $\varepsilon_p$  and the tortuosity  $\tau_p$  have to be considered. The expression of the effective Knudsen diffusion  $D_{Knud,eff}$  is presented in Eq.V-13.

$$D_{Knud,eff} = \frac{\varepsilon_p}{\tau_p} D_{Knud} \quad m^2 \cdot s^{-1} \quad \text{Eq.V-13}$$

The particle porosity  $\varepsilon_p$  is the percentage of void into a particle. It can be calculated from the ratio of the apparent  $\rho_{app}$  and true  $\rho_{true}$  densities.

$$\varepsilon_p = 1 - \frac{\rho_{app}}{\rho_{true}} \quad \text{Eq.V-14}$$

The tortuosity is an evaluation of the “geometrical disorder” of the porosity. It estimates the “non straight-lined” directions in the porous materials. Tortuosity is correlated to the porosity. As any analytical techniques provides information about the tortuosity, literature stated about the value of the tortuosity according to the level of porosity [5]:

- If  $\varepsilon_p < 0.9$  so  $\tau_p = 1.5$
- If  $\varepsilon_p > 0.9$   $\tau_p = 1$

### 2.1.2. **Reaction at the surface**

Once the reactant particles reach the surface of the catalyst, they react on active sites. The reaction could be highly complex to describe since it can involve several elementary reactions, diffusion onto

the surface of the reactant (spill-over), reactions with molecules in the gas phase. Regarding the catalytic methane reaction, it has been highlighted that it consists in a series of dehydrogenations following the mechanism [6]:



where: \* is an active site at the catalyst surface

The adsorption of the carbon atom, from the methane particle, on active sites is irreversible and form the carbon deposit at the surface. The global reaction can be expressed such as Eq.V-20:



The mechanism presented above supposed that the surface of the catalyst is homogeneous (only one type of active sites at the surface). However if we assume that two types of active sites (with a different reactivity) are present at the surface, the global reaction remains the same. However the reaction rates constant will differ.



Thus, the expression of the Knudsen diffusion will be utilized to model the transport of the hydrogen molecule at the surface. The production source term which corresponds to the boundary limit at the pore wall is the global expression of the methane cracking reaction. In the model two types of active sites with a different reactivity (for example: minerals and oxygen groups) are considered.

## 2.2. Description of the hydrogen concentration evolution into a micropore

To get better insights into the deactivation of the surface over the methane cracking reaction on biochars, a 2-D model is proposed in this section to describe the hydrogen concentration evolution in space and time into a pore of a biochars particle and the deactivation of the surface (see Figure V-9).

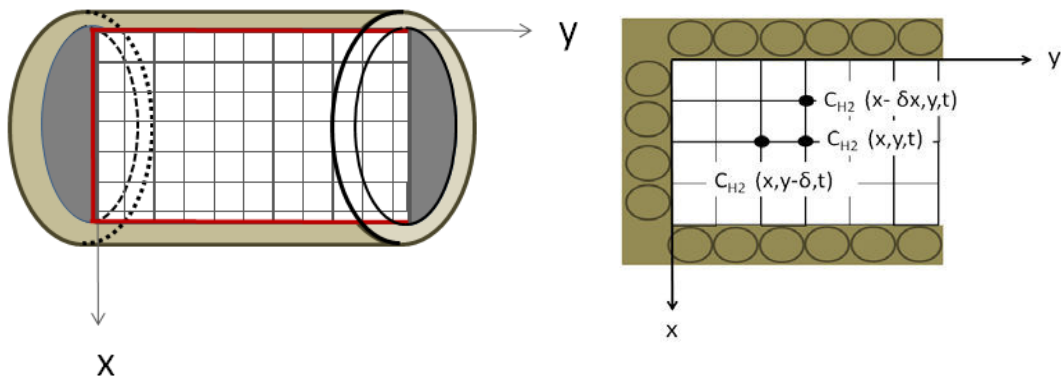


Figure V-9: Illustration of the 2-D model of hydrogen concentration evolution into a cylindrical-shaped pore over time

### 2.2.1. Goal of the model

The goal of this model is to predict the evolution over time of the hydrogen concentration at the output of the pore which is dependent from the deactivation process of the surface and the diffusion into the pore. A typical shape of deactivation for the hydrogen production is usually observed during experiments of methane cracking on biochars which consists in a first quick and significant deactivation in the early stages of the reaction followed by a steadier deactivation in the long-term. This deactivation pattern is the sum of different complex mechanisms occurring on the surface over time. From the experimental data and the literature, a sequence of different steps to model the deactivation of the surface is proposed in the next section. Thus, the comparison of the deactivation

pattern from the model to the experimental data should give insights into the reliability of the different assumptions which have been proposed and should provide insights into the deactivation mechanism.

### 2.2.1. Phases description

This model divides the deactivation process into three different phases which are presented in the Figure V-10. The phases differ from the availability and the reactivity of the active sites at the biochars surface. In a first approach, to simplify the model, only two types of active sites at the biochars surface and the coke deposit have been taken into consideration. The type 1 of active site could be assimilated to minerals (the most reactive sites with a reaction rate constant  $k_{min}$ ). The type 2 could be oxygen groups ( $k_{ox}$ ).

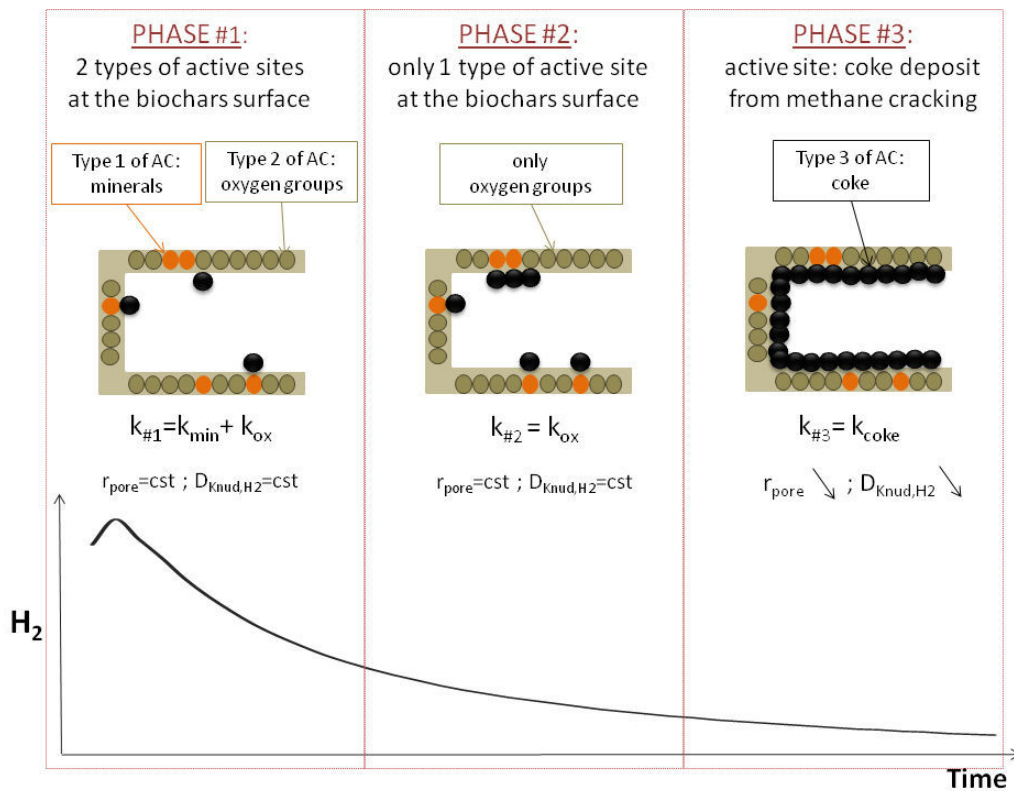


Figure V-10: Scheme of the three phases in the pore model

To simplify the model description, the following assumptions are taken into account:

- During the phase 1, the catalyst surface is fresh, the active sites of type 1 and 2 are available. Thus, the global reaction rate constant is the addition of reaction rate constant of each type of active sites (balanced by the surface coverage of each type of site). During the reaction,

active sites are blocked by coke deposit. Once one type of active sites is completely covered the phase 1 is finished.

- During the phase 2, only one type of active sites is available on the surface since the active sites 1 have been completely covered by coke deposit during the phase 1. Thus, the global reaction rate constant is only equal to the reaction rate constant of the remaining active site. This phase 2 lasts until the complete cover of the surface.
- During the phase 3, the catalytic methane cracking occur on coke deposit. From experimental data, the coke particle should be much less reactive ( $k_{coke}$ ) than the active sites from the biochars surface. In fact, experimental results have highlighted that the hydrogen production continuously decreased over the reaction. This phase is finished once the pore volume is completely filled.

### 2.2.2. **Hypotheses**

To build the model different hypotheses have been taken into consideration:

- cylindrical shaped pore ( $\tau_p=1$ )
- methane chemisorption occurs by monolayer. A monolayer should be entirely filled before starting a new one
- for 1 active site, only 1 reaction could occur and thus only one atom of carbon can be chemisorbed on it
- into the pore, the unique driving force is the diffusion of the specie from the more concentrated areas (pore walls) to the less one (outlet of the pore)
- the methane concentration is the same at each point of the surface and equal to the input methane concentration

### 2.2.3. **Partial mass balance for hydrogen into the micropore**

The global expression for a material balance in a defined volume can be expressed such as in Eq.V-23. The accumulation over time into the volume is equal to the difference of the input and the output of the material into the volume and its disappearance of production from reaction inside the volume [7] [8].

$$\left\{ \begin{array}{l} \text{accumulation} \\ \text{of material into} \\ \text{a defined volume} \end{array} \right\} = \left\{ \begin{array}{l} \text{Input flux} \\ \text{of material} \\ \text{into the volume} \end{array} \right\} - \left\{ \begin{array}{l} \text{Output flux} \\ \text{of material} \\ \text{into the volume} \end{array} \right\} + \left\{ \begin{array}{l} \text{Production} \\ \text{or loss of material} \\ \text{by reaction} \end{array} \right\} \quad \text{Eq.V-23}$$

Regarding the hydrogen, it is a product from the methane cracking reaction at the biochars surface. Thus, no entrance of hydrogen into the pore is considered, only an output flux. The partial continuity equation for the hydrogen can be expressed such as in Eq.V-24.

$$\frac{\partial C_{H_2}}{\partial t} = -\text{div } \dot{N}_{H_2} + r_{H_2} \quad \text{Eq.V-24}$$

The terms  $\frac{\partial C_{H_2}}{\partial t}$  and  $\dot{N}_{H_2}$  represent the accumulation of hydrogen into the pore over the time and the output flux respectively. Into a pore, the only driving force is the diffusion. Thus, the term  $\dot{N}_{H_2}$  can be expressed such as in Eq.V-25.

$$\dot{N}_{H_2} = -D_{Knud,H_2} \cdot \overrightarrow{\text{grad}}(C_{H_2}) \quad \text{Eq.V-25}$$

The reaction term  $r_{H_2}$  represents the hydrogen production from the methane cracking reaction at the biochars surface. The reaction only occurs at the pore walls and not into the pore volume (its expression is given in the next section). Thus, into the volume of the pore the partial continuity equation for the hydrogen (in 2-dimensions) can be expressed such as:

$$\frac{\partial C_{H_2}}{\partial t} = D_{Knud,H_2} \left( \frac{\partial^2 C_{H_2}}{\partial x^2} + \frac{\partial^2 C_{H_2}}{\partial y^2} \right) \quad \text{Eq.V-26}$$

#### 2.2.4. Numerical method solving

To solve the continuity equation into the pore the Finite Difference Method has been employed [9] [10]. This method consists in discretize the space  $(x, y)$  into a regular and square mesh. Then the linearized continuity equation is solved at each point of the mesh.

To perform the calculation of the hydrogen concentration in the overall volume of the pore, the pore diameter ( $d_{pore}$ ) and pore length ( $L_{pore}$ ) are divided into  $(M + 1)$  and  $(N + 1)$  calculations points respectively using the same mesh size ( $e$ ) (see Eq.V-27).

$$M + 1 = \frac{d_{pore}}{e} \quad \text{Eq.V-27}$$

$$N + 1 = \frac{L_{pore}}{e}$$

Thus,  $x_i$  varies from 0 to  $(M + 1)$ , where  $x_0$  and  $x_{M+1}$  correspond to the pore walls. Similarly,  $y_j$  varies from 0 to  $(N + 1)$ , where  $y_0$  corresponds to a pore wall and  $y_{N+1}$  corresponds to the output of the pore. Then, this is important to note that the positions:  $i = 0$ ,  $i = M + 1$ ,  $j = 0$  and  $j = N + 1$  are known hydrogen concentrations of the problem (boundary conditions).

Regarding the time discretization, the calculations are performed every  $\Delta t$  which is determined from the Eq.V-28 where  $t$  is the total time of the reaction and  $n$  is the number of iterations.

$$\Delta t = \frac{t}{n} \quad \text{Eq.V-28}$$

To linearize the second derivative in the continuity equation (see Eq.V-26), a limited development of  $C_{H_2}$  in Taylor serie at the 3<sup>rd</sup> order close to  $(x,y)$  has been utilized. If the mesh size ( $e$ ) is equal in the  $x$  and  $y$  directions, an estimation of the second derivative is:

$$\left( \frac{\partial^2 C_{H_2}}{\partial x^2} + \frac{\partial^2 C_{H_2}}{\partial y^2} \right)_t \quad \text{Eq.V-29}$$

$$= \frac{1}{e^2} (-4C_{H_2}(x, y, t) + C_{H_2}(x - e, y, t) + C_{H_2}(x + e, y, t) + C_{H_2}(x, y - e, t) + C_{H_2}(x, y + e, t))$$

The time could also be discretized in utilizing a time mesh and the time first derivative can be expressed as:

$$\frac{\partial C_{H_2}}{\partial t} = \frac{C_{H_2}(x, y, t) - C_{H_2}(x, y, t - \Delta t)}{\Delta t} \quad \text{Eq.V-30}$$

The partial continuity equation (see Eq.V-26) can be then expressed as presented in Eq.V-31.

$$C_{H_2}(x, y, t) - C_{H_2}(x, y, t - \Delta t) \quad \text{Eq.V-31}$$

$$= \frac{D_{Knud, H_2} \cdot \Delta t}{e^2} (-4C_{H_2}(x, y, t) + C_{H_2}(x - e, y, t) + C_{H_2}(x + e, y, t) + C_{H_2}(x, y - e, t) + C_{H_2}(x, y + e, t))$$

If we assume that  $\sigma = \frac{D_{H_2} \cdot \Delta t}{e^2}$  and using the notations presented in the beginning of the paragraph, Eq.V-31 becomes:

$$(1 + 4\sigma) \cdot C_{H_2}(i, j, n + 1) - \sigma \cdot C_{H_2}(i - 1, j, n + 1) - \sigma \cdot C_{H_2}(i + 1, j, n + 1) \quad \text{Eq.V-32}$$

$$- \sigma \cdot C_{H_2}(i, j - 1, n + 1) - \sigma \cdot C_{H_2}(i, j + 1, n + 1) = C_{H_2}(i, j, n)$$

$$1 \leq i \leq M \text{ and } 1 \leq j \leq N$$

(Extreme values:  $i = 0$ ,  $i = M + 1$ ,  $j = 0$  and  $j = N + 1$  are excluded from the calculations since they are boundary conditions)

The system can be represented by a vectorial expression:

$$A \cdot C_{H_2, n+1} = B \quad \text{Eq.V-33}$$

where:

-  $A$  is the jacobian matrix of the system (pentadiagonal matrix with a diagonal of  $(1 + 4\sigma)$  and 4 extra-diagonals of  $-\sigma$ )

-  $C_{H_2, n+1}$  represents the vector of the unknown hydrogen concentrations into the pore at the instant  $n + 1$  (the calculated vector).

-  $B$  represents the second member vector containing the values of  $C_{H_2, n}$  at the instant  $n$  and the hydrogen concentrations at the boundary limits.

At the initial point, the reaction did not start at the pore walls the hydrogen concentration is equal to zero in the entire pore (see Eq.V-34).

$$\text{Initial condition} \quad C_{H_2}(\forall x, \forall y, t = 0) = 0 \quad \text{Eq.V-34}$$

Then, hydrogen is produced from the methane cracking reaction on the free active sites of the surface and diffuses through the pore volume up to the output of the pore in which it is carried out by the bulk flow in the reactor. Eq.V-35 presents the boundary expressions at the three pore walls and the output of the pore over time.

$$\begin{aligned} \text{Boundary conditions} \quad C_{H_2}(x = 0, \forall y, \forall t) & \quad \text{Eq.V-35} \\ & = C_{H_2}(x = d_{pore}, \forall y, \forall t) = C_{H_2}(\forall x, y = 0, \forall t) \\ & = C_{H_2, surf, t} \\ C_{H_2}(\forall x, y = L_{pore}, \forall t) & = 0 \end{aligned}$$

### 2.2.4.1. Expression of instantaneous hydrogen production $C_{H2,surf,t}$

The reaction at the pore walls is considered to produce instantaneous gaseous hydrogen which will diffuse through the pore and carbon which is deposited on active sites over the reaction. The concentration of hydrogen  $C_{H2,surf,t}$  at the pore walls at the instant is calculated from Eq.V-36. It is dependent from the methane concentration  $C_{CH4,0}$  (kept constant) and the reaction rate constants ( $k_1$  and  $k_2$ ) of the active sites multiplied by the free surface percentages of each active sites at the instant  $t$  ( $\frac{S_{l1,t}}{S_{tot,pore}}$  and  $\frac{S_{l2,t}}{S_{tot,pore}}$ ). A factor 2 is applied due to the stoichiometry of the methane cracking reaction (for the disappearance of 1 mole of methane two moles of hydrogen are produced).

$$C_{H2,surf,t} = 2 \cdot \frac{k_1 S_{l1,t} + k_2 S_{l2,t}}{S_{tot,pore}} \cdot C_{CH4,0} \cdot \Delta t \quad \text{mol/m}^3 \quad \text{Eq.V-36}$$

However, the terms  $k_1, S_{l1,t}, k_2, S_{l2,t}$  are unknown. The following section describes the method which has been developed to obtain these parameters.

### 2.2.4.2. Estimating the intrinsic reaction rate (parametrization): $k_1, S_{l1,t}, k_2, S_{l2,t}$

- **Introduction of the parameter  $f_1$  to express  $k_1$  and  $k_2$  in function of  $k_0$  (experimentally determined in the section 1.2)**

The intrinsic reaction rates  $k_1$  and  $k_2$  are not known. This section proposes to determine their values from the calculation of the apparent initial reaction rate constant  $k_0$ , presented in the section 1.2 of this chapter. The intrinsic reaction rate which is the true rate at the biochars surface should differ from the apparent reaction rate. However, as we are interested in the shape of the deactivation of the hydrogen production and not to the accurate value of production in a first approach,  $k_0$  could be used. A new parameter  $f_1$  is introduced to distinguish the part of reactivity of the active sites 1 ( $k_1$ ) to the one of active sites 2 ( $k_2$ ). The higher the reactivity of active sites 1 (minerals) compare to active sites 2 (oxygen groups), the higher the value of  $f_1$  (which is comprised between 0 and 1). The expression of  $k_1$  and  $k_2$  are expressed in Eq.V-37. The sensitivity of the

model toward the factor  $f_1$  has been tested. This point is discussed more in details in the section 2.2.5.

$$\begin{aligned} k_1 &= f_1 \cdot k_0 & s^{-1} & \text{Eq.V-37} \\ k_2 &= (1 - f_1) \cdot k_0 \end{aligned}$$

- **Introduction of the parameter  $f_2$  to express  $S_{l1,t=0}$  and  $S_{l2,t=0}$  in function of  $S_{tot,pore}$**

The expression of the hydrogen concentration at the pore walls (eq.Eq.V-36) is dependent from the free surface at the instant t of the active sites 1 and 2. The initial distribution of active sites 1 and 2 is arbitrary evaluated by introducing a second factor  $f_2$  which is multiplied by the total pore surface  $S_{tot,pore}$  to evaluate the initial free surface of active site 1  $S_{l1,t=0}$ . The free surface of the active site 2 is the remaining surface (see Eq.V-38). As for the factor  $f_1$ , a sensitivity study of the influence of the factor  $f_2$  is discussed in the Results section (section 2.3).

$$\begin{aligned} S_{l1,t=0} &= f_2 \cdot S_{tot,pore} & m^2 & \text{Eq.V-38} \\ S_{l2,t=0} &= (1 - f_2) \cdot S_{tot,pore} \end{aligned}$$

However the free surface for each active site is time-dependent. The coke deposit over time diminishes the free active surface. At each instant t, the free surface area for each active sites is equal to their total initial surface of which is subtracted the surface blocked by coke deposit (see Eq.V-39). The surface deactivated of each active site is calculated from the total surface deactivated balanced by the factor  $f_1$  which represents the reactivity of each active site. In fact, the more reactive the active site, the faster its surface is occupied by carbon deposit.

$$\begin{aligned} S_{l1,t} &= S_{l1,t=0} - f_1 \cdot S_{c,t} & m^2 & \text{Eq.V-39} \\ S_{l2,t} &= S_{l2,t=0} - (1 - f_1) \cdot S_{c,t} \end{aligned}$$

Finally, the free surface at the instant  $t$ , for both types of active sites, is dependent from the surface deactivated by coke deposit at the same time  $S_{c,t}$ . The total surface  $S_{c,t}$  occupied by coke deposit at the instant  $t$  is given by Eq.V-40. Such as the hydrogen production, the coke deposit is function of the methane cracking reaction. In fact, it is calculated from the surface covered by the carbon particles ( $S_{part,carbon} \cdot N_a \cdot n_{c,t}$ ) at the time  $t$  which is added to the surface already covered at the time  $t-1$ . The term  $S_{part,carbon}$  represents the surface of one particle of carbon, the term  $N_a$  is the Avogadro number and the term  $n_{c,t}$  is the number of carbon moles produced from the reaction at  $t$ . This latter is calculated from Eq.V-41.

$$S_{c,t} = S_{part,carbon} \cdot N_a \cdot n_{c,t} + S_{c,t-1} \quad m^2 \quad \text{Eq.V-40}$$

The number of moles of carbon  $n_{c,t}$  at the time  $t$  is calculated from the product of the surface concentration of carbon produced by the reaction at the same instant  $C_{c,t}$  and the total surface of the pore  $S_{tot,pore}$ . The surface concentration  $C_{c,t}$  at the time  $t$  is calculated such as the hydrogen concentration ( $C_{H_2,surf,t}$ ; see Eq.V-36), from the reaction of the methane cracking at the surface.

$$n_{c,t} = C_{c,t} \cdot S_{tot,pore} \quad mol \quad \text{Eq.V-41}$$

$$C_{c,t} = \frac{(k_1 S_{l1,t} + k_2 S_{l2,t})}{S_{tot,pore}} \cdot C_{CH_4,0} / a \cdot \Delta t \quad mol/m^2 \quad \text{Eq.V-42}$$

The parameter  $a$  has been used to adjust a volumetric concentration expression to a surface concentration one for the expression of the surface covered by coke over time (see Eq.V-43). It is based on the relationship between the apparent density  $\rho_{app}$  and the true density  $\rho_{true}$  of the char particles. It is dependent from the specific surface area  $S_{sp}$  of the particle, the particle  $\varepsilon_p$  and bed particle  $\varepsilon_b$  porosities.

$$a = (1 - \varepsilon_p) \cdot (1 - \varepsilon_b) \cdot \rho_{true} \cdot S_{sp} \quad m^{-1} \quad \text{Eq.V-43}$$

Thus, the model has been simulated using the Matlab® software. The calculation algorithm is provided in Appendice.2. Parameters which have been tested and results of the study are presented in the following sections.

#### 2.2.4.3. Summary of the numerical resolution of the hydrogen concentration evolution into the pore and coke deposit

To solve the equation continuity with respect to the hydrogen concentration at the different locations of the pore (Eq.V-33; linear system of differential equations), the input data are the initial (Eq.V-34) and the boundary conditions (Eq.V-35). In the Eq.V-35, the expression of  $C_{H_2,surf,t}$  has been determined as follows:

- a first parameterization to determine the reaction rate constants  $k_1$  and  $k_2$  for the active sites # 1 and #2 respectively has been performed by introducing the factor  $f_1$  and the experimental value of the initial apparent reaction rate constant  $k_0$  (Eq.V-37).
- a second parameterization to evaluate the initial free surface areas of the different active sites 1 and 2 required to introduce the factor  $f_2$  (Eq.V-39).

#### 2.2.5. Parameters which will be tested

The hydrogen concentration at the output of the pore is dependent on various parameters: geometrical parameter regarding the pore structure, term of reaction at the surface, expression of deactivation and so on. Several hypotheses have been proposed in the section 2.2.2 to simplify the model in the first approach. Hence, the pore is considered to be cylindrical, and the surface is composed of two types of active sites, methane concentration is considered constant at the pore walls, the methane molecule adsorbed by monolayer during the phase 1 and 2.

In this study, two parameters are investigated: the distribution and the reactivity of the active sites ( $f_1$  and  $f_2$ ). The influence of the difference of reactivity ( $f_1$ ) and the initial distribution of the active sites on the pore walls surface ( $f_2$ ) are investigated. These two parameters are related to the source term of the hydrogen production at the biochars surface. They should reflect the complexity of the biochars surface regarding the heterogeneity of active sites. Previous characterization presented in the Chapter III, highlighted the several types of active sites which were depicted onto the biochars

surface. The model should help in determining the influence of the availability and the reactivity of the different types of active sites at the surface.

## 2.3. Results

### 2.3.1. *Hydrogen concentration profile into a micropore*

As described in the section 2.3 of Chapter II, pores are classified into three categories according to their diameter size:

- micropore:  $d_{pore} < 2$  nm
- mesopore:  $2 < d_{pore} < 20$  nm
- macropore:  $d_{pore} > 50$  nm

Results of characterization presented in Chapter III highlighted that biochars mainly contained micropores. Thus, a pore diameter equal to  $d_{pore} = 1.4$  nm has been utilized in the model. The determination of a mean value of pore length is difficult to obtain from experimental data. In addition, literature did not provide extensive values. Thus, in a first approach, a pore length of  $L_{pore} = 14$  nm has been chosen. Figure V-11 presents the hydrogen concentration profile into a micropore ( $d_{pore} = 1.4$  nm,  $L_{pore} = 14$  nm).



**Figure V-11: Hydrogen concentration profile into a micropore:  $d_{pore} = 1.4$  nm,  $L_{pore} = 14$  nm, 1<sup>st</sup> iteration (1s)**

One can observe on Figure V-11 that the hydrogen concentration is almost homogeneous into the micropore. The Knudsen diffusion has been calculated and reaches  $D_{Knud,H_2} = 1.49 \times 10^{-6} m^2/s$ . To evaluate the time for the hydrogen to diffuse from the walls to the center of the pore, the characteristic time  $\tau$  can be calculated (see Eq.V-44) [11]. If we consider that the characteristic length  $L_{characteristic}$  is the pore radius  $r_{pore}$ , the characteristic time is estimated to be  $3.28 \times 10^{-13}$  s.

$$\tau_{dif} = \frac{L_{characteristic}^2}{D_{Knud,H2}} \quad s \quad \text{Eq.V-44}$$

Figure V-12 presents the hydrogen concentration gradient into a micropore ( $d_{pore} = 1.4 \text{ nm}$ ) at two different times: (A)  $t=1e^{-13} \text{ s}$  and (B)  $t=1e^{-12} \text{ s}$ . On Figure V-12.A, one can observe that the hydrogen did not have time to diffuse through the volume to reach the center of the pore since the time of the first iteration ( $t=1e^{-13} \text{ s}$ ) was below the characteristic time  $\tau$  ( $3.28 \times 10^{-13} \text{ s}$ ) whereas on Figure V-12.B, hydrogen concentration is more homogeneous through the radius of the pore ( $t_{1st \text{ it}} = 1 \times 10^{-12} \text{ s} > \tau = 3.28 \times 10^{-13} \text{ s}$ ). Thus, in this model (with the hypotheses proposed above) the diffusion of the hydrogen is fast into the pore.

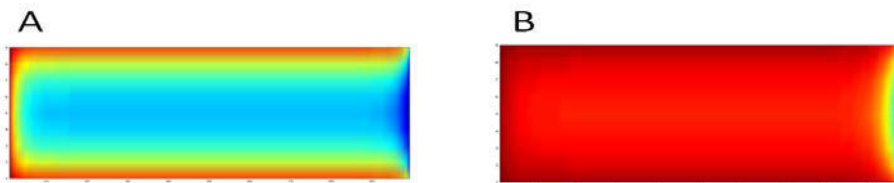


**Figure V-12: Diffusion into a micropore for two different times of 1<sup>st</sup> iteration: (A)  $t=1e^{-13} \text{ s}$ , (B)  $t=1e^{-12} \text{ s}$ ,  $d_{pore} = 1.4 \text{ nm}$  and  $L_{pore}=14 \text{ nm}$**

In the model, the production of hydrogen has been considered homogeneous at the pore wall and a methane constant concentration was applied at the pore surface to calculate the hydrogen production. If the methane diffusion into the pore has been taken into consideration, a stronger gradient of concentration through the pore should be observed.

### 2.3.2. *Hydrogen production evolution over time during phases 1 and 2*

This part presents the hydrogen evolution over time during the phase 1 (which corresponds to the period of time in each the two kind of chemical species are active) and phase 2 (only one type of active site is available).

- ***Influence of the initial surface distribution of the active sites (parameter  $f_2$ )***

First the influence of the surface distribution ( $f_2$ ) of the actives sites is investigated. Three cases have been studied:

- 1<sup>st</sup>:  $f_2 = 1/4$

This means that active sites 1 (minerals) represent 1/4 of the total pore surface and active sites 2 (oxygen groups) cover ¾ of the surface

It could be assimilated to the raw biochars where the most reactive sites are less numerous at the surface

- 2<sup>nd</sup>:  $f_2 = 1/2$  \_ equal initial distribution \_
- 3<sup>rd</sup>:  $f_2 = 3/4$  \_ minerals are predominant at the surface

This is representative of a functionalized biochars in which the concentration of the most reactive sites has been enhanced.

Figure V-13 presents the mean hydrogen production over time at the output of the pore for the three conditions of the initial active sites surface distribution ( $f_2$ ) during phase one and two until reaching the complete coverage of the surface. One can observe that the highest production is at the initial point for the three curves. Then the production is diminished due to the deactivation of the active sites at the surface. A quick deactivation is visible in the early stages and then the production decreases more steadily.

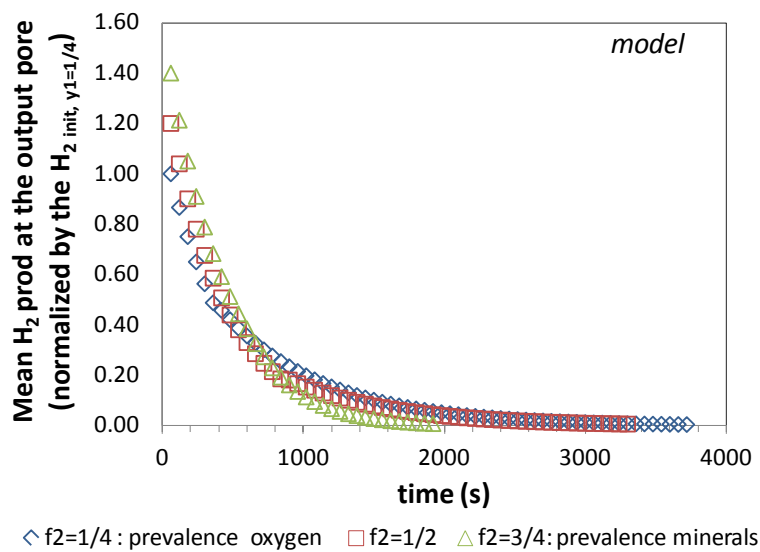


**Figure V-13: Mean hydrogen production at the output pore over time (during phase 1 and 2) for different initial distribution of the two types of active sites ( $f_2$ : ¼, ½ and ¾),  $f_1=1/2$ ,  $d_{pore}=1.4$  nm,  $L_{pore}=14$  nm**

Results of the three simulations are presented in Table V-1. Different parameters were impacted by the change of the initial active sites distribution at the surface. In fact, the initial hydrogen

production differed according to the active sites distribution. The higher the initial surface of active site 1 (the most reactive), the higher the initial hydrogen production. It impacts the duration of the phase 1 and the types of active sites which will be first deactivated. In the cases #1 and #2, the minerals are first deactivated since they cover less of the middle or exactly the middle of the surface. In the case #3, even if the deactivation of the active sites #1 is faster, the active sites #2 are first deactivated because they covered a significantly smaller part of the surface (1/4). The time to complete the total covering of the surface is also dependent from the initial distribution of the active sites. In fact, the higher the initial surface of active sites #1, the faster the surface is covered.

**Table V-1: Results of the three modeling where the initial distribution of the active sites at the surface has been modified (  $f_2$ :  $\frac{1}{4}$ ,  $\frac{1}{2}$  and  $\frac{3}{4}$ )**

Model #	Minerals cover: ( $f_2$ , of the surface)	Initial hydrogen value (normalized)	First sites to be deactivated	Duration of phase 1 (s)	Time to completely cover the pore surface (s)
1	1/4	1	minerals	360	3720
2	1/2	1.2	minerals	840	3300
3	3/4	1.4	oxygen groups	600	1920

Trends of hydrogen production deactivation are coherent with the experimental data. In fact, the hydrogen production curves from the different model showed a high initial hydrogen production and then a decrease due to the deactivation of the surface. The investigation of the influence of the active sites initial concentrations on the hydrogen production highlighted that the initial hydrogen production, the time of the phases 1 and 2 and the sites first deactivated were dependent from this parameter. The different trends seem to be in agreement with the experimental data (see Figure V-14). In fact, experimentally, if the initial surface of the most reactive sites (active sites 1: minerals) is enhanced the initial hydrogen production is enhanced as it is shown in the model. In addition, the phase 1 duration seems to be extended as well when the concentration of active sites is enhanced. Thus, trends presented in the model seem to be coherent with the experimental data. However, direct comparisons should be considered carefully since it has been highlighted experimentally that various parameters differed from the raw biochars and the K-chars (mean size of the pore diameter, pore volume, specific surface area). In the model the same pore volume was taken into consideration. The discussion is focused on the trend observed for the hydrogen production modifying one parameter (the initial surface of each active site).

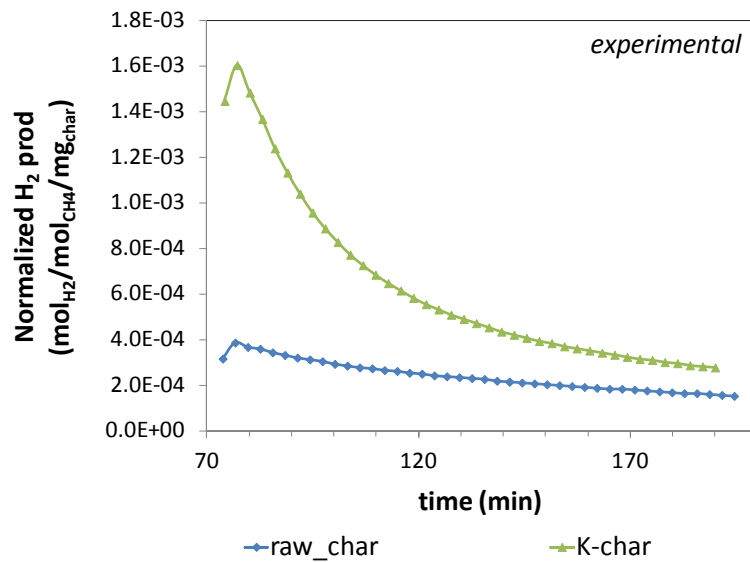


Figure V-14: Experimental results for the raw and K-chars

- **Influence of the difference of reactivity of the active sites (parameter  $f_1$ )**

The influence of the difference of reactivity of the two active sites has been investigated ( $f_1$ ). Three calculations were performed: (where  $k_1$  is the reaction rate constant of the most reactive sites: minerals)

- 1<sup>st</sup> model:  $k_1=2 k_2$  ( $f_1=2/3$ )
- 2<sup>nd</sup> model:  $k_1=4 k_2$  ( $f_1=4/5$ )
- 3<sup>rd</sup> model:  $k_1=9k_2$  ( $f_1=9/10$ )

Figure V-15 presents the mean hydrogen production at the output of the pore for the three models ( $f_1$ : 2/3, 4/5, 9/10). Global shape of the hydrogen curves is similar to the previous paragraph and to the experimental data: a high initial hydrogen production and then a progressive diminution over time.

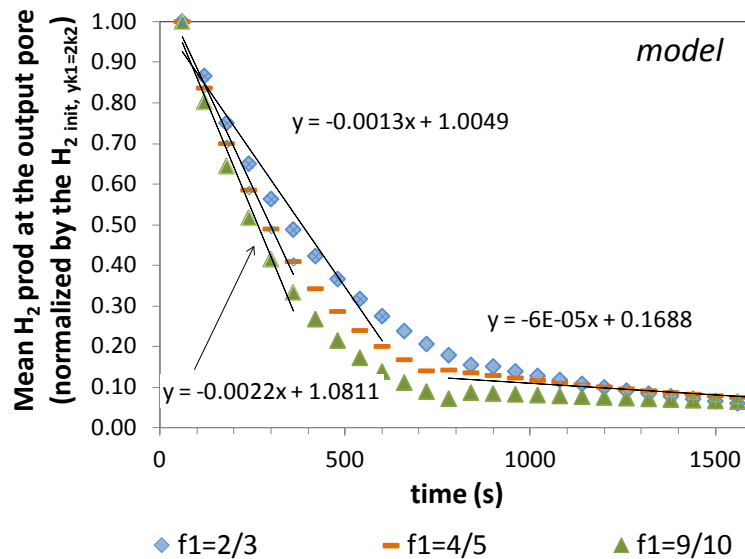
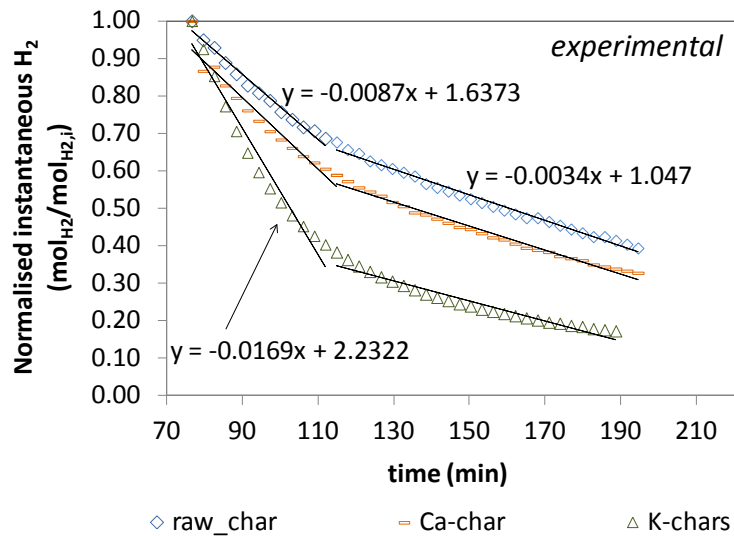


Figure V-15: Influence of the difference of reactivity of the active sites ( $f_1$ : 2/3, 4/5, 9/10),  
 $f_2=1/2$ ,  $d_{pore}=1.4$  nm,  $L_{pore}=14$  nm

Table V-2 presents results of the hydrogen curves which are shown in Figure V-15. One can observe that the difference of reactivity of the active sites did not impact the same parameters than their initial surface distribution. In fact, the difference of reactivity did not impact the initial hydrogen production. However the initial slope of deactivation has been modified. The higher the difference of reactivity between the active sites, the higher the initial slope. As for the distribution of the surface at the initial point, the change in reactivity of active sites #1 modified the time to reach the complete cover of the pore surface. The higher the active site #1 reactivity, the faster they are deactivated. During the phase 2, the reaction is only possible on the active sites 2. Thus, the lower their reactivity, the longer the time to reach the complete coverage.

Table V-2: Results of the three models with different active sites reactivities ( $f_1$ : 2/3, 4/5 and 9/10)

Model #	Difference of reactivity ( $f_1$ )	Initial slop	First sites to be deactivated	Duration of phase 1 (s)	Time to completely cover the pore surface (s)
1	2/3	$1.9e^{-2}$	minerals	840	3300
2	4/5	$2.3e^{-2}$	minerals	720	5700
3	9/10	$2.7e^{-2}$	minerals	780	8400



**Figure V-16: Experimental data, hydrogen production during methane cracking on raw biochar, Ca-char and K-char**

Thus, the sensitivity study of the hydrogen production at the output of the pore in function of the difference of reactivity of the active sites ( $f_1$ ) showed that this parameter influenced the initial slope of the deactivation of the hydrogen production and the duration to reach the total cover of the pore surface. The higher the reactivity of the active sites, the sharper the initial slope of deactivation. This trend is also observed in the experimental data set. In fact, in the chapter IV, it has been highlighted that the K-char was the most reactive followed by the Ca-char and then the raw biochars. One can observe on Figure V-16 that the trend for the initial slope presented in the model is in agreement with the experimental data:  $\text{slope}_{\text{K-char}, i} > \text{slope}_{\text{Ca-char}, i} > \text{slope}_{\text{raw-char}, i}$ . However, even if the deactivation rate constants (in the model and experimentally) are in the same order of magnitude, the values are not comparable. In fact, further experimental researches are required to quantify the difference of reactivity.

### 2.3.3. Hydrogen production during phase 3

If we consider that the coke deposit onto the biochars surface is reactive and could potentially crack the methane molecule, hydrogen should still be produced after the complete coverage of the biochars surface (after phases 1 and 2). Hence, during phase 3, methane could react on the carbon deposit from previous methane cracking reaction that has already occurred. However the reactivity of the coke particle should be significantly smaller than the one of the inherent active sites of the

surface since from experimental data, one could observe that the hydrogen production kept diminishing over the reaction.

A hypothesis which has been proposed for the model of the phases 1 and 2 was a monolayer adsorption on the active sites of the surface. In fact, as long as active sites were available at the biochars surface, the chemisorption of methane molecules should preferentially occur on these sites since they are significantly more reactive than the coke deposit. On the contrary, during phase 3 this hypothesis cannot be supported anymore since the reactivity of all the active sites is identical. Thus, during this phase, methane molecule chemisorption could potentially be a multi-layer adsorption. New methane molecules which enter into the pore could react on every coke particle in the pore. The hydrogen production should be stopped once the pore volume is totally filled or the entrance of the pore is blocked. Hence, during this phase, the total pore volume is not constant anymore and should decrease as the reaction progresses. Thus, the model which has been previously presented could not be utilized to simulate the reaction+diffusion phenomena during the phase 3. A numerical model which takes into consideration the modifications of geometry of the pore during the reaction should be developed. This will be further discussed in the "Conclusion and Prospects" section.

#### 2.3.4. ***Partial conclusion on the results of the model***

A model of hydrogen reaction/diffusion into a micropore has been developed to get better insights into the mechanism of deactivation of the biochars surface. The goal of the model was to compare the hydrogen production profile over time at the output of the pore to the experimental data of deactivation pattern. For this first approach, several simplifying hypotheses have been proposed such as a cylindrical pore structure, a constant methane concentration into the pore, only two types of active sites and a monolayer adsorption on the biochars surface. The sensitivity of the hydrogen production to 2 different parameters has been tested: the reactivity and the surface distribution of the active sites. The concentration gradient of hydrogen into the pore was sensitive to the geometrical values (length of the pore). However, in the present model of micropore in which the methane concentration at the pore wall was kept constant, the concentration into the pore was found to be almost homogeneous into the entire volume (only a gradient close to the output of the pore).

Regarding the sensitivity of the hydrogen production toward the reactivity and the initial distribution of the active sites, results of simulation highlighted that these two parameters influenced differently the deactivation. The initial surface distribution of the active sites impacted the initial hydrogen

production, the type of active sites which was the first deactivated and the time to complete phase 1 and 2. Regarding the difference of reactivity of the active sites, they also impacted the time to complete the phase 1 and 2. In addition, they influenced the initial slope of the hydrogen deactivation. The trends observed were in agreement with the experimental results. This means that the hypotheses previously proposed, in particular the monolayer adsorption were not inconsistent. However, further experimental researches and improvements of the model presented are required to provide simulated values of hydrogen production to compare to the experimental data. This point is also discussed in the Conclusion and Prospect section.

### 3. Conclusion

This chapter was focused on theoretical aspects of the catalytic methane cracking reaction on biochars. The determination of the kinetics parameters and the mode of deactivation were investigated. A parametric study has been performed in a fixed bed reactor which led to determine the initial apparent global kinetics parameters for the methane cracking on raw biochars. The power law of the reaction rate has been found to be of first-order regarding methane. The reaction rate was estimated at  $32 \text{ s}^{-1}$  and the activation energy at  $192 \text{ kJ/mol}$ . The result of activation energy is in agreement with previous results published in the literature for other carbonaceous catalysts. In fact, Muradov et al. [1] claimed that the activation energies of activated carbons, coal activated carbons and carbon blacks were comprised between 160-201, 186-198 and 205-236 kJ/mol respectively. Regarding the mode of deactivation, the coke deposit concentration empirical equation (Voories) was fitted on the experimental data of mass gain during the methane cracking reaction on the raw biochars. An acceptable fit was obtained which seemed to confirm that the coke deposit was the main deactivation mode during the methane cracking reaction into biochars. However the fit slightly differs from the experimental data after 100 min on stream which should indicate that modification in the deactivation treatment occurred. Thus, it seemed that the complex deactivation process of the surface could not be represented by only one equation for the overall period of the reaction.

A model has been proposed in the second section of this chapter, to get better insights into the deactivation mechanism at the biochars surface coupled with the phenomenon of transport into the pores of the biochars. A 2-D model representing the hydrogen concentration evolution into a micropore of the biochars and the deactivation of the surface has been developed. The goal of this model was to compare the deactivation pattern of the hydrogen production at the output of the pore to the experimental data. Several assumptions have been proposed for the first approach: a

simple cylindrical-shaped pore, a monolayer of methane chemisorption on the active sites of the surface, a constant methane concentration at the surface and only two types of active sites. The influence of 2 parameters: the reactivity and the initial distribution onto the pore surface of the active sites were tested. The different simplifying hypotheses of this model lead to a quite homogeneous hydrogen concentration into the pore volume. The initial distribution of the active sites impacted the initial hydrogen production while the difference of reactivity influenced the initial slope of deactivation. Both parameters influenced the time to complete the phases 1 and 2. Results from the simulation were in agreement with the experimental data. In fact, the higher the initial surface of the most reactive site (minerals impregnation), the higher the initial hydrogen production. The higher the reactivity of the active sites, the faster the initial deactivation (comparison between the K-chars and Ca-chars). Thus, this model provided insights into the interpretation of the deactivation pattern of hydrogen production. The model has shown that the fact to increase the difference between the two active sites in terms of surface distribution or reactivity led to a stronger deactivation in the early stages. If a steady hydrogen production is requested, a homogeneity in the active sites properties should be respected.

Thus, the biochars could compete between other carbonaceous materials to catalyze the methane cracking. They catalyzed methane cracking reaction and the activation energy required was similar to value presented in the literature for activated carbons. A functionalization treatment can be performed to enhance their reactivity. However, from the simulation and the experimental results, the positive impact will be mainly observed during the early stages of the reaction. Coke deposit over the process will fatally diminish the gain of activity provided by the functionalization treatment. To counterbalance the loss of activity on stream, a regeneration process should be considered to refresh the biochars surface. This point is further developed in the "Prospects" section.

## Bibliography

- [1] N. Muradov, F. Smith, and A. T-Raissi, "Catalytic activity of carbons for methane decomposition reaction," *Catal. Today*, vol. 102–103, pp. 225–233, May 2005.
- [2] R. Klaewkla, M. Arend, and W. F. Hoelderich, *A Review of Mass Transfer Controlling the Reaction Rate in Heterogeneous Catalytic Systems*, no. 3. IN Tech, 2011.
- [3] A. Zoulalian, "Transferts de matière et de chaleur au sein des catalyseurs," in *Techniques de l'ingénieur*, 1975, pp. 1–28.
- [4] B. Weber, J.-J. Ehrhardt, and A. Thomy, "Surface des solides-Physisorption.Chimisorption.Ségrégation," vol. 33, no. 0, 1988, pp. 0–20.
- [5] F. Mermoud, "Gazéification de charbon de bois à la vapeur d'eau : de la particule isolée au lit fixe continu," Institut national polytechnique de Toulouse, 2006.
- [6] A. M. Amin, E. Croiset, and W. Epling, "Review of methane catalytic cracking for hydrogen production," *Int. J. Hydrogen Energy*, vol. 36, no. 4, pp. 2904–2935, Feb. 2011.
- [7] R. B. Bird, W. E. Stewart, and Lightfoot Edwin N., *Transport phenomena*. 2002.
- [8] W. J. Beek, K. M. K. Muttzall, and J. W. van Heuven, *Transport phenomena*. 2000.
- [9] E. Saadjan, *Phénomène de transport et leurs résolutions numériques*. 1993.
- [10] P. Spiteri, "Méthode des différences finies pour les EDP d'évolution," in *Techniques de l'ingénieur*, 2002, pp. p.1–11.
- [11] S. Stringel, "High temperature gasification of millimetric wood particles between 800°C and 1400°C," 2011.

## **Conclusions and Prospects**



## 1. Conclusions

This research work takes part in the global dynamic to reinforce the competitiveness of the gasification process. The focus was on the valorization of the solid residue called the biochars as a catalyst which could be directly reused in the process to clean and upgrade the syngas. This study was the second thesis work on this subject in collaboration between the RAPSODEE center at the Ecole de Mines d'Albi-Carmaux, Columbia University and now the City College of New York. The previous study highlighted the catalytic potential of the biochars and investigated the relationship with the surface properties. The goal of this present PhD work was to go deeper in the interpretations of the interactions between the physico-chemical properties of the biochars and their reactivity during the catalytic reaction.

To study the catalytic behavior of the biochars, the methane cracking reaction has been chosen for two main reasons: first the methane is the second by-product in the gasification process (after the CO<sub>2</sub>) and it is a model molecule for the C-H breaking (present in all the hydrocarbons). Previous investigations highlighted that four surface properties should be involved in the biochar reactivity: oxygen functions, minerals content, carbon matrix and textural properties. However, these surface properties are complex and could vary according to the biomass feedstocks, the gasification conditions, the post-treatment and the methane cracking reaction conditions. In addition, it has been highlighted in the literature that catalysts surface is progressively deactivated due to carbon deposit which blocks the access to the active sites and clog the pores. Thus, this coke deposit should modify the interactions between the methane molecule and the active sites from the biochars surface.

This PhD work investigated the different aspects previously presented to get a better understanding of the biochars reactivity and especially toward methane cracking. The final goal required intermediate steps such as the production of biochars. In this study, biochars were produced from the pyro-gasification of poplar wood under steam at 750°C. The operating conditions for the gasification process were never changed. However, the biochars were functionalized to modify their intrinsic physico-chemical properties. In fact, two functionalization treatments (oxygenation and Alkali and Alkaline Earth Minerals: AAEMs impregnation) were performed to enhance the concentration of chemical species which have been depicted to be active sites for methane cracking. Then, a set of characterization was carried out to evaluate the efficiency and the selectivity of the treatments on the targeted chemical groups at the biochars surface (oxygen groups and minerals content). Further characterizations were performed on the raw and functionalized biochars to analyze the impact of the functionalization treatments on surface properties such as the carbon

matrix structure and the textural properties. Then, this global set of surface characterizations has been connected to the results of catalytic methane cracking tests performed on the raw and functionalized biochars to investigate their relationship. The initial activity was studied separately. In fact, the surface deactivation has to be taken into account regarding the activity of the catalyst on stream. This deactivation mechanism was complex to understand. A modeling at the pore scale has been performed in complement to get better insights into the phenomenon. Thus, the research work approached 4 main aspects:

- 1) Functionalization treatments to enhance the reactivity of biochars surface,
- 2) Characterization of raw and functionalized biochars surface properties
- 3) Catalytic methane cracking tests on biochars and investigation of the interaction with the surface properties
- 4) Kinetics study and modeling at the pore scale of the surface deactivation and hydrogen diffusion into a micropore.

Good insights were provided in the different sections presented above:

- **Functionalization treatments**

The challenge regarding the functionalization was to determine suitable treatments and methods. Two different functionalizations have been selected: an O<sub>2</sub> gas-phase treatment and a minerals impregnation using a nitrate salts solution (calcium and potassium). These two functionalization processes have been selected to increase the amount of chemical species which were depicted to be active sites for methane cracking: oxygen functions and AAEMs minerals content.

- ***O<sub>2</sub> gas-phase treatment:***

An O<sub>2</sub> gas-phase treatment has been carried out at different temperatures and duration times to increase the oxygen content at the biochars surface. This method has been selected among the other ones (liquid impregnation, ozone treatment) since it was depicted in the literature to be as efficient as the other treatments regarding the oxygen chemisorption. However, this process should not decrease the specific surface area and pore volume compared to liquid treatment notably.

The O<sub>2</sub> gas-phase treatment was successful since the increase of the O-containing groups concentration at the surface of the oxygenated biochars was confirmed by FTIR and TPD characterizations. It has been also emphasized that the operating conditions impacted the efficacy and the selectivity of the oxygenation. In fact, the treatment has been performed at different

temperatures (280, 340 and 400°C) and for several duration times (2, 4, 8h). The total amount of oxygen functions at the biochars surface has been evaluated by deconvolution of the TPD results. At 280°C, the maximum increase of the total oxygen concentration was of 50%. At 340 and 400°C, it reached 73 and 110% respectively. These results highlighted that the increase of temperature increased the amount of oxygen chemisorbed onto the biochars surface. The duration time also increased the chemisorption. However some limits were observed since the saturation was reached from 4h of treatment. Thus, the oxygenation at 340 and 400°C revealed to be the most effective. Regarding the selectivity, the oxygenation favored the formation of weak acids such as lactone, anhydrides, hydroxyl or phenol (and ethers but neutral function). The basic groups such as quinone and pyrone-like functions were not removed from the surface but were not enhanced as well. On the contrary, carboxylic acids which were not stable at the oxygenation temperature desorbed from the surface. This phenomenon can be explained by the fact that basic groups were the main functions at the raw biochar surface. Thus, during the oxygenation, the oxygen reacted with some quinone or pyrone at the surface to form more complex groups such as lactone or anhydride functions and then a new equilibrium has been reached.

- ***Minerals impregnation of calcium and potassium:***

Several methods, such as wet and dry impregnations, have been proposed in the literature to enhance the concentration of minerals at the biochars surface. In this study, a wet impregnation during 6 hours into a nitrate solution of calcium or potassium has been performed on raw poplar wood prior to gasification. In fact, the wet impregnation should enhance the penetration of the minerals into the pores of the wood and thus increased the dispersion of minerals at the subsequent biochar surface. The gasification has been performed in the same conditions such as for the raw biochars. Three impregnated biochars were prepared: Ca-chars, K-chars and Ca+K-chars to investigate the separate role of the calcium and potassium and the potential synergic effect of their both concentration enhancement.

The characterization of the biochars surface post-impregnation revealed that the process was successful. In fact, X-ray fluorescence analyses highlighted that the calcium content was increased 8 times at the Ca-chars surface compared to raw biochar and the potassium was enhanced 7 times at the K-chars surface. Regarding the Ca+K-chars, a similar concentration of calcium and potassium was obtained (2.2 wt%) onto the surface. XRD analyses revealed that minerals were in carbonate and oxide forms at the biochars surface. This is coherent with the fact that the gasification process is an oxidizing process. ESEM pictures highlighted a good dispersion of the particles at the surface with distinct structural forms according to the structures of the species. Carbonates and oxides were

mainly identified at the surface, even if more complex structures such as alumino-silicates were detected as well. Regarding the Ca+K-chars, a complex  $K_2(Ca(CO_3)_2)$  has been identified.

Thus, the two functionalization treatments successfully increased the chemical species which were targeted. The analytical techniques have been properly selected to provide insights into the type and the amount of the chemical species obtained after the functionalization treatments. Additional characterizations were performed to obtain a global screening of the physico-chemical properties of the raw and functionalized biochars which are depicted to be involved in the methane cracking reaction.

- **Characterization of the raw and functionalized biochars surface properties**

The previous section emphasized that the functionalization treatments impacted the oxygen content and the AAEMs concentrations in the oxygenated and minerals impregnated biochars respectively. However, from the literature, we knew that functionalization treatments could also potentially affect the distribution of the carbon structures and the textural properties. Thus, additional characterizations such as BET analyses, Raman spectroscopy and Transmission Electron Microscopy (TEM) were performed to investigate the textural properties and the carbons structures of the raw and functionalized biochars. In fact the total pore volume, the median pore diameter and the specific surface area are key points in the catalytic reaction since they are the interface between the reactant and the active sites at the surface. Thus, this is primordial to characterize the textural properties. BET analyses revealed that the textural properties were modified according to the functionalization treatment and the operating conditions. In fact, the oxygenation at 280°C and the mineral impregnation tended to decrease the specific surface area and total micropore volume due to oxygen chemisorption and minerals impregnation respectively. The oxygenation at 280°C decreased the specific surface area and the total pore volume up to 14 and 6 % of their initial values. The minerals impregnation decreased these two parameters up to 47 and 63% respectively. On the contrary, the oxygenations at 340 and 400°C tended to increase the total pore volume (by 38 and 47% respectively) and specific surface area (by 22 and 30% respectively) due to the enhancement of the combustion reaction which burnt a part of the carbonaceous matrix.

The characterization of the carbon structures is also of great interest since the biochar are turbostratic carbons containing short range well-ordered graphitic structures and amorphous carbons such as graphene-sheets containing “in-plane” defects, aromatic rings or aliphatic chains. The literature highlighted that the reactivity of these different structures was different. In a global trend, the functionalization treatments tended to increase the disorder of the carbon matrix. In fact,

the embedding of the minerals and the insertion of the oxygen atoms tended to enhance the defects into the graphene-like sheets and concentration of aromatic systems. An increase of 20% is observable for the concentration of the carbon structures containing “in-plane” defects and the large aromatic systems (represented by the D-band). However at 340°C, the combustion reaction during the oxygenation process consumed a part of the aliphatic chains (decreased by 25% at 400°C) and the small aromatic systems (decreased by 40% at 400°C) which led biochars with more disordered graphene-like sheets.

- **Catalytic methane cracking tests**

Catalytic methane cracking tests were performed in a plug flow reactor and in a thermogravimetric analyzer both coupled with a gas chromatograph analyzer. Methane cracking tests first confirmed that raw biochars catalyzed the reaction at 700°C. The reaction mainly produced hydrogen and carbon deposit. Carbon monoxide and carbon dioxide were also detected but in smaller quantity. Catalytic tests performed on functionalized biochars highlighted their better efficiency compared to the raw biochars, especially the minerals impregnated biochars. In fact, the minerals have been depicted to be the most reactive since the initial hydrogen production was doubled to quadrupled with the increase in concentration of the minerals. The potassium showed the best performances due to the formation of long needle-shaped potassium carbonates particles during the heating. The calcium species were also efficient. However their dispersion at the biochars surface after the heating was not as good as the potassium particles on the K-chars. The simultaneous addition of the potassium and the calcium did not lead to a positive synergetic effect since the performances of the Ca+K-chars were below the mathematical average of the performances of the K-chars and Ca-chars. As far as the oxygenated biochars are concerned, conclusions on their influence are not straightforward. In fact, to get an understanding of the catalytic methane cracking on the oxygenated biochars, all the physico-chemical modifications have to be taken into account. The increase of the oxygenated functions tended to enhance the reactivity of the biochars. However, the specific surface area loss for the biochars oxygenated 8h at 280°C counterbalanced the positive effect of the increase of oxygen functions and did not lead to an increase of the initial hydrogen production.

Deactivation, due to coke deposit was observed for all the biochars. A strong decrease in the hydrogen production at the early stages of the reaction due to the loss of activity of the active sites and then a progressive stabilization were observed. Thus, two deactivation regimes have been identified. In the regime 1, the deactivation rate for the minerals impregnated biochars and the biochars oxygenated 2h at 280 and 340°C was 2 to 20 times higher than the one of the raw biochar. Then, the deactivation rate was lowered which led to a more stable hydrogen production. However,

the deactivation rate for the minerals impregnated biochars in the regime 2 remained 3 times higher than the one of the raw biochar. ESEM analyses highlighted coke deposit onto minerals and carbon surface of the biochars which should block the active sites and clog the pores.

- **Kinetics and modeling at the pore scale of the biochars surface deactivation and hydrogen diffusion into a micropore**

A global apparent kinetics study has been performed from a parametric study of the methane cracking on raw biochars at the laboratory scale (from 700 to 800°C), since the thermal methane cracking occurs at 850°C. It has been found that the reaction rate can be expressed such as equation of the first order regarding the methane partial pressure. The study also lead to determine the reaction rate constant ( $32 \text{ s}^{-1}$ ) and the activation energy (192 kJ/mol). The kinetics study highlighted that biochars could compete with other carbonaceous materials regarding methane cracking since its activation energy is similar to those found in the literature for activated carbons or carbon blacks.

A model of hydrogen production into a pore and deactivation of the surface have been proposed in order to get insights into the mechanism of coke deposit and its influence on the deactivation pattern of the hydrogen production. It has been shown that the hydrogen production is sensitive to the characteristics of the active sites such as their reaction rate and their initial surface coverage. Results of the models were in good agreement with the experimental data. Thus, it has been concluded that the increase in reactivity of a type of active sites or the increasing of its concentration at the surface leads to a significant increase of the hydrogen production in the early stages. However it also caused a stronger deactivation of the surface on stream.

The present study proposes a global investigation of the reactivity of the biochars for the catalytic methane cracking reaction. In fact, the characterization of the surface properties has been correlated to the catalytic performances during the methane cracking reaction to provide insights into their interactions. The experimental data of the methane cracking tests supported a kinetics study at the reactor scale and the development of a model at the pore scale. Thus, this work provides insights into the parameters which influence the methane cracking reaction (at the microscopic and macroscopic scales). It proposes different ways to enhance the reactivity of the biochars and also highlights the limits. Thus, this work contributes to a better understanding of the biochars surface reactivity. However, new questions arise from the present results and could be the subject of a new research project.

## 2. Prospects

The previous section summed up the main conclusions on this research work. However, new questions came up from the results obtained. This section is dedicated to the different prospects for future research investigations.

- **Characterization of the biochars surface over the methane cracking reaction**

In this study, characterization of the four physico-chemical surface properties depicted to be involved in the biochars catalytic role (oxygen groups, minerals, carbon matrix structure and textural properties) have been extensively studied at the initial point and the final point of the methane cracking tests. Some characterizations have been also performed on biochars which have been heated in the same conditions than for the methane cracking tests (under pure N<sub>2</sub>, up to 700°C with an heating rate of 20°C/min) but which have not been used for the catalytic reaction (the test has been stopped after the heating ramp). In the Chapter IV, these characterizations provided insights into the interactions between the biochars surface and the methane cracking reaction in the early stages of the reaction and their final state. However, it has been highlighted that the deactivation of the biochar surface followed two different regimes during the reaction: a faster deactivation during the first hour, followed by a progressive deactivation of the hydrogen production. To go further in the understanding of the deactivation process, it would be of great interest to perform additional characterizations after 1 hour of methane cracking. The four physico-chemical properties could be investigated with the same analytical tools already presented. These characterizations, coupled with those already obtained after two hours of treatment, should provide information to better understand the coke deposit mechanism.

In addition, the coke deposit has been highlighted to clog the pore. Thus, specific investigations regarding the textural properties evolution during the reaction should be carried out. A set of experimentations should consist in performing the same methane cracking tests and stop the reaction at different times to monitor accurately the evolution of the total pore volume, median pore diameter and specific surface area. Thus, it should provide information on the impact of the coke deposit on the pore volume evolution, its impact on the pore structure and the specific surface area.

- **Regeneration of the biochars surface after a methane cracking experiment**

Regeneration process is commonly performed to enhance the life-time of commercial metal-based catalysts. It consists in heating the deactivated catalyst under a specific atmosphere to get back to the surface of the fresh catalyst by removing the coke deposit. The regeneration can be performed in interweaving cycle of methane cracking and sequence of regeneration. According to the type of reaction and catalyst, the atmosphere used during the regeneration sequence can vary. A sequence of nitrogen, which is a non-reactive atmosphere, could enhance the reactivity by cleaning the micropore of the gas products which could favor the inverse reaction. Sequence under oxidative atmosphere such as steam, carbon dioxide or even air should react with catalyst [1], [2], [3]. The point is to determine, if the atmosphere reacts with the coke deposit or with structures from the catalyst surface.

Preliminary tests have been performed by introducing regeneration sequences under pure nitrogen in between methane cracking cycles. Three cycles of methane cracking (of 45 min each) at 700°C were carried out and were separated by sequence of 15 min under pure nitrogen. The hydrogen production has been monitored during the whole experiment using a gas chromatograph. Figure.P. 1 presents the hydrogen production during the three cycles. One can observe that the hydrogen production is directly stopped at the end of a 45 min cycle. The hydrogen production at the beginning of the cycles 2 follows the deactivation pattern observed during the cycle 1. No real amelioration due to the 15 min of nitrogen sequence was observed. The same observation could be highlighted for the cycle 3. Thus, the introduction of a regeneration cycle under pure nitrogen was not satisfying to enhance the reactivity of the biochars.

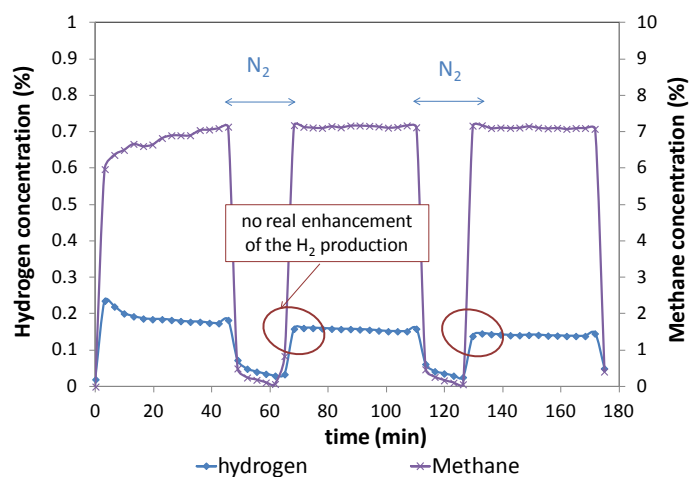


**Figure.P. 1: Three cycles of methane cracking of 45 min with in between sequences of 15 min of pure nitrogen, 7% CH<sub>4</sub>/93% N<sub>2</sub>, 15 mL/min, 700°C, 50 mg raw biochar**

A second test was performed under steam. This test was carried out in a thermogravimetric analyzer on a biochar which has been utilized in a previous catalytic methane cracking test at 700°C during two hours. The biochar has been heated up to 700°C with an heating rate of 20°C/min under a mixture of nitrogen and steam with a relative humidity of 50% at 40°C. Figure.P. 2 presents the mass loss during the regeneration step. On Figure.P. 2, a total mass loss of 7 wt% at the end of the test is observable which means that the steam reacted with the biochars surface. The dTG curve shows that reactions occurred at 100°C (drying; 0.5 wt% loss) and at 650°C (1.9 wt% loss) which should results from the reaction of the steam with the biochar surface. In addition, during the heating and the plateau at 700°C, mass losses were registered (4.1 and 1.8 wt%) which should also correspond to reactions of the biochar surface with steam. However, the mass loss could be due to gasification reaction (or devolatilization of some remaining volatile organics) or it could be due to the removal of the carbon deposit. It is not possible to conclude on the type of reaction with the present results. An experimental protocol should be developed to perform in a row a methane cracking cycle with steam regeneration sequences in between. The tests should be performed in the thermogravimetric instrument coupled with a micro gas chromatograph analyzer to be able to correlate the mass loss with the gas production. In addition, the mass gain during the methane cracking due to carbon deposit and the mass loss during the regeneration step should be compared. Thus, this preliminary test highlighted that the steam regeneration could be efficient. In addition, literature highlighted the regain of efficacy of catalyst after a steam regeneration treatment [4]. Thus, further research works should be performed to develop an adapted method to evaluate the performances of the regeneration process.

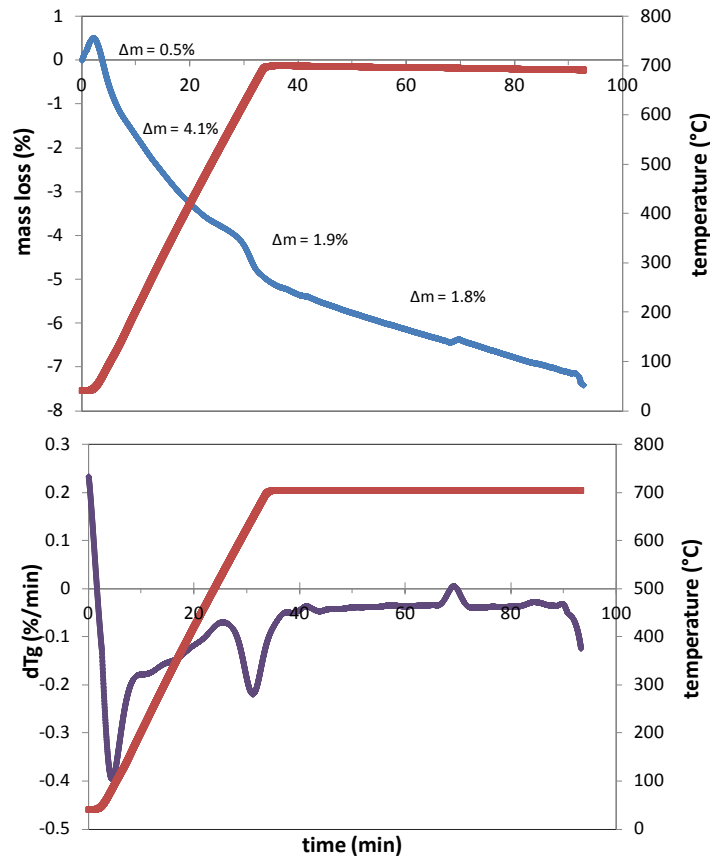


**Figure.P. 2: Mass loss and derivative during the regeneration step of deactivated raw biochar catalyst (utilized for a 2h methane cracking test at 700°C), 10 mg, 50% relative humidity at 40°C, 20°C/min, 700°C, 1h.**

- **Dry and steam methane reforming under biochars**

In this study, catalytic methane cracking tests have been performed on biochars without gaseous co-reactant, in order to get better insights into the interaction of the biochars surface with the methane molecule. However, it has been highlighted that the deactivation of the surface occurred quickly. The previous paragraph, in this Prospect section, proposed to perform regeneration steps using an oxidant atmosphere, in between methane cracking cycles, to remove the coke deposit. However, a second option which consists in directly introducing the oxidant gas with the methane to perform the methane cracking reaction could be considered. Steam reforming of methane on metal based catalysts is a well-known process which has been industrialized since the early 20<sup>th</sup> century to notably produce hydrogen and methanol. The equation reaction is presented in Eq.C. 1, it is an endothermic reaction which required high temperature ( $T > 800^{\circ}\text{C}$ ). The steam reforming of methane, in stoichiometric conditions, leads to a  $H_2/CO$  ratio of 3 [5].



From several years, a growing interest for the dry reforming (using  $CO_2$  as oxidant reactant) is observed. In fact, both reactants  $CO_2$  and  $CH_4$  are greenhouse gases. The dry reforming could be a way to mitigate the climate change and to produce high energetic syngas. In addition, the reaction (presented in Eq.C. 2) leads to obtain a  $H_2/CO$  ratio of 1 which could be further utilized in carbonylation processes. Some researches investigations have been performed on the dry reforming. Fidalgo et al. [6] (presented in the Chapter I) published a review on the dry reforming of methane on carbonaceous catalysts.



The dry reforming is more endothermic than the steam gasification which means that higher temperature is required to perform the reaction. In addition, sintering of the catalyst due to the high temperature has been also reported. Hence, the dry reforming is a promising reaction. However, due to the different issues presented this reaction is less industrialized than the steam reforming.

Thus, steam and dry reforming present advantages and drawbacks. The choice of the co-reactant should be done in function of the further applications and according to the operating conditions limitations.

- **Improvement of the modeling at the pore scale**

In this study, we proposed a modeling at the pore scale to better understand the deactivation process of the biochar surface and the hydrogen diffusion into the micropore during the methane cracking reaction. However, some parameters required to develop the model such as the intrinsic reaction rate constants and the initial surface covered by each type of catalysts were not known. Thus, in a first approach, some assumptions have been made to develop the modeling. To improve the model results, additional experiments should be performed to determine these parameters. For example, to obtain the intrinsic reaction rate of the oxygen groups and the minerals functions, a set of catalytic methane cracking experiments should be carried out on the functionalized biochars. The

set of experiments could be similar to the one presented in the Chapter V on the raw biochar (varying the methane partial pressure and temperature). The experimental data could be then used to perform a kinetics study. However, to obtain the intrinsic kinetics parameter, a Langmuir-Hinshelwood model should be rather used than a Power Law equation. In fact, Langmuir-Hinshelwood model is based on the reaction mechanism at the catalyst surface. It describes the kinetics expression of the limiting step in the methane cracking reaction. Thus, once these reaction rate constants are determined they could be introduced in the modeling.

This “Prospect” section provides 4 development paths to go further in the understanding of the biochars reactivity, the deactivation mechanism and the enhancement of its long-term stability. The different suggestions can be studied separately. The associated researches are of great interest since they would take part of a global project to enhance the competitiveness of the gasification technology.

## Bibliography

- [1] L. Bednarczuk, P. Ramírez de la Piscina, and N. Homs, “H<sub>2</sub>-production from CO<sub>2</sub>-assisted ethanol steam reforming: The regeneration of Ni-based catalysts,” *Int. J. Hydrogen Energy*, vol. 40, no. 15, pp. 5256–5263, 2015.
- [2] R. Aiello, J. E. Fiscus, H.-C. zur Loye, and M. D. Amiridis, “Hydrogen production via the direct cracking of methane over Ni/SiO<sub>2</sub>: catalyst deactivation and regeneration,” *Appl. Catal. A Gen.*, vol. 192, no. 2, pp. 227–234, 2000.
- [3] K. Lipiäinen, P. Hagelberg, J. Aittamaa, I. Eilos, J. Hiltunen, V. . Niemi, and a. O. . Krause, “Novel equipment for testing catalytic cracking and catalyst regeneration with short contact times,” *Appl. Catal. A Gen.*, vol. 183, no. 2, pp. 411–421, 1999.
- [4] A. M. Amin, E. Croiset, and W. Epling, “Review of methane catalytic cracking for hydrogen production,” *Int. J. Hydrogen Energy*, vol. 36, no. 4, pp. 2904–2935, 2011.
- [5] A. Rakib, “Valorisation du méthane en hydrogène par reformage catalytique,” 2013.
- [6] B. Fidalgo and J. Á. Menéndez, “Carbon materials as catalysts for decomposition and CO<sub>2</sub> reforming of methane: A review,” *Chinese J. Catal.*, vol. 32, no. 1, pp. 207–216, 2011.

# Appendix.1:

## Matlab program for the numerical solving of the hydrogen diffusion into a micropore

- **Main program:**

```

clear all
close all

% Diffusion coefficient H2
MH2=0.002; % Molar mass kg/mol
T=973; % K (700C)
rporei=0.7e-9; % Pore radius m (7 A)
R=8.314; % Gas constant J/mol.K
DKnudH2= 2/3*rporei*sqrt(8*R*T/(pi*MH2)); % Knudsen coef m2/s 700°C
tau= rporei*rporei/DKnudH2;

% Geometry
% pore
dpore= 1.4e-9; % Pore diameter m (1,4nm)
lpore= 1.4e-8; % Pore length m (14 nm)

% carbon atom
dcarbon= 140.0e-12; % Carbon particle diameter m
Scarbon= pi* (dcarbon/2)^2; % Carbon particle surface m

%Source term : reaction at the pore surface
% reaction rate constant
k0=32; % Initial coefficient
(exp)s-1
x1=9/10; % active site reactivity 1
x2=1/10; % active site 2 reactivity
k1=x1*k0; % reaction rate const site
1
k2=x2*k0; % reaction rate const site
2

% calculation of the term a
Ssp= 600e3; % Ssp chars m2/kg
rhotrue= 1800; % true density chars kg/m3
epspart= 0.9; % particle porosity
epsplit= 0.4; % bed particle porosity
a= Ssp*rhotrue*(1-epspart)*(1-epsplit); % m-1

CCH40= 0.876; % initial CH4 conc mol/m3
Na= 6.02e23; % Avogadro number mol-1
Stotpore= pi*(dpore/2)^2+2*pi*(dpore/2)*lpore % total pore surface m2

```

## Appendix

---

```
% space mesh
e=dcarbon;
M= floor(dpore/e);
N= floor(Lpore/e);
M2= M*N;

% time mesh :
Deltat = 1e-12;
sigmaC = Deltat*DKnudH2/(e*e);
eq

nsec = 1 * 1e-12;
Nt = floor(nsec/Deltat);

% Jacobian matrix
A=jacobpore (M,N, sigmaC);

% initialisation
CCH2sortie=zeros (M,Nt);
CH2 = zeros (M2,1);
CH2surf=0;
t = 0;
S1init= 1/2*Stotpore;
S2init= 1/2*Stotpore
S1=1/2*Stotpore;
S2=1/2*Stotpore;
Sc1=0;
Sc2=0;
SCc=0;

% Loop "for"
for k=1:Nt
    t = t + Deltat;

    if Sc1 < S1init

        SCc= pi*(dcarbon/2)^2*Na*(k1*S1+k2*S2)/a*CCH40*(Deltat)+SCc;

        Sc1=x1*SCc;
        Sc2=x2*SCc;

        S1=S1init-Sc1;
        S2=S2init-Sc2;

    else

        S1=0;
        SCc= pi*(dcarbon/2)^2*Na*(k2*S2)/a*CCH40*(Deltat)+ SCc;
        Sc2=SCc-Sc1;

        k1=0;
        S2=S2init-Sc2;

    end

    B = secmembrepore (M,N, sigmaC, CH2surf, CH2); % 2nd member calculations
```

```

CH2=A\B % H2 conc in the pore at
t
CCH2=reshape(CH2,M,N); % restructuration for fig
pcolor(CCH2); % figure
shading interp % figure
drawnow % figure
CCH2sortie(:,k)=CH2(M2-M+1 : M2); % storage H2conc output
pore

SCcsortie(:,k)= SCc;
CH2surfsortie(:,k)= CH2surf;
tsortie(:,k)=t;
Ntsortie(:,k)=k;
Sc1sortie(:,k)= Sc1;
Sc2sortie(:,k)= Sc2;
S1libre(:,k)=S1;
S2libre(:,k)=S2;
k1sortie(:,k)=k1;
k2sortie(:,k)=k2;

end

```

- **Program for second member calculation B:**

```

function B=secmembre(M,N,sigmaC,CH2surf,CH2)

M2 = M*N;
k=1:M;
k3=1:N;
B=zeros(M2,1); % init 0 colum dim N*M=M2
B(k)=B(k) + CH2surf; % surface reaction
B(M*(k3-1)+1) = B(M*(k3-1)+1) + CH2surf;
B(M*k3) = B(M*k3) + CH2surf;
B(M2-M+k) = B(M2-M+k) ;
B=CH2+sigmaC*B; % final descon member

```

- **Calculation of the Jacobian matrix A:**

```

function A=jacobpore(M,N,sigmaC)

M2 = M*N;
k = 1:M;
k2 = 1:M2;
k3 = 1:N;
km = 1:(M2-1);
kmm = 1:(M2-M);
F = sparse(k2,k2,4,M2,M2) ...
+ sparse(km+1,km,-1,M2,M2) ...
+ sparse(km,km+1,-1,M2,M2) ...
+ sparse(kmm+M,kmm,-1,M2,M2) ...
+ sparse(kmm,kmm+M,-1,M2,M2);
F(M*(k3-1)+1,M*k3)=0;
F(M*k3,M*(k3-1)+1)=0;

spy(F)
I=sparse(k2,k2,1,M2,M2);
A=I+sigmaC*F;

```



# Nomenclature

## Abbreviation

BET	Brunauer, Emmett and Teller
ESEM	Electron Scanning Environmental Microscopy
EDS	Electron Dispersive Spectroscopy
FTIR	Fourier Transform InfraRed
TEM	Transmission Electron Microscopy
TPD	Temperature Programmed Desorption
XRD	X-Ray Diffraction
XRF	X-Ray Fluorescence

Symbol	Definition	Unit
$\alpha$	methane partial order	-
$\varepsilon$	porosity	-
$\theta$	angle	°
$\theta_a$	coverage of adsorbate a	-
$\lambda$	wavelength	m
$\mu$	viscosity	Pa.s <sup>-1</sup>
$\xi$	adsorbate cross sectional area	m <sup>2</sup>
$\pi$	Pi number	
$\rho$	density	kg.m <sup>-3</sup>
$\sigma$	adimensional number $\frac{\Delta t \cdot D_{Knud}}{e^2}$	-
$\tau$	tortuosity	-
$\tau_{dif}$	characteristic time of diffusion	s
$\psi$	shape factor	-

Indice	Definition
a	adsorbate
ads	adsorption
app	apparent
b	bed
c	carbon
des	desorption
eq	equivalent
g	gas
Knud	Knudsen
l	free
mf	minimum fluidization
p	particle
r	reaction
surf	surface
tot	total

0 initial

Symbol	Definition
div	operator divergence
grad	operator gradient

Symbol	Definition	Unit
a	particle surface area per unit volume packed bed	$\text{m}^{-1}$
C	concentration	$\text{mol.m}^{-3}$
d	diameter	m
D	diffusion	$\text{m}^2.\text{s}^{-1}$
e	spatial mesh	-
$f_1$	factor 1 : initial active site surface distribution	-
$f_2$	factor 2 : distribution active site reactivity distribution	-
F	molar flow rate	$\text{mol.s}^{-1}$
G	Gibbs free energy	$\text{J.mol}^{-1}$
H	enthalpy	$\text{J.mol}^{-1}$
k	reaction rate constant	(depend)
K	equilibrium constant	-
L	length	m
m	mass	kg
M	molecular mass	$\text{mol.kg}^{-1}$
$\dot{N}$	molar flux	$\text{mol.m}^{-2}.\text{s}^{-1}$
Na	Avogadro number	$\text{mol}^{-1}$
n	number of moles	mol
P	pressure	Pa
$P_0$	saturation vapour pressure	Pa
r	reaction rate	$\text{mol.m}^{-3}.\text{s}^{-1}$
R	gas constant	$\text{J.mol}^{-1}.\text{K}^{-1}$
S	entropy	$\text{J.kg}^{-1}.\text{mol}^{-1}$
S tot or	surface	$\text{m}^2$
t	time	s
T	temperature	K
U	speed	$\text{m.s}^{-1}$
V	volume	$\text{m}^3$
X	conversion rate	-

# List of Figures

Figure I-1: Van Krevelen diagram which compares the chemical composition of different fuels .....	10
Figure I-2: Reaction scheme of biomass pyro-gasification [8] .....	13
Figure I-3: Scheme of an Updraft and Downdraft gasifiers [5] .....	18
Figure I-4: Scheme of fluidized bed gasifiers design: a) bubbling FBG and b) circulating FBG [17] .....	19
Figure I-5: Illustration of the armchair and zig-zag configurations of graphene.....	22
Figure I-6: Illustration of turbostratic and graphite structures .....	22
Figure I-7: Three different point defects in graphene: (a) a mono-vacancy defect, (b) a di-vacancy defect, and (c) a Stone-Wales defect [29].....	22
Figure I-8: Fitting of Raman spectrum and functions distributions adapted from [33].....	23
Figure I-9: Example of functional groups that can potentially exist on the biochar surface [40] .....	26
Figure I-10: Schematic presentation of different matrix types (a) non-porous particle (b) microporous particle (c) macroporous particle [42].....	27
Figure I-11: Illustration of the types of pores [35] .....	27
Figure I-12: Yields of char, gas and liquid on dependence of heating temperature from fluidized-bed during fast pyrolysis (empty symbol) and slow pyrolysis (full symbol) [9] .....	29
Figure I-13: Modification of the biochar carbon structure versus temperatures [43], [26] .....	30
Figure I-14: Changes in Raman spectra during the gasification of char in air at 400°C in TGA (height-normalised Raman intensity [49] .....	33
Figure I-15: General scheme of the potassium catalyzed water vapour gasification: $KxOy+$ , and $KxOy-$ do not necessarily mark the same species [61] .....	35
Figure I-16: Reactivity towards steam for 14 biomass biochars with respect to AAEM content Group I: $[K] + [Na] > [Ca]$ , group II $[Ca] > [K] + [Na]$ , group III high $[SiO_2]$ [68].....	35
Figure I-17: Relationship between mobility of particles supported on graphite and their bulk melting temperatures [73] .....	37
Figure I-18: Illustration of the energetic barrier in the non-catalyzed and catalyzed reactions.....	44
Figure I-19: Hydrogen production (%vol) for the different catalysts tested, T:850°C, methane flow:20 mL/min [113].....	47
Figure I-20: Catalytic performance of different char samples for methane cracking [19].....	48
Figure I-21: Catalyst deactivation for $CH_4$ cracking reaction [19] .....	49
Figure I-22: Carbon deposited per initial catalyst mass for the runs carried out at 900°C until deactivation versus surface area (left axis) and versus total pore volume (right axis) of the fresh catalyst [112] .....	50
Figure I-23: Initial activity from methane conversion and carbon accumulated as a function of the BET surface area of the fresh catalyst T=850°C [111] .....	50
Figure I-24: Initial decomposition rate versus amount of surface oxygenated groups desorbed in TPD runs as CO (left axis) and $CO_2$ (right axis) [112].....	52
Figure I-25: Comparison of $H_2$ productions from the catalytic cracking of methane on ash, char and char that has been heated to 1000°C prior to the reaction [19] .....	53
Figure I-26: Change of the XRD pattern (a) and $d_{002}$ (b) during the test carried out at T=950°C and GHSV=360 $h^{-1}$ (gas hourly space velocity) [110].....	54

Figure II-1: Picture of poplar wood chips .....	65
Figure II-2: Picture of the fluidized bed at RAPSODEE center .....	66
Figure II-3: scheme of the fluidized bed reactor .....	67
Figure II-4: The different regions of fluidization according to the gas velocity [1] .....	69
Figure II-5: Temperature profile for the pyro-gasification of poplar wood chips in the fluidized bed .	70
Figure II-6: Recorded temperatures in the reaction zone during the poplar wood pyro-gasification at 750°C during 30 min under a mixture of 90% H <sub>2</sub> O / 10% N <sub>2</sub> .....	70
Figure II-7: Wet impregnation of the poplar wood chips.....	71
Figure II-8: Chembet Pulsar TPD instrument from Quantachrome company.....	72
Figure II-9: Scheme of the plug flow reactor (Chembet instrument coupled with the micro gas chromatograph) .....	72
Figure II-10: Temperature program of the oxygenation in the Chembet Reactor coupled with the micro gas chromatograph .....	73
Figure II-11: Temperature program of the preliminary methane cracking tests on raw biochars in the ChemBet instrument .....	75
Figure II-12: Temperature program of the methane cracking experiments .....	76
Figure II-13: Dupont Thermogravimetric Analyzer (TGA) used for methane cracking tests over a bed of biochars .....	77
Figure II-14: Scheme of the experimental device used in the methane cracking experiments over a bed of biochars (Dupont TGA + gas chromatograph) .....	77
Figure II-15: Hydrogen production during methane cracking in the TGA (700°C, 80 mL/min, 10% CH <sub>4</sub> /90% N <sub>2</sub> ).....	78
Figure II-16: Figure of biochars from poplar wood pyro-gasification .....	79
Figure II-17: Scheme of the X-ray fluorescence phenomenon ©Copyright Amptek [4].....	81
Figure II-18: Illustration of the adsorption isotherm of type I characteristic from the microporous material according to the IUPAC classification [7]).....	84
Figure II-19: Scheme of CO and CO <sub>2</sub> peak assignments desorption versus temperature (from gas chromatograph analyses).....	89
Figure II-20 : Example of Curve-fitting of the TCD signal during TPD (TPR Win Software® Pulsar) .....	90
Figure II-21: Raman active modes .....	92
Figure II-22: Example of Raman spectrum deconvolution using the Peakfit program on Matlab® .....	93
Figure II-23: Illustration of the different parts of a Transmission Electron Microscope .....	96
Figure III-1: FTIR spectrum of the raw biochar .....	102
Figure III-2: TPD analysis of the raw biochar (empty symbol CO <sub>2</sub> ; full symbol CO) and corresponding temperature ranges of oxygenated functions (underlined text: functions desorbing into CO; not underlined text: functions desorbing into CO <sub>2</sub> ) .....	103
Figure III-3: Distribution of the oxygenated functions at the raw biochar surface.....	104
Figure III-4: X-ray diffraction pattern of the raw biochar.....	105
Figure III-5: ESEM pictures of the minerals dispersion at different locations of the raw biochar surface and with different magnitudes.....	106
Figure III-6: Illustration of Raman spectra of ordered structures: graphene and graphite [6] .....	107

Figure III-7: Illustration of a Raman spectrum deconvolution of the raw biochar into 10 peaks using the Matlab® software.....	108
Figure III-8: Distribution of main carbon structures in the raw biochar .....	109
Figure III-9: Adsorption isotherm of argon on raw biochar (at 77 K after 20h of outgassing at 200°C).....	109
Figure III-10: Scheme to sum up the physico-chemical surface properties of the raw biochar .....	111
Figure III-11: Scheme of the characterizations which have been performed during and post O <sub>2</sub> gas-phase treatment.....	112
Figure III-12: Gas production during the oxygenation at 400°C during 2h: (A) CO <sub>2</sub> gas production during the heating under inert atmosphere up to the oxygenation temperature; (B) CO <sub>2</sub> and CO productions during the oxygenation.....	113
Figure III-13: FTIR spectra of the raw and oxygenated biochars.....	114
Figure III-14: TPD profiles of the raw and oxygenated biochars at 280°C for 2, 4, 8 and 16h: a) peak assignment (underlined text: functions desorbing into CO; not underlined text: functions desorbing into CO <sub>2</sub> ); b) CO <sub>2</sub> desorption; c) CO desorption.....	115
Figure III-15: Distribution of the oxygenated functions (mol%) for the raw biochar (left) and biochar oxygenated at 280°C during 8h (right) .....	117
Figure III-16: TPD profiles of the biochars oxygenated at 280, 340 and 400°C for 2h: a) peak assignment (underlined text: functions desorbing into CO; not underlined text: functions desorbing into CO <sub>2</sub> ); b) CO <sub>2</sub> desorption; c) CO desorption .....	118
Figure III-17: Distribution of the oxygenated functions (mol%) for the biochars oxygenated at 340°C (left) and 400°C (right).....	119
Figure III-18: X-ray patterns of the oxygenated biochars.....	121
Figure III-19: Raman spectra of the raw biochars and the biochars oxygenated at 280°C.....	123
Figure III-20: Evolution of the main carbon structures over the oxygenation at 280°C .....	124
Figure III-21: Raman spectra of the raw biochars and biochars oxygenated for 2h at 280, 340 and 400°C .....	125
Figure III-22: Evolution of the main carbon structures for raw biochar and biochars oxygenated at 280, 340 and 400°C for 2 hours.....	126
Figure III-23: Bright field TEM images of samples (A) raw_char, (B) ox2h_280C, (C) ox2h_400C, and (D) ox8h_280C. Insets: corresponding SAED patterns.....	127
Figure III-24: HRTEM images of samples raw_char (A), ox2h_280C (B), ox2h_400C (C), and ox8h_280C.....	128
Figure III-25: Illustration of the physico-chemical properties modifications over the oxygenation process for different times at 280°C .....	131

Figure IV-1: Comparison of the hydrogen production from the methane cracking at 700°C, 10%CH <sub>4</sub> on the raw and mineral impregnated biochars.....	156
Figure IV-2: Comparison of the hydrogen production during the methane cracking at 700°C, 20% CH <sub>4</sub> for the raw and oxygenated biochars .....	158
Figure IV-3: Illustration of the initial active sites role and the potential clogging by carbon deposit .....	160
Figure IV-4: Relation between the surface properties and the initial hydrogen production.....	161
Figure IV-5: Normalized initial hydrogen production (mol <sub>H<sub>2</sub></sub> /mol <sub>CH<sub>4</sub></sub> /mg <sub>char</sub> ) versus textural properties (A) specific surface area, (B) total pore volume and (C) average pore diameter of the biochars at t <sub>0</sub> (which have been characterized in the Chapter III) .....	163

Figure IV-6: Carbon structures at the biochars surface.....	164
Figure IV-7: Normalized initial hydrogen production versus "in-plane" defects amount in the carbon matrix of biochars at $t_0$ .....	165
Figure IV-8: Normalized initial $H_2$ production versus ratios of "in-plane" defects over the different others main carbon structures: (A) graphite, (B) small aromatic rings and (C) aliphatic chains of the biochars at $t_0$ .....	166
Figure IV-9: Scheme of the possible mechanism of lactone desorption during heating and the remaining charged carbon structures .....	168
Figure IV-10: Scheme of the quinone attraction of the hydrogen atom from the methane molecule .....	168
Figure IV-11: Normalized moles of (A) $CO_2$ and (B) CO produced during the heating of the raw and oxygenated biochars up to the reaction temperature at $700^\circ C$ with $20^\circ C/min$ .....	169
Figure IV-12: Normalized (A) $CO_2$ and (B) CO productions ( $mol/mg_{char}$ ) during the heating up to $700^\circ C$ prior to methane cracking on the raw and functionalized biochars .....	170
Figure IV-13: Normalized hydrogen production versus oxygenated functions desorbed during the heating prior to methane introduction (A) $CO_2$ , (B) CO .....	171
Figure IV-14: Comparison of the TPD curves of the raw biochars and biochars oxygenated at $280^\circ C$ (2 and 8h) and at $340^\circ C$ 2h and the remaining oxygenated functions at $700^\circ C$ .....	172
Figure IV-15: Hydrogen and carbon monoxide productions during the methane cracking at $700^\circ C$ , 20% $CH_4$ on the raw biochars .....	172
Figure IV-16: Comparison of the initial hydrogen productions ( $mol_{H_2}/mol_{CH_4}/mg_{char}$ ) of the different mineral impregnated biochars in function of their calcium and potassium loading (wt%) .....	174
Figure IV-17: Minerals transformations during the heating for K-chars and Ca-chars and the minerals composition at $t_0$ and $t_1$ .....	175
Figure IV-18: ESEM pictures of the needle-shaped $K_2CO_3$ crystals on the K-chars surface at different locations of the surface and for different magnitudes: (A) x800, (B) x1600, (C) x3200, (D) x 6400 at $t_1$ .....	176
Figure IV-19: ESEM images of (A) Ca-chars and (B) K-chars for a magnitude x1600 at $t_1$ .....	177
Figure IV-20: ESEM pictures at different locations of the Ca+K-chars at $t_1$ .....	178
Figure IV-21: Interaction between deactivation and modification of the surface properties .....	180
Figure IV-22: Methane cracking reaction on raw and minerals impregnated biochars in a thermogravimetric analyzer: (A) cumulative hydrogen production, (B) mass gain .....	181
Figure IV-23: ESEM pictures of the carbon deposit at the surface of the (A) Ca-chars and (B) Ca+K-chars after 2h (at $t_f$ ) of methane cracking at $700^\circ C$ .....	181
Figure IV-24: ESEM pictures of the raw biochars after 2h (at $t_f$ ) of methane cracking at $700^\circ C$ .....	182
Figure IV-25: Comparison of the hydrogen and carbon monoxide productions for the (A) raw chars and (B) biochars oxygenated 2h at $340^\circ C$ during the methane cracking for 2h at $700^\circ C$ .....	183
Figure IV-26: Illustration of the main conclusions on the interaction between the physico-chemical properties and the biochars reactivity .....	187
Figure V-1: Different scales for modeling.....	192
Figure V-2: Mass balance on a section $dV$ of the plug flow reactor .....	193

Figure V-3: Comparison of the hydrogen production in function of (A) the methane partial pressure (0.07, 0.15 and 0.21 bar) and (B) the temperature (650, 700 and 800°C) for 50 mg of biochars (residence time 1.8 s) and a total flow rate of 15 mL/min.....	196
Figure V-4: Plot of $\ln(r_0)$ in function of $\ln(C_{CH_4,0})$ for the determination of the methane partial pressure ( $\alpha$ ) and the reaction rate constant ( $k_0$ ).....	197
Figure V-5: Plot of $\ln(k_0)$ in function of $1/T$ to determine the activation energy ( $E_a$ ).....	197
Figure V-6: Fit of the mass gain over time during the methane cracking on raw biochars at 700°C during 2h (80 mL/min, 10% CH <sub>4</sub> /90%N <sub>2</sub> ).....	198
Figure V-7: Illustration of the methane reaction at the pore wall which produces hydrogen and coke deposit.....	199
Figure V-8: Scheme of the reaction process in a porous catalyst [3].....	200
Figure V-9: Illustration of the 2-D model of hydrogen concentration evolution into a cylindrical-shaped pore over time .....	203
Figure V-10: Scheme of the three phases in the pore model .....	204
Figure V-11: Hydrogen concentration profile into a micropore: $d_{pore} = 1.4$ nm, $L_{pore} = 14$ nm, 1 <sup>st</sup> iteration (1s) .....	214
Figure V-12: Diffusion into a micropore for two different times of 1 <sup>st</sup> iteration: (A) $t = 1e^{-13}$ s, .....	215
Figure V-13: Mean hydrogen production at the output pore over time (during phase 1 and 2) for different initial distribution of the two types of active sites ( $f_2: \frac{1}{4}, \frac{1}{2}$ and $\frac{3}{4}$ ), $f_1 = 1/2$ , $d_{pore} = 1.4$ nm, $L_{pore} = 14$ nm .....	216
Figure V-14: Experimental results for the raw and K-chars .....	218
Figure V-15: Influence of the difference of reactivity of the actives sites ( $f_1: 2/3, 4/5, 9/10$ ), $f_2 = 1/2$ , $d_{pore} = 1.4$ nm, $L_{pore} = 14$ nm .....	219
Figure V-16: Experimental data, hydrogen production during methane cracking on raw biochar, Ca-char and K-char .....	220

## **Gasification biochar reactivity toward methane cracking**

This study is focused on the reactivity of biochar to catalyze the methane cracking reaction. Biochar was produced from steam gasification of poplar wood (750°C, 30 min, 20°C/min, 90% $H_2O$ /10% $N_2$ , fluidized bed) and then functionalized by an  $O_2$  gas-phase treatment and a wet impregnation into nitrate salts solutions to increase oxygen functions and minerals (calcium and potassium) concentrations at the biochar surface respectively. A set of characterization was performed on the raw and functionalized biochars to evaluate their surface physico-chemical properties. The oxygenated functions, the mineral particles, the carbonaceous structures and the textural properties (specific surface area and porosity) were analyzed. Results showed that the two functionalization treatments increased the concentration of the targeted functions and modified the carbon structures and the textural properties as well. Methane cracking tests were then performed on the biochars to compare their activities and correlate with their physico-chemical properties. It has been highlighted the minerals particles of potassium and calcium are the main active sites of the biochar surface. In fact, the reactivity of the impregnated biochars was twice to 4 times higher than the one of the raw biochar. The porosity of the biochar is the second most important criteria to notably obtain a good dispersion of the minerals particles. Basic oxygenated functions and disordered carbonaceous structures (defaults into the graphene sheets) are reactive as well. However, coke deposition progressively deactivated the biochars surface over the reaction in any case. A model at the pore scale has been proposed to better understand the surface deactivation.

Keywords: Biochar, Reactivity, Functionalization, Surface Characterization, Methane Cracking, Deactivation

## **Etude de la réactivité du biochar issu de la gazéification : application à la réaction du craquage du méthane**

Cette étude porte sur la compréhension et l'amélioration de la réactivité des charbons pour la catalyse de la réaction du craquage du méthane. Pour ce projet, nous avons produit des charbons à partir de la gazéification de bois de peuplier à 750°C sous vapeur d'eau. Par la suite, deux traitements de fonctionnalisation ont été appliqués. D'une part, une oxygénation en phase gaz a été réalisée pour augmenter la concentration des sites oxygénés. D'autre part, une imprégnation en phase liquide dans différentes solutions de sel de nitrate (calcium et potassium) a permis d'accroître la quantité de minéraux. Les propriétés physico-chimiques (structure carbonée, sites oxygénés, minéraux et porosité/surface spécifique) des charbons bruts et fonctionnalisés ont été caractérisées. Les résultats ont montré que les deux traitements de fonctionnalisation ont augmenté la concentration des sites actifs visés. Par ailleurs, les évolutions des propriétés texturales et de la structure carbonée lors des deux fonctionnalisations ont été mises en évidence. Les tests catalytiques du craquage du méthane sur les différents charbons, à 700°C, ont montré que les minéraux sont les sites les plus réactifs vis-à-vis de cette réaction. Les fonctions oxygénées basiques et les défauts de structure sont également des sites actifs. Une diminution de l'efficacité lors du craquage a été observée due à la désactivation progressive de la surface des biochars. Le développement d'un modèle, à l'échelle du pore, a permis de montrer que la concentration initiale de sites actifs à la surface et leur différence de réactivité étaient deux paramètres importants dans la prédiction du comportement de désactivation de la surface.

Mots clés : Charbon, Réactivité, Fonctionnalisation, Caractérisation de Surface, Craquage du Méthane, Désactivation